

NO9605292

LARS KETIL HEILL

NEI - NO -- 674

MAGNETIC PROPERTIES OF HIGH
TEMPERATURE SUPERCONDUCTORS
AC SUSCEPTIBILITY AND MAGNETOSTRICTION STUDIES

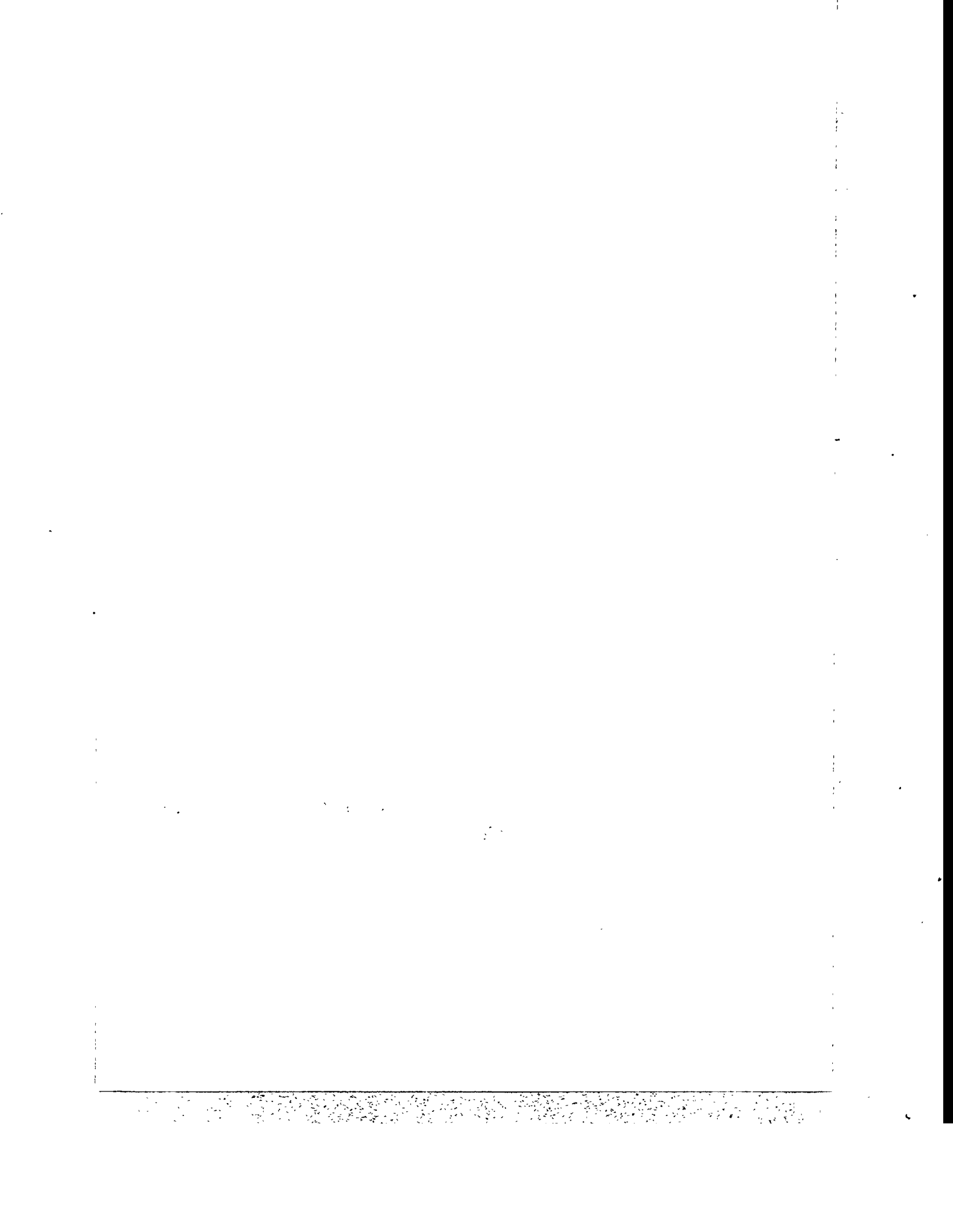


NTH
UNIVERSITETET I TRONDHEIM
NORGES TEKNISKE HØGSKOLE

DOKTOR INGENIØRAVHANDLING 1995:44
INSTITUTT FOR FYSIKK
TRONDHEIM

DISTRIBUTION OF THIS DOCUMENT IS UNLIMITED

RB



NEI-No--674

Lars Ketil Heill

**Magnetic properties of
high temperature superconductors**

ac susceptibility and magnetostriiction studies

Trondheim, May 1995

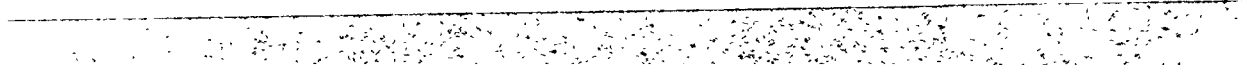
DISTRIBUTION OF THIS DOCUMENT IS UNLIMITED

A thesis submitted to The University of Trondheim, The Norwegian Institute of Technology
in partial fulfillment of the requirements for the degree of Dr.Ing.

MASTER

DISCLAIMER

**Portions of this document may be illegible
in electronic image products. Images are
produced from the best available original
document.**



Preface

This thesis comprises the results of my work on magnetic properties of high temperature superconductors at the Department of physics at the Norwegian Institute of Technology in Trondheim from March 1991 to February 1995, and at The University of Tokyo from January to March in 1993.

In Trondheim my interest has been concentrated on the ac magnetic response of the melt-powder-melt-growth (MPMG) $\text{YBa}_2\text{Cu}_3\text{O}_7$ with Y_2BaCuO_5 insulating inclusions and single crystal $\text{YBa}_2\text{Cu}_3\text{O}_7$ materials. During the stay in Tokyo I studied magnetostriction, size changes, in the $\text{Bi}_2\text{Sr}_2\text{CaCu}_2\text{O}_8$ material. The length of the time periods above are reflected in this thesis as the major part is on the work on ac magnetic response, Chapters 3 to 11, whereas the final Chapter 12 presents the results on magnetostriction.

I entered the lively and confusing field of superconductivity in 1991 without any experience in experimental work. The transiton proved surprisingly smooth, and I owe much of that to cooperation and helpful and friendly attitudes of my coworkers.

Acknowledgements

Thanks are due to my adviser professor Kristian Fossheim who let me into his group and serious research in physics, and who provided the opportunity to visit Tokyo.

All my friends and colleagues from the years in the superconductivity group deserve special thanks for all the collaboration, help, fun and sharing of problems: Marcin Slaski, Lise T. Sagdahl and Michael G. Karkut who I worked closely with on the ac magnetic experiments; Pål Tuset and Olav Magnar Nes

deserve special thanks in particular for valuable help in the lab; Ellen D. Tuset has always been a joy to work with; Svein Gjølmesli, Wu Ting and all our students have given their share to the life of our group. Extra special thanks go to Michael for being a great guy in an out of the lab!

Thanks are due to Alse Sudbø and to Valerii M. Vinokur for their inspiring lecture series in the fall of 1991, and for their valuable input to our work, then and later.

Invaluable technical assistance has been provided by Rolf Dahl, Kjell Ramsøskar, Arnold Bjølstad and his staff the mechanical workshop and the staff at the electronics workshop.

The MPMG sample was kindly provided by M. Murakami, H. Fujimoto, N. Koshizuka and S. Tanaka at ISTEC SRL in Tokyo, and the single crystal was supplied by F. Gencer, J. S. Abell and C. E. Gough at the University of Birmingham.

In Tokyo, Tomioka, Nantoh and his Miki, and Kimura, were great friends who let Jorunn and me share a part of their always fascinating Japan; Ikuta, Hirota and *all* the others in the lab deserve many thanks for their cooperation and the neverending opportunity for interesting conversations in the lab and out to lunch. I owe great thanks to the professors Kihio and Kitazawa for giving me this unique peek into a very different culture by letting me into their group, and into the interesting field of magnetostriction and magnetostriction measurements. Takashi Suzuki and his colleagues at Hiroshima University deserve my thanks for inviting Jorunn and me to visit their lab and for their generous hospitality.

A scholarship from The Research Council of Norway is greatly acknowledged. Additional funding of my participation in conferences home and abroad has been provided by The Norwegian Institute of Technology and the group. The Research Council of Norway, The Norwegian Institute of Technology, Norsk Hydro and SINTEF Applied Physics have given their contributions to the research in the group.

But the love and joy of my life, my wife Jorunn and my son Brage, deserve the greatest thanks for their patience, support and inspiration!

Trondheim, May 1995

Publications

Publications

The following list contains all publications I have contributed to. This thesis consists of work reported in these publications, but also of a substantial amount of yet unpublished analysis that has been performed in the process of writing the thesis. Parts of the work have also been presented as posters or oral contributions at conferences and seminars.

- ◊ M. Slaski, L. T. Sagdahl, L. K. Heill, K. Fossheim, M. Murakami, H. Fujimoto, N. Koshizuka and S. Tanaka: *Anisotropy of the irreversibility line in MPMG $YBa_2Cu_3O_7$ with Y_2BaCuO_5 inclusions*, Physica C 185–189 (1991) 2495.
- ◊ M. Slaski, L. T. Sagdahl, L. K. Heill, K. Fossheim, M. Murakami, H. Fujimoto, N. Koshizuka and S. Tanaka: *Excitation field dependence, frequency dependence and anisotropy of the irreversibility line in MPMG $YBa_2Cu_3O_7$ with Y_2BaCuO_5 inclusions*, Supercond. Sci. Technol. 5 (1992) S340.
- ◊ K. Fossheim, M. G. Karkut, L. K. Heill, M. Slaski, L. T. Sagdahl, V. M. Vinokur, M. Murakami, H. Fujimoto, N. Koshizuka, S. Tanaka, F. Gencer, J. S. Abell and C. E. Gough: *Flux dynamics and irreversibility in $YBa_2Cu_3O_7$ with Y_2BaCuO_5 inclusions and in single crystal $YBa_2Cu_3O_7$* , Physica Scripta T 42 (1992) 20.
- ◊ M. G. Karkut, L. K. Heill, V. M. Vinokur, M. Slaski, L. T. Sagdahl, E. D. Tuset and K. Fossheim: *ac response of $YBa_2Cu_3O_7$ with Y_2BaCuO_5 inclusions and of single crystal $YBa_2Cu_3O_7$: similarities, differences and anomalies*, Cryogenics 33 (1993) 60.

- ◊ M. G. Karkut, L. K. Heill, M. Slaski, L. T. Sagdahl and K. Fossheim: *Anisotropy and strong pinning in $YBa_2Cu_3O_7$ with Y_2BaCuO_5 inclusions in Phase transitions and relaxation in system with competing energy scales*, ed. T. Riste and D. Sherrington, Kluwer, The Netherlands (1993) 119.
- ◊ M. G. Karkut, M. Slaski, L. K. Heill, L. T. Sagdahl and K. Fossheim: *The ac magnetic response of $YBa_2Cu_3O_7$ with Y_2BaCuO_5 inclusions and of single-crystal $YBa_2Cu_3O_7$: a comparative study*, Physica C **215** (1993) 19.
- ◊ N. Hirota, H. Ikuta, L. K. Heill, T. Yasunaka, K. Kishio and K. Kitazawa: *Magnetostriction and flux creep in high- T_c superconductor single crystals*, Physica B **194–196** (1994) 1847.
- ◊ L. K. Heill, M. G. Karkut, M. Slaski, L. T. Sagdahl and K. Fossheim: *Anisotropic strong pinning in melt-processed $YBa_2Cu_3O_7$ in Critical currents in superconductors*, ed. H. W. Weber, World Scientific, Singapore (1994), 403.
- ◊ L. K. Heill, H. Ikuta, N. Hirota, K. Kishio and K. Kitazawa: *Magnetostriction relaxation in high- T_c superconductors*, Physica C **235–240** (1994) 2925.
- ◊ L. K. Heill, M. G. Karkut, M. Slaski and K. Fossheim: *Anomalous ac magnetic response in an $YBa_2Cu_3O_7$ crystal with $\vec{H} \perp \hat{c}$* , Physica C **235–240** (1994) 3191.

Contents

Preface	iii
Publications	v
Abstract	xiii
1 Introduction	1
1.1 Historical background and applications	1
1.2 The motivation and focus of this thesis	3
References	5
2 Magnetic properties of high temperature superconductors	7
2.1 Basic properties	7
2.1.1 The Ginzburg-Landau picture	7
2.1.2 Type II superconductivity	8
2.1.3 Pinning	10
2.2 Materials	11
2.2.1 $\text{YBa}_2\text{Cu}_3\text{O}_{7-\delta}$	12
2.2.2 $\text{Bi}_2\text{Sr}_2\text{CaCu}_2\text{O}_{8+y}$	13

2.2.3	Pinning	13
2.2.4	Anisotropy	14
2.3	Physics of the flux line system	14
2.3.1	The critical state	15
2.3.2	Flux flow and thermal activation	16
2.3.3	Thermal fluctuations and melting of the flux line lattice	20
2.3.4	Vortex glass	21
2.3.5	The irreversibility line	21
	References	23
3	ac magnetic response	29
3.1	ac permeability	29
3.2	Model calculations	31
3.2.1	The Bean critical state	31
3.2.2	The ohmic regime	33
3.2.3	Cole-Cole analysis	36
3.3	ac permeability as a probe	36
3.4	Probing irreversibility with ac permeability	39
3.4.1	The irreversibility line from the loss peak maximum .	39
3.4.2	Frequency dependence	40
3.4.3	The loss peak maximum as a measure of flux penetration	40
3.4.4	Obtaining the irreversibility line from ac magnetic experiments	43
3.4.5	Resistivity, current-voltage characteristics and ac magnetic response	45

References	49
4 Experimental	55
4.1 The ac susceptibility apparatus	55
4.2 Samples	57
4.2.1 The MPMG sample	57
4.2.2 The single crystal (SC) sample	58
References	61
5 Introductory ac permeability results	63
6 Loss peak lines	73
6.1 Anisotropic loss peak and irreversibility lines	73
6.1.1 Anisotropic melting of the flux line lattice	74
6.1.2 Anisotropic intrinsic pinning	75
6.2 Power-law fits	76
6.3 The origins of the power-laws	78
6.3.1 The spin glass analogy	78
6.3.2 Thermal activation	78
6.3.3 Flux line lattice melting	79
6.3.4 Vortex glass transition	80
6.4 Summary and conclusions	80
References	83
7 Frequency dependence	87
7.1 Loss peak lines	87

7.2 Thermal activation	91
7.2.1 Energy barriers	94
7.3 Vortex glass	100
7.4 Linear and non-linear behaviour	103
7.5 Summary and conclusions	106
References	109
8 Amplitude dependence	111
8.1 Loss peak lines	111
8.2 Anisotropic ac response	113
8.3 Anisotropic depinned region and intersecting loss peak lines . .	117
8.4 Temperature dependence of the current density	118
8.4.1 Extracting current density from ac permeability	119
8.4.2 Discussion	121
8.5 Linear and non-linear behaviour	123
8.5.1 Field parallel to the <i>ab</i> -plane	125
8.5.2 Field along the <i>c</i> -axis	125
8.5.3 Field dependent response	128
8.6 Summary and conclusions	128
References	131
9 More on linear and non-linear response	133
References	137
10 Anisotropic strong pinning by Y_2BaCuO_5 inclusions	139

10.1 Irreversibility lines for fields along the <i>c</i> -axis	139
10.2 Pinning by Y_2BaCuO_5 inclusions and related defects	141
10.3 Strong pinning at the $\text{YBa}_2\text{Cu}_3\text{O}_7/\text{Y}_2\text{BaCuO}_5$ interface	143
10.4 Field parallel to the <i>ab</i> -plane	145
10.4.1 No shift of the irreversibility line	145
10.4.2 Anisotropic pinning energies and forces	145
10.4.3 Substantial ac losses	146
10.5 Summary and conclusions	147
References	149
11 The anomalous response in the SC sample	151
11.1 Excitation field dependence	152
11.2 Origin of the anomaly	155
11.2.1 Granularity?	155
11.2.2 "Oriented granularity" due to cracks?	156
11.2.3 Misorientation?	156
11.2.4 Phase transition?	157
11.2.5 Peak effect: non-monotonic (critical) current density? .	158
11.3 Summary and conclusions	159
References	161
12 Magnetostriction in single crystal $\text{Bi}_2\text{Sr}_2\text{CaCu}_2\text{O}_8$	163
12.1 Introduction	163
12.2 Experimental	164
12.3 Pinning-induced magnetostriction	165

12.4 Results and Discussion	168
12.4.1 Hysteresis loops	168
12.4.2 Relaxation curves	171
12.5 Summary and Conclusions	176
References	177
 A ac permeability of an infinite slab in the Bean critical state	 179
 B Critical current density from magnetization and magnetostriiction data	 183

Abstract

We have measured the ac magnetic response function $\mu = \mu' + i\mu''$ in melt-powder-melt-growth (MPMG) $\text{YBa}_2\text{Cu}_3\text{O}_7$ (Y123) with insulating $\text{Y}_2\text{Ba}_2\text{Cu}_3\text{O}_5$ (Y211) and in single crystal $\text{YBa}_2\text{Cu}_3\text{O}_7$ (SC) in applied dc fields up to 8 T, oriented both parallel and perpendicular to the crystalline *c*-axis. Both samples are cubes with sides of about 1 mm. The response of the two samples has been mapped out as a function of temperature *T*, excitation field amplitude *h_{ac}* and frequency *f*, dc field *H_{dc}*, and field orientation. The locus of μ'' maxima in the *H-T* plane defines the loss peak line (LPL). For small amplitudes and frequencies the LPL is close to the irreversibility line (IL).

Our measurements show that for both samples the LPL, and hence the IL, exists at higher temperatures and fields for $\vec{H} \perp \hat{c}$ than for $\vec{H} \parallel \hat{c}$. This is consistent with the ideas of anisotropic melting of the flux line lattice (FLL) and the anisotropic intrinsic pinning due to the layered structure of the material.

Power-law fits

$$H(T^*) = H_0(1 - T^*/T_c)^n$$

to the LPLs give exponents $n \approx 1.4\text{--}1.6$ similar to a large number of other published exponents for LPLs and ILs, and it is not possible to separate between the different model descriptions of the flux line system since they all may give exponents in this range.

For the $\vec{H} \parallel \hat{c}$ orientation we observe strong frequency but weak amplitude dependence. The opposite is seen for $\vec{H} \perp \hat{c}$: weak frequency but strong amplitude dependence.

The measured response for $\vec{H} \parallel \hat{c}$ is intermediate between linear (ohmic) and extremely non-linear (Bean critical state). For $\vec{H} \perp \hat{c}$ the response is strongly non-linear.

For $\vec{H} \parallel \hat{c}$ we are close to but above the transition into a vortex solid state, and by extrapolation from the frequency dependent LPLs we obtain an estimate for the vortex glass transition line that has a power-law temperature dependence with an exponent of 1.5.

For $\vec{H} \perp \hat{c}$ the response is consistent with that expected in a vortex solid, and by scaling the amplitude dependent μ' we find a temperature dependence of the (critical) current density that is well described by a power-law with an exponent of $\frac{3}{2}$.

Thermal activation analysis results in pinning barriers

$$U(H, T) \approx U_0 \frac{(1 - T/T_c)^{3/2}}{H}$$

that describe our system well for both samples for $\vec{H} \parallel \hat{c}$ and for the SC sample for $\vec{H} \perp \hat{c}$. This barrier is consistent with the power-law found for the current density.

For $\vec{H} \parallel \hat{c}$ the Y211 inclusions in the MPMG sample have the effect of moving the LPL, and the IL, to higher fields and temperatures compared to the SC sample, and we believe that this is due to strong pinning at the abrupt Y123/Y211 interfaces. For the $\vec{H} \perp \hat{c}$ orientation the MPMG and SC LPLs, and ILs, are identical, and simple anisotropy considerations indicate that interface pinning should be much weaker in this orientation.

The overall ac losses are however larger in the MPMG sample when $\vec{H} \perp \hat{c}$ reflecting reduced barriers against vortex motion. Instead of providing additional pinning in this orientation, the Y211 inclusions seem to have a deleterious effect by wiping out other pins and reducing the intrinsic pinning by interrupting the CuO₂ layers over large areas.

We observe anomalous loss peaks $\mu''(T)$ for the SC sample for intermediate fields $\vec{H} \perp \hat{c}$: an extra “feature” (or “peak”) appears, and the FWHM blows up dramatically. The two features might possibly represent two separate phase transitions, a weak remnant of a high temperature melting transition and a low temperature vortex glass transition.

We have measured large magnetostriction (size changes) in a flat single crystal Bi₂Sr₂CaCu₂O₈ sample at low temperature and in fields up to 6 T applied along the *c*-axis. The behaviour is well described by the pinning-induced magnetostriction model. Left to relax, the sample size is restored slower than the magnetization vanishes.

Introduction

1.1 Historical background and applications

The history of superconductivity was initiated in 1911 as Heike Kamerlingh-Onnes measured vanishing resistance in a rod of solid mercury (Hg) below 4.2 K [1]. After 1911 superconductivity has been found in more than 20 metals, in a few semiconductors under high pressure or as very thin films and in thousands of alloys. The highest critical temperature T_c of these *low* temperature superconductors is only about 23 K in Nb_3Ge [2]. Large scale use of superconducting technology is hindered by the need to use the highly volatile liquid helium as coolant, and high field superconducting magnets and the extremely sensitive field detectors (SQUIDS; Superconducting QUantum Interference Devices) are mostly limited to laboratory and hospital use.

Since the discovery of *high* temperature superconductivity by Bednorz and Müller, now Nobel laureates, in 1986 [3], an enormous amount of work has been laid down. With the discovery of $\text{YBa}_2\text{Cu}_3\text{O}_7$ in 1987 [4] the “magic” limit of 77 K, the temperature of the inexpensive and easy to handle liquid nitrogen coolant, was surpassed. Later on new compounds in the cuprate family of superconductors have moved the critical temperatures even further up. See Table 1.1. A report suggesting superconductivity at 250 K (resistivity drop onset near 280 K!) in an artificial cuprate of the BiSrCaCuO family was published but later redrawn [10], but the hope for room temperature superconductivity still lives.

Large scale use of high temperature superconductors is not yet possible. While

Table 1.1: Some high temperature superconductors with critical temperatures and year of discovery with References.

Compound	T_c (K)	Discovered
$(La_{1-x}Ba_x)_2CuO_4$	35	1986 [3]
$(La_{1-x}Sr_x)_2CuO_4$	36	1987 [5]
$YBa_2Cu_3O_7$	92	1987 [4]
$Bi_2Sr_2CaCu_2O_8$	80	1988 [6]
$Bi_2Sr_2Ca_2Cu_3O_8$	110	1988 [7]
$Tl_2Ca_2Ba_2Cu_3O_{10}$	125	1988 [8]
$HgBa_2Ca_2Cu_3O_8$	135	1993 [9]

the metals and alloys with low critical temperatures are easily made into wires and other arbitrarily large or shaped designs, the fabrication of the cuprates is much more difficult. Ceramic samples made up of small grains with random orientation relative to each other have weak intergranular links resulting in low bulk critical currents that are also considerably reduced in magnetic fields. Single crystal samples have only been produced with maximum dimensions of a few millimeters. The brittleness of the cuprates is of course also a major problem.

Much effort is put into making wires and tapes of silver clad $Bi_2Sr_2CaCu_2O_8$ and $Bi_2Sr_2Ca_2Cu_3O_8$ for use as cables or in magnets, but still more work is needed to improve their performance.

Thin films have however already been put into use as compact high performance microwave filters and mixers. Conductus Inc. even offer commercial SQUIDs for educational purposes; "Mr. SQUID" and "Dr. SQUID" for the basic and advanced levels, respectively.

Naturally, the shielding capabilities of the superconductors are also of interest. Experiments aimed at shielding out *e.g.* environmental magnetic noise using plasma sprayed $YBa_2Cu_3O_7$ coatings have been performed [11].

The melt-process-melt-growth (MPMG) material ($YBa_2Cu_3O_7$ with insulating Y_2BaCuO_5 inclusions) [12] is a promising bulk material boasting large critical current densities and levitation forces. Frictionless magnetic bearings for high speed rotors [13, 14], contactless transport systems [15] and energy storing flywheels have already been demonstrated [16, and References therein]. This thesis includes extensive studies of the magnetic properties of a sample of the MPMG material.

1.2 The motivation and focus of this thesis

Two very important factors deciding whether a high temperature superconducting material is potentially useful for applications are that

- it has the required quality such as high critical current density or large levitation forces, and that
- it can be manufactured in large enough quantities and specimen sizes.

Sintering has been used to move beyond the millimeter sizes of single crystal $\text{YBa}_2\text{Cu}_3\text{O}_7$ (YBCO), but the weak-link problem resulting from the granular structure severely limit the transport capabilities. Melt-processing has helped to reduce this problem significantly [12, 17–20], and the MPMG material combines quality with quantity (see above).

The ac susceptibility work making up the major part of this thesis was initially aimed at comparing the magnetic properties of the MPMG YBCO material with those of single crystal YBCO. Of particular interest was, and still is, the position of the irreversibility line below which a useful critical current density exists.

The anisotropy is another important topic, which is why the rarely used cube geometry was chosen for our samples. This shape has the advantage that it allows direct comparison of data for different orientations of the sample with respect to the direction of the applied field. The disadvantage is that the different superconducting properties are inherently difficult to calculate, and comparison to theoretical models is non-trivial.

Eventually, our interest was concentrated more on the statics and dynamics of the vortex system, the different vortex states and the linearity of the ac magnetic response.

The author was fortunate enough to work as a guest at the University of Tokyo for three months on the magnetostriction (size changes in magnetic fields) of $\text{Bi}_2\text{Sr}_2\text{CaCu}_2\text{O}_8$ (BSCCO). The stresses caused by magnetic pressure are so large at low temperatures that the sample may in fact break.

Chapter 2 contains the theory relevant to our work and presents the YBCO and BSCCO materials we use. Chapter 3 concentrates on ac magnetic response in general and its qualities as a probe of the vortex system in particular. Exper-

imental details for our ac susceptibility measurements are given in Chapter 4 before introductory results of our ac magnetic experiments follow in Chapter 5. Loss peak lines and their anisotropic behaviour are presented and discussed in Chapter 6. The excitation field frequency and amplitude dependence of the ac magnetic response are the topics of Chapters 7 and 8, respectively. The short Chapter 9 presents additional analysis of the linearity of the response. Chapter 10 concentrates on the anisotropic strong pinning observed in our MPMG sample while Chapter 11 addresses the anomalous response observed in our single crystal YBCO sample. Finally, Chapter 12 presents our magnetostriction work.

References

- [1] H. Kamerlingh-Onnes, Akad.van Wetenschappen (Amst.) **14** (113) (1911) 818.
- [2] J. R. Gavalier, Appl. Phys. Lett. **23** (1973) 480.
- [3] J. G. Bednorz and K. A. Müller, Z. Phys. B **64** (1986) 189.
- [4] M. K. Wu, J. R. Ashburn, C. J. Torng, P. H. Hor, R. L. Meng, L. Gao, Z. J. Huang, Y. Q. Wang and C. W. Chu, Phys. Rev. Lett. **58** (1987) 908.
- [5] R. J. Cava, A. Santoro, D. W. Johnson and W. W. Rhodes, Phys. Rev. B **35** (1987) 6716.
- [6] H. Maeda, Y. Tanaka, M. Fukutomi and T. Asano, Jpn. J. Appl. Phys. **27** (1988) L209.
- [7] U. Endo, S. Koyama and T. Kawai, Jpn. J. Appl. Phys. **27** (1988) L1476.
- [8] Z. Z. Sheng and A. M. Hermann, Nature **332** (1988) 55.
- [9] A. Schilling, M. Cantoni, J. D. Guo and H. R. Ott, Nature **363** (1993) 56.
- [10] M. Laguës, X. M. Xie, H. Tebbji, X. Z. Xu, V. Mairet, C. Hatterer, C. F. Beuran, C. Deville-Cavellin, Science **262** (1993) 1850.
- [11] H. Hemmes, H. Rogalla, R. Chaouadi and J. Cornelis in *Critical Currents in Superconductors*, ed. H. W. Weber, World Scientific, Singapore (1994) 651.
- [12] M. Murakami, Mod. Phys. Lett. B **4** (1990) 163.
- [13] F. C. Moon and P.-Z. Chang, Appl. Phys. Lett. **56** (1990) 397.

- [14] B. R. Weinberger, L. Lynds and J. R. Hull, *Supercond. Sci. Technol.* **3** (1990) 381.
- [15] D. Wolfshtein, T. E. Seidel, D. W. Johnson Jr. and W. W. Rhodes, *J. Supercond.* **2** (1989) 211.
- [16] *Melt Processed High-Temperature Superconductors*, ed. M. Murakami, World Scientific, Singapore 1992.
- [17] S. Jin, T. H. Tiefel, R. C. Sherwood, M. E. Davis, R. B. van Dover, G. W. Kammlott, R. A. Fastnacht and H. D. Keith, *Appl. Phys. Lett.* **52** (1988) 2074.
- [18] K. Salama, V. Salvamanickam, L. Gao and K. Sun, *Appl. Phys. Lett.* **54** (1989) 2352.
- [19] P. McGinn, W. Chen, N. Zhu, M. Lanagan and U. Balachandran, *Appl. Phys. Lett.* **57** (1990) 1455.
- [20] V. Salvamanickam, C. Partsinevelos, A. V. McGuire and K. Salama, *Appl. Phys. Lett.* **60** (1992) 3313.

Magnetic properties of high temperature superconductors

In this Chapter we present the background for our own experiments and analyses in later Chapters. First, basic properties are described within the phenomenological Ginzburg-Landau (GL) theory [1] and we summarize the characteristics of type II superconductors and introduce pinning. Second, we introduce the two materials we use in our experiments, $\text{YBa}_2\text{Cu}_3\text{O}_7$ (YBCO) and $\text{Bi}_2\text{Sr}_2\text{CaCu}_2\text{O}_8$ (BSCCO). Third, we very briefly review relevant theories and models for the statics and dynamics of the flux line system in type II superconductors.

2.1 Basic properties

2.1.1 The Ginzburg-Landau picture

Central to the GL theory [1] is the complex-order parameter in the form of the pseudo wave function $\psi(\vec{r})$. Its magnitude is a measure of superconducting order and vanishes at the critical temperature T_c . The local density of superconducting electrons n_s is given by $n_s = |\psi(\vec{r})|^2$. A key feature of the GL theory — as opposed to the London theory [2] — is its ability to deal with spatial variations in n_s . The GL coherence length $\xi(T)$ is the characteristic length scale over which the order parameter changes. The other important length scale is the magnetic penetration depth $\lambda(T)$, the length scale over which the

flux density B varies. The GL theory was originally developed from an expansion of the free energy in $|\psi|^2$ and $|\nabla\psi|^2$ and should therefore work best close to T_c , but it has proven useful at all temperatures.

2.1.2 Type II superconductivity

On approaching T_c both the characteristic length scales diverge in the same way:

$$\lambda(T) \approx \lambda(0)/\sqrt{1-t} \quad (2.1)$$

$$\xi(T) \approx \xi(0)/\sqrt{1-t} \quad (2.2)$$

where the reduced temperature $t = T/T_c$. The then almost temperature independent ratio

$$\kappa = \frac{\lambda}{\xi}, \quad (2.3)$$

the GL parameter, characterizes the behaviour of the superconductor in magnetic field:

If $\kappa < 1/\sqrt{2}$ we have *type I* superconductivity. The energy of the domain walls separating normal and superconducting regions is positive, and the domain walls meander through the sample in the intermediate state observed when the sample shape dictates non-zero demagnetization. Below the thermodynamic critical field $H_c(T)$ no flux enters the superconducting regions of the sample beyond the penetration depth.

On the other hand, if $\kappa > 1/\sqrt{2}$ we have *type II* superconductivity. The domain wall energy is negative and a subdivision into a large number of small normal regions dispersed throughout the superconducting material is energetically preferred. Above the lower critical field $H_{c1}(T)$ flux then penetrates the sample in the form of thin filaments of flux: flux lines or vortices with a normal core of size $\approx 2\xi$ with a high flux density (the maximum is about twice the upper critical flux density $\mu_0 H_{c2}$ [3, Chapter 5]). Around the vortex, supercurrents circulate generating the core, trapping a total flux $\Phi_0 = h/2e = 2.07 \times 10^{-15}$ Wb, one flux quantum. The magnetic field decays over a distance λ . The magnitude of the order parameter far from the vortex is $|\psi(r \rightarrow \infty)| = \psi_\infty$. See Figure 2.1. With increasing applied field the distance between the vortices decreases. Due to their mutual interaction the vortices form a regular flux line lattice (FLL) [4]. The close-packed triangular (or hexagonal) lattice provides

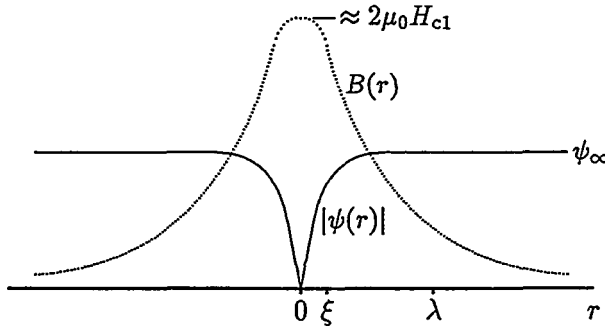


Figure 2.1: Schematic of the local magnetic flux density $B(r)$ and the magnitude of the superconducting order parameter $|\psi(r)|$ of an isolated vortex.

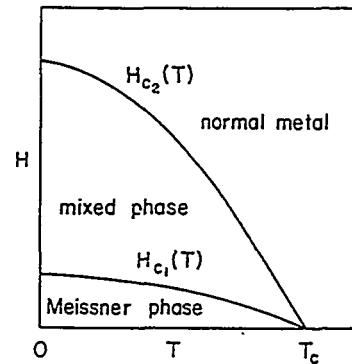


Figure 2.2: Mean-field phase diagram for a type II superconductor. Below $H_{c1}(T)$ we are in the Meissner state. The mixed state is found between $H_{c1}(T)$ and $H_{c2}(T)$. Above $H_{c2}(T)$ we find the normal metallic phase. See text. The drawing is from Reference [5].

the largest vortex separation $a_\Delta = (4/3)^{1/4} \sqrt{\Phi_0/B}$ and hence the lowest interaction energy. Eventually the applied field reaches the upper critical field H_{c2} where the vortex cores overlap and the order parameter and superconductivity vanishes.¹ The superconductor is said to be in the mixed state when the field is in the range H_{c1} to H_{c2} . See Figure 2.2. The high temperature oxide superconductors are all of type II with large GL parameters $\kappa \sim 100$. The lower and upper critical fields are related to the thermodynamical critical field [3,5]:

$$H_{c1} = \frac{\Phi_0}{\mu_0 \lambda^2} \ln \frac{\lambda}{\xi} , \quad H_{c2} = \frac{2\Phi_0}{\mu_0 \xi^2} , \quad H_c = \frac{\sqrt{2}\Phi_0}{\mu_0 \lambda \xi} , \quad (2.4)$$

and

$$H_{c1} = \frac{1}{\sqrt{2}} \frac{\ln \kappa}{\kappa} H_c , \quad H_{c2} = \sqrt{2}\kappa H_c , \quad H_{c1} = \frac{1}{2} \frac{\ln \kappa}{\kappa^2} H_{c2} . \quad (2.5)$$

If a current is applied normal to the flux lines in a perfect sample of a type II superconductor it will exert a Lorentz type force on the FLL moving it across

¹Of course, there is a $H_{c3} \approx 1.7H_{c2}$ due to nucleation of superconductivity at surfaces, and superconducting fluctuations exist above H_{c2} , but this is not important here.

the sample. The moving flux produces an electric field and hence there is resistance and dissipation. The maximum current density that can be applied loss free, the critical current density j_c , is therefore zero in fields larger than H_{c1} , and the sample is strictly not superconducting. Also, since flux can flow freely in and out of the sample there will be no difference between the zero-field cooled (ZFC) and the field cooled (FC) magnetization; the magnetization is reversible.

2.1.3 Pinning

For applications high critical current densities are necessary. The FLL should be *pinned* to the material, *i.e.* it should not move when exposed to external forces. If flux threads the sample the free energy increases since the superconducting order parameter is reduced in the vortices. If however the flux occupy regions in the sample where the order parameter is already reduced there is no or little extra increase of free energy. Thus, regions of the sample where the order parameter is reduced (either intrinsically or due to lattice defects such as dislocations, voids, interstitials, grain boundaries and vacancies) act as pinning centers.²

For example, to a good approximation the normal core of a vortex occupies an area $\pi\xi^2$. A vortex in a fully superconducting region costs an energy, per unit length of the vortex, $\frac{1}{2}\mu_0H_c^2\pi\xi^2$, whereas in a region where the order parameter is reduced to a fraction $p < 1$ of its maximum value it costs only $p\frac{1}{2}\mu_0H_c^2\pi\xi^2$. Here we have used the condensation energy density $\frac{1}{2}\mu_0H_c^2$, and $H_c = H_{c2}/\sqrt{2}\kappa$.

Local variations of the magnetic field due to sample inhomogeneities can also interact with vortices and provide pinning.

The elasticity of the FLL is also important for pinning. A completely rigid FLL cannot be pinned by a large number of randomly distributed (weak) pins since all configurations are equivalent. On the other hand a single strong pin is enough to pin the rigid FLL. A soft FLL can be pinned since the individual vortices are able to adjust their positions locally to fit the distribution of random pins.

²A pinning center causes a sideways displacement u of a section of length L of an elastic vortex. If the pin is weak, $u \ll L$, and if the pin is strong, $u \sim L$.

Table 2.1: Some material and GL parameters of $\text{YBa}_2\text{Cu}_3\text{O}_7$ and $\text{Bi}_2\text{Sr}_2\text{CaCu}_2\text{O}_8$. The last four parameters were collected from the review of Blatter *et al.* [5].

Parameter	Symbol	$\text{YBa}_2\text{Cu}_3\text{O}_7$	$\text{Bi}_2\text{Sr}_2\text{CaCu}_2\text{O}_8$
Lattice constants	a	3.8 Å	3.8 Å
	b	3.9 Å	3.8 Å
	c	11.7 Å	30.8 Å
Interplanar distance ^a	s	12 Å	15 Å
Coherence length ^b	$\xi(0)$	9–13 Å	15–30 Å
Penetration depth ^c	$\lambda(0)$	1000 Å	1000 Å
Anisotropy ratio ^d	$\gamma = 1/\varepsilon$	5–7	50–100

^aThe distance between CuO_2 double layers.

^bThe tabulated $\xi(0)$ is the in-plane GL coherence length ξ_{ab} at $T = 0$. Along the c -axis we have $\xi_c = \xi_{ab}/\gamma$.

^cThe tabulated $\lambda(0)$ is the in-plane GL penetration depth λ_{ab} at $T = 0$. Along the c -axis we have $\lambda_c = \gamma\lambda_{ab}$.

^dThe square root of the effective mass anisotropy ratio $\Gamma = M/m = m_c/m_{ab} = 1/\varepsilon^2 > 1$.

2.2 Materials

The major part of this thesis is devoted to measurements on $\text{YBa}_2\text{Cu}_3\text{O}_{7-\delta}$, by far the most studied of the high temperature superconductors. The other material used is the also popular $\text{Bi}_2\text{Sr}_2\text{CaCu}_2\text{O}_{8+y}$. Some characteristics of the high temperature oxide or cuprate superconductors are

- the high critical temperatures,
- their layered structures and the large anisotropies, and
- the small coherence lengths ξ_{ab} and ξ_c ; $\xi(0)$ is typically on the order of 10 Å, about an order of magnitude lower than for the low temperature superconductors, and the materials are therefore sensitive to small defects and impurities, and thermal fluctuations are important.

In Table 2.1 we present some data on the two materials. Their structures are shown in Figure 2.3.

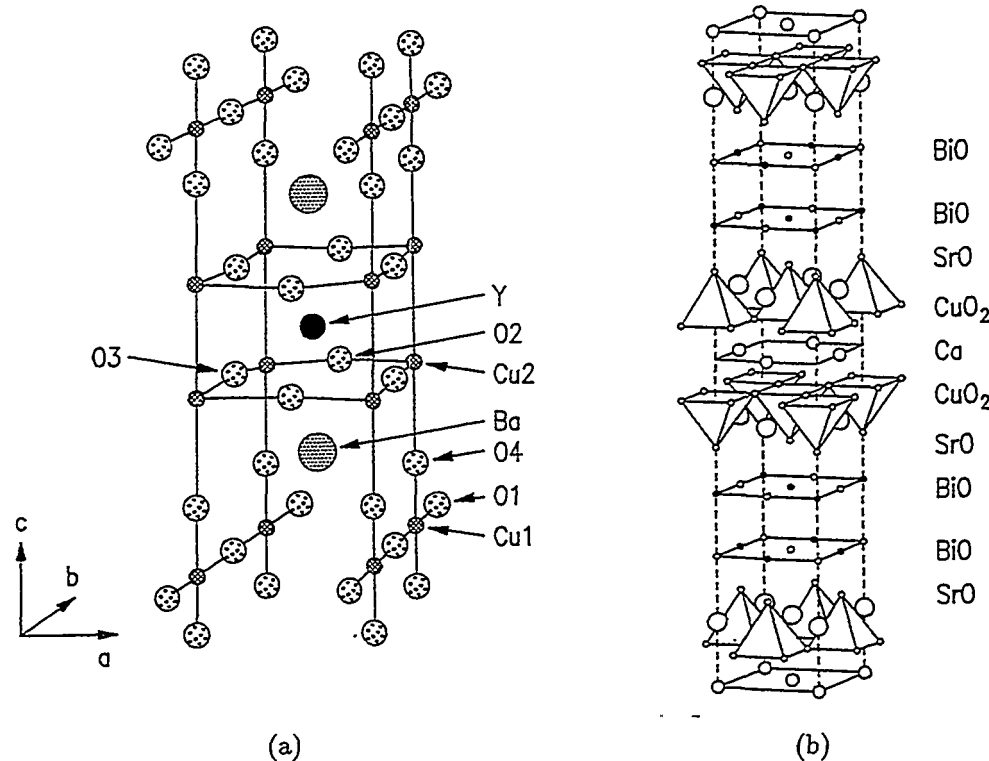


Figure 2.3: Schematic structure of (a) $\text{YBa}_2\text{Cu}_3\text{O}_7$ and (b) $\text{Bi}_2\text{Sr}_2\text{Ca}\text{Cu}_2\text{O}_8$.

2.2.1 $\text{YBa}_2\text{Cu}_3\text{O}_{7-\delta}$

Centered in the YBCO unit cell is an Y layer separating two CuO₂ layers parallel to the crystalline *ab*-plane. The latter are considered responsible for the superconductivity (in all the cuprates). Within the charge transfer model [6] charge moves between the conduction layer (the Y and CuO₂ layers) and the charge reservoir layers (with the BaO layer and the CuO chains) above and below. The CuO chains oriented along the crystalline *b*-axis contribute to the conductivity, and also cause a small anisotropy within the *ab*-plane: The vortex lattice anisotropy has been measured from Bitter-pattern observations on different YBCO crystals by Dolan *et al.* [7]. They found λ_b to be about 1.11–1.15 times larger than λ_a . The crystalline anisotropy is very small in that *b* exceeds *a* by only about 2%. During the processing at high temperatures YBCO is tetragonal, but upon cooling to room temperature the structure un-

dergoes a transition into this orthorombic phase. The transition results in the formation of twin planes separating domains of interchanged a and b axes. The coupling along the c -axis between the CuO_2 layers is believed to occur via the CuO chains and is relatively weak, and the conduction in the ab -plane is considerably larger than along the c -axis. This anisotropy is reflected in the other important parameters, *e.g.* those in Table 2.1, and the critical fields.³

In our work we have also performed experiments on the melt-powder-melt-growth (MPMG) YBCO-based material [23]. It has large critical current densities and levitation forces presumably due to pinning by the insulating Y_2BaCuO_5 inclusions scattered throughout its $\text{YBa}_2\text{Cu}_3\text{O}_7$ matrix. See Sub-section 4.2.1 for details on the processing of this material.

2.2.2 $\text{Bi}_2\text{Sr}_2\text{CaCu}_2\text{O}_{8+\gamma}$

In the BSCCO unit cell the CuO_2 layers are sandwiched between the insulating BiO double layers. The latter are believed to act as charge reservoirs and to provide the coupling between the CuO_2 double layers of neighbouring unit cells. This coupling is even weaker than in YBCO, and consequently the anisotropy is much more pronounced, as is evident from Table 2.1. There is however no anisotropy within the ab -plane, and BSCCO is twin free.

2.2.3 Pinning

The highest critical temperatures for YBCO is obtained for oxygen deficiencies around $\delta \sim 0.1$, optimizing the number of charge carriers in the CuO_2 layers. The vacant oxygen sites provide efficient collective pinning [5]. The twin planes provide strong pinning, see for example the works of Kwok *et al.* [9–11]. Also, since the superconductivity takes place mainly in the CuO_2 layers, the layers in between have a reduced order parameter and can provide strong intrinsic pinning as suggested by Tachiki and Takahashi [12] and experimentally confirmed by Kwok *et al.* [13]. To boost the pinning capabilities artificial defects can be introduced. Irradiation by protons [14, 15], neutrons [16–19] and heavy ions [20–22] is demonstrated to add extra pinning and increase the critical

³The H_{c2} of (2.4) attains an extra anisotropy factor $1/\varepsilon_\vartheta$, and H_{c1} (in a London approximation) a factor $\varepsilon/\varepsilon_{\pi/2-\vartheta}$. Here the angle dependent anisotropy parameter $\varepsilon_\vartheta = [\varepsilon^2 \cos^2 \vartheta + \sin^2 \vartheta]^{1/2}$, where $\varepsilon = 1/\gamma < 1$ is the (inverse) anisotropy parameter in Table 2.1 and ϑ is the angle between the applied field H and the ab -plane [5].

current density, as do insulating inclusions, such as the Y_2BaCuO_5 inclusions in the melt-processed materials [17, 24–28], like the MPMG material [23] we present extensive measurements on in this thesis.

2.2.4 Anisotropy

Provided the anisotropy is not too extreme, the continuous anisotropic GL description is able to account for much of the essential physics. The anisotropy enters as an effective-mass tensor. If its coordinate axes are aligned with the crystallographic axes, the tensor is diagonal with components m_a , m_b and m_c normalized so that $m_a m_b m_c = 1$. The penetration depths and coherence lengths along the principal axes are then $\lambda_i = \lambda \sqrt{m_i}$ and $\xi_i = \xi / \sqrt{m_i}$, respectively, and $\lambda = \sqrt[3]{\lambda_a \lambda_b \lambda_c}$ and $\xi = \sqrt[3]{\xi_a \xi_b \xi_c}$. Here $i = a, b$ or c . Assuming that the a and b axes are equivalent we reproduce the result in Table 2.1: $\lambda_c = \sqrt{m_c/m_{ab}} \lambda_{ab} = \gamma \lambda_{ab}$ and $\xi_c = \sqrt{m_{ab}/m_c} \xi_{ab} = \xi_{ab}/\gamma$.

The anisotropic GL description works well when all penetration depths and coherence lengths are much larger than the unit cell dimensions. However, although ξ_c diverges at T_c it will soon get smaller than the distance s between CuO_2 double layers as the temperature is decreased. When this happens (within only a few K below T_c for YBCO and within less than 1 K below T_c for BSCCO), a description in terms of the Lawrence-Doniach model [29] is more appropriate. A flux line along the c -axis is modified to a stack of “pancake” (point) vortices connected through weak Josephson vortices across the layers. Above a certain crossover field $B_{2D} = \Phi_0/\gamma^2 s^2$ the interlayer coupling is so weak that the flux will behave in a quasi two-dimensional fashion; the pancakes of a flux line decouple. Using the parameter values listed in Table 2.1 we find that $B_{2D} > 30$ T for YBCO, but for BSCCO the crossover field can be as low as ≈ 0.1 T.

2.3 Physics of the flux line system

In the following we will briefly introduce some concepts and models appropriate to our work on the statics and dynamics of the flux line system. More specific details will, when relevant, be embedded in the discussions of our results in later Chapters. A very much more comprehensive and complete review has been published by Blatter *et al.* [5].

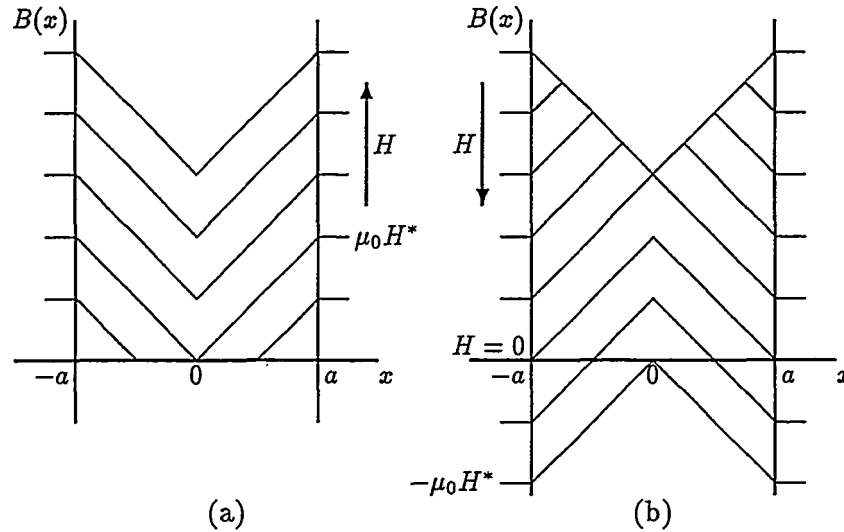


Figure 2.4: Flux profiles in the Bean critical state model for (a) increasing and (b) decreasing applied field H . The flux front reaches the center for $H = H^*$. Here H_{c1} is set to zero for simplicity.

2.3.1 The critical state

In the critical state the magnitude of the current density equals the critical current density everywhere in the superconductor:

$$|\vec{j}| = j_c \quad . \quad (2.6)$$

The central point in the critical state model of Bean [30, 31] is the balance between driving forces and pinning forces at equilibrium setting up flux gradients. The model describes how the flux distribution changes when the applied field or current changes. This is governed by

$$j_c = \frac{1}{\mu_0} |\nabla \times \vec{B}| \stackrel{1D}{=} \frac{1}{\mu_0} \left| \frac{\partial B}{\partial x} \right| \quad (2.7)$$

which is (2.6) on a more explicit form using the Maxwell equation $\vec{j} = \nabla \times \vec{B} / \mu_0$. See for example Reference [32] for a derivation. For example, if the applied magnetic field is increased, flux will penetrate the sample until the condition (2.7) is restored, see Figure 2.4. Bean originally considered the case where the critical current density j_c is independent of the (local) flux density, *i.e.* $j_c(B) = \text{const.}$, and with this approximation the model is often called the

Bean critical state model. Other forms include linear decay of j_c with B : $j_c(B) = j_0(1 - |B|/B_0)$ [33, 34], exponential decay: $j_c(B) = j_0 \exp(-|B|/B_0)$ [35, 36], and the popular Kim model: $j_c(B) = j_0/(1 + |B|/B_0)$ [37]. They are all equivalent to lowest order in $|B|/B_0$ and approach the Bean model for small flux densities or large B_0 .

The critical state model is good at low temperature where thermally activated flux motion is negligible. At higher temperatures the current densities will decay over time, and this is a topic of the next Subsection.

2.3.2 Flux flow and thermal activation

Flux motion and dissipation is seen where the static critical state model no longer applies: in regimes where $j \gg j_c$, and at finite temperatures where there is a finite probability for vortices or bundles of vortices to jump from one pinning site to another.

Flux flow

At fields or temperatures where $j \gg j_c$ the Lorentz driving force dominates over the pinning force and the vortices *flow* across the sample. Their motion is only limited by a viscous drag force $-\eta v$ where η is a viscous drag coefficient and v is the vortex velocity. One origin of this dissipation mechanism may be the eddy currents of the moving vortices that pass through the normal, resistive cores [38]. Another contribution to the dissipation may be due to a retarded relaxation of the superconducting order parameter ψ caused by the core motion [39]. The ohmic (linear I - V characteristics) flux flow resistivity is

$$\rho_{\text{ff}} \simeq \rho_n \frac{B}{B_{c2}} \quad (2.8)$$

where ρ_n is the normal state resistivity and $B_{c2} \equiv \mu_0 H_{c2}$ [38]. An intuitive first guess gives the same result: the resistivity is proportional to the number of vortices and has to extrapolate to ρ_n as superconductivity disappears at H_{c2} . While (2.8) works well at low fields and temperatures, corrections are important at high fields and close to T_c . In the high temperature superconductors the flux flow regime extends quite far down in field and temperature, limiting the regime useful for applications.

Classical creep

For current densities $j < j_c$ flux can still move due to thermal activation at finite temperatures. This phenomenon is known as *creep* and was introduced by Anderson [40] and by Anderson and Kim [41]. They pictured the creep process as bundles⁴ of flux lines jumping between adjacent pinning sites with a jump rate (transition probability) of the usual activation form

$$R = \omega_0 e^{-U(j,B,T)/k_B T} \quad (2.9)$$

where $U(j, B, T)$ is the pinning barrier, or activation energy, for hopping in the direction of the Lorentz force and the attempt frequency $\omega_0 \equiv 1/\tau_0$ characterizes the vibration of vortices within the pinning wells. Feigel'man *et al.* arrived at an attempt frequency $\omega_0 = (x_{\text{hop}}\omega_m B/\mu_0 a^2 T)|\partial U(j)/\partial j|$ where x_{hop} is the hopping distance of the bundle, ω_m the microscopic attempt frequency and a the sample size [42]. In (2.9) we have neglected backwards hopping (against the Lorentz force) since in the Anderson-Kim (AK) model [40, 41] we operate at high current densities: $1 - j/j_c \ll 1$.

When thermal activation is responsible for the decay,

$$U(j(t)) = k_B T \ln(1 + t/t_0) \quad (2.10)$$

where t_0 is some normalizing time for the relaxation experiment [43, 44]. With the unity term in the logarithm we ensure that $U(j_c) = 0$ for $j(t = 0) = j_c$. This is, except for the additional unity term, equivalent to (2.9) when $R \rightarrow 1/t$. The original AK result for a sawtooth pinning potential is

$$U(j) = U_0(1 - j/j_c) \quad ; \quad j \approx j_c \quad . \quad (2.11)$$

Combining the above two Equations we find logarithmic decay of the current density:

$$j(t) = j_c \left[1 - \frac{k_B T}{U_0} \ln \left(1 + \frac{t}{\tau_0} \right) \right] \quad (2.12)$$

and similarly for the magnetization, as shown by Beasley *et al.* [45]. With the more realistic sinusoidal pinning potential [43, 46],

$$j(t) = j_c \left[1 - \left(\frac{k_B T}{U_0} \ln \left(1 + \frac{t}{\tau_{3/2}} \right) \right)^{2/3} \right] \quad (2.13)$$

⁴Bundles jump as a unit since λ , the range of the repulsive interaction between vortices, is usually (*i.e.* for high enough fields) larger than the intervortex distance $\approx a_0 = \sqrt{\Phi_0/B}$: From Table 2.1 we find $\lambda \sim 1000 \text{ \AA}$, and at 1 T $a_0 \sim 500 \text{ \AA}$. At about 0.25 T $\lambda = a_0$.

but the difference from (2.12) is not readily resolved in experiments. The relaxing magnetization is straightforwardly found from (2.12) or (2.13) in the relevant regime, *i.e.* at low temperatures where U is large, or j is close to j_c , by replacing $j(t)$ with $M(t)$ and $j_c = j(t=0)$ with $M(0)$ — this results *e.g.* from the Bean critical state at low temperatures, which decays keeping the linear flux profile [44].

For the conventional low temperature superconductors the creep is extremely slow and $j \approx j_c$ for very long times, so that the AK model applies. In high temperature superconductors the decay is much faster resulting in giant flux creep [47] since the temperatures are high and the pinning energies are small due to the short coherence lengths (the large anisotropies also contribute). Now, when j is not nearly equal to j_c the AK model is no longer adequate and the cases $j < j_c$ and $j \ll j_c$ have to be considered. The latter is of special interest when we want to probe the system using as small perturbations as possible, which usually means applying small currents or excitation fields.

Collective creep

In the theory of collective flux creep (CFC) [48], the barriers diverge as the current density vanishes according to the non-linear form

$$U(j) = U_0[(j_c/j)^\mu - 1] \quad (2.14)$$

and

$$j(t) = j_c \left[1 + \frac{k_B T}{U_0} \ln \left(1 + \frac{t}{t_0} \right) \right]^{-1/\mu}. \quad (2.15)$$

The value of the exponent μ depends on which pinning regime we are in.⁵ For small values $\mu \ll 1$, $U \approx U_0 \ln(j_c/j)$ when the unity term in (2.14) is dropped.⁶ An interpolation formula between (2.12) and (2.15) is [42, 52]

$$j(t) = j_c \left[1 + \mu \frac{k_B T}{U_c} \ln \left(1 + \frac{t}{t_0} \right) \right]^{-1/\mu}. \quad (2.16)$$

⁵For three dimensional flux creep: In the single-vortex regime at low temperatures and fields $\mu = 1/7$, at higher fields we have collectively pinned small vortex bundles ($R_b \ll \lambda_L$) and $\mu = 3/2$, and for the large bundles ($R_b \gg \lambda_L$) at still higher fields $\mu = 7/9$. R_b is the size of the bundle and λ_L is the London penetration depth ($\lambda_L = \sqrt{2}\lambda(0)$). CDW (charge density wave) type pinning occurs for displacements on the order of the vortex separation a_0 and $\mu = 1/2$ [49]. See References [42] or [5, Chapter IV]. For two dimensional flux creep $\mu = 9/8$ [50].

⁶This logarithmic dependence has been found as an exact result when $\vec{H} \perp \hat{c}$ and the vortex motion is governed by intrinsic pinning [51].

where $U_c = \mu U_0$. The AK case corresponds to an exponent $\mu = -1$.

The CFC model is based on the collective pinning theory of Larkin and Ovchinnikov [53, 54]. In this theory a vortex is collectively pinned by a number of randomly distributed weak pins in the sense that segments of length L_c , the collective pinning length, are pinned independently. Each of the weak pins cause only a small distortion ($\ll a_0$) of the FLL ($L_c \gg \xi$), but the local distortions may add up over longer distances until finally the long range order is broken. The region where the long range order is preserved (distortions $u \leq \xi$) defines the correlation volume V_c . The CFC model considers the elasticity of the FLL. A consequence is that the hopping flux bundles consist of a large number of subbundles of volume V_c that hop together since the bulk modulus is much larger than the shear modulus ($C_{11} \gg C_{66}$) at fields $H \gg H_{c1}$; the flux creeps collectively. This means that the effective pinning barrier increases — a large number of weak pins can efficiently pin the flux line system.

Thermally activated flux flow (TAFF)

Creep takes place when $j \sim j_c$ and $k_B T \ll U$, i.e. the Lorentz driving force density $\vec{F}_L = \vec{j} \times \vec{B}$ competes with the pinning force density \vec{F}_p . On the other hand, in the small current density limit $j \ll j_c$, but at high temperatures $k_B T \sim U$, we are in a regime of thermally activated flux flow (TAFF) [55–57]. As such, the creep and TAFF pictures are two limiting cases of the same physical picture with flux motion driven by the Lorentz force and/or thermal jumps in the direction of the flux density gradient.

The diffusive TAFF behaviour is expected in the vortex liquid at high temperatures $T > T_m$, where T_m is the vortex lattice melting temperature, and the finite barriers against plastic motion cut off the diverging elastic barriers (see above on collective creep) at low current densities $j \ll j_c$ [5]. The response is ohmic with a non-zero resistivity

$$\rho_{\text{TAFF}} = \rho_0 e^{-U/k_B T} \quad (2.17)$$

where $\rho_0 \propto \rho_{\text{ff}} \approx \rho_n H / H_{c2}$; ρ_n is the normal state resistivity (at T_c). Here U is often set to the barrier against plastic motion of vortices, U_{pl} .

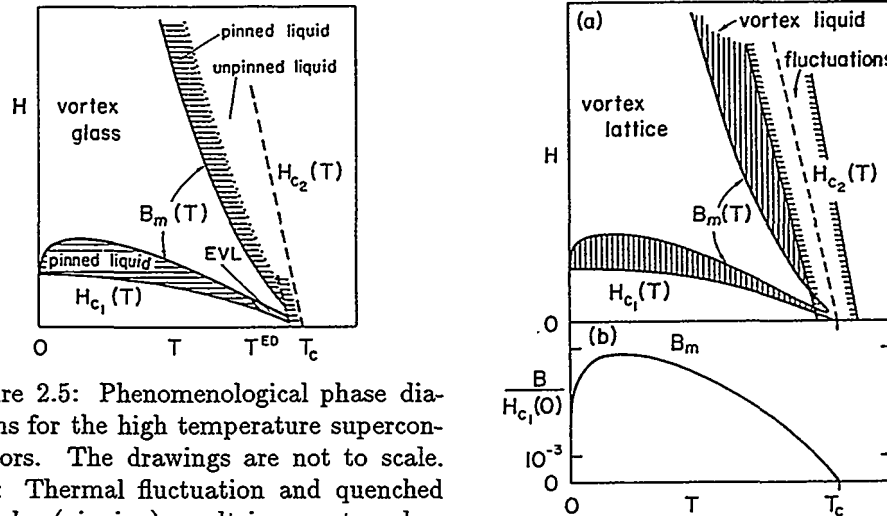


Figure 2.5: Phenomenological phase diagrams for the high temperature superconductors. The drawings are not to scale. Left: Thermal fluctuation and quenched disorder (pinning) result in a vortex glass (VG) state inside the melting line (here: $B_m(T)$). The VG melts into a pinned liquid (TAFF regime) that is unpinned at higher fields and temperatures (flux flow regime). An unpinned entangled vortex liquid (EVL) is observed close to T_c . Right (relevant for YBCO): The Abrikosov vortex lattice melts into an unpinned liquid. $B_m(T)$ is here the phase transition while $H_{c2}(T)$ marks a crossover where $|\psi|$ decreases rapidly for increasing temperatures, and fluctuations are important within about 1 K of $H_{c2}(T)$. The lower part is drawn to scale and shows the shape of the melting line. From Reference [5].

2.3.3 Thermal fluctuations and melting of the flux line lattice

Thermal agitation can cause melting of a lattice. The Lindemann criterion [58] states that melting occurs when the rms thermal displacement (of the vortices) equals some fraction c_L of the lattice constant:

$$\sqrt{\langle u^2(T_m) \rangle_{\text{thermal}}} \approx c_L a_0 \quad . \quad (2.18)$$

This fraction is known as the Lindemann number, typically set to $c_L \sim 0.1\text{--}0.2$. The theory of FLL melting by Houghton *et al.* [59] does not take pinning into account, and in three dimensions melting of the FLL is probably a 1st order transition as indicated by Monte Carlo simulations [60] and measurements on clean samples [61–67]. In Figure 2.5 we show a phase diagram illustrating melting of the vortex lattice. See Figure 2.6 for an illustration of the FLL.

2.3.4 Vortex glass

In the presence of disorder and pinning a vortex glass (VG) phase with no long-range translational order of the FLL has been proposed [68, 69]. The transition from the solid VG to the liquid is continuous. Central in a VG is the diverging pinning barrier in the limit of small current density:

$$U(j) \sim 1/j^\mu \rightarrow 0 \quad \text{as } j \rightarrow 0 \quad (2.19)$$

and as a consequence the linear resistivity is truly zero in this limit. $0 < \mu \leq 1$ is the glassy exponent [5]. The theory of weak collective pinning (see above) seems well suited for describing the VG phase [5]. At the VG transition temperature T_g both the VG correlation length

$$\xi_{\text{VG}}(T) \propto \frac{1}{|T - T_g|^\nu} \quad (2.20)$$

and the characteristic relaxation time

$$\tau_{\text{VG}} \propto \xi_{\text{VG}}^z(T) \quad (2.21)$$

diverge. Upon cooling from the ohmic vortex liquid phase the resistivity vanishes as

$$\rho \propto (T - T_g)^{\nu(z+2-D)} \quad (2.22)$$

when $j \rightarrow 0$ and true superconductivity is a characteristic of the VG phase. Here D is the dimensionality of the vortex system. Figure 2.5 is a phase diagram that shows how the vortex glass melts into a pinned vortex liquid. In Figure 2.6 we illustrate the vortex configurations of the major vortex states: the Meissner phase, the vortex lattice (FLL) and the vortex glass.

2.3.5 The irreversibility line

The IL was first observed in the cuprate superconductors using dc magnetization by Müller et al. [71]. $H_{\text{irr}}(T)$, or $H(T_{\text{irr}})$, was defined as the point where the magnetization curves break up into a field cooled (FC) and a zero-field cooled (ZFC) branch. Below the IL the FC and ZFC curves are separate, signalling irreversible magnetic behaviour. Above the IL they fall on top of each other and the system is reversible. The IL exists also in the conventional low temperature superconductors, but their large activation barriers put H_{irr} very close to H_{c2} . In the cuprate superconductors the lossy (resistive) reversible

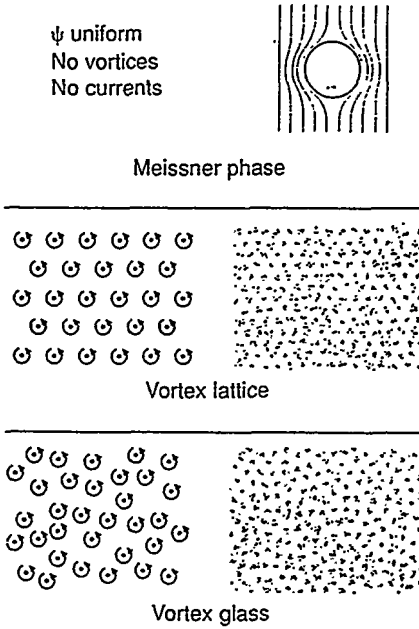


Figure 2.6: Ordered phases of a type II superconductor: the Meissner phase with all flux expelled (top), the ordered vortex lattice (FLL) (middle) and the disorderd vortex glass (bottom). For the latter two, the dots and arrows on the left mark the vortex cores and the circulating currents, respectively, and the images on the right illustrate the vortex arrangement from decoration experiments with fine magnetic par-ticles. From Reference [70].

region $H_{\text{irr}} < H < H_{c2}$ is very large, which is unfortunate from an applications point of view.

The nature of the IL has been a topic of debate. The IL has been identified with several different physical pictures, and an abundance of different experimental methods have been used in attempts to locate the IL.

In the TAFF and creep pictures the IL has been interpreted as a depinning line, a crossover from slow to fast dynamics of thermally activated flux lines. It will consequently depend on the time constant of the experiment, and also on the sample size and shape, and is as such not an intrinsic property of the material.

In the pinning independent melting picture substantial supercurrents can only flow below the melting temperature T_m where the FLL is an Abrikosov lattice [4]. T_m has then been a candidate for T_{irr} .

In the vortex glass picture, which is closely connected with weak collective pinning [5], the continuous transition from the low temperature vortex glass phase to the melted phase has been identified as an IL.

References

- [1] V. L. Ginzburg and L. D. Landau, *Zh. Experim. i Teor. Fiz.* **20** (1950) 1064.
- [2] F. London and H. London, *Proc. Roy. Soc. A* **149** (1935) 71.
- [3] M. Tinkham, *Introduction to Superconductivity*, McGraw-Hill, New York (1975).
- [4] A. Abrikosov, *Soviet Phys. J. E. T. P.* **5** (1957) 1174.
- [5] G. Blatter, M. V. Feigel'man, V. B. Geshkenbein, A. I. Larkin and V. M. Vinokur in *Vortices in high temperature superconductors*, preprint, ETH, Zürich (1993) 538 pages. *Rev. Mod. Phys.* **66** (1994) 1125.
- [6] R. J. Cava, A. W. Hewat, E. A. Hewat, B. Batlogg, M. Marezio, K. M. Rabe, J. J. Krajewski, W. F. Peck Jr. and L. W. Rupp Jr., *Physica C* **165** (1990) 419.
- [7] G. J. Dolan, F. Holtzberg, C. Feild and T. R. Dinger, *Phys. Rev. Lett.* **62** (1989) 2184.
- [8] M. Murakami, *Mod. Phys. Lett. B* **4** (1990) 163.
- [9] W. K. Kwok, S. Fleshler, U. Welp, V. M. Vinokur, J. Downey, G. W. Crabtree and M. M. Miller, *Phys. Rev. Lett.* **69** (1992) 3370.
- [10] W. K. Kwok, J. A. Fendrich, U. Welp, S. Fleshler, J. Downey and G. W. Crabtree, *Phys. Rev. Lett.* **73** (1994) 1088.
- [11] W. K. Kwok, J. A. Fendrich, C. J. van der Beek and G. W. Crabtree, *Phys. Rev. Lett.* **73** (1994) 2614.
- [12] M. Tachiki and S. Takahashi, *Solid State Commun.* **70** (1989) 291.

- [13] W. K. Kwok, U. Welp, V. M. Vinokur, S. Fleshler, J. Downey and G. W. Crabtree, Phys. Rev. Lett. **67** (1991) 390.
- [14] L. Civale, A. D. Marwick, M. W. McElfresh, T. K. Worthington, A. P. Malozemoff, F. H. Holtzberg, J. R. Thompson and M. A. Kirk, Phys. Rev. Lett. **65** (1990) 1164.
- [15] L. Civale, M. W. McElfresh, A. D. Marwick, F. Holtzberg, C. Feild, J. R. Thompson and D. K. Christen, Phys. Rev. B **43** (1991) 13732.
- [16] K. Fischer, G. Leitner, G. Fuchs, M. Schubert, B. Schlobach, A. Gladun and C. Rodig, Cryogenics **33** (1993) 97.
- [17] M. Wacenovsky, R. Miletich, H. W. Weber and M. Murakami, Cryogenics **33** (1993) 70.
- [18] F. M. Sauerzopf, H. P. Wiesinger, H. W. Weber, G. W. Crabtree, M. C. Frischherz and M. A. Kirk, Supercond. Sci. Technol. **5** (1992) 105.
- [19] F. M. Sauerzopf, H. P. Wiesinger, W. Krtscha, H. W. Weber, M. C. Frischherz and H. Gerstenberg, Cryogenics **33** (1993) 8.
- [20] L. Civale, A. D. Marwick, T. K. Worthington, M. A. Kirk, J. R. Thompson, L. Krusin-Elbaum, Y. Sun, J. R. Clem and F. Holtzberg, Phys. Rev. Lett. **67** (1991) 648.
- [21] C. J. van der Beek, M. Konczykowski, V. M. Vinokur, G. W. Crabtree, T. W. Li and P. H. Kes, preprint (1995).
- [22] C. J. van der Beek, M. Konczykowski, V. M. Vinokur, T. W. Li, P. H. Kes and G. W. Crabtree, Phys. Rev. Lett. **74** (1995) 1214.
- [23] M. Murakami, Mod. Phys. Lett. B **4** (1990) 163.
- [24] M. Slaski, L. T. Sagdahl, L. K. Heill, K. Fossheim, M. Murakami, H. Fujimoto, N. Koshizuka and S. Tanaka, Supercond. Sci. Technol. **5** (1992) S340; *idem*, Physica C **185-189** (1991) 2495.
- [25] K. Fossheim, M. G. Karkut, L. K. Heill, M. Slaski, L. T. Sagdahl, V. M. Vinokur, M. Murakami, H. Fujimoto, N. Koshizuka, S. Tanaka, F. Gencer, J. S. Abell and C. E. Gough, Physica Scripta T **42** (1992) 20.
- [26] M. G. Karkut, L. K. Heill, V. M. Vinokur, M. Slaski, L. T. Sagdahl, E. D. Tuset and K. Fossheim, Cryogenics **33** (1993) 60.

- [27] M. G. Karkut, M. Slaski, L. K. Heill, L. T. Sagdahl and K. Fossheim, Physica C **215** (1993) 19.
 - [28] M. Wacenovsky, R. Miletich and H. W. Weber, Supercond. Sci. Technol. **5** (1992) S184.
 - [29] W. E. Lawrence and S. Doniach in *Proceedings of the 12th International Conference on Low Temperature Physics*, ed. E. Kanda, Academic Press of Japan, Kyoto (1971) page 361.
 - [30] C. P. Bean, Phys. Rev. Lett. **8** (1962) 250.
 - [31] C. P. Bean, Rev. Mod. Phys. **36** (1964) 31.
 - [32] P. G. de Gennes, *Superconductivity in Metals and Alloys*, W. A. Benjamin Inc., New York (1966) pages 83f.
 - [33] J. H. P. Watson, J. Appl. Phys. **39** (1968) 3406.
 - [34] H. Dersch and G. Blatter, Phys. Rev. B **38** (1988) 11391.
 - [35] G. Ravi Kumar and P. Chadda, Phys. Rev. B **39** (1989) 4704.
 - [36] D.-X. Chen, A. Sanchez and J. Munos, J. Appl. Phys. **67** (1990) 3430.
 - [37] Y. B. Kim, C. F. Hempstead and A. R. Strnad, Phys. Rev. **129** (1963) 528.
 - [38] J. Bardeen and M. J. Stephen, Phys. Rev. **140** (1965) 1197.
 - [39] M. Tinkham, Phys. Rev. Lett. **13** (1964) 804.
 - [40] P. W. Anderson, Phys. Rev. Lett. **9** (1962) 309.
 - [41] P. W. Anderson and Y. B. Kim, Rev. Mod. Phys. **36** (1964) 39.
 - [42] M. V. Feigel'man, V. B. Geshkenbein and V. M. Vinokur, Phys. Rev. B **43** (1991) 6263.
 - [43] V. B. Geshkenbein and A. I. Larkin, Zh. Eksp. Teor. Fiz. **95** (1989) 108.
 - [44] C. J. van der Beek, G. J. Nieuwenhuys, P. H. Kes, H. G. Schnack and R. Griessen, Physica C **197** (1992) 320.
 - [45] M. R. Beasley, R. Labusch and W. W. Webb, Phys. Rev. **181** (1969) 682.
 - [46] R. Griessen, Physica C **172** (1991) 441.
-

- [47] Y. Yeshurun and A. P. Malozemoff, Phys. Rev. Lett. **60** (1988) 2202.
- [48] M. V. Feigel'man, V. B. Geshkenbein, A. I. Larkin and V. M. Vinokur, Phys. Rev. Lett. **63** (1989) 2303.
- [49] T. Nattermann, Phys. Rev. Lett. **64** (1990) 2454.
- [50] M. V. Feigel'man, V. B. Geshkenbein and A. I. Larkin, Physica C **167** (1990) 177.
- [51] G. Blatter, B. I. Ivlev and J. Rhyner, Phys. Rev. Lett. **66** (1991) 2392.
- [52] V. B. Geshkenbein, A. I. Larkin, M. V. Feigel'man and V. Vinokur, Physica C **162–164** (1989) 239.
- [53] A. I. Larkin and Yu. N. Ovchinnikov, Zh. Eksp. Teor. Fiz. **65** (1973) 1704.
- [54] A. I. Larkin and Yu. N. Ovchinnikov, J. Low. Temp. Phys. **34** (1979) 409.
- [55] P. H. Kes, J. Aarts, J. van den Berg, C. J. van der Beek and J. A. Mydosh, Supercond. Sci. Technol. **1** (1989) 242.
- [56] C. J. van der Beek and P. H. Kes, Phys. Rev. B **43** (1991) 13032.
- [57] T. T. M. Palstra, B. Batlogg, R. B. van Dover, L. F. Schneemeyer and J. V. Waszczak, Phys. Rev. B **41** (1991) 6621.
- [58] F. Lindemann, Phys. Z **11** (1910) 69.
- [59] A. Houghton, R. A. Pelcovits and A. Sudbø, Phys. Rev. B **40** (1989) 6763.
- [60] R. E. Hetzel, A. Sudbø and D. A. Huse, Phys. Rev. Lett. **69** (1992) 518.
- [61] H. Safar, P. L. Gammel, D. A. Huse, D. J. Bishop, J. P. Rice and D. M. Ginsberg, Phys. Rev. Lett. **69** (1992) 824.
- [62] H. Safar, P. L. Gammel, D. A. Huse, D. J. Bishop, W. C. Lee, J. Giapintzakis and D. M. Ginsberg, Phys. Rev. Lett. **70** (1993) 3800.
- [63] H. Safar, P. L. Gammel, D. A. Huse, G. B. Alers, D. J. Bishop, W. C. Lee, J. Giapintzakis and D. M. Ginsberg, preprint.
- [64] W. K. Kwok, S. Fleshler, U. Welp, V. M. Vinokur, J. Downey, G. W. Crabtree and M. M. Miller, Phys. Rev. Lett. **69** (1992) 3370.
- [65] W. K. Kwok, J. Fendrich, U. Welp, S. Fleshler, J. Downey and G. W. Crabtree, Phys. Rev. Lett. **72** (1994) 1088.

- [66] W. K. Kwok, J. Fendrich, S. Fleshler, U. Welp, J. Downey and G. W. Crabtree, Phys. Rev. Lett. **72** (1994) 1092.
- [67] W. K. Kwok, J. A. Fendrich, C. J. van der Beek and G. W. Crabtree, Phys. Rev. Lett. **73** (1994) 2614.
- [68] M. P. A. Fisher, Phys. Rev. Lett. **62** (1989) 1415.
- [69] D. S. Fisher, M. P. A. Fisher and D. A. Huse, Phys. Rev. B **43** (1991) 130.
- [70] D. A. Huse, M. P. A. Fisher and D. S. Fisher; Nature **358** (1992) 553.
- [71] K. A. Müller, M. Takashige and J. G. Bednorz, Phys. Rev. Lett. **58** (1987) 1143.

ac magnetic response

In this introductory Chapter we present the fundamentals and background of the ac susceptibility technique used to probe the flux statics and dynamics of our superconducting samples.

The first two Sections present the essential parameter, the ac permeability μ or, equivalently, susceptibility $\chi = \mu - 1$. The fundamental definitions and physical origin, and the related mathematics are followed by model results for two important cases: the Bean critical state [1–4] and the ohmic resistive state. In the third Section we look at what information ac magnetic measurements can provide on the physical state of the sample. The fourth and final Section consider in greater depth how ac permeability can probe irreversibility and the vortex states.

3.1 ac permeability

When a conductor is exposed to time-varying external magnetic fields $\tilde{H}_e(t)$, a screening current (in normal conductors: eddy current) density \tilde{j} is set up inside the conductor in an attempt to counteract the change in the flux, in accordance with Lenz' law. The induction $\tilde{B}(t)$ inside the sample connects via Faraday's law, $\nabla \times \tilde{E} = -\partial \tilde{B}/\partial t$, to the induced electric field $\tilde{E}(t)$ generating a screening current \tilde{j} and a dissipation rate of the energy density $\tilde{j} \cdot \tilde{E}$.

Small screening (eddy) currents will allow large amounts of flux to enter and leave the sample easily in each cycle so that $B \approx \mu_0 H_e$ and the losses are large.

Large screening currents block large amounts of flux from entering the sample, causing B to differ from $\mu_0 H_e$, thus keeping the losses small.

When considering the ac losses, the complex permeability $\mu = \mu' + i\mu''$, related to the complex susceptibility χ via $\mu = \chi + 1$, enters as a useful quantity. The applied field and the induction can be split into dc and ac parts,

$$H_e = H_{dc} + h_{ac} \cos \omega t , \text{ and} \quad (3.1)$$

$$B = B_{dc} + b_{ac}(t) , \quad (3.2)$$

when we assume an harmonic external ac field with angular frequency ω . Here we suppress the position dependence of the induction in the notation, and also simplify to one spatial dimension. Since $b_{ac}(t)$ is periodic, it can be expanded in a Fourier time series:

$$\bar{b}_{ac}(t) = \mu_0 h_{ac} \sum_{n=1}^{\infty} (\mu'_n \cos n\omega t + \mu''_n \sin n\omega t) \quad (3.3)$$

where

$$\mu'_n = \frac{\omega}{\pi \mu_0 h_{ac}} \int_0^{2\pi/\omega} \bar{b}_{ac}(t) \cos n\omega t dt , \text{ and} \quad (3.4a)$$

$$\mu''_n = \frac{\omega}{\pi \mu_0 h_{ac}} \int_0^{2\pi/\omega} \bar{b}_{ac}(t) \sin n\omega t dt . \quad (3.4b)$$

The bar over $b_{ac}(t)$ indicates that a sample (spatial) average is taken, *i.e.* $\bar{b}_{ac}(t)$ is equivalent to the ac magnetization $m_{ac}(t) = (\mu_0 V)^{-1} \int_V b_{ac}(t) dV$ with V as the sample volume.

In our measurements we study only the fundamental components of the permeability, *i.e.* μ'_1 and μ''_1 . In Reference [5] the higher harmonics have been investigated in $\text{YBa}_2\text{Cu}_3\text{O}_{7-\delta}$. For simplicity we drop the subscripts and write only μ' and μ'' . Equations (3.4a) and (3.4b) then reduce to

$$\mu' = \frac{\omega}{\pi \mu_0 h_{ac}} \int_0^{2\pi/\omega} \bar{b}_{ac}(t) \cos \omega t dt \quad (3.5a)$$

$$\mu'' = \frac{\omega}{\pi \mu_0 h_{ac}} \int_0^{2\pi/\omega} \bar{b}_{ac}(t) \sin \omega t dt \quad (3.5b)$$

as seen in Reference [6], for example. From this, we identify μ' as the component of the induction in the sample that is in-phase with the driving field and μ'' as the corresponding out-of-phase component. μ' is also called the inductive component and μ'' the resistive or lossy component.

The reason for calling μ'' the lossy component is that it is a direct measure of the hysteretic loss in the sample. The area A_{hyst} of the hysteresis loop is

$$A_{\text{hyst}} = \oint H_a d\bar{B} = \int_0^{2\pi/\omega} (H_{\text{dc}} + h_{\text{ac}} \cos \omega t) \frac{d\bar{b}_{\text{ac}}}{dt} dt . \quad (3.6)$$

Only the $n = 1$ term of (3.3) survives the integration and

$$A_{\text{hyst}} = \pi \mu_0 h_{\text{ac}}^2 \mu'' . \quad (3.7)$$

Since the loss per cycle and unit volume is equal to the area of the hysteresis loop [7], it is hence proportional to the out-of-phase component of the ac permeability μ'' .

An alternative, physical way to define the (fundamental) ac permeability is

$$\mu = \int_V B dV / \int_V H dV , \quad (3.8)$$

see for example Reference [8]. The integrals run over the sample volume V .

3.2 Model calculations

In free space $\mu' = 1$ and $\mu' = 0$ and in a superconductor in the Meissner state both $\mu' \approx 0$ and $\mu'' \approx 0$. In this Section we will look closer at the intermediate regime of the mixed state of a type-II superconductor and consider two important cases where flux penetrates into the bulk of the sample: the Bean critical state [1-4] and the ohmic regime. Of course, the samples we measure are cubes, and so the following discussion on exactly solvable geometries is only a guide to our experimental results.

3.2.1 The Bean critical state

We assume that $H_{\text{dc}} \gg h_{\text{ac}}$, i.e. that the probing ac field is only a small perturbation on top of a large dc field, and that, for field changes $\sim h_{\text{ac}}$, we are in a Bean critical state with linear flux profiles. The magnetic field is applied parallel to the surface.

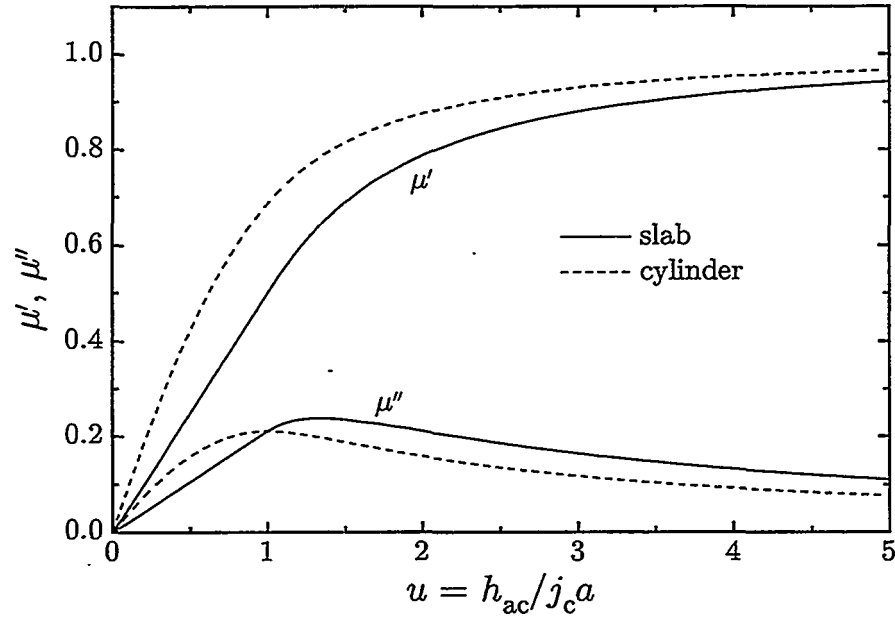


Figure 3.1: ac permeability $\mu = \mu' + i\mu''$ vs. $u = h_{ac}/j_c a$ for an infinite slab of thickness $2a$ and an infinite cylinder of radius a in the Bean critical state.

Introducing the relative penetration depth $u = h_{ac}/j_c a$ the ac permeability for an infinite slab of thickness $2a$ is, see Appendix A,

$$\mu' = \frac{1}{2}u \quad , \quad \mu'' = \frac{2}{3\pi}u \quad (3.9a)$$

for $u < 1$ (incomplete penetration), and

$$\begin{aligned} \mu' &= 1 - \frac{1}{\pi} \left[\left(1 - \frac{u}{2}\right) \arccos\left(1 - \frac{2}{u}\right) - \left(\frac{4}{3} - u - \frac{4}{3u}\right) \sqrt{\frac{1}{u} - \frac{1}{u^2}} \right] \quad , \\ \mu'' &= \frac{2}{\pi u} \left(1 - \frac{2}{3u}\right) \end{aligned} \quad (3.9b)$$

for $u > 1$ (complete penetration). See Figure 3.1. Here, u is a measure of penetration since h_{ac}/j_c is the distance the field penetrates into the sample. As u increases flux penetrates further into the sample, reaching the center when $u = 1$. We note that the loss peak reaches its maximum value $\mu''_{\max} = 3/4\pi = 0.24$ when $u = u^* = 4/3$, i.e. just after the flux has reached the center.

For an infinite cylinder of radius a the permeability is [7,9]

$$\mu' = u \left(1 - \frac{5}{16}u^2 \right) , \quad \mu'' = \frac{4}{3\pi} u \left(1 - \frac{u}{2} \right) \quad (3.10a)$$

for $u < 1$, and

$$\begin{aligned} \mu' = 1 + \frac{2}{\pi} & \left[\left(-1 + u - \frac{5}{16}u^2 \right) \arcsin \frac{1}{\sqrt{u}} \right. \\ & \left. + \left(-\frac{1}{3u} + \frac{1}{2} - \frac{19}{24}u + \frac{5}{16}u^2 \right) \sqrt{\frac{1}{u} - \frac{1}{u^2}} \right] , \\ \mu'' = \frac{4}{3\pi u} & \left(1 - \frac{1}{2u} \right) \end{aligned} \quad (3.10b)$$

for $u > 1$. See Figure 3.1. Again, $u = h_{ac}/j_c a$ measures the penetration, but now $\mu''_{\max} = 2/3\pi = 0.21$ and $u^* = 1$; μ'' peaks just when the flux penetrates to the center.

3.2.2 The ohmic regime

In materials with Ohmic I - V behaviour the penetration of the magnetic field is characterized by a skin depth δ_s . It follows directly from Ohm's law

$$\vec{E} = \rho \vec{j} \quad (3.11)$$

and Maxwell's equations,

$$\nabla \times \vec{E} = -\frac{\partial \vec{B}}{\partial t} \quad (3.12a)$$

$$\nabla \times \vec{B} = \mu_0 \vec{j} + \epsilon_0 \mu_0 \frac{\partial \vec{E}}{\partial t} \approx \mu_0 \vec{j} \quad (3.12b)$$

$$\nabla \cdot \vec{B} = 0 , \quad (3.12c)$$

where the approximation in equation (3.12b) is valid for good conductors in fields that do not vary extremely rapidly.¹

¹The term $\epsilon_0 \mu_0 \partial_t E$ is dropped since it will be much smaller than the term $\mu_0 j$ when the resistivity ρ is small: We compare j and $|\epsilon_0 \partial_t E| = \epsilon_0 \omega E = \epsilon_0 \omega \rho j$. Whenever $1/\rho \omega \gg \epsilon_0$ our approximation is valid. And with superconductors, and most metals in fact, we are on solid ground since the resistivity is small for all reasonable frequencies ω . For metals such as copper, silver, gold, iron and aluminum, $\rho \sim 0.1\text{--}1 \mu\Omega\text{cm}$, which makes the approximation valid for frequencies $\omega \ll 10^{19}\text{--}10^{20} \text{ s}^{-1}$, and the limit is rather set by the plasma frequencies $\omega_p \sim 10^{14}\text{--}10^{15} \text{ s}^{-1}$. The normal state resistivity for YBCO, say, is about $50 \mu\Omega\text{cm}$.

Taking the curl of equation (3.12b), making the Fourier *ansatz* $\vec{B} \sim e^{-i\omega t}$, $\vec{E} \sim e^{-i\omega t}$ and using equations (3.11) and (3.12c), we get

$$\begin{aligned}\nabla \times (\nabla \times \vec{B}) &= \nabla(\nabla \cdot \vec{B}) - \nabla^2 \vec{B} = \mu_0 \nabla \times \left(\frac{1}{\rho} \vec{E} \right) = \frac{\mu_0}{\rho} \nabla \times \vec{E} \\ &= \frac{\mu_0}{\rho} \left(-\frac{\partial \vec{B}}{\partial t} \right) = \frac{i\mu_0 \omega}{\rho} \vec{B}\end{aligned}\quad (3.13)$$

or

$$\left\{ \nabla^2 + k^2 \right\} \vec{B} = 0 \quad (3.14)$$

where

$$k^2 \equiv \frac{i\mu_0 \omega}{\rho} \Rightarrow k = (1+i) \sqrt{\frac{\mu_0 \omega}{2\rho}} \equiv (1+i)/\delta_s , \quad (3.15)$$

and we recognize δ_s as the characteristic size for the field change, *i.e.* a penetration depth. We define the relative penetration depth $1/u = \delta_s/a$.

We need to specify boundary conditions to determine the relevant solutions of equation (3.14) for the ac induction b_{ac} for different geometries. Below we present the solutions for three exactly solvable geometries — the infinite slab, cylinder and half-space — for applied fields h_{ac} parallel to the surfaces. The ac permeability is calculated using (3.8).

The infinite slab is of thickness $2a$, centered about $x = 0$ (or occupying the interval $0 \leq x \leq 2a$), and our two boundary conditions are that the field is continuous at the surfaces $x = \pm a$ (or $x = 0, 2a$). The solution is

$$b_{ac}(x) = \mu_0 h_{ac} \frac{\cos(kx)}{\cos(ka)} , \quad (3.16)$$

yielding

$$\mu' = \frac{1}{2u} \frac{\sinh 2u + \sin 2u}{\cosh 2u + \cos 2u} , \quad \mu'' = \frac{1}{2u} \frac{\sinh 2u - \sin 2u}{\cosh 2u + \cos 2u} . \quad (3.17)$$

μ'' peaks to $\mu''_{\max} = 0.417$ at $u = u^* = 1.127$. See Figure 3.2.

With the infinite cylinder axis along $r = 0$, the boundary conditions are $b_{ac}(a) = \mu_0 h_{ac}$, where a is the radius, and $\partial b_{ac}/\partial r|_{r=0} = 0$ (the current must vanish in the center). Solving, we get

$$b_{ac}(r) = \mu_0 h_{ac} \frac{J_0(kr)}{J_0(ka)} \quad (3.18)$$

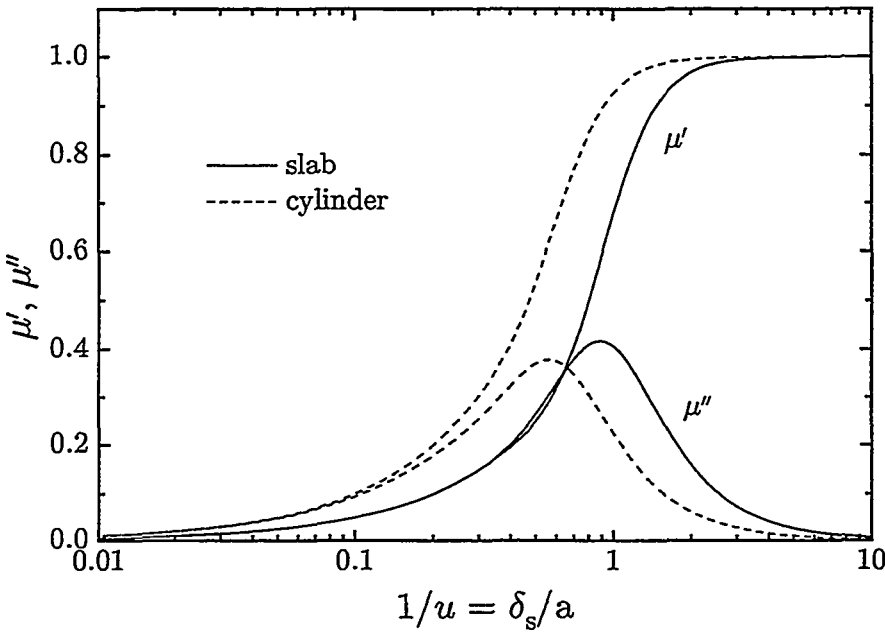


Figure 3.2: Magnetic permeability for an infinite slab and an infinite cylinder in the Ohmic regime as a function of the relative penetration depth $1/u = \delta_s/a = \sqrt{2\rho/\mu_0\omega}/a$.

where J_0 is the Bessel function of the 1st kind and order 0 (zero). The permeability μ is given as

$$\mu = \frac{2}{a^2 \mu_0 h_{ac}} \int_0^a dr r b_{ac}(r) = \frac{2}{ka} \frac{J_1(ka)}{J_0(ka)} = \frac{2}{(1+i)u} \frac{J_1((1+i)u)}{J_0((1+i)u)} \quad (3.19)$$

where $u \equiv a/\delta_s$ and J_1 is the Bessel function of the 1st kind and order 1. See Figure 3.2. μ'' peaks at $u = u^* = 1.77838$, reaching $\mu''_{\max} = 0.377$.

If we let our sample occupy the infinite half-space $x > 0$, our boundary conditions are $b_{ac}(x = 0) = \mu_0 h_{ac}$ and $b_{ac}(x \rightarrow \infty) = 0$. Our solution is then simply

$$b_{ac}(x) = \mu_0 h_{ac} e^{ikx} = \mu_0 h_{ac} e^{ix/\delta_s} e^{-x/\delta_s} \quad (3.20)$$

and, not surprisingly,

$$\mu = 0 \quad . \quad (3.21)$$

3.2.3 Cole-Cole analysis

Sometimes it can be useful to represent the complex ac permeability in an Argand diagram or complex plane locus — a so-called Cole-Cole plot [10],² i.e. a parametric plot of the imaginary component, μ'' , against the real component, μ' . The free parameter can be the frequency f (or ω), the resistivity ρ or the sample size a in an ohmic regime, or the amplitude h_{ac} , the critical current density j_c or the sample size a in a Bean critical state, for example. Typically, in the laboratory the free parameter in each experimental run is the temperature T . As the temperature changes, the resistivity or the critical current density also change. Examples of μ scans where the amplitude is the control parameter can also be found [11]. van de Klundert *et al.* used Cole-Cole plots in their work on hollow and solid superconducting cylinders above and below T_c where they found that normal currents contribute to the ac behaviour of surface superconductivity [12]. Emmen *et al.* used a Cole-Cole plot *en passant* in a comparison with a Debye model and found the TAFF model to describe the field, frequency and temperature dependence of the ac susceptibility of BSCCO single crystals with $\vec{H} \parallel \hat{c}$ [13]. Wacenowsky *et al.* compared results on an neutron-irradiated MPMG sample with exact calculations for the Bean critical state model and for the skin depth picture and found the response to be intermediate between the two models [14]. Ling and Budnick compared experimental data on Nb₃Al and YBCO crystals to three different models (relaxational, diffusive (ohmic) and Bean critical-state) for the ac magnetic response of superconductors, and found different models to apply for different field orientations and configurations [15].

In Figure 3.3 we replot the ac permeabilities of Figures 3.1 and 3.2. We immediately see the differences due to sample geometry and state.

3.3 ac permeability as a probe

In addition to being a measure of the ac losses, cf. (3.7), the ac permeability can also provide information on the details of the electromagnetic or thermodynamic state of the sample. The previous Section illustrates for example how it can differentiate between a Bean critical state and ohmic behaviour, where the principal differences are that in the former case μ depends on the excitation

²Cole and Cole [10] used this kind of representation of dielectric constants in a study of dispersion and absorption in dielectrics.

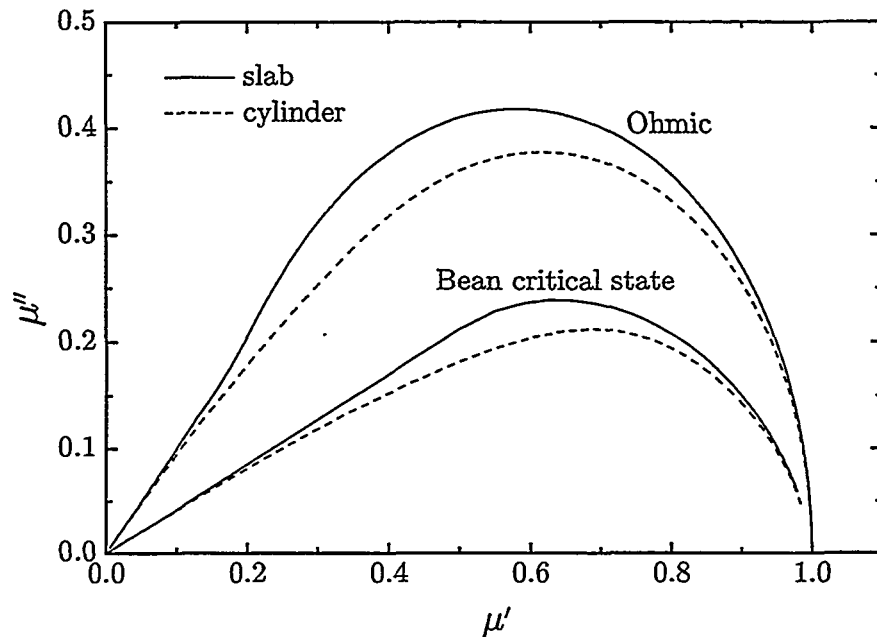


Figure 3.3: Cole-Cole parametric plots of the complex ac permeability for an infinite cylinder and an infinite slab in both an ohmic and a Bean critical state.

field amplitude h_{ac} but not on the frequency f (or ω) while in the latter the exact opposite is true.

A physical picture of the loss peak in a generic superconductor is as follows: At low temperatures all the (ac) flux is shielded out and there are of course no ac magnetic losses. Increasing the temperature, more and more flux enters the sample leading to increased losses. Above the temperature where the flux has reached the center (approximately) the ac magnetic losses decrease since more and more of the material is normal conducting.

Of course, a similar picture can be drawn for normal conductors. Here eddy currents are responsible for the losses. Since the resistivity changes very slowly with temperature, the loss peak would, however, be very broad.

Virtues of the ac permeability technique include the high sensitivity, generally better than dc resistivity measurements, and the extra information that can be obtained from phase detection and the additional parameter, the frequency.

Ideally,³ one can derive important information such as the critical current density j_c (in a Bean critical state) or the resistivity ρ (when in an ohmic regime) of the sample, or the internal losses, and map the dependence of these quantities on external parameters such as temperature T and magnetic field H ; vital information for understanding the physics of the superconductors and hence for applications.

The critical current density j_c can be obtained from ac susceptibility data when in a Bean critical state, with [16–21] or without [22–25] a dc bias field. Analysis based on the higher harmonics has also been performed [2]. The method applied is typically using the peak of μ'' to derive j_c . From expressions for the peak condition, such as in connection with (3.9b) or (3.10b),

$$j_c(H, T) = \alpha \frac{h_{ac}^*}{a} \quad (3.22)$$

where $\alpha \sim 1$ is a geometry dependent factor ($\alpha = 3/4$ for an infinite slab and $\alpha = 1$ for an infinite cylinder). The asterisk denotes the value of the quantity at the peak, see Figure 3.1.

Similarly, in an ohmic regime the resistivity $\rho(H, T)$ can be determined as

$$\rho(H, T) = \alpha^2 \frac{\mu_0 \omega^*}{2a^2} \quad (3.23)$$

where again $\alpha \sim 1$ depends on the sample geometry ($\alpha = 1.127$ for an infinite slab and $\alpha = 1.778$ for an infinite cylinder; see (3.17) and (3.19)) and the asterisk on ω indicate that the value at the peak should be used, see Figure 3.2.

The proportionality between the hysteretic losses and μ'' , the loss peak, as expressed in (3.7) can be utilized to find the lower critical field H_{c1} . The ac field will cycle through the hysteresis. In zero field, if $h_{ac} < H_{c1}$ there will be no hysteresis and $\mu'' = 0$. If $h_{ac} > H_{c1}$ the area of the hysteresis loop is non-zero and $\mu'' > 0$. Measuring $\mu''(T)$ at fixed h_{ac} [26] or $\mu''(h_{ac})$ at fixed T [27–29] can then give an upper limit for H_{c1} . The same principle applies to finding the upper critical field H_{c2} .

We should bear in mind that loss mechanisms other than magnetic hysteresis can contribute to μ'' [30]. Frequency dependence can also result from, e.g.,

³In the real world, factors such as non-ideal sample shapes and sizes will of course complicate quantitative analysis, e.g. by introducing demagnetization effects, and material imperfections from the manufacturing process give rise to a plethora of wanted and unwanted (from both an applications as well as a physical description point of view) effects.

flux creep or flux flow [13, 31, 32], eddy currents of normal electrons [33] and viscous damping of the vortex lattice [9, 33].

Above the irreversibility line (IL), see Chapter 2, a vortex liquid state with ohmic response is expected [34] and μ will depend on the frequency of the applied ac field but not on the amplitude. Below the IL a vortex solid state with non-linear response due to pinning is expected [34] with a pronounced amplitude dependence of μ but no, or only a weak, frequency dependence. Hence, in principle the position of the IL in the H - T plane can then be determined by carefully varying the amplitude and frequency and observing where the behaviour changes [19]. In a simple physical picture the loss peak occurs when crossing the IL: At low temperatures the vortices form a pinned solid or lattice with little or no dissipative motion of flux. The losses increase as the lattice depins allowing more flux to move, but then decrease as the viscosity decreases towards T_c . Below we go into the relation between the IL and the ac magnetic response in more detail.

3.4 Probing irreversibility with ac permeability

We refer to Chapter 2 for a brief introduction to the irreversibility line (IL), the line in the H - T plane that separates reversible from irreversible behaviour.

Since the first observation of irreversible magnetization in the cuprate superconductors [35] many groups have used ac permeability/susceptibility in studies the vortex dynamics [13, 28, 36–61], often in an attempt to determine the onset of pinning and irreversibility in the H - T plane from the position of the peak in the lossy component μ'' [13, 28, 36, 38, 41–53, 61]. The appearance of higher harmonics, in particular the 3rd, in the ac permeability has been used as another criterion [54–57, 59, 60]. The onset of the 3rd harmonic would correspond to a value of j_c closer to zero than the position of the peak in the fundamental harmonic — Arndt *et al.* claim a difference in the j_c level of 3 orders of magnitude [60] — making it a better IL in the sense that the IL separates regions of non-zero and zero critical currents.

3.4.1 The irreversibility line from the loss peak maximum

The rationale for using the loss peak maximum to locate the IL was given by Malozemoff *et al.* [36] as follows:

[The peak] occurs when vortex lines are thermally activating very rapidly across the pinning barriers, corresponding to a point where irreversible magnetization, and the critical current which depends on it, drop below measureable levels given the experimental measurement times.

These authors also stated that $j_c > 0$ below the IL and $j_c = 0$ above it. This is in line with the very simple physical picture given at the end of Section 3.3.

But in a Bean critical state, say, the loss peak occurs for a constant ratio j_c/h_{ac} for a fixed sample size. Consequently, loss peak lines, taken at a fixed finite h_{ac} , are then not true ILs but rather critical current countours, i.e. lines of constant $j_c > 0$ (see for example Reference [62]).

3.4.2 Frequency dependence

We note in the above quote the emphasis on the experimental time scale: Paraphrasing Gömöry and Takács [62], irreversibility is, in general, the existence of a non-equilibrium state over a period of time equal to or larger than the time scale of the observation; in ac measurements the time scale is $1/f$. One can visualize vortices sitting in pinning potential wells trying to get out with a characteristic attempt time τ_0 . If the experimental frequency $f > 1/\tau_0$ the vortices will not have time to leave the pinning sites during a cycle, they shuttle back and forth at the bottom of the potential well, and the system appears pinned, whereas if $f < 1/\tau_0$ the vortices will have a good chance of escaping their wells since they are allowed many attempts at it in each cycle, and the system appears unpinned. Hence the choice of frequency has important bearing on the result. It is a well known fact that the ILs defined from the maxima in μ'' shift with frequency [8, 13, 36, 38, 45–47, 49–52, 62]. The physical reason for this is simply that μ'' peaks about the moment the flux front reaches the sample center, and this penetration depends on the frequency through the skin penetration depth in (3.24) below or through the relaxation of the screening current $j(t)$ in (3.25) below.

3.4.3 The loss peak maximum as a measure of flux penetration

As we saw above in Section 3.2 the loss component of the permeability reaches a maximum when the flux front arrives at about the sample center, i.e. when

the ac penetration depth λ_{ac} is approximately equal to half the relevant sample size a .

Linear response

If the peak in μ'' occurs in the ohmic, or linear, domain,

$$\lambda_{\text{ac}} = \delta_s = \sqrt{\frac{2\rho(T)}{\mu_0\omega}} \quad (3.24)$$

and the frequency dependence is obvious. The resistivity $\rho(T)$ may be described by the activation formula $\rho = \rho_0 \exp[-U(H, T)/k_B T]$ in the TAFF regime (see Subsection 2.3.2). At higher temperatures, the resistivity is due to flux flow and is given approximately by $\rho_{\text{ff}} = \rho_n H / H_{c2}$ [63] where ρ_n is the normal state resistivity. In these regions of linear I - V behaviour, the induced currents j are proportional to the applied ac field amplitude h_{ac} and $\mu(H, T)$ does not depend on h_{ac} .

Non-linear response

When the I - V characteristics are non-linear, which is the case when pinning is important, such as in the vortex glass (VG) state [64, 65], or even if the amplitude, and hence current, becomes sufficiently large, then $\mu(H, T)$ will depend on the amplitude h_{ac} [66]. Here, below the IL, the resistivity is strongly non-linear [67–71] where now, in the collective flux creep (CFC) model [72, 73], $\rho \approx \rho_0 \exp[-U(j)/k_B T]$ with the strongly non-linear current dependent activation energy $U(j) = U_c[(j_c/j) - 1]^\mu$ where j and j_c are the current density in the sample and its critical current density, respectively, and the exponent $\mu > 0$ depends on the dimensionality of the vortex system. Then in the low current limit of this collective creep/VG picture, $\lim_{j \rightarrow 0} \rho = 0$ and a true superconducting state is realized. Creep processes are relevant, but it has been shown that the distribution of the flux in a vortex glass regime is analogous to that in the Bean critical state: B , or specifically in ac magnetic experiments b_{ac} , drops linearly from the surface and the corresponding current density j is constant over the depth of the flux penetration except for an exponentially narrow region near the front of the flux (if the demagnetization factor is small) [66, 74]. In the region of constant j the ac penetration depth is given by.

$$\lambda_{\text{ac}} = L_B = \frac{h_{\text{ac}}}{j(t)} \quad . \quad (3.25)$$

The temporal nature important in ac experiments enters as j relaxes in time due to thermally activated processes. From (2.16) we have for dynamic measurements that $j(t) = j_c [1 + \mu(k_B T/U_c) \ln(1+t/t_0)]^{-1/\mu}$. In ac experiments, the time t is the characteristic time of the experiment, i.e. $1/f$, or $1/\omega$. t_0 is again some attempt time. Existing experimental data on t_0 are quite uncertain [8] in that they span a wide range: from 10^{-12} –1 s, with perhaps a preference towards the nanosecond scale [8, 21, 75, 76]. Note that under ac excitation the actual current j may be quite close to j_c provided the frequency is high enough, i.e. $\omega t_0 \geq 1$. The ac field and current will penetrate a distance $\lambda_{ac} = L_B$, see (3.25), into the sample, and a peak in μ'' will be observed approximately when the sample center is reached. In this non-linear regime μ will depend on the ac field amplitude but only weakly on the frequency.

Degrees of non-linearity

The ohmic regime and the Bean critical state are the two extremes on a “linearity scale”, and we could of course interpolate between them. Formally, this has been done by Rhyner with a smooth power-law I - V characteristic [77] that can also be expressed as [78]

$$\vec{E} = \left| \frac{j}{j_c} \right|^\sigma \rho \vec{j} \quad (3.26)$$

where the resistivity ρ in general will depend on field, temperature, current density and frequency. See Figure 3.4. The exponent σ is then a measure of the degree of non-linearity. In physical terms it is expressed as $\sigma = U/k_B T$ [78], and the ohmic flux flow regime results as $U = 0$ (or $U \ll k_B T$) and $\sigma = 0$, whereas the pinned Bean critical state results as $U \rightarrow \infty$ (or $U \gg k_B T$) and $\sigma \rightarrow \infty$. From this we can also define a generalized ac penetration depth

$$\lambda_{ac} = \left(\frac{h_{ac}}{j} \right)^{\frac{\sigma}{\sigma+2}} \left(\frac{2\rho}{\mu_0 \omega} \right)^{\frac{1}{\sigma+2}} \quad (3.27)$$

that interpolates between (3.24) and (3.25) [78]. In principle it is possible to derive the value of the exponent σ from the amplitude and frequency dependencies of the measured response when $\lambda_{ac} = \alpha a$ at the loss peak maximum. The geometry dependent factor $\alpha \sim 1$, as for (3.22) and (3.23). By simultaneously varying h_{ac} and f (or ω) while fixing the loss peak temperature T^* , the exponent is obtained as

$$\sigma = \ln \frac{2\rho}{\mu_0 \omega \alpha^2 a^2} / \ln \frac{\alpha a j}{h_{ac}} \quad (3.28)$$

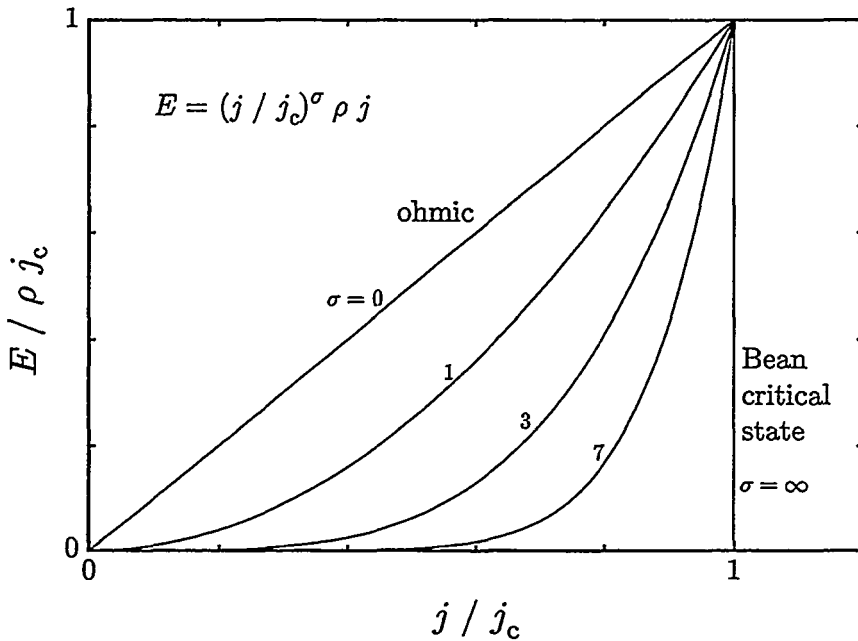


Figure 3.4: I - V curves after (3.26) for different degrees of non-linearity.

The above procedure can be realized in the lab if the temperature is kept constant and for a set of frequencies the permeability is recorded while the amplitude is swept across the peak.

3.4.4 Obtaining the irreversibility line from ac magnetic experiments

Geshkenbein *et al.* [8] give a recipe for obtaining the IL or the VG line: Starting in the ohmic regime with a high frequency, the full peak in $\mu''(T)$ will occur above the vortex glass temperature T_g . Lowering the frequency we move the maximum, at T^* , down in temperature. In the limit $f \rightarrow 0$ and $j \propto h_{ac} \rightarrow 0$, equivalent to the VG criterion $\rho \rightarrow 0$ for $j \rightarrow 0$, we should approach the true T_g defining the IL in this model. This is of course not realisable in the laboratory since finite amplitudes and frequencies must be used: For a very small frequency a finite amplitude would move T^* below T_g into the non-linear region where ρ depends strongly on h_{ac} through j . One could of course

extrapolate to $f = 0$ from $f > 0$ e.g. as described in Reference [79], but h_{ac} still remains finite. However, using an effective resistivity $\rho_{\text{eff}} = E(j^*)/j^*$, where $E \propto \exp(-\text{const.}/j^\mu)$ and where the asterisk denotes the value at the loss peak maximum, we see that using very small h_{ac} we will move T^* up towards T_g as h_{ac} decreases further.

In principle it is then possible to distinguish between a vortex liquid and a vortex glass state by carefully monitoring the response as the excitation field amplitude and frequency are varied: The onset of non-linearity signals the transition into a VG [66]. $\mu(H, T)$ can be related to the linear and/or non-linear portions of the I - V curves. Since the IL describes the onset of pinning and with it the onset of non-linearity, $\mu(H, T)$ can be considered a probe of irreversibility.

This procedure is essentially what Civale *et al.* followed for experiments on a thin platelet of YBCO [19]. They moved the loss peak maximum from a linear (non-pinning) to a non-linear (pinning) regime by adjusting the frequency.

ac susceptibility measurements have also been used to obtain VG parameters, the exponents ν and z and of course T_g , using a different approach: Recently Kötzler *et al.* carefully converted measured susceptibility data into linear dynamic conductivity which they consequently scaled [80].

With the formula (2.15) for the collective creep current density, $j(t) = j_c[1 + (k_B T/U_0) \ln(1+t/t_0)]^{-1/\mu}$, and the expression (3.25) for the penetration depth we find that at the loss peak maximum the amplitude and frequency are related by

$$h_{\text{ac}} = \alpha a j_c \left[1 + \frac{k_B T^*}{U_0} \ln \left(1 + \frac{f_0}{f} \right) \right]^{-1/\mu} \quad (3.29)$$

$$\approx \alpha a j_c \left[\frac{k_B T^*}{U_0} \ln \frac{f_0}{f} \right]^{-1/\mu} \quad (3.30)$$

and the collective creep/VG exponent is then

$$\mu = \ln \left[1 + \frac{k_B T^*}{U_0} \ln \left(1 + \frac{f_0}{f} \right) \right] / \ln \frac{\alpha a j_c}{h_{\text{ac}}} \quad (3.31)$$

$$\approx \ln \left[\frac{k_B T^*}{U_0} \ln \frac{f_0}{f} \right] / \ln \frac{\alpha a j_c}{h_{\text{ac}}} \quad (3.32)$$

where again the geometry dependent factor α is on the order of unity. The approximations are good at low current densities and frequencies. So by vary-

ing the excitation field amplitude and frequency while carefully keeping T^* constant the exponent μ can in principle be found.

3.4.5 Resistivity, current-voltage characteristics and ac magnetic response

Since most of the evidence advanced to support the VG picture has been the presentation of I - V characteristics of YBCO samples, we will elaborate briefly and qualitatively on the relation between the resistivity $\rho(H, T)$, the I - V characteristics and the permeability $\mu''(H, T)$. As noted above, the peak in μ'' will occur at a temperature T^* when the flux penetrates to the center of the sample. Starting from the ohmic regime, this happens when $\rho(T) = \rho^* \approx \frac{1}{2}\mu_0 a^2 \omega$. Thus for a fixed sample size a and for linear (ohmic) resistance, ρ^* will depend on ω and the loss peak can be shifted to higher or lower temperatures by increasing or decreasing the frequency.

In Figure 3.5 we present a schematic $\rho(T)$ curve. Here the values we are considering are less than, say, 1% of the normal state resistivity ρ_n . The curve is divided into the higher temperature linear portion which is independent of h_{ac} and the non-linear portion which is dependent upon h_{ac} . A given frequency and sample size fix ρ^* , and the temperature at which ρ^* intersects the $\rho(H, T)$ curve will coincide with the temperature of the peak in $\mu''(H, T)$, T^* .

We point out that the resistivity must decrease rapidly with temperature in order to see a loss peak over an observable temperature range. This is because the abscissa of Figure 3.2 is logarithmic. For example, if the residual resistivity in a normal metal such as platinum is greater than ρ^* at low temperatures, then one never sees a loss peak but only an approximately constant value of $\mu''(H, T)$. Similarly, the more rapid the decrease in $\rho(T)$ the sharper the peak in $\mu''(T)$ will be (see Figures 3.2 and 3.5). We recall this because these are general characteristic of the ac magnetic response of conductors and hence there is no *a priori* reason that a transition from, say, a vortex liquid to a vortex solid will necessarily produce a peak in the loss component of the permeability. The peak position is determined by the selected sample size and frequency. These experimental parameters must be judiciously chosen and the ac response must be studied as a function of amplitude and frequency in order to determine the loss peak that differentiates between linear and non-linear regimes.

We will now try to illustrate this using the schematic I - V characteristics of an

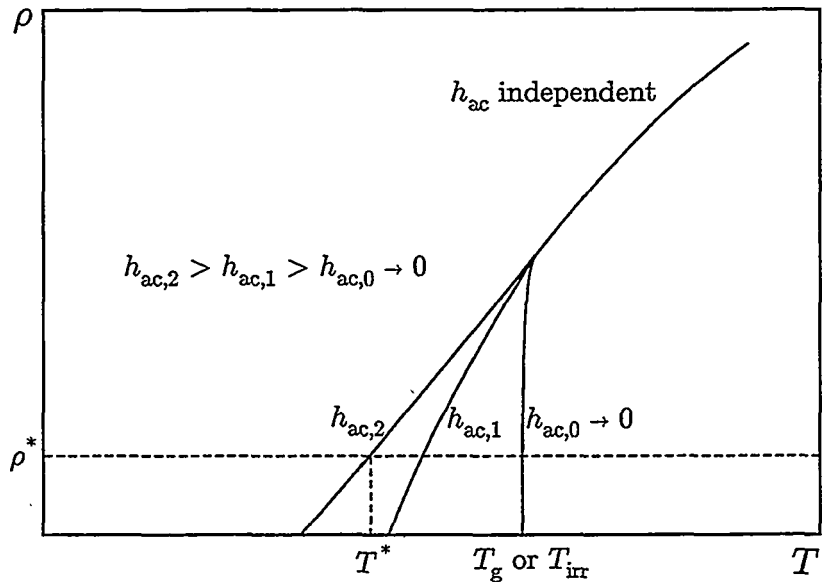


Figure 3.5: An idealization of the resistivity (not to scale) *vs.* temperature for different values of the ac field amplitude h_{ac} . In the limit $h_{ac} \rightarrow 0$, T_g marks the point where the resistivity becomes zero as the current ($\propto h_{ac}$) vanishes and the system enters the vortex glass phase. The peak in μ'' has its maximum at T^* when the resistivity intersects the horizontal dashed line at $\rho^* \approx \frac{1}{2}\mu_0 a^2 \omega$. For increasing h_{ac} the resistivity $\rho(T)$ shifts to the left and the intersection with ρ^* will occur at a lower temperature.

YBCO superconductor as shown in Figure 3.6. This is a composite of published I - V curves [67–71] that identify the transition into a vortex glass regime by the I - V isotherms that exhibit downward curvature. The dashed line marks the transition into the VG state. We can identify essentially three regions of the I - V characteristics which will have different effects on the ac response:

1. Small currents, meaning also small driving amplitude h_{ac} : Above T_g the I - V characteristics are linear and any loss peak occurring here will be frequency dependent and amplitude independent. If the conditions are such that the temperature scan crosses T_g then for $T > T_g$, $\mu''(H, T)$ should be frequency dependent and amplitude independent, while for $T < T_g$ amplitude dependence should be observed, and little or no frequency dependence since the Bean critical state is static. Of course, the ampli-

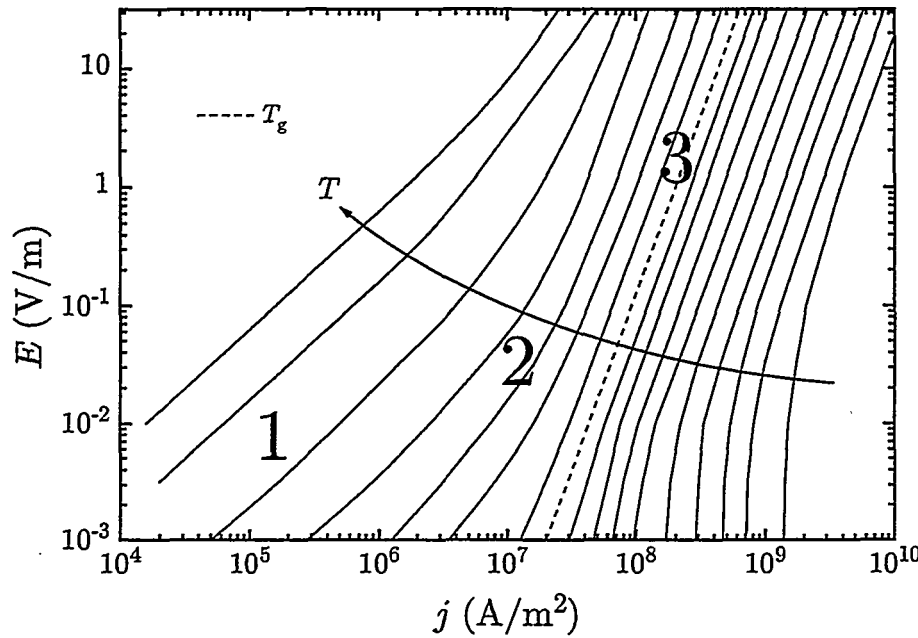


Figure 3.6: Schematic I - V isotherms of an YBCO single crystal in a magnetic field applied parallel to the c -axis. The dashed line marks the glass transition temperature T_g below which the curves fall exponentially. The temperature decreases in equal steps from top to bottom or from left to right. Region 1 marks linear (ohmic) I - V behaviour, region 2 indicates non-linear behaviour above T_g and region 3 is when $d \log E / d \log j \approx 3$ both above and below T_g .

tude independence can be a difficult condition to fulfill since increasing h_{ac} means increasing j and, in general, the linear region exists only for small j . As can be seen in Figure 3.6 above T_g , as j increases the slope $d \log E / d \log j$ increases from 1 to a limiting value of about 3 [67]: the system response is no longer linear. This brings us to the next region:

2. The intermediate current density regime: Here $d \log E / d \log j > 1$ above T_g and the frequency dependence should be strong, but, because of the non-linearity, some amplitude dependence should be evident.
3. Large currents: If j_c is large enough, $d \log E / d \log j$ approaches 3 above T_g and the ac magnetic response should be almost identical to the response below T_g .

Our schematic picture of the I - V characteristics is for $\vec{H} \parallel \hat{c}$. To our knowledge similar curves probing similar regions of voltage and current for $\vec{H} \perp \hat{c}$ are rare and not conclusive [81]. Recall that when $\vec{h}_{\text{ac}} \parallel \hat{c}$ in ac magnetic experiments currents flow in the CuO₂ planes and the use of the I - V characteristics is easily justified. However, for $\vec{h}_{\text{ac}} \perp \hat{c}$ the currents responsible for most of the dissipation are flowing parallel to the c -axis and the use of Figure 3.6 becomes more problematic.

We will use the above considerations to guide us in interpreting our ac permeability data. We realize of course that the loci of points determined by the peak maxima in $\mu''(H, T)$ associated in the past with the IL, represent dynamically determined boundaries in the H - T plane, and are not, in general, phase boundaries. These lines can be frequency and amplitude dependent, and in principle these parameters can be used to locate the "true" IL following the guidelines given above.

References

- [1] C. P. Bean, Phys. Rev. Lett. **8** (1962) 250.
- [2] C. P. Bean, Rev. Mod. Phys. **36** (1964) 31.
- [3] H. London, Phys. Letters **6** (1963) 162.
- [4] Y. B. Kim, C. F. Hempstead and A. R. Strnad, Phys. Rev. **129** (1963) 528.
- [5] T. Ishida and R. B. Goldfarb, Phys. Rev. B **41** (1990) 8937.
- [6] K.-H. Müller, Physica C **159** (1989) 717.
- [7] J. R. Clem in *Magnetic Susceptibility of Superconductors and Other Spin Systems*, ed. R. A. Hein, T. L. Francavilla and D. H. Liebenberg, Plenum Press, New York (1991).
- [8] V. B. Geshkenbein, V. M. Vinokur and R. Fehrenbacher, Phys. Rev. B **43** (1991) 3748.
- [9] J. R. Clem, H. R. Kerchner and S. T. Sekula, Phys. Rev. B **14** (1976) 1893.
- [10] K. S. Cole and R. H. Cole, J. chem. Phys. **9** (1941) 341.
- [11] S. Gjølmesli and K. Fossheim, Physica C **220** (1994) 33.
- [12] L. J. M. van de Klundert, E. A. Gijsbertse and L. C. van der Marel, Physica **69** (1973) 159.
- [13] J. H. P. M. Emmen, V. A. M. Brabers and W. J. M. de Jonge, Physica C **176** (1991) 137.

- [14] M. Wacenowsky, R. Miletich, H. W. Weber and M. Murakami, *Cryogenics* **33** (1993) 70.
- [15] X. Ling and J. I. Budnick in *Magnetic Susceptibility of Superconductors and Other Spin Systems*, ed. R. A. Hein, T. L. Francavilla and D. H. Liebenberg, Plenum Press, New York (1991).
- [16] D.-X. Chen, J. Nogués and K. V. Rao, *Cryogenics* **29** (1989) 800.
- [17] R. W. Rollins, H. Küpfer and W. Gey, *J. Appl. Phys.* **45** (1974) 5392.
- [18] H. Küpfer, I. Apfelstedt, R. Flükiger, C. Keller, R. Meier-Hirmer, B. Runtsch, A. Turowski, U. Wiech and T. Wolf, *Cryogenics* **29** (1989) 268.
- [19] L. Civale, T. K. Worthington, L. Krusin-Elbaum and F. Holtzberg in *Magnetic Susceptibility of Superconductors and Other Spin Systems*, ed. R. A. Hein, T. L. Francavilla and D. H. Liebenberg, Plenum Press, New York (1991) page 313.
- [20] L. Fàbrega, J. Fontcuberta, S. Piñol, C. J. van der Beek and P. H. Kes, *Phys. Rev. B* **47** (1993) 15250.
- [21] L. Fàbrega, J. Fontcuberta, L. Civale and S. Piñol, *Phys. Rev. B* **50** (1994) 1199.
- [22] J. R. Clem, *Physica C* **153–155** (1988) 50.
- [23] F. Gömöry and P. Lobotka, *Solid State Comm.* **66** (1988) 645.
- [24] S. D. Murphy, K. Renouard, R. Crittenden and S. M. Bhagat, *Solid State Comm.* **69** (1989) 367.
- [25] J. Z. Sun, M. J. Scharen, L.C. Bourne and J. R. Schrieffer, *Phys. Rev. B* **44** (1991) 5275.
- [26] R. B. Goldfarb, A. F. Clark, A. I. Braginski and A. J. Panson, *Cryogenics* **27** (1987) 475; R. B. Goldfarb, A. F. Clark, A. J. Panson and A. I. Braginski in *High Temperature Superconductors*, ed. D. U. Gubser and M. Schluter, Materials Research Society, Pittsburgh EA-11 (1987) 261.
- [27] E. Babić, Ž. Marohnić, Đ. Drobac and M. Prester, *Int. J. Mod. Phys. B* **1** (1987) 973.
- [28] Ch. Heinzel, Ch. Neumann and P. Zieman, *Europhys. Lett.* **13** (1990) 531.

- [29] E. W. Collings, M. D. Sumption and W. J. Carr Jr., Supercond. Sci. Technol. **5** (1992) S248.
 - [30] R. B. Goldfarb, M. Lelental and C. A. Thompson in *Magnetic Susceptibility of Superconductors and Other Spin Systems*, ed. R. A. Hein, T. L. Francavilla and D. H. Liebenberg, Plenum Press, New York (1991).
 - [31] M. Nikolo and R. B. Goldfarb, Phys. Rev. B **39** (1989) 6615.
 - [32] T. T. M. Palstra, B. Batlogg, R. B. van Dover, L. F. Schneemeyer and J. V. Waszczak, Phys. Rev. B **41** (1990) 6621.
 - [33] R. A. Hein, Phys. Rev. B **33** (1986) 7539.
 - [34] See for example G. Blatter, M. V. Feigel'man, V. B. Geshkenbein, A. I. Larkin and V. M. Vinokur in *Vortices in high temperature superconductors*, preprint, ETH, Zürich (1993) 538 pages, also: Rev. Mod. Phys. **66** (1994) 1125, and References therein.
 - [35] K. A. Müller, M. Takashige and J. G. Bednorz, Phys. Rev. Lett. **58** (1987) 1143.
 - [36] A. P. Malozemoff, T. K. Worthington, Y. Yeshurun, F. Holtzberg and P. H. Kes, Phys. Rev. B **38** (1988) 7203.
 - [37] J. van den Berg, C. J. van der Beek, P. H. Kes, J. A. Mydosh, M. J. V. Menken and A. A. Menovsky, Supercond. Sci. Technol. **1** (1989) 249.
 - [38] A. Gupta, P. Esquinazi, H. F. Braun and H. W. Neumüller, Europhys. Lett. **10** (1989) 663.
 - [39] P. L. Gammel, J. Appl. Phys. **67** (1990) 4676.
 - [40] J. H. P. M. Emmen, V. A. M. Brabers and W. J. M. de Jonge, Physica C **176** (1991) 137.
 - [41] C. J. van der Beek and P. H. Kes, Phys. Rev. B **43** (1991) 13032.
 - [42] L. Civale, A. D. Marwick, M. W. McElfresh, T. K. Worthington, A. P. Malozemoff, F. H. Holtzberg, J. R. Thompson and M. A. Kirk, Phys. Rev. Lett. **65** (1990) 1164.
 - [43] L. Civale, T. K. Worthington and A. Gupta, Phys. Rev. B **43** (1991) 5425.
-

- [44] L. Civale, A. D. Marwick, T. K. Worthington, M. A. Kirk, J. R. Thompson, L. Krusin-Elbaum, Y. Sun, J. R. Clem and F. Holtzberg, Phys. Rev. Lett. **67** (1991) 648.
- [45] Ph. Seng, R. Gross, U. Baier, M. Rupp, D. Koelle, R. P. Huebner, P. Schmitt, G. Saemann-Ischenko and L. Schultz, Physica C **192** (1992) 403.
- [46] M. Wacenovsky, R. Miletich and H. W. Weber, Supercond. Sci. Technol. **5** (1992) S184.
- [47] M. Wacenovsky, R. Miletich, H. W. Weber and M. Murakami, Cryogenics **33** (1993) 70.
- [48] C. J. van der Beek, M. Essers, P. H. Kes, M. J. V. Menken and A. A. Menovsky, Supercond. Sci. Technol. **5** (1992) S260.
- [49] M. Slaski, L. T. Sagdahl, L. K. Heill, K. Fossheim, M. Murakami, H. Fujimoto, N. Koshizuka and S. Tanaka, Supercond. Sci. Technol. **5** (1992) S340; *idem*, Physica C **185-189** (1991) 2495.
- [50] K. Fossheim, M. G. Karkut, L. K. Heill, M. Slaski, L. T. Sagdahl, V. M. Vinokur, M. Murakami, H. Fujimoto, N. Koshizuka, S. Tanaka, F. Gencer, J. S. Abell and C. E. Gough, Physica Scripta T **42** (1992) 20.
- [51] M. G. Karkut, L. K. Heill, V. M. Vinokur, M. Slaski, L. T. Sagdahl, E. D. Tuset and K. Fossheim, Cryogenics **33** (1993) 60.
- [52] M. G. Karkut, M. Slaski, L. K. Heill, L. T. Sagdahl and K. Fossheim, Physica C **215** (1993) 19.
- [53] R. B. Flippin, T. R. Askew, J. A. Fendrich and B. M. Vlcek, Physica C **228** (1994) 85.
- [54] T. Ishida, J. Franz and J. Reiner, Physica C **202** (1992) 356.
- [55] A. Shaulov and D. Dorman, Appl. Phys. Lett. **53** (1988) 2680.
- [56] L. A. Angurel, F. Lera, A. Badía, C. Rillo, R. Navarro, J. Bartolomé, J. Melero, J. Flokstra and R. P. J. IJsselsteijn in *Proceedings of the EMRS-ICAM'91, High T_c superconductor thin films*, Strasbourg (France) 1991, Elsevier Science Publishers (1992) 141.
- [57] K. Yamamoto, H. Mazaki, H. Yasuoka, T. Terashima and Y. Bando, Physica C **192** (1992) 47.

- [58] L. Krusin-Elbaum, L. Civale, F. Holtzberg and C. Feild, Physica A **200** (1993) 314.
- [59] T. Arndt, F. Schmidt, J. Franz, J. Reiner, W. Schauer and S. Klaumünzer in *Applied Superconductivity*, ed. H. C. Freyhardt, DGM Informationsgesellschaft, Oberursel, Germany (1993) 763.
- [60] T. Arndt, F. Schmidt, H. Reiner and W. Schauer in *Critical Currents in Superconductors*, ed. H. W. Weber, World Scientific, Singapore (1994) 260.
- [61] H. B. Sun, K. N. R. Taylor and G. J. Russell, Physica C **227** (1994) 55.
- [62] F. Gömöry and S. Takács, Physica C **217** (1993) 297.
- [63] J. Bardeen and M. J. Stephen, Phys. Rev. **140** (1965) 1197.
- [64] M. P. A. Fisher, Phys. Rev. Lett. **62** (1989) 1415.
- [65] D. S. Fisher, M. P. A. Fisher and D. A. Huse, Phys. Rev. B **43** (1991) 130.
- [66] C. J. van der Beek, V. B. Geshkenbein and V. M. Vinokur, Phys. Rev. B **48** (1993) 3393.
- [67] R. H. Koch, V. Foglietti, W. J. Gallagher, G. Koren, A. Gupta and M. P. A. Fisher, Phys. Rev. Lett. **63** (1989) 1511.
- [68] T. K. Worthington, F. H. Holtzberg and C. A. Feild, Cryogenics **30** (1990) 417.
- [69] P. L. Gammel, L. F. Schneemeyer and D. J. Bishop, Phys. Rev. Lett. **66** (1991) 953.
- [70] E. Sandvold and C. Rossel, Physica C **190** (1992) 309.
- [71] H. Safar, P. L. Gammel, D. J. Bishop, D. B. Mitzi and A. Kapitulnik, Phys. Rev. Lett. **68** (1992) 2672.
- [72] A. I. Larkin and Yu. N. Ovchinnikov, Zh. Eksp. Teor. Fiz. **65** (1973) 1704.
- [73] A. I. Larkin and Yu. N. Ovchinnikov, J. Low. Temp. Phys. **34** (1979) 409.
- [74] V. M. Vinokur, M. V. Feigel'man and V. B. Geshkenbein, Phys. Rev. Lett. **67** (1991) 915.

- [75] L. Fábregas, B. Martínez, J. Fontcuberta and S. Piñol, Phys. Rev. B. 48 (1993) 13840.
- [76] L. Fábregas, J. Fontcuberta and S. Piñol, Physica C 224 (1994) 99.
- [77] J. Rhyner, Physica C 212 (1993) 292.
- [78] J Gilchrist and T. Dombre, Phys. Rev. B 49 (1994) 1466.
- [79] A. Kapitulnik in *Phenomenology and Applications of High Temperature Superconductors*, ed.s K. S. Bedell, M. Inui, D. E. Meltzer, J. R. Schrieffer and S. Doniach, Addison Wesley, Reading, Massachusetts, USA (1992) page 34.
- [80] J. Kötzler, M. Kaufmann, G. Nakielski, R. Behr and W. Assmus, Phys. Rev. Lett. 72 (1994) 2081.
- [81] M. Charalambous, J. Chaussy and P. Lejay, Phys. Rev. B 45 (1992) 5091.

Experimental

4.1 The ac susceptibility apparatus

Below we describe the in-house built ac susceptometer [1] with coils, sample holder, electronics, preparations and basic data transformations used in our measurements of ac magnetic response. Nikolo has recently published a highly useful guide aimed at the superconductivity audience that goes into great detail on “alternating current susceptibility measurements and alternating current susceptometer design” [2].

In ac susceptibility measurements an applied ac excitation field causes currents or magnetic fields to be set up in the sample. This response induces a voltage V_p in a pick-up coil mounted on the sample. This voltage is proportional to the sample’s complex ac permeability $\mu = \mu' + i\mu''$. The permeability is related to the susceptibility χ through $\mu = \chi + 1$. For harmonic signals

$$V_p = -n \frac{d\Phi}{dt} = inA\omega\mu\mu_0 h_{ac} \quad (4.1)$$

where n and A are the number of turns in and the area of the pick-up coil, respectively, and ω and h_{ac} are the excitation field (angular) frequency and amplitude, respectively.

Figure 4.1 illustrate the probe part of the ac susceptometer. A ceramic Al_2O_3 (alsint) tube with inner diameter 5 mm holds the platinum thermometer (Lake Shore Pt-1000) inside an alsint cylinder at the top. The sample is glued with GE varnish to one end of another alsint cylinder that is inserted into the tube

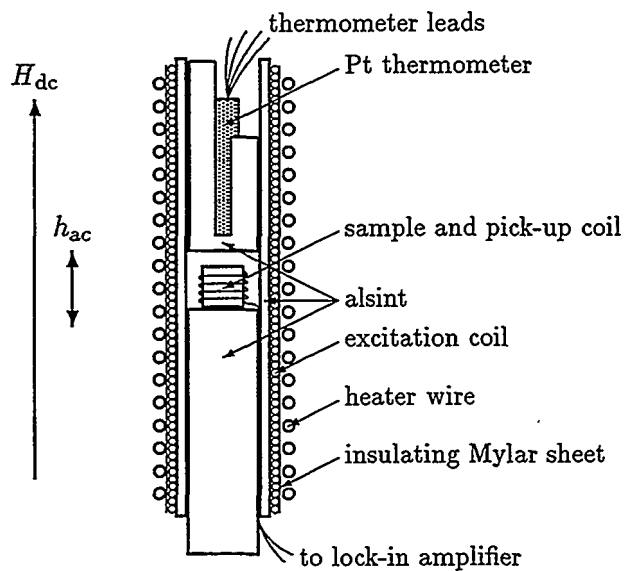


Figure 4.1: Schematic of the coils, sample holder, heater and thermometer of the ac susceptometer.

from the bottom, placing the sample in the center. The 10–30 turn pick-up coil is wound directly and tightly around the sample using 0.04 mm Cu wire, and the leads follow a small groove along the cylinder and out. The excitation coil is wound on the outside of the alsint tube. An insulating Mylar sheet separates it from the 20Ω twisted heater wire wrapped around the outside. The probe sits inside two stainless steel chambers at the bottom end of the cryostat.

Alsint is an insulator that will not distort the signals by setting up its own electric or magnetic response (eddy currents). It will on the other hand provide good thermal contact between the principal parts, the sample on the sample holder, the heater and the thermometer, due to its high thermal conductivity. Its low thermal expansion makes alsint well suited for use in low temperature cryostats. To further enhance temperature stability and uniformity the sample and probe system are immersed in a He gas atmosphere.

The temperature controller (Linear Research) can then provide 10 mK stability over a temperature range from 4.2 to 300 K (liquid He to room temperature). A DMM (Keithley 196) reads the resistance of the platinum thermometer. Excitation fields with frequencies f from around 10 Hz up to 121 000 Hz and amplitudes $\mu_0 h_{ac}$ in the range 0.001–3 mT are set up with a function generator

(HP 8116A).¹ The output ac current is monitored by a DMM (Keithley 195A).² The signal from the pick-up coil is fed to a two-phase lock-in amplifier (PAR 5210 or PAR 5302) that records the real and imaginary parts of the pick-up coil voltage, *i.e.* the ac permeability components, μ' and μ'' , respectively. The susceptometer is controlled from a personal computer via a General Purpose Interface Bus (GPIB). The system is fully automated, except that the coolant (liquid nitrogen) has to be refilled manually. The external static magnetic field $\mu_0 H_{dc}$ is provided by a 10 T superconducting magnet (Magnex Model E5010) with a bore of 87 mm and is also controlled manually.

The phase is kept constant during each measurement so that $\mu'' = 0$ at 100 K, *i.e.* in the normal state. Working temperatures T ranged from around 60 K (in the cold magnet, with no extra pumping) to 100 K, and dc fields $\mu_0 H_{dc}$ from 0–8 T. All measurements are done during heating after cooling below T_c in zero ac field. The applied ac and dc magnetic fields are always parallel.

The signal V_p , see Equation (4.1), was recorded on file. The demagnetization factors of the samples were not determined, hence μ is not calibrated. The temperature is corrected for magnetoresistance in the platinum thermometer when measuring in applied dc field.

4.2 Samples

In this Section we describe the making and preparation of the YBCO samples used for our ac susceptibility measurements, and present their physical characteristics. We note in advance that the samples are both cubes of about the same size, hence having demagnetization factors that are almost equal and the same for both principal orientations $\vec{H} \parallel \hat{c}$ and $\vec{H} \perp \hat{c}$. Data for the two samples are therefore directly comparable.

4.2.1 The MPMG sample

The sample was prepared by M. Murakami, H. Fujimoto, N. Koshizuka and S. Tanaka at ISTECSRL in Tokyo using the Melt-Powder-Melt-Growth (MPMG) process described by Murakami [3, 4].

¹The upper limit for the amplitude will depend on the frequency through the transfer function of the function generator; see for example Nikolo [2].

²The finite sampling rate of the DMM determines the lower limit for the frequency.

The notation used for our sample is MPMG Y1.8 from the process and the yttrium content; the starting powders of Y_2O_3 , BaCO_3 and CuO were mixed in the ratio $\text{Y}:\text{Ba}:\text{Cu}=1.8:2.4:3.4$. The powders were calcined at 900°C for 8 hours, melted at 1350°C for 20 minutes (MPMG) and then quenched using Cu plates. The quenched material was crushed into powder (MPMG) and pressed into pellets 3 cm in diameter and 2 cm in thickness. These pellets are heated to 1100°C for 20 minutes and cooled to 1000°C at a rate of $100^\circ\text{C}/\text{hour}$ followed by slow cooling at a rate of $1^\circ\text{C}/\text{hour}$ down to 900°C (MPMG) and then furnace cooled to room temperature. These processes were conducted in air. Finally the pellets were annealed in flowing oxygen at 450°C .

The crystalline sample used for the ac susceptibility measurements was cut from a pellet. The crystalline orientation was determined by a two-axis diffractometer with graphite monochromatized $\text{Cu K}\alpha_1$ radiation. TEM observations were performed at 400 kV with a point resolution of 0.17 nm. The critical current density j_c , as obtained from the width of the magnetization hysteresis loop, is 200 MA/m^2 at 77 K in zero field and 80 MA/m^2 in a field of 1 T applied parallel to the crystalline *c*-axis.

Figure 4.2 shows an optical (a) and a TEM (b) micrograph of the sample. In (a) we see fine non-superconducting “green phase” Y_2BaCuO_5 (Y211) inclusions dispersed in the otherwise crystalline $\text{YBa}_2\text{Cu}_3\text{O}_7$ (Y123) matrix. The inclusions are on the order of (*sub*) μm in size. In (b) we see an almost spherical inclusion with diameter $\sim 0.2 \mu\text{m}$. Twin boundaries are clearly visible and some of them terminate on the inclusion. The Y211 inclusions occupy about 20% of the volume of our sample.

Our MPMG sample is almost cubic in shape with dimensions $1.38 \times 1.29 \times 1.25 \text{ mm}^3$ and has an onset T_c of 90.40 K .

4.2.2 The single crystal (SC) sample

The single crystal $\text{YBa}_2\text{Cu}_3\text{O}_{7-\delta}$ sample (SC) was made by F. Gencer, J. S. Abell and C. E. Gough at the University of Birmingham. The method is described by Gencer and Abell in Reference [5].

The starting powders of Y_2O_2 , BaCO_3 and CuO were mixed in the ratio $\text{Y}:\text{Ba}:\text{Cu}=1:2:3$. These starting materials were milled in ethanol for 3–4 hours and then reacted at 950°C for 24 hours with an intermediate grinding step. The prereacted powder was mixed with 2% NaCl-KCl flux (50 wt% NaCl and

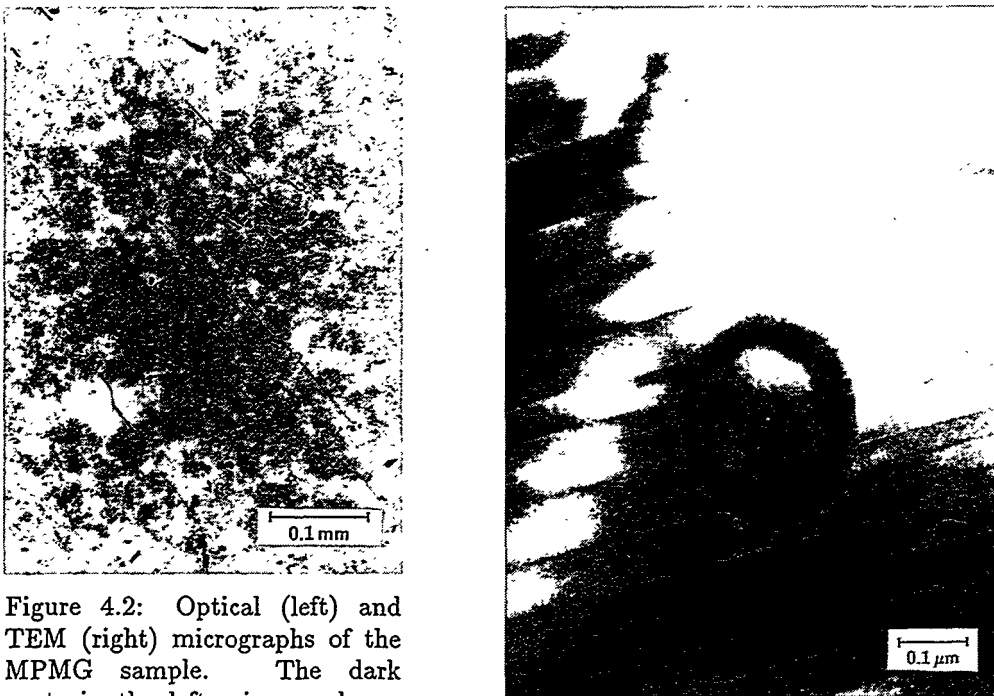
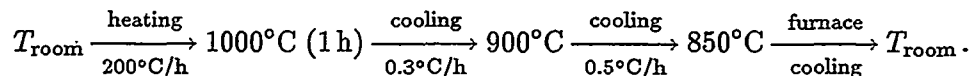


Figure 4.2: Optical (left) and TEM (right) micrographs of the MPMG sample. The dark spots in the left micrograph are Y_2BaCuO_5 (Y211) material included in the $\text{YBa}_2\text{Cu}_3\text{O}_7$ (Y123) matrix. In the TEM image we see a $0.2 \mu\text{m}$ Y211 inclusion inbetween twin boundaries. Note that the dark ring is not an amorphous region, but merely a defocusing effect. The crystalline *c*-axis lies in the paper plane.

50 wt% KCl) and put into an alumina crucible. The temperature cycle used for the crystal growth was



The crystals were held at 425°C in 200 bar of oxygen for 10 days and subsequently furnace cooled to room temperature.

X-ray microanalysis was performed with a JEOL 840A SEM operating at 40 kV. Traces of secondary phases (Y_2BaCuO and CuO) were observed. No significant levels of Na or K were detected. The orientation was established by Laue X-ray diffraction. Twins were observed under polarized light in an optical microscope. The oxygen content was not measured, but the sample makers estimate that δ is about 0.2–0.3 [6].

A near cubic crystal with dimensions $1.100 \times 1.065 \times 1.015 \text{ mm}^3$ was selected for the ac susceptibility measurements. Its critical temperature is 88.55 K.

References

- [1] S. Gjølmesli, Hovedfagsoppgave, NTH, Trondheim (1989) (unpublished);
L. T. Sagdahl, Diploma thesis, NTH, Trondheim (1990) (unpublished); L.
T. Sagdahl, Ph.D. thesis, NTH, Trondheim (1994) (unpublished).
- [2] M. Nikolo, preprint, to be published in Am. J. Phys. **62** (December 1994).
- [3] M. Murakami, Mod. Phys. Lett. B **4** (1990) 163.
- [4] *Melt Processed High-Temperature Superconductors*, ed. M. Murakami,
World Scientific, Singapore (1992).
- [5] F. Gencer and J. S. Abell, Journal of Crystal Growth **112** (1991) 337.
- [6] F. Gencer, private communication.

Introductory ac permeability results

We start our discussion of the ac magnetic response observed in our samples by presenting a number of plots of the $\mu(T)$ data we have taken. There are several reasons for this:

- It serves as an introduction to what follows; this selection functions as a rough guide to the topics to be discussed,
- it provides a valuable visual, or qualitative, image of the background material,
- it can be used for reference during the discussions, and
- it is always helpful to see the raw data.

From the selection of plots we see that key elements will be

material differences:

A major point is to find materials for applications, and here we investigate the effect of distributing small inclusions of non-superconducting material, Y_2BaCuO_5 , throughout the $YBa_2Cu_3O_7$ crystalline matrix, in particular the effect this has on the IL and on the critical current density, and what mechanisms lie behind the differences.

dc field dependence:

The behaviour of superconductors in the field-temperature phase space, and in particular around the IL $H_{\text{irr}}(T)$, is paramount for our understanding of the underlying physics and for applications.

anisotropy (dependence on field orientation with main crystallographic axes):

High temperature superconductors are characterized by often highly anisotropic, and it is of great interest and importance, *e.g.* in application design, to see and understand how this manifests itself in the macroscopic behaviour. Important clues to the superconducting mechanisms can also be found.

amplitude dependence:

The amplitude of the ac magnetic signal is intimately connected to the screening currents in the superconductor, and varying it can produce different responses. For example: A small amplitude gives only a small perturbation of the vortex system and linear response can be expected whereas a larger amplitude could drive the system into non-linear behaviour — and ultimately out of the superconducting state altogether as the induced currents reach or pass the level of the critical current.

frequency dependence:

Frequency can easily be varied over several decades to probe the time constants of the system, *e.g.* how long a vortex can be expected to sit in a pinning potential, a parameter that holds important information of what vortex state the superconductor is in: slow or frozen dynamics is expected for a vortex solid whereas fast dynamics is expected for a vortex liquid.

Temperature of course remains an important free parameter. The plots are raw data with the measured voltages (in microvolts) divided by the values for the frequency (in hertz) and the excitation coil current (in milliamperes) along the vertical axes (the data in Figures 5.1 to 5.2 are exceptions in that they are normalized after first having the background subtracted). The data are corrected for the magnetoresistance of the platinum thermometer.

Raw data

From the $\mu(T)$ data presented in Figures 5.1 and 5.2, and also in Figures 5.3 to 5.6, we see that the transition in $\mu'(T)$ or the peak in $\mu''(T)$ broadens with increasing applied dc field. This is the ac magnetic counterpart to the broadening of the resistive transition with field in high temperature superconductors: in the skin effect picture of Section 3.2 the resistive broadening should lead to a broadening of the ac permability transition. See Figure 3.2 and (3.24).

Comparing the response of the MPMG and SC samples, we see that they behave in very much the same way when the magnetic field is applied along the crystalline c -axis; this is valid for the dependencies upon both dc field and ac field amplitude and frequency. See Figures 5.1, 5.3, and 5.5.

For the opposite orientation, with $\vec{H} \perp \hat{c}$, Figure 5.2 immediately reveal that the transition is substantially wider in the MPMG sample than in the SC sample. The same can be seen from Figure 5.4, with a notable exception for the lower field, 0.4 T: Here we observe an anomalous broadening and change of general shape of the transition for the SC sample. The same anomaly manifests itself in the SC 1 T curve in 5.2. The same exception is found comparing the response of the samples in Figure 5.6. We defer, however, the discussion on this anomalous behaviour to Chapter 11.

Figure 5.7 summarizes the above two paragraphs in that the width of the transition is approximately the same for both samples when $\vec{H} \parallel \hat{c}$ whereas for $\vec{H} \perp \hat{c}$ the transition is very much broader for the MPMG sample than for the SC sample — for the latter, the width is even smaller than for $\vec{H} \parallel \hat{c}$. The anomaly is also strikingly present as a peak between 0 and 1 T.

One notable difference between the two samples is seen in the peak maxima μ''_{\max} : While μ''_{\max} for the SC sample is almost constant, it varies with H_{dc} for the MPMG sample, see Figure 5.1 for $\vec{H} \parallel \hat{c}$ and Figure 5.2 for $\vec{H} \perp \hat{c}$. Why this happens is not clear, but it could be linked to some field dependence of the pinning energy of the Y211 inclusions.

Figures 5.3 and 5.4 show that the amplitude dependence is very weak for both samples for the $\vec{H} \parallel \hat{c}$ orientation, but very strong for the MPMG sample and strong for the SC sample for the $\vec{H} \perp \hat{c}$ orientation. Figures 5.5 and 5.6 show that the frequency dependence is strong and very similar for the two samples for the $\vec{H} \parallel \hat{c}$ orientation, but for the $\vec{H} \perp \hat{c}$ orientation the influence of changing the frequency is considerably less and again quite similar for the two samples.

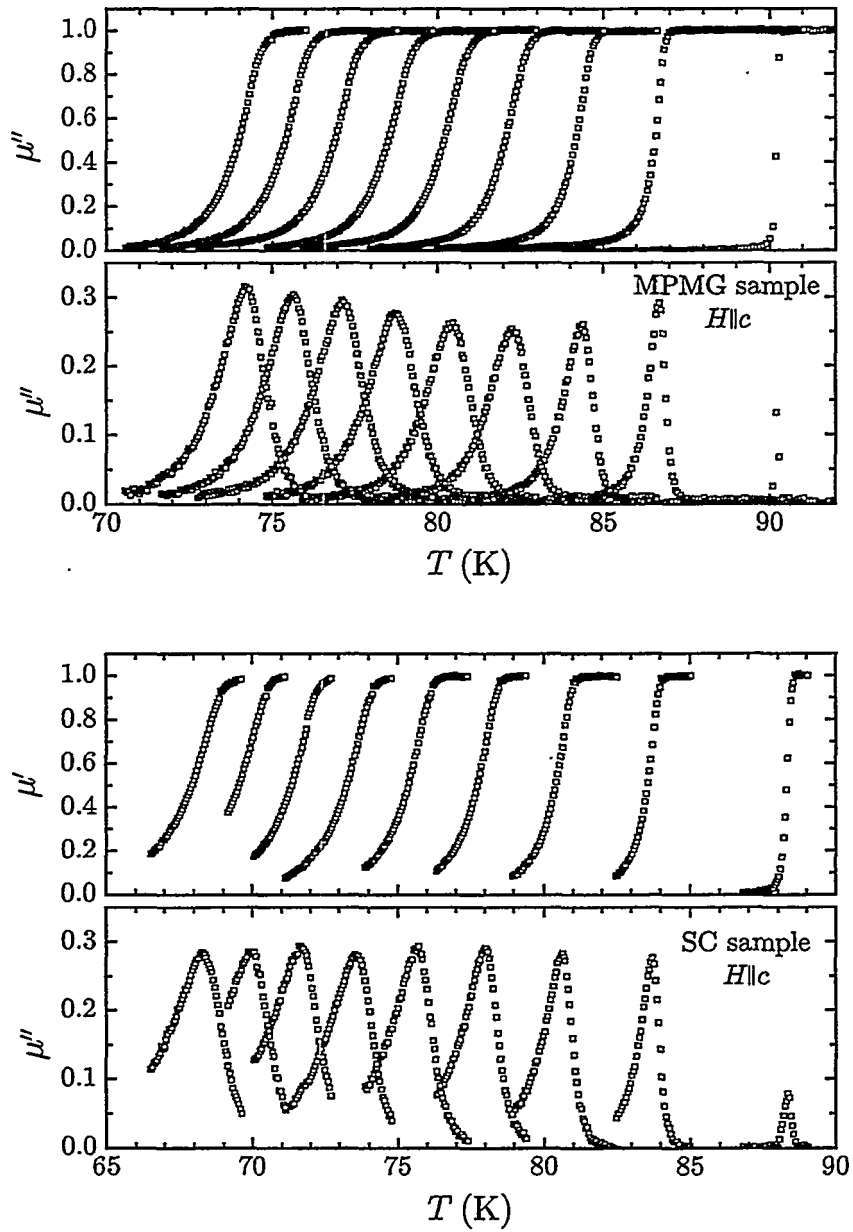


Figure 5.1: ac permeability $\mu(T)$ for the MPMG (top) and SC (bottom) samples for dc fields 0, 1, 2, ..., 8 T (right to left) applied parallel to the crystalline c -axis. The excitation field amplitude and frequency are 0.1 mT and 121 Hz, respectively. Here we have subtracted the background and normalized the signal.

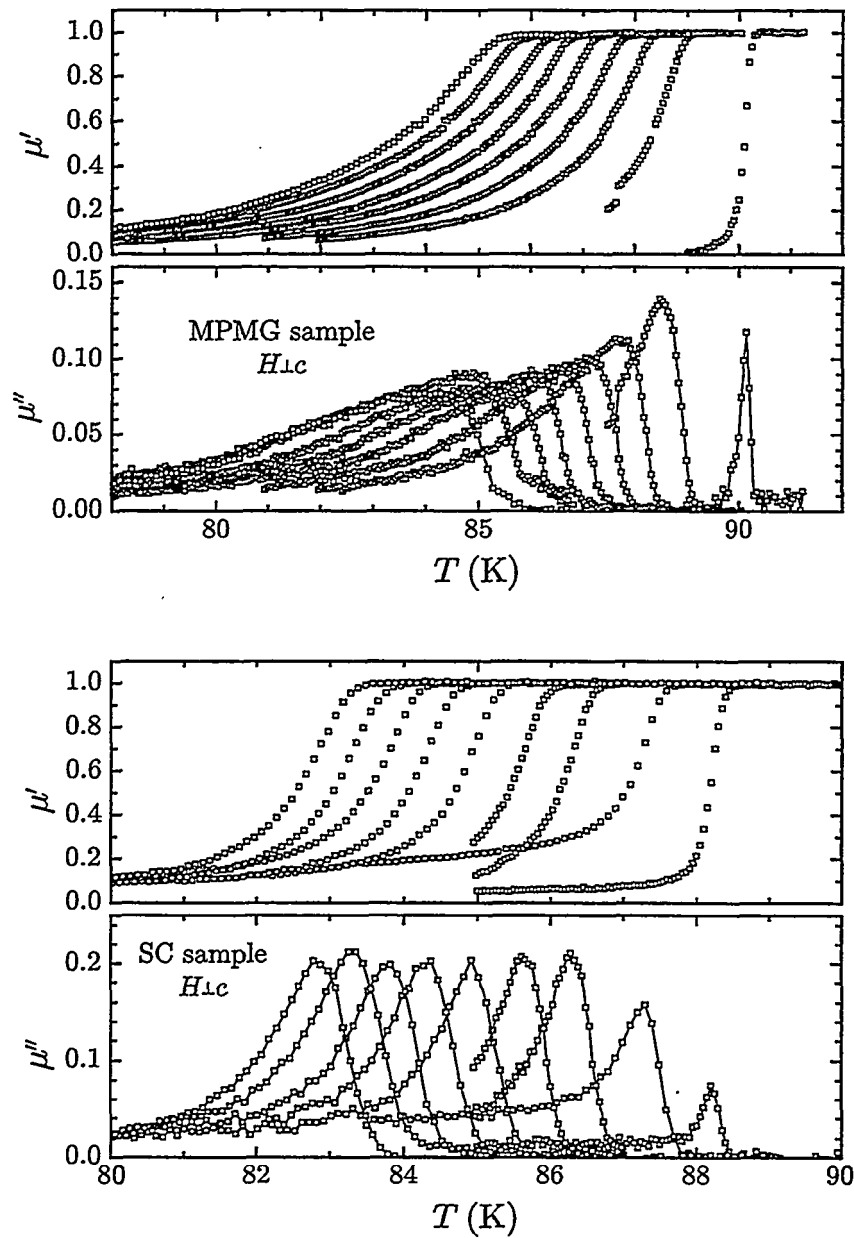


Figure 5.2: ac permeability $\mu(T)$ for the MPMG (top) and SC (bottom) samples for dc fields $0, 1, 2, \dots, 8$ T (right to left) applied perpendicular to the crystalline c -axis. The excitation field amplitude and frequency are 0.1 mT and 121 Hz, respectively. Here we have subtracted the background and normalized the signal.

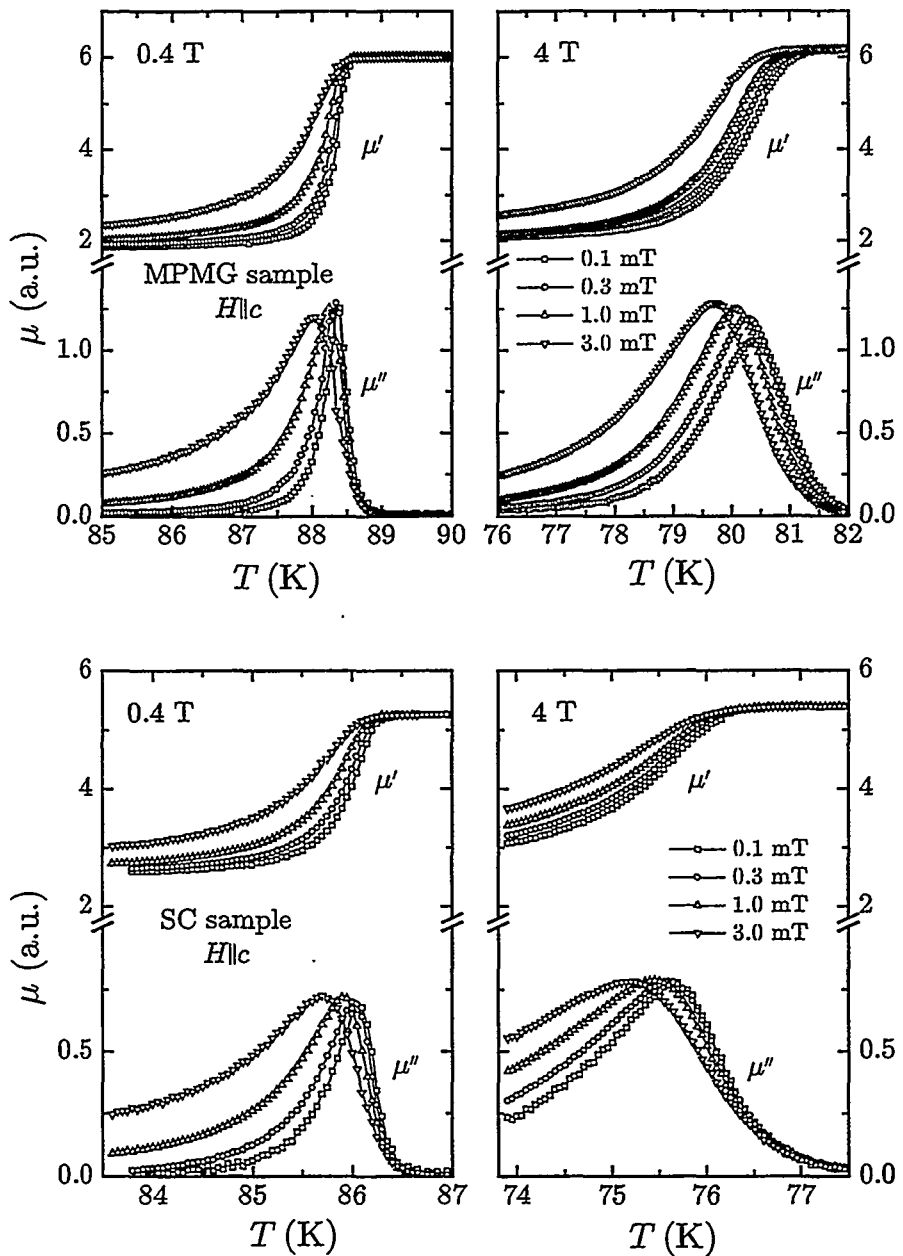


Figure 5.3: ac permeability $\mu(T)$ for the MPMG (top) and SC (bottom) samples in dc fields 0.4 (left) and 4 T (right) applied parallel to the crystalline c -axis for excitation field amplitudes 0.1, 0.3, 1.0 and 3.0 mT (right to left). The frequency is 121 Hz.

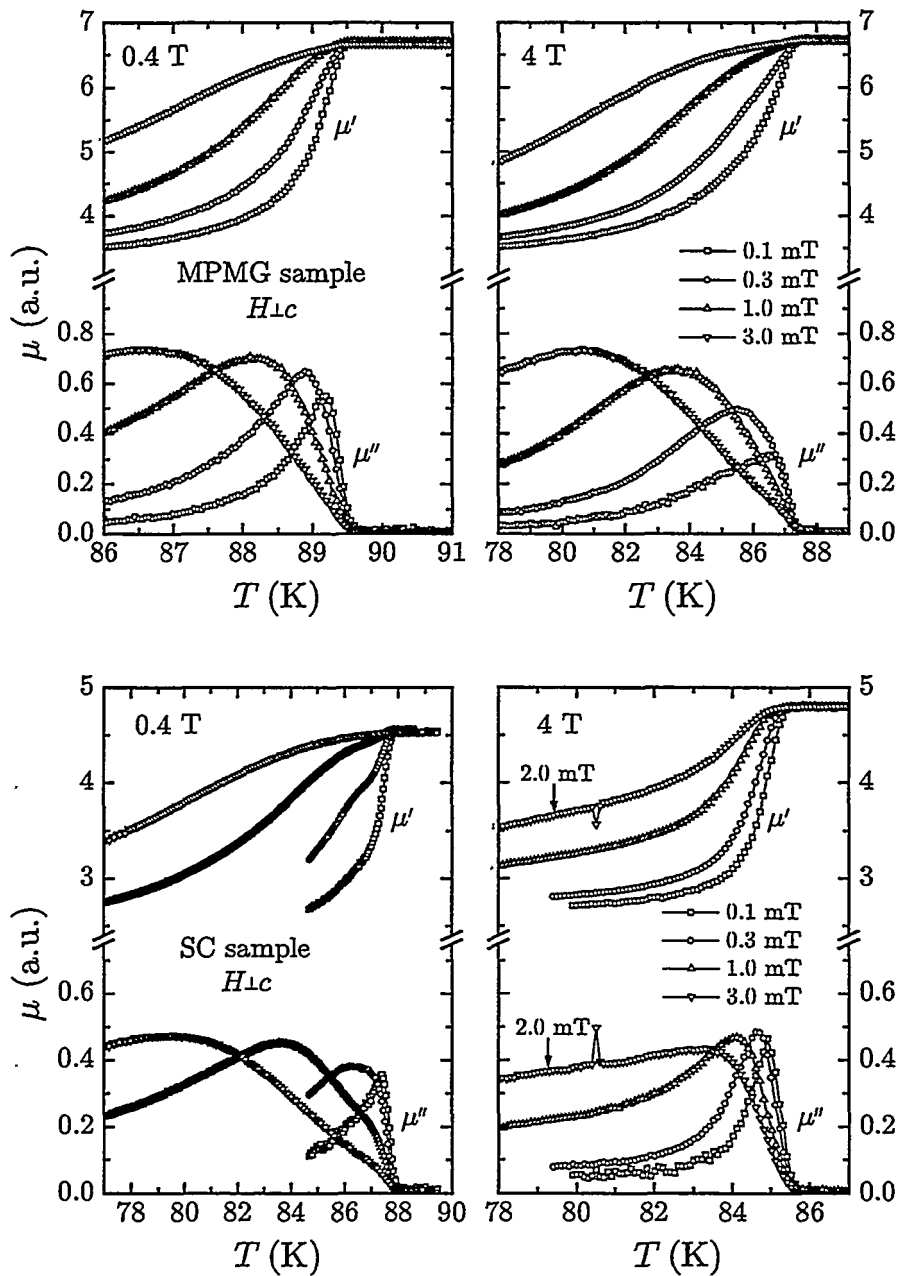


Figure 5.4: ac permeability $\mu(T)$ for the MPMG (top) and SC (bottom) samples in dc fields 0.4 (left) and 4 T (right) applied perpendicular to the crystalline c -axis for excitation field amplitudes 0.1, 0.3, 1.0 and 3.0 mT (right to left). The frequency is 121 Hz.

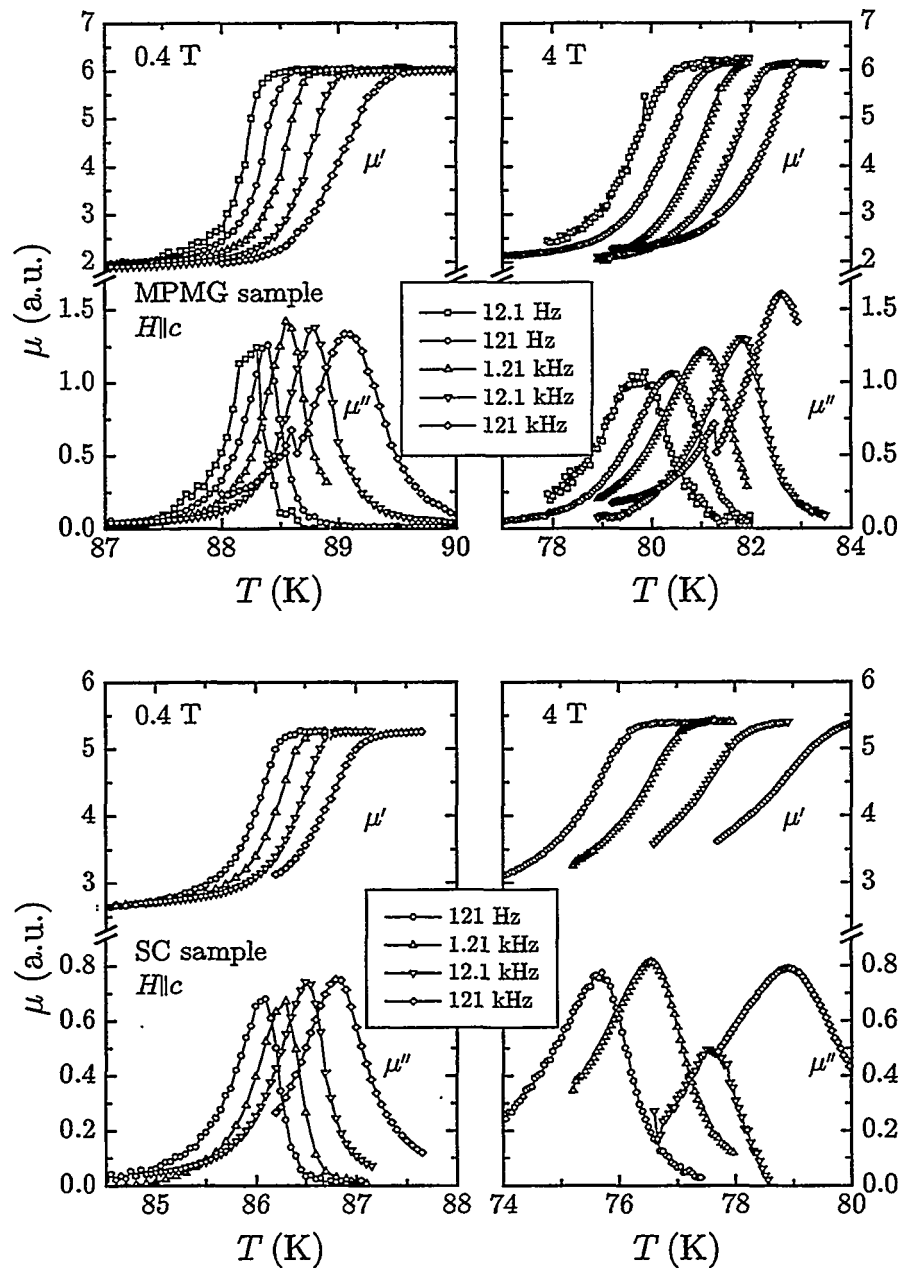


Figure 5.5: ac permeability $\mu(T)$ for the MPMG (top) and SC (bottom) samples in dc fields 0.4 (left) and 4 T (right) applied parallel to the crystalline c -axis for excitation field frequencies 12.1 (MPMG only), 121, 1210, 12100 and 121000 Hz (left to right). The amplitude is 0.1 mT.

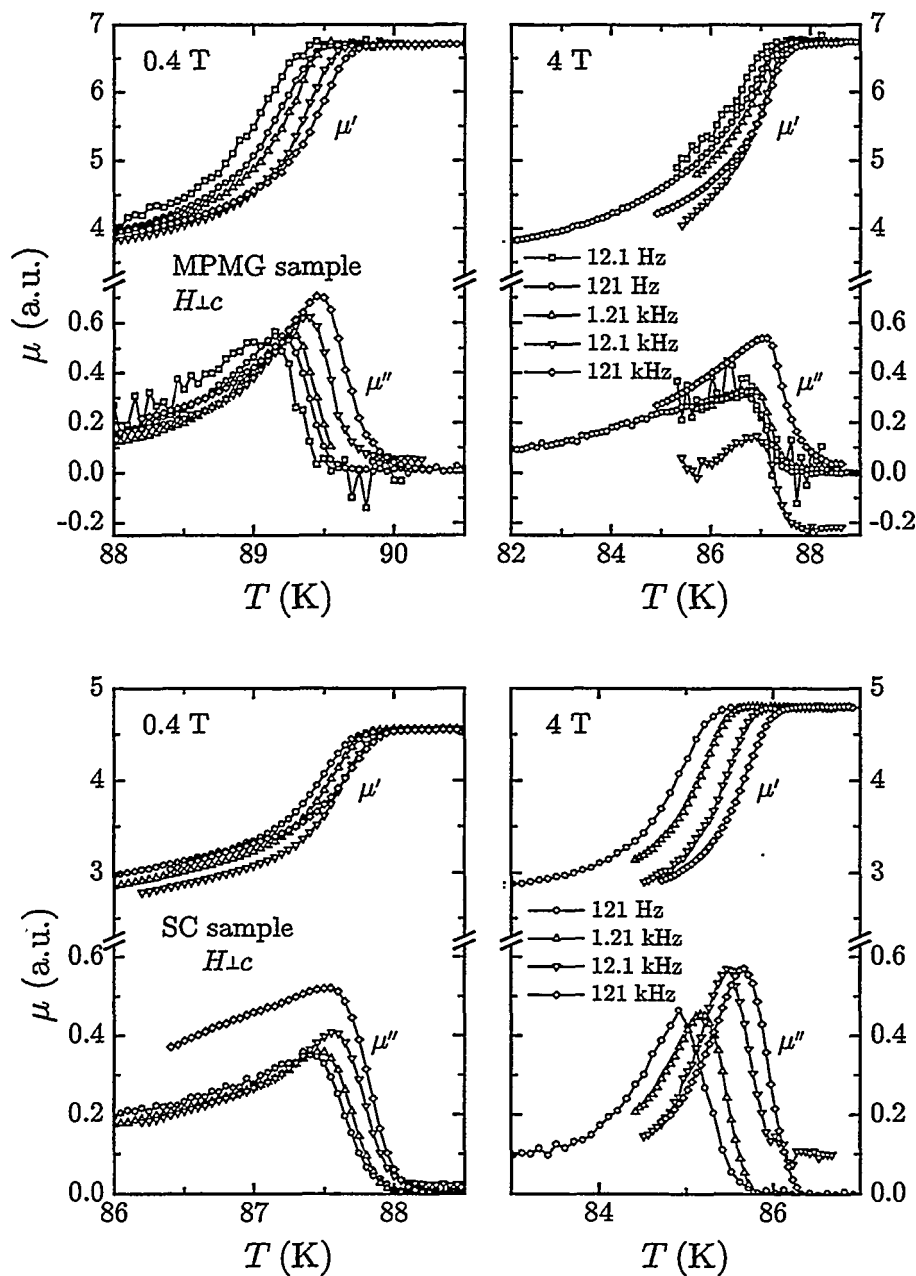


Figure 5.6: ac permeability $\mu(T)$ for the MPMG (top) and SC (bottom) samples in dc fields 0.4 (left) and 4 T (right) applied perpendicular to the crystalline c -axis for excitation field frequencies 12.1 (MPMG only), 121, 1210, 12100 and 121000 Hz (left to right). The amplitude is 0.1 mT.

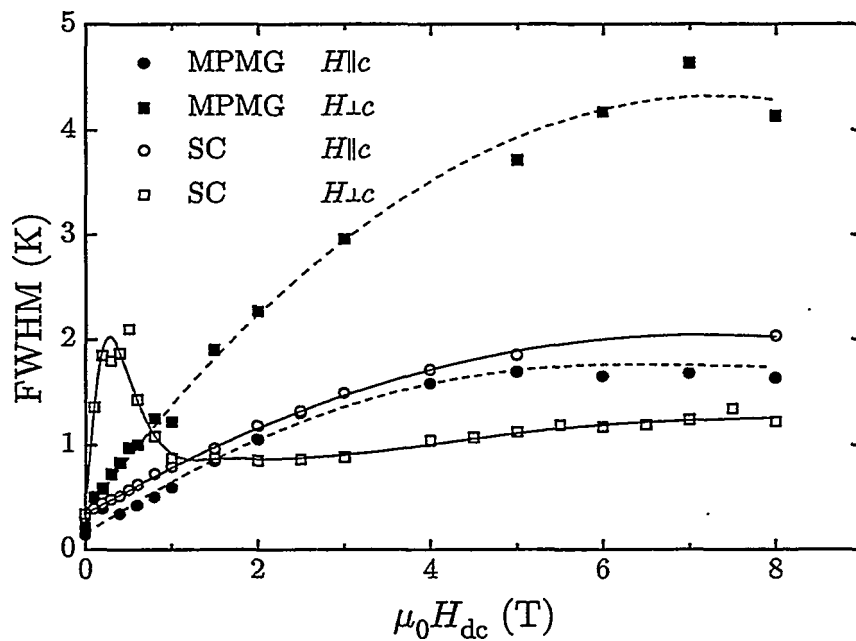


Figure 5.7: The full width at half maximum (FWHM) of $\mu''(H, T)$ vs. applied dc field for the MPMG and the SC samples with the field both parallel and perpendicular to the crystalline c -axis. The excitation field amplitude and frequency are 0.1 mT and 121 Hz, respectively. The solid and dashed lines are guides to the eye.

Loss peak lines

The irreversibility line (IL) has attracted much attention from the high temperature superconductivity community, but there is still no general agreement as to what it is and how it can be found experimentally, see Subsection 2.3.5. ac magnetic measurements have often been used with the temperature position of the loss peak maximum, T^* , defining T_{irr} , even though the loss peak appears about the moment the flux front reaches the center of the sample. Under the right circumstances (see below and Subsection 3.4.4), T^* can be a good approximation to T_{irr} . In this Chapter we present the loss peak lines (LPLs) $\mu_0 H_{\text{dc}}(T^*)$ measured for our samples and compare them to results in the literature and to various models where the concept of an IL has been discussed.

The loci of the loss peak maxima in the H - T plane is presented for both samples and both orientations in Figure 6.1, and we also include $\vec{H} \parallel \hat{c}$ data for a MPMG Y1.2 (Y12) sample similar in size and shape to the MPMG sample, but with a lower yttrium content. The excitation field amplitude and frequency are 0.1 mT and 121 Hz, respectively.

6.1 Anisotropic loss peak and irreversibility lines

Since, for small amplitudes and frequencies, these LPLs $T^*(H)$ are close to the true ILs [1–3] (see also Subsection 3.4.4) we can immediately conclude that for both samples the irreversibility temperature $T_{\text{irr}}(H)$ is considerably higher for $\vec{H} \perp \hat{c}$ than for $\vec{H} \parallel \hat{c}$. Remember that the cube shape of our samples validates

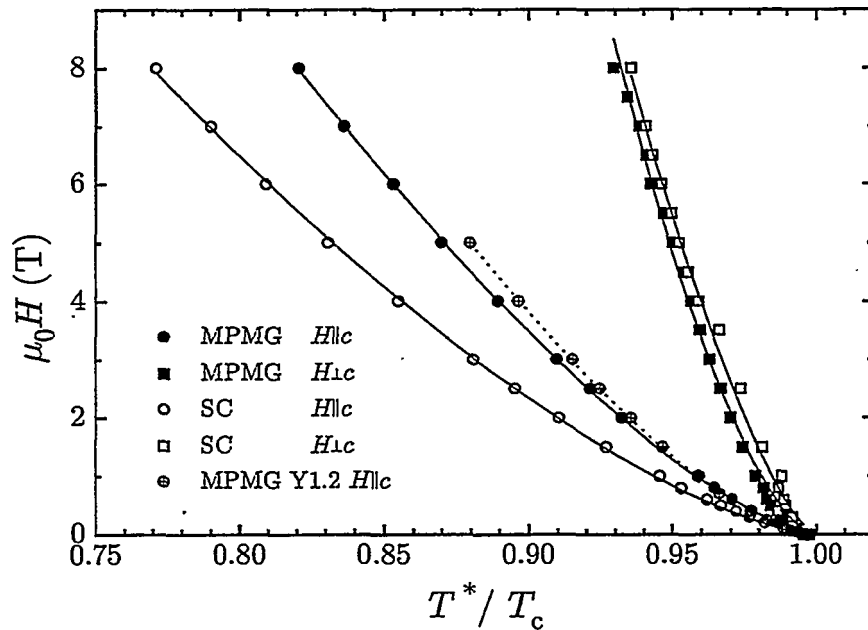


Figure 6.1: The position of the peak in μ'' in the field-(reduced) temperature plane for the MPMG and SC samples for the two principal orientations of the field, $\vec{H} \parallel \hat{c}$ and $\vec{H} \perp \hat{c}$, and for the Y12 sample for $\vec{H} \parallel \hat{c}$. The amplitude and frequency of the ac excitation field are 0.1 mT and 121 Hz, respectively. The solid and dotted lines are best fits to the formula $\mu_0 H_{dc}(T^*) = \mu_0 H_0(1 - T^*/T_c)^n$; see Table 6.2 below for details on the fits.

such a comparison. The dimensions of the MPMG and SC samples are not exactly the same, there is a difference of roughly 20%, see Section 4.2, but the effect on the penetration is minimal: it corresponds to only a small fraction of a kelvin in the temperature position of a loss peak maximum.

6.1.1 Anisotropic melting of the flux line lattice

This is in good agreement with the expected melting of the vortex lattice due to thermal fluctuations, using the Lindemann criterion (see Subsection 2.3.3), when the crystalline anisotropy is taken into account: Blatter *et al.* [5] used a scaling approach to move from isotropic to anisotropic superconductors on a Ginzburg-Landau or London level, and deduced an orientation dependent

melting temperature

$$T_m(\vartheta) = 4\epsilon\epsilon_0 c_L^2 \sqrt{\frac{\Phi_0}{\epsilon_B B}} \quad (6.1)$$

where $\epsilon^2 = 1/\gamma^2 = m/M < 1$ is the effective mass anisotropy ratio; see Table 2.1. $\epsilon_\vartheta^2 = \epsilon^2 \cos^2 \vartheta + \sin^2 \vartheta$ where ϑ is the angle of the field relative to the CuO₂ planes. $c_L \sim 0.1-0.2$ is the Lindemann number. From (6.1) we get

$$T_{m\parallel} = T_m(\vec{H} \parallel \hat{c}) = T_m(\vartheta = \pi/2) = 4\epsilon\epsilon_0 c_L^2 \sqrt{\frac{\Phi_0}{B}} \quad (6.2a)$$

$$T_{m\perp} = T_m(\vec{H} \perp \hat{c}) = T_m(\vartheta = 0) = 4\sqrt{\epsilon}\epsilon_0 c_L^2 \sqrt{\frac{\Phi_0}{B}} \quad (6.2b)$$

and $T_{m\parallel} < T_{m\perp}$. Using the values for ϵ in Table 2.1 for YBCO, we find that $T_{m\parallel} = \sqrt{\epsilon} T_{m\perp} \approx 0.4 T_{m\perp}$. The fundamental anisotropy is clearly demonstrated, but the ratio is not what we observe in Figure 6.1 where it is temperature and/or field dependent. For one thing, we expect the anisotropic melting temperature to converge to T_c when $H \rightarrow 0$ for all orientations, and this does not come out of the theory of Blatter *et al.* [5].

6.1.2 Anisotropic intrinsic pinning

Another, qualitative way to explain the difference in melting temperatures for the two different orientations is as follows: When the magnetic field is parallel to the CuO₂ planes ($\vec{H} \perp \hat{c}$) the flux lines are largely confined in one dimension between the planes because it is energetically the more favourable place to be since the order parameter is lower there. This is the basis of the strong intrinsic pinning picture of Tachiki and Takahashi [6] who calculate the maximum pinning force to occur when $\xi_c/s \approx 0.3$. Here ξ_c is the coherence length along the *c*-axis and *s* is the interplanar distance. In the high temperature oxide superconductors where $s \sim 10 \text{ \AA}$, ξ_c is small enough ($\sim 1-10 \text{ \AA}$)¹ over a substantial temperature range² to let the pinning force reach this maximum. Although the

¹At $T = 0$ $\xi_c \approx 2 \text{ \AA}$ for YBCO, see Table 2.1. For temperatures T from $0.75 T_c$ to $0.99 T_c$ multiply by factors 2 to 10.

²The anisotropic Ginzburg-Landau description is not valid in this temperature regime where coherence lengths and penetration depths are not (much) larger than the unit cell dimensions. Instead, another theory taking into account the discreteness of the atomic structure (along the *c*-axis, since ξ_c is smaller than ξ_{ab}) is called for, e.g. the Lawrence-Doniach theory [7] where superconductivity within the layers is described in Ginzburg-Landau terms and current flow between the layers via the Josephson effect. See Reference [8].

Table 6.1: Fitting parameters from fitting the loss peak lines in Figure 6.1 to a power-law of the form (6.3): $\mu_0 H(T^*) = \mu_0 H_0(1 - T^*/T_c)^n$. The excitation field amplitude and frequency are 0.1 mT and 121 Hz, respectively.

Sample	$\vec{H} \parallel \hat{c}$		$\vec{H} \perp \hat{c}$	
	$\mu_0 H_0$ (T)	n	$\mu_0 H_0$ (T)	n
MPMG	91	1.42	648	1.63
SC	70	1.47	401	1.43
Y12	121	1.50	—	—

flux lines, sandwiched between the CuO₂ planes, are then very easily moved in and out by external magnetic pressure, they should be expected to be quite well ordered in a long-range pattern since they repel each other over a long distance.³ Only close to T_c can one expect this ordering to be disrupted by thermal agitation, to a large extent by production of thermally activated kinks in the vortex lines. With the applied field perpendicular to the CuO₂ planes ($\vec{H} \parallel \hat{c}$), on the other hand, the situation is different: the vortices are free to move in two dimensions, in both sideways directions. Furthermore, they may be regarded as somewhat soft in the sense that they can be considered more or less as embryonic pancake vortices [10] because of the anisotropy. Thermal disconnection and reconnection as well as large amplitude thermal motion in the a and b directions are therefore possible. So it is not surprising that an $\vec{H} \parallel \hat{c}$ vortex structure melts more easily than an $\vec{H} \perp \hat{c}$ vortex structure.

6.2 Power-law fits

Loss peak lines are often fitted to some function, very often of the power law form [11–24]

$$\mu_0 H_{dc}(T^*) = \mu_0 H_0(1 - T^*/T_c)^n \quad . \quad (6.3)$$

From our data in Figure 6.1 we get the fitting parameters displayed in Table 6.2. See also Tables 7.1, 8.1 and 7.3 for results for other frequencies (see Figure 7.1), amplitudes (see Figure 8.1) and estimates of the vortex glass transition lines (see Figure 7.8). The solid lines in Figure 6.1 are best fits to

³This is due to the large penetration depths λ of high temperature superconductors; at $T = 0$, $\lambda_{ab} \approx 10^3$ Å for YBCO. For temperatures T from $0.75 T_c$ to $0.99 T_c$ multiply by factors 2 to 10. See Table 2.1. Remember that the vortex-vortex interaction energy falls off as $\exp(-r/\lambda)/\sqrt{r}$ at large distances, where r is the vortex-vortex separation. See Reference [9, page 149].

(6.3) using the tabulated parameter values. This fit can of course never be exact since in zero field T^* will always lie below T_c since the loss peak will have a finite width. This could be used to advocate using the onset of the 3rd harmonic to define an IL from ac magnetic measurements: there would be no zero field discrepancy then.

From Table 6.2 we see that the exponents range from 1.42 to 1.50 in all the tabulated cases, with the exception of the $\vec{H} \perp \hat{c}$ orientation for the MPMG sample where $n = 1.63$. These values are all fairly close to $\frac{3}{2}$. In Table 7.1 we list fitting parameters for other frequencies, and observe a spread in the values for n of about 0.1 (0.3 for the MPMG sample with $\vec{H} \perp \hat{c}$). The average values for the MPMG and SC samples with $\vec{H} \parallel \hat{c}$ are 1.41 and 1.42, respectively, which is midway between $\frac{4}{3}$ and $\frac{3}{2}$. The spread contains some experimental uncertainty, and for all frequencies except 121 Hz there are relatively few points (typically 6) on the LPL. It is therefore difficult to say if there really is a trend of increasing exponent values for decreasing frequency, as we might be led to believe from Table 7.1. The spread in n for the selection of amplitudes in Table 8.1 is small, about 0.03 when $\vec{H} \parallel \hat{c}$. The extreme increase in n with increasing amplitude observed for the MPMG sample in the $\vec{H} \perp \hat{c}$ orientation is probably due to remarkably easy penetration since the flux lines sit in weak-pinning regions between the CuO₂ planes and slide easily in and out, and since here the Y211 inclusions reduces the existing barriers even more. See Section 8.1 and Subsection 10.4.3. For an LPL to lie close to the IL, the frequency and amplitude should be small (see Subsection 3.4.4), and the spread in the power-law exponents for the LPLs does not necessarily invalidate the LPLs in Figure 6.1 as reasonable approximations to the true IL. As frequency and amplitude are increased we move away from the IL and minor changes in the shape of the LPLs would not be improbable.

The value $n \approx \frac{3}{2}$ for the exponent of the LPL, or the IL, is often reported [11, 12, 15, 19, 21, 24–26], but also $n \approx \frac{4}{3}$ is seen [15, 27–29], together with an abundance of other values ranging from about 1 for a Tl₂Ba₂CaCu₂O₈ single crystal with $\vec{H} \perp \hat{c}$ [15] to, at least, 3.7 for an YBCO thin film at fields below 1.3 T [18]. Krusin-Elbaum *et al.* find both the value $\frac{3}{2}$, at low fields, and the value $\frac{4}{3}$, at high fields for a twinned YBCO crystal, and attribute the transition between them, taking place around $\sim 0.05\text{--}0.1\text{ T}$ due to thermal softening of the vortex cores [17], as suggested by Feigel'man and Vinokur [30].⁴ By comparing field cooled and zero-field cooled dc magnetization for an MPMG

⁴From later measurements on a piece of the MPMG sample we have not seen traces of such a transition for fields $\vec{H} \parallel \hat{c}$ in the range 0.005–0.15 T (in steps of 0.01 T) or above [31].

sample Kung *et al.* found $n = \frac{3}{2}$ for $\vec{H} \parallel \hat{c}$ [21]. ac susceptibility measurements on MPMG material from Murakami, who supplied us with our MPMG sample, gave $n = \frac{3}{2}$ for $\vec{H} \parallel \hat{c}$, but $n = 2$ for $\vec{H} \perp \hat{c}$ [25, 26].

Heinzel *et al.* considered anisotropy and from ac susceptibility experiments reported $n = \frac{3}{2}$ when $\vec{H} \perp \hat{c}$, and $n = \frac{4}{3}$ when $\vec{H} \parallel \hat{c}$ for a single crystal and two epitaxial films of YBCO, as well as for a $Tl_2Ba_2CaCu_2O_8$ single crystal [15]. They attributed the difference to intrinsically different pinning potentials seen by vortices in the two orientations. Wacenovsky *et al.* also observed anisotropic exponents in their ac susceptibility measurements, but found $n = \frac{3}{2}$ for $\vec{H} \parallel \hat{c}$ and $n = 2$ for $\vec{H} \perp \hat{c}$ in their MPMG sample both before and after subjecting it to fast neutron irradiation [26]; see also an earlier paper from the same group [25]. The exponents in Table 7.1 for the MPMG sample conform to this: the fits give the larger n for $\vec{H} \perp \hat{c}$. For the SC sample the exponents are similar for both orientations. Anyway, the prefactors $\mu_0 H_0$ ensure that the $\vec{H} \perp \hat{c}$ loss peak lines lie far above the $\vec{H} \parallel \hat{c}$ loss peak lines.

6.3 The origins of the power-laws

6.3.1 The spin glass analogy

Initially, the power-law form, with an exponent $n = \frac{3}{2}$, for the IL was used by Müller *et al.* [11] to analyse magnetization measurements on a sintered sample of $(La_{1-x}Ba_x)_2CuO_4$. The line was taken to be a quasi de Almeida-Thouless line separating equilibrium from metastable behaviour in the (dc) susceptibility; more generally, the line marks the onset of irreversible behaviour [32]. An analogy to spin glass was used, for which de Almeida and Thouless had derived such a power law separating ergodic and non-ergodic regions in the H - T plane [33]. The glass analogy was drawn because of the similarity between the spin glass and randomly distributed superconducting grains connected to each other through weak Josephson junctions.

6.3.2 Thermal activation

Yeshurun and Malozemoff [20] gave an alternative explanation for the IL they measured in a single crystal sample: The large thermal activation of the high temperature superconductor causes irreversible magnetic behaviour below an

IL of the same power-law form and even with the same exponent reported by Müller *et al.*. Of course, the same thermal activation argument for the IL applies to conventional low temperature superconductors, but their larger coherence lengths and hence higher activation energies for flux jumps place the IL very close to the upper critical field line $H_{c2}(T)$ where it would be much more difficult to observe.

6.3.3 Flux line lattice melting

In the theory for FLL melting by Houghton *et al.* [34], the melting line has a power-law form with an exponent 2 at low fields, *i.e.* near T_c . At higher fields the exponent is closer to 1. The melting line can be interpreted as being the IL since only below it can large supercurrents flow (a FLL melts into an unpinned liquid, whereas a vortex glass melts into a pinned liquid [36]). It has been established theoretically [37] and experimentally [38, 39] that the melting of the FLL is a 1st order phase transition in three dimensions.⁵ Experiments find smooth and continuous changes in the vicinity of the IL which could of course be the result of smearing by disorder [35]. Charalambous *et al.* [40] reported such a melting line for the $\vec{H} \perp \hat{c}$ orientation with exponent 1.7, which is close to our value for the MPMG sample in this orientation. Fendrich *et al.* [41] recently observed the same also for the $\vec{H} \parallel \hat{c}$ orientation in an untwinned crystal and gave a power-law melting line $H_m(T)$ with an exponent 1.4, which is close to our LPL exponents for this orientation. They also demonstrated how the clean 1st order melting transition can be made to disappear by introducing point disorder and pinning through electron irradiation; the authors contend that the induced point disorder prevents the vortex liquid from freezing into an Abrikosov lattice at the original freezing/melting temperature T_m and shifts vortex solidification to lower temperatures.⁶ After irradiation, annealing was then used to reduce the density of point defects and recover the same sharp melting transition, with hysteresis. For the $\vec{H} \perp \hat{c}$ orientation, annealing reduced the number of point defects leading to reduced disorder and

⁵Contrary to a fairly widespread belief, hysteresis does in principle *not* indicate a thermodynamic phase transition, which is an equilibrium phenomenon, since hysteresis is a non-equilibrium phenomenon.

⁶This could agree with the “vortex slush” of Worthington *et al.* [42]: In a clean sample, the melting and vortex glass temperatures T_m and T_g are equal and 1st order melting is observed. In somewhat disordered sample the transition temperatures separate and $T_g < T_m$. The coexistence of T_m and T_g goes away in a disordered sample where only T_g is observed. See also Reference [43].

enabled freezing of the vortex liquid at T_m . Worthington *et al.* have reported a melting line with an exponent $\frac{3}{2}$ for heavy ion-irradiated YBCO crystals [42]. Furthermore, in clean, untwinned single crystals evidence for a 1st order vortex melting transition hysteretic in both temperature and magnetic field has been published [38, 39, 44–48]. From torsional oscillator experiments on an untwinned YBCO single crystal Farrell *et al.* reported a melting line with a power-law exponent close to the theoretically predicted value: 1.99 [49]. Giapintzakis *et al.* interpreted ac susceptibility data with multiple loss peaks for samples of similar quality in terms of melting and found an exponent 1.85 [50].

6.3.4 Vortex glass transition

For the vortex glass (VG) phase, Fisher *et al.* expected a power-law behaviour $\sim (1 - T_g/T_c)^{2\nu}$ [43]. Here T_g is the VG temperature below which the vortex system is frozen into a disorder (glassy) solid, and ν is the exponent with which the coherence length diverges at T_g . Close to T_c they expect that $\nu \simeq \frac{2}{3}$ due to critical fluctuations, giving us an exponent $\frac{4}{3}$. (There appears, however, to be no connection between the experimental ν and the power-law exponent; see below.) The LPL of Worthington *et al.*, coinciding with the onset of j_c , did indeed have this form, though the authors were reluctant to claim that they had observed a VG [29]. Other experiments have however reported values for ν quite different from $\frac{2}{3}$, ranging from 0.7 to 3.1 [51, and references therein]. Seng *et al.* reported a VG power-law exponent for $\vec{H} \parallel \hat{c}$ of 1.7, the same as for their LPLs taken at a number of different frequencies, for an YBCO film [14]. Their results are therefore similar to ours, except we find exponents $\sim 1.4\text{--}1.6$. Ling and Budnick [52] showed how using a constant j_c criterion to determine the IL, the exponent $\frac{3}{2}$ can be obtained from the collective pinning theory [53, 54]. From VG scaling of frequency dependent ac susceptibility data on a twinned YBCO crystal Kötzler *et al.* found that their VG lines followed power-laws with exponents 1.5 (but $\nu = 3.1$) and 2.3 (but $\nu = 1.6$) for the $\vec{H} \parallel \hat{c}$ and $\vec{H} \perp \hat{c}$ orientations, respectively [51]. We note that our estimates for the VG line exponent agree with this result for $\vec{H} \parallel \hat{c}$.

6.4 Summary and conclusions

In summary, our measurements show that the irreversibility line exists at higher temperatures and fields for $\vec{H} \perp \hat{c}$ than for $\vec{H} \parallel \hat{c}$, in agreement with pub-

lished results. This is consistent with a picture of anisotropic melting of the FLL and the anisotropic intrinsic pinning due to the layered structure of the material.

Power-law fits

$$H(T^*) = H_0(1 - T^*/T_c)^n$$

to the LPLs give exponents $n \approx 1.4\text{--}1.6$ similar to a large number of other published exponents for LPLs and ILs.

Considering the LPL power-laws representative for the ILs we find it hard to separate between the different model descriptions of the flux line system since they all may give exponents ~ 1.5 . In view of the wide range of n values and their dependence on experimental parameters (*e.g.* frequency) one should proceed with extreme caution in evaluating the meaning of such power-law behaviours. It would be very difficult to draw a solid conclusion from our measured values as to what model applies in our case. Nevertheless, for $\tilde{H} \parallel \hat{c}$ at least, a power-law describes our experimental LPLs, and hence maybe also the ILs, very well.

References

- [1] K. Fossheim, M. G. Karkut, L. K. Heill, M. Slaski, L. T. Sagdahl, V. M. Vinokur, M. Murakami, H. Fujimoto, N. Koshizuka, S. Tanaka, F. Gencer, J. S. Abell and C. E. Gough, *Physica Scripta T* **42** (1992) 20.
- [2] M. G. Karkut, L. K. Heill, V. M. Vinokur, M. Slaski, L. T. Sagdahl, E. D. Tuset and K. Fossheim, *Cryogenics* **33** (1993) 60.
- [3] V. B. Geshkenbein, V. M. Vinokur and R. Fehrenbacher, *Phys. Rev. B* **43** (1991) 3748.
- [4] F. Lindemann, *Phys. Z* **11** (1910) 69.
- [5] G. Blatter, V. B. Geshkenbein and A. I. Larkin, *Phys. Rev. Lett.* **68** (1992) 875.
- [6] M. Tachiki and S. Takahashi, *Solid State Commun.* **70** (1989) 291.
- [7] W. E. Lawrence and S. Doniach in *Proceedings of the 12th International Conference on Low Temperature Physics*, ed. E. Kanda, Academic Press of Japan, Kyoto (1971) page 361.
- [8] J. R. Clem in *Vortex dynamics in the high-temperature superconductors*, preprint from *The International Cryogenic Materials Conference, 1994 Topical Conference, The Critical State in Superconductors*, Honolulu, Hawaii, USA, October 1994. Proceedings to be published by World Scientific, Singapore (1995).
- [9] M. Tinkham, *Introduction to Superconductivity*, McGraw-Hill, New York (1975).
- [10] J. R. Clem, *Phys. Rev. B* **44** (1991) 7737.

- [11] K. A. Müller, M. Takashige and J. G. Bednorz, Phys. Rev. Lett. **58** (1987) 1143.
- [12] A. P. Malozemoff, T. K. Worthington, Y. Yeshurun, F. Holtzberg and P. H. Kes, Phys. Rev. B **38** (1988) 7203.
- [13] A. Gupta, P. Esquinasi, H. F. Braun and H.-W. Neumüller, Phys. Rev. Lett. **69** (1989) 1869.
- [14] Ph. Seng, R. Gross, U. Baier, M. Rupp, D. Koelle, R. P. Huebner, P. Schmitt, G. Saemann-Ischenko and L. Schultz, Physica C **192** (1992) 403.
- [15] Ch. Heinzel, Ch. Neumann and P. Ziemann, Europhys. Lett. **13** (1990) 531.
- [16] L. A. Angurel, F. Lera, A. Badía, C. Rillo, R. Navarro, J. Bartolomé, J. Melero, J. Flokstra and R. P. J. IJsselsteijn in *Proceedings of the EMRS-ICAM'91, High T_c superconductor thin films*, Strasbourg (France) 1991, Elsevier Science Publishers (1992) 141.
- [17] L. Krusin-Elbaum, L. Civale, F. Holtzberg and C. Feild, Physica A **200** (1993) 314.
- [18] T. Arndt, F. Schmidt, H. Reiner and W. Schauer in *Critical Currents in Superconductors*, ed. H. W. Weber, World Scientific, Singapore (1994) 260.
- [19] F. Gömöry and S. Takács, Physica C **217** (1993) 297.
- [20] Y. Yeshurun and M. Malozemoff, Phys. Rev. Lett. **60** (1988) 2202.
- [21] P. J. Kung, M. P. Maley, M. E. McHenry, J. O. Willis, J. Y. Coulter, M. Murakami and S. Tanaka, Phys. Rev. B **46** (1992) 6427.
- [22] W. Gawalek, T. Habisreuther, K. Fischer, G. Bruchlos and P. Görnert, Cryogenics **33** (1993) 65.
- [23] K. Fischer, G. Leitner, G. Fuchs, M. Schubert, B. Schlobach, A. Gladun and C. Rodig, Cryogenics **33** (1993) 97.
- [24] H. B. Sun, K. N. R. Taylor and G. J. Russell, Physica C **227** (1994) 55.
- [25] M. Wacenovsky, R. Miletich and H. W. Weber, Supercond. Sci. Technol. **5** (1992) S184.

- [26] M. Wacenovsky, R. Miletich, H. W. Weber and M. Murakami, Cryogenics **33** (1993) 70.
- [27] T. K. Worthington, W. J. Gallagher, T. R. Dinger, F. Holtzberg, D. L. Kaiser and R. L. Sandstrom, Physica C **153-155** (1987) 32.
- [28] B. Oh, K. Char, A. D. Kent, M. Naito, M. R. Beasley, T. H. Geballe, R. H. Hammond, A. Kapitulnik and J. M. Graybeal, Phys. Rev. B **37** (1988) 7861.
- [29] T. K. Worthington, F. H. Holtzberg and C. A. Feild, Cryogenics **30** (1990) 417.
- [30] M. V. Feigel'man and V. M. Vinokur, Phys. Rev. B **41** (1990) 8986.
- [31] L. K. Heill and M. G. Karkut, unpublished.
- [32] I. Morgenstern, K. A. Müller and J. G. Bednorz, Z. Phys. B **69** (1987) 33.
- [33] J. R. L. de Almeida and D. J. Thouless, J. Phys. A **11** (1978) 983.
- [34] A. Houghton, R. A. Pelcovits and A. Sudbø, Phys. Rev. B **40** (1989) 6763.
- [35] D. R. Nelson in *Phenomenology and Applications of High Temperature Superconductors*, ed.s K. S. Bedell, M. Inui, D. E. Meltzer, J. R. Schrieffer and S. Doniach, Addison Wesley, Reading, Massachusetts, USA (1992) page 230.
- [36] G. Blatter, M. V. Feigel'man, V. B. Geshkenbein, A. I. Larkin and V. M. Vinokur in *Vortices in high temperature superconductors*, preprint, ETH, Zürich (1993) 538 pages. Rev. Mod. Phys. **66** (1994) 1125.
- [37] R. E. Hetzel, A. Sudbø and D. A. Huse, Phys. Rev. Lett. **69** (1992) 518.
- [38] H. Safar, P. L. Gammel, D. A. Huse, D. J. Bishop, J. P. Rice and D. M. Ginsberg, Phys. Rev. Lett. **69** (1992) 824.
- [39] W. K. Kwok, S. Fleshler, U. Welp, V. M. Vinokur, J. Downey, G. W. Crabtree and M. M. Miller, Phys. Rev. Lett. **69** (1992) 3370.
- [40] M. Charalambous, J. Chaussy and P. Lejay, Phys. Rev. B **45** (1992) 5091.
- [41] J. A. Fendrich, W. K. Kwok, J. Giapintzakis, C. J. van der Beek, V. M. Vinokur, S. Fleshler, U. Welp, H. K. Viswanathan and G. W. Crabtree, Phys. Rev. Lett. **74** (1995) 1210.

- [42] T. K. Worthington, M. P. A. Fisher, D. A. Huse, J. Toner, A. D. Marwick, T. Zabel, C. A. Feild and F. Holtzberg, Phys. Rev. B **46** (1992) 11854.
- [43] D. S. Fisher, M. P. A. Fisher and D. A. Huse, Phys. Rev. B **43** (1991) 130.
- [44] H. Safar, P. L. Gammel, D. A. Huse, D. J. Bishop, W. C. Lee, J. Giapintzakis and D. M. Ginsberg, Phys. Rev. Lett **70** (1993) 3800.
- [45] H. Safar, P. L. Gammel, D. A. Huse, G. B. Alers, D. J. Bishop, W. C. Lee, J. Giapintzakis and D. M. Ginsberg, preprint.
- [46] W. K. Kwok, J. Fendrich, U. Welp, S. Fleshler, J. Downey and G. W. Crabtree, Phys. Rev. Lett. **72** (1994) 1088.
- [47] W. K. Kwok, J. Fendrich, S. Fleshler, U. Welp, J. Downey and G. W. Crabtree, Phys. Rev. Lett. **72** (1994) 1092.
- [48] W. K. Kwok, J. A. Fendrich, C. J. van der Beek and G. W. Crabtree, Phys. Rev. Lett. **73** (1994) 2614.
- [49] D. E. Farrell, J. P. Rice and D. M. Ginsberg, Phys. Rev. Lett. **67** (1991) 1165.
- [50] J. Giapintzakis, R. L. Neiman, D. M. Ginsberg and M. A. Kirk, preprint (1994).
- [51] J. Kötzler, M. Kaufmann, G. Nakielski, R. Behr and W. Assmus, Phys. Rev. Lett. **72** (1994) 2081.
- [52] X. Ling and J. I. Budnick in *Magnetic Susceptibility of Superconductors and Other Spin Systems*, ed. R. A. Hein, T. L. Francavilla and D. H. Liebenberg, Plenum Press, New York (1991).
- [53] A. I. Larkin and Yu. N. Ovchinnikov, Zh. Eksp. Teor. Fiz. **65** (1973) 1704.
- [54] A. I. Larkin and Yu. N. Ovchinnikov, J. Low. Temp. Phys. **34** (1979) 409.

Frequency dependence

Crucial for the understanding of the flux system is knowledge of the temporal behaviour. The frequency of the dynamic ac magnetic measurements lets us probe this very important part of the physics as described in earlier Chapters. In the following we will investigate how the frequency dependence provides information on the motion of flux in our samples and on the linearity or non-linearity of the ac response. A central point is the behaviour of the pinning barriers that the probing vortices face. Changing the frequency effectively moves the system between different resistive regimes or vortex states. Throughout, the amplitude is kept constant at 0.1 mT.

7.1 Loss peak lines

In Figure 7.1 we plot loss peak lines (LPLs) taken at different frequencies spanning four orders of magnitude from 12.1 to 121 000 Hz for both the MPMG and the SC samples with $\vec{H} \parallel \hat{c}$ and $\vec{H} \perp \hat{c}$. We see that the two samples respond similarly to changing frequencies. The LPLs are clearly much more frequency dependent for $\vec{H} \parallel \hat{c}$ than for $\vec{H} \perp \hat{c}$. For fields from 1.5 T and up, the increase in temperature of the LPL on going from 12.1 to 121 000 Hz is 3–4 times greater for $\vec{H} \parallel \hat{c}$ than for $\vec{H} \perp \hat{c}$. Referring to the extreme cases, linear (ohmic) and non-linear response, we can say that in the $\vec{H} \parallel \hat{c}$ orientation the samples behave ohmic-like with strong frequency dependence, whereas in the $\vec{H} \perp \hat{c}$ orientation the samples are closer to the non-linear regime with weaker frequency dependence as discussed in Chapter 3. Table 7.1 lists fitting param-

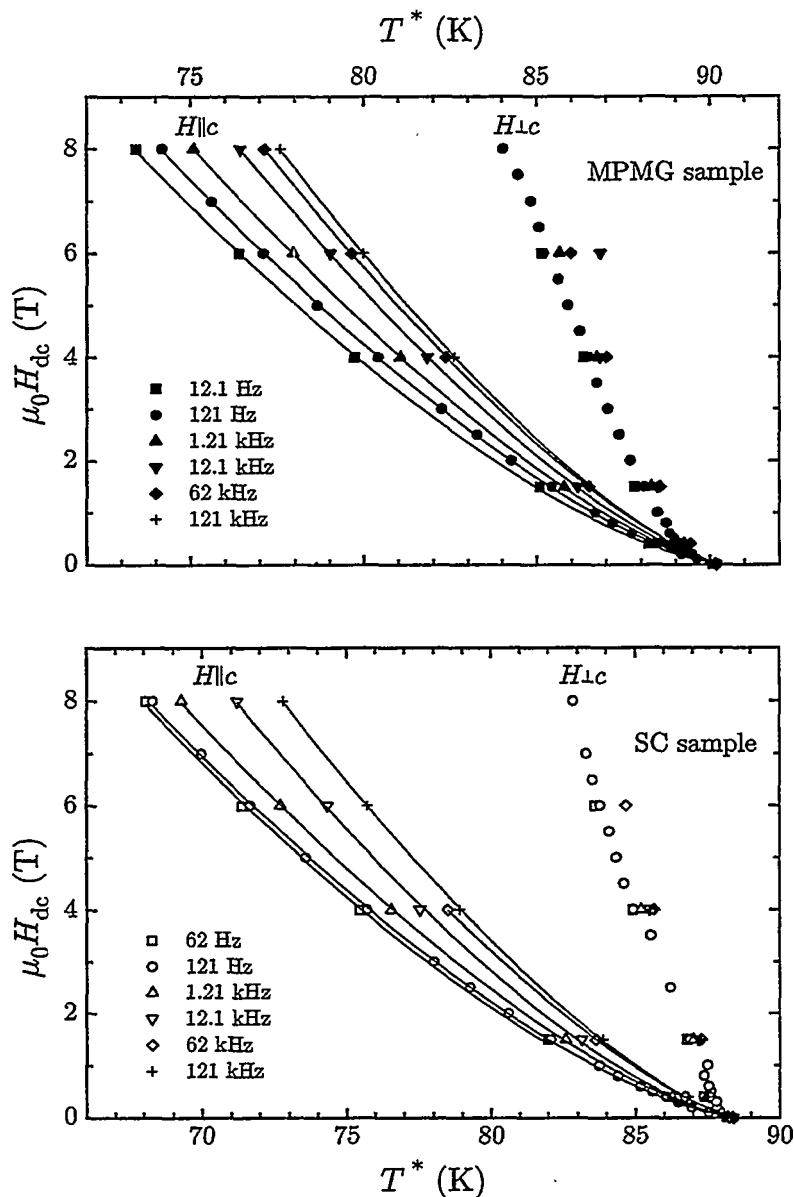


Figure 7.1: Loss peak lines LPLs of the MPMG (top) and the SC (bottom) samples plotted for different excitation field frequencies for $\vec{H} \parallel \hat{c}$ and $\vec{H} \perp \hat{c}$. The excitation field amplitude is 0.1 mT. The LPLs move to higher fields and temperatures as the frequency is increased. This effect is much stronger when $\vec{H} \parallel \hat{c}$ than when $\vec{H} \perp \hat{c}$. The solid lines for $\vec{H} \parallel \hat{c}$ are best fits to (6.3), and the details of the fits are listed in Table 7.1 for both samples and both orientations.

Table 7.1: Fitting parameters from fitting the loss peak lines in Figure 7.1 to a power-law of the form (6.3): $\mu_0 H(T^*) = \mu_0 H_0 (1 - T^*/T_c)^n$. $\mu_0 h_{ac} = 0.1 \text{ mT}$ and $f = 121 \text{ Hz}$.

Sample	f (Hz)	$\vec{H} \parallel \hat{c}$		$\vec{H} \perp \hat{c}$	
		$\mu_0 H_0$ (T)	n	$\mu_0 H_0$ (T)	n
MPMG	12.1	93	1.47	1135	1.84
	121	91	1.42	648	1.63
	1210	96	1.40	969	1.72
	12100	111	1.41	944	1.69
	62000	111	1.37	784	1.61
	121000	119	1.38	672	1.57
	Average: ^a	97	1.41	707	1.64
SC	62	73	1.51	427	1.47
	121	70	1.47	401	1.43
	1210	72	1.44	627	1.54
	12100	87	1.47	650	1.51
	62000	78	1.37	602	1.47
	121000	88	1.39	878	1.57
	Average: ^a	75	1.42	414	1.44
Y12	121	121	1.50	—	—

^aWeighted with respect to the least square errors for the individual fits.

etes for the LPLs.

In Figure 7.2 we replot the data of Figure 7.1 as T^* vs. $\log f$. Here we see more clearly the progressive increase of the loss peak temperature with frequency. For $\vec{H} \perp \hat{c}$ the slope is roughly constant over the range of dc fields for both samples. The overall change in T^* is less than 1 K. In contrast to this is the larger increase in T^* vs. f for increasing applied dc fields parallel to the c -axis. This behaviour is, within the skin effect picture, in general agreement with the dc resistivity behaviour: for a fixed excitation amplitude and frequency, the peak in $\mu''(H, T)$ will occur for $\rho^*(H, T) \propto f$. Thus by increasing f , ρ^* increases and hence the temperature position of the peak shifts to a higher value, as is evident from Figures 3.5. We note that the shift in temperature is less for $\vec{H} \perp \hat{c}$ than for $\vec{H} \parallel \hat{c}$ for the same frequency shift. In the skin effect picture, this would imply that the resistivity changes more rapidly with temperature for the former orientation than for the latter. This agrees with the observation that the transition broadening in dc field is much more pronounced for $\vec{H} \parallel \hat{c}$

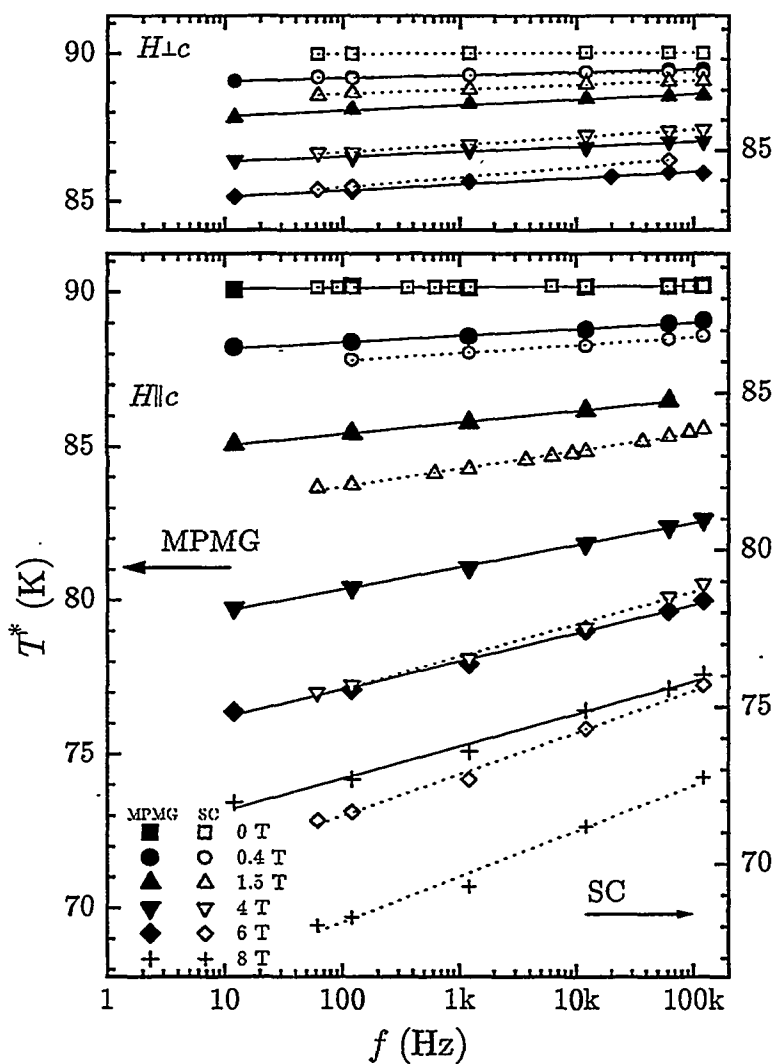


Figure 7.2: The temperature position of the loss peak maxima, T^* , vs. $\log f$ for both the MPMG (left axis) and the SC (right axis) samples for both the $\vec{H} \perp \hat{c}$ (top) and $\vec{H} \parallel \hat{c}$ (bottom) orientations. The solid and dashed lines are straight line fits to help guide the eye. Since the T_c 's of the two samples are different, we have set the ranges of the vertical axes such that the left and right axes both correspond to the same reduced temperature ranges, i.e. $0.93\text{--}1.01 T_c$ for $\vec{H} \perp \hat{c}$ and $0.75\text{--}1.01 T_c$ for $\vec{H} \parallel \hat{c}$, to allow for direct comparison of the two samples. The amplitude is 0.1 mT.

than for $\vec{H} \perp \hat{c}$ [1].

7.2 Thermal activation

In Figures 7.3 and 7.4 we plot $\log f$ vs. $1/T^*$ for different applied dc fields for the $\vec{H} \parallel \hat{c}$ and $\vec{H} \perp \hat{c}$ orientations. In a skin depth picture this is equivalent to the common Arrhenius plots of $\log \rho$ vs. $1/T$, and we indicate this by adding the right ρ^* -axes where the values are obtained from naively assuming that the loss peak maxima occur when the skin depth is approximately equal to half the sample size (full penetration¹) and $\rho^* \approx \pi \mu_0 f^* d^2$ (for our samples, $\rho^* \approx 10^{-4} f^*$ using lab units $\mu\Omega\text{cm}$ and Hz). We see that the highest frequency (121 kHz) corresponds to a resistivity level of about $10 \mu\Omega\text{cm}$, which is not far below the normal state resistivity at T_c , $\rho_n \approx 50 \mu\Omega\text{cm}$. So if we were to measure at higher frequencies, we would expect very weak shifts of the loss peak temperatures T^* with frequency above about 1 MHz as we would be above T_c where the resistivity changes slowly with temperature. While for $\vec{H} \parallel \hat{c}$ the relevant resistivity is that for current flowing in the ab -planes, ρ_{ab} , for $\vec{H} \perp \hat{c}$ there are two relevant resistivities, the one for current flowing across the ab -planes, ρ_c , and ρ_{ab} , and the use of a single resistivity in this case is of course questionable; hence the notation ρ_{eff} (effective resistivity) in Figure 7.4.

For $\vec{H} \parallel \hat{c}$ we find good straight line fits down to 121 Hz, with only minor deviations for lower frequencies (12.1 and 62 Hz for the MPMG and SC sample, respectively), indicating activated behaviour: $f^* = f_0 \exp(-U(H, T^*)/k_B T^*)$. However, the prefactor f_0 attains unphysical values: $\log f_0 \sim 75-420$ (50-350) for the MPMG (SC) sample for fields from 8 down to 0.4 T! These values result from not taking into account the temperature dependence of the pinning barrier $U(H, T)$. A first approximation to an upper bound for the prefactor is found by extrapolating to T_c where $U \rightarrow 0$. Doing this for the data in Figure 7.3 we note that they extrapolate to T_c for the more reasonable $f_0 \sim 10^{15} \text{ Hz}$, plus/minus two-three orders of magnitude, for both samples.

Thermally activated flux motion can result from creep or diffusion mechanisms. When the induced screening current density j is close to $j_c(H, T)$ and the thermal energy $k_B T \ll U(H, T)$ vortex motion is driven by a Lorentz force $F_L = Bj$ against the comparable opposing (bulk) pinning force F_p , but thermal

¹Strictly speaking, an ohmic sample is of course always penetrated, but the magnitude of the magnetic induction at the center is exponentially small compared to the induction close to the surface for skin depths smaller than the sample size.

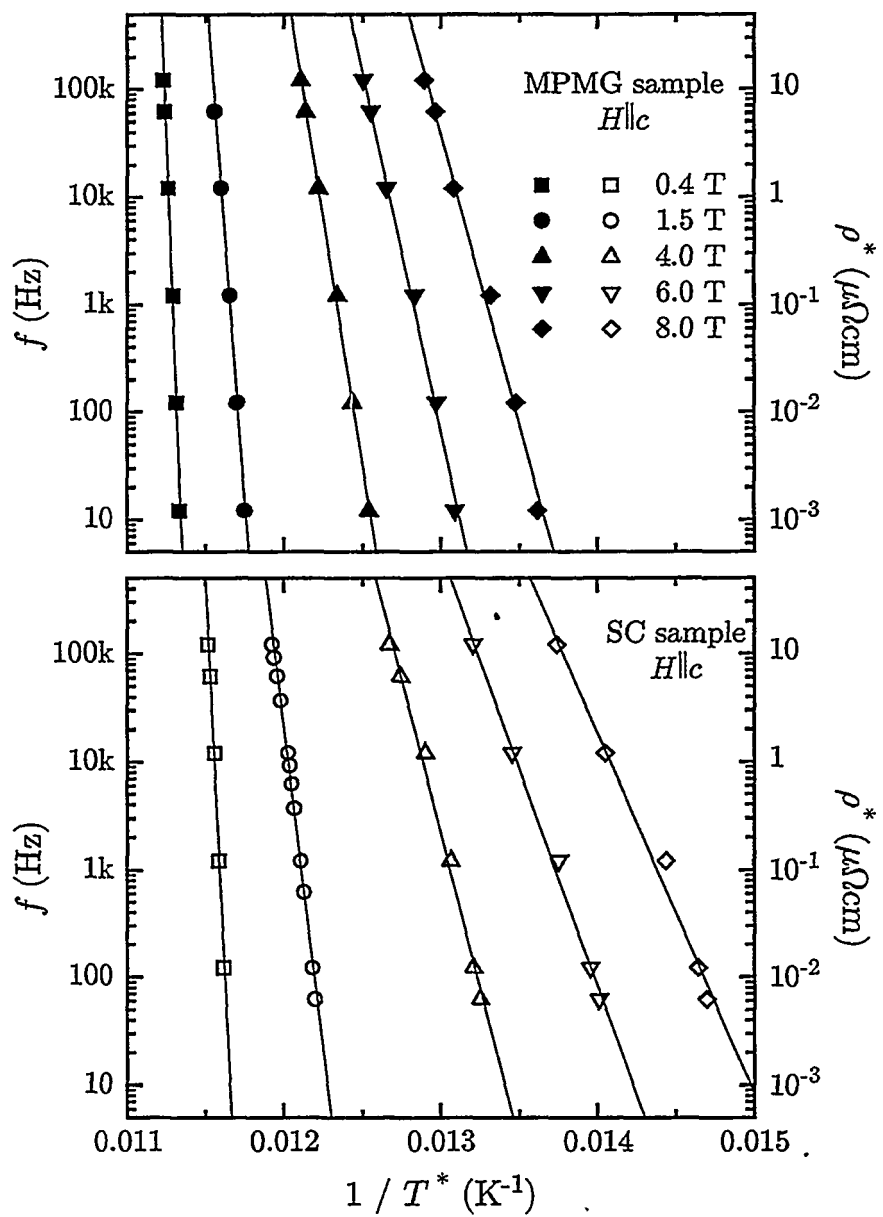


Figure 7.3: Arrhenius plots for the MPMG (top) and SC (bottom) samples for different fields $H \parallel c$. The solid lines are straight line fits. The right axes show the resistivities obtained assuming a skin depth picture. The amplitude is 0.1 mT.

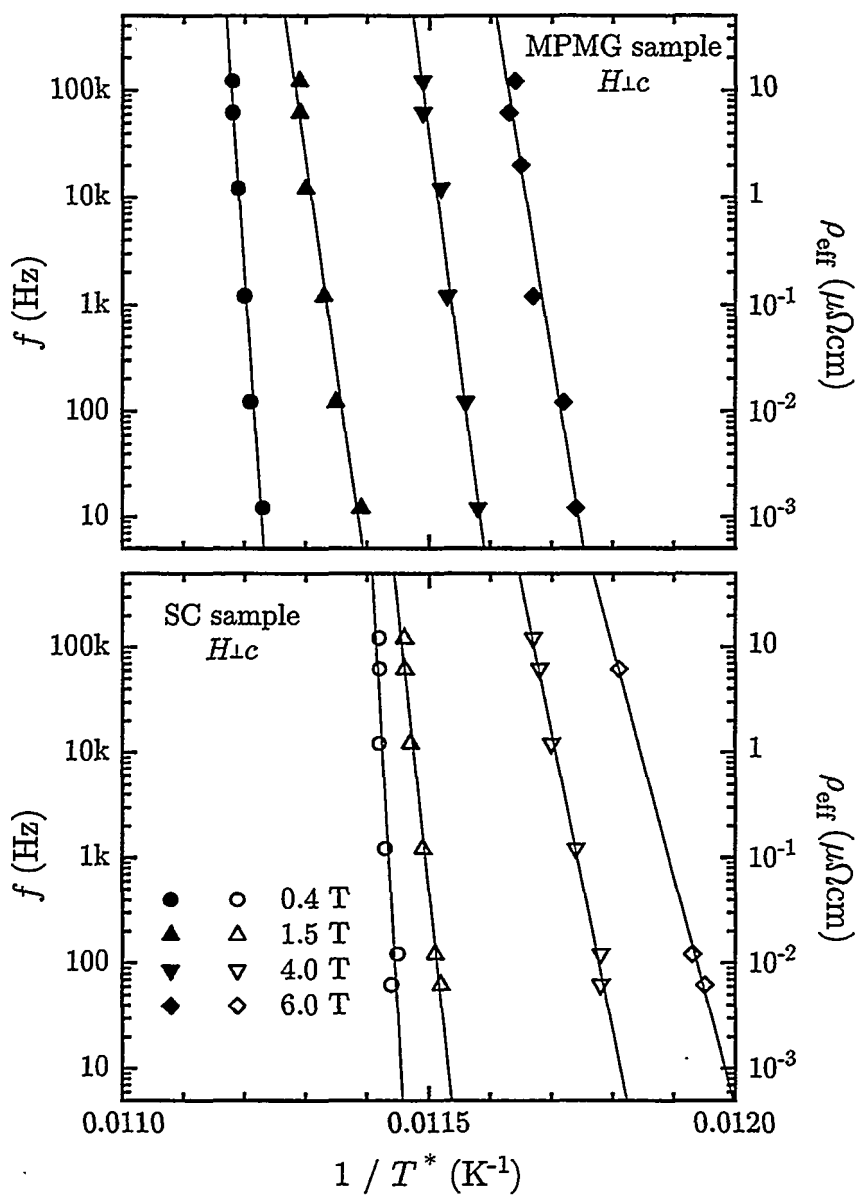


Figure 7.4: Arrhenius plots for the MPMG (top) and SC (bottom) samples for different fields $\vec{H} \perp \hat{c}$. The solid lines are straight line fits. The right axes show the resistivities obtained assuming a skin depth picture, and the quotation marks indicate that the use of a single resistivity in this orientation is questionable. The amplitude is 0.1 mT.

jumps lower the critical current density j_c by a factor $g[k_B T/U(H, T) \ln(1 + f_0/f)] < 1$ (see for example Reference [2]) and we have creep. On the other hand, when $j \ll j_c(H, T)$ and the Lorentz force is negligible compared to the pinning force, but the thermal energy $k_B T$ is on the order of the activation, or pinning, barrier $U(H, T)$ we are in a regime of thermally activated flux flow, the TAFF regime [3–5].

When flux creep is taken into account in a Bean critical state model, we have at the loss peak maximum

$$h_{ac} = g \left[\frac{k_B T^*}{U(H, T^*)} \ln \left(1 + \frac{f_0}{f} \right) \right] j_c(H, T^*) a \quad (7.1)$$

with a as the relevant sample dimension, and both amplitude dependence, indicative of non-linear ac response, and an Arrhenius like frequency dependence are the results. The g functional was introduced in the above paragraph.

In the TAFF regime, the ac penetration depth is a skin depth with ρ_{TAFF} as the resistivity:

$$\lambda_{ac} = \sqrt{\frac{\rho_{TAFF}}{\pi \mu_0 f}} = \sqrt{\frac{\rho_0}{\pi \mu_0 f}} e^{-U(H, T)/2k_B T} \quad (7.2)$$

See Subsection 2.3.2 on the TAFF resistivity prefactor ρ_0 . From (7.2) we expect Arrhenius like frequency dependence, but the ac response is linear since there is no amplitude dependence.

7.2.1 Energy barriers

The slopes of our Arrhenius fits can then give estimates for the barriers against thermally activated flux motion, U , irrespective of whether the underlying mechanism is creep or diffusion. If we disregard any temperature dependence of the barriers, our slopes give values in the range 3–13 eV for the field range used (the same values as for $q = 1$ in Table 7.2). These results are similar to those of Palstra *et al.* [5], but the barriers are extremely high (1 eV corresponds to $\sim 10^4$ K) since we have yet to consider the temperature dependence. This is why we get the unphysically high attempt frequencies above. But we operate quite close to T_c , and here we expect the effective barriers to drop and ultimately vanish as T_c is approached from below. The barriers are often taken to be a product of the condensation energy $\sim H_c(T)^2$ and some combination of fundamental lengths, such as the coherence length $\xi(T)$, the penetration depth

$\lambda(T)$, the intervortex distance $a_0 \sim B^{-1/2}$ or the distance between pinning centers [6, page 176], some of which show extreme behaviour and diverge or vanish at T_c . Assuming $U(H, T) \propto H_c(T)^2 \xi(T)^n$ with n ranging from 0 to 3, see for example Reference [7], Palstra *et al.* found [5] $U(H, T) = U(H, 0)(1 - t^2)^q / (1 + t^2)^{q-2}$ with $t = T/T_c$ and $q = 2 - n/2$ in the range 0.5–2, a form also used by Seng *et al.* [8]. Close to T_c the temperature dependent factor can be approximated² by $4(1 - t)^q$, but for simplicity we drop the factor 4 and adapt the tidier power-law form

$$U(H, T) = U(H, 0)(1 - t)^q . \quad (7.3)$$

A popular value for the pinning barrier exponent is $q = \frac{3}{2}$. A simple scaling argument of Krusin-Elbaum *et al.* gave this result: U is a product of the condensation energy $\propto H_c^2$ and the excitation volume $a_0^2 \xi$, where $a_0^2 = \Phi_0/B$,³ and the Ginzburg-Landau theory gives $H_c \propto (1 - t)$ and $\xi \propto (1 - t)^{-1/2}$ [9]. Introducing such power-law temperature dependencies, we also get closer to approximating the slight negative curvature in our Arrhenius plots, best seen at the highest fields. In our narrow temperature (or frequency) windows however, the effect cannot be appreciated in the plots.

Simplest case: $q = 1$

With $q = 1$

$$\log f = \log f_0 + \log e \frac{U(H, 0)}{k_B} \left(\frac{1}{T_c} - \frac{1}{T} \right) \quad (7.4)$$

where $e = 2.71828\dots$. The extra term $\propto U(H, 0)/k_B T_c$ will seriously modify the unphysical values, and the large spread, for the attempt frequency found above by disregarding the temperature dependence of the pinning potential. However, the same values as before including the temperature dependence are found for the slope and hence for $U(H, 0)$. In Figure 7.5 we plot $U(H, 0)$ obtained from fits to (7.3) with $q = 1$ for both samples. The dotted lines are fits to a power-law

$$U(H, 0) = \frac{U_0}{H^\eta} \quad (7.5)$$

and the exponents obtained are $\eta \approx 0.7$ for both the MPMG and the SC samples. The quality of the fit is very good for the SC sample, and quite

²The approximation is good to lower and lower t as q increases. For $q = 1$ ($q = \frac{3}{2}$) the error is less than 10% for $t > 0.95$ (0.93), and for $t = 0.75$ the error is about 40%.

³For sufficiently large fields the area available to each individual flux line is limited by the intervortex separation squared, $\simeq a_0^2$.

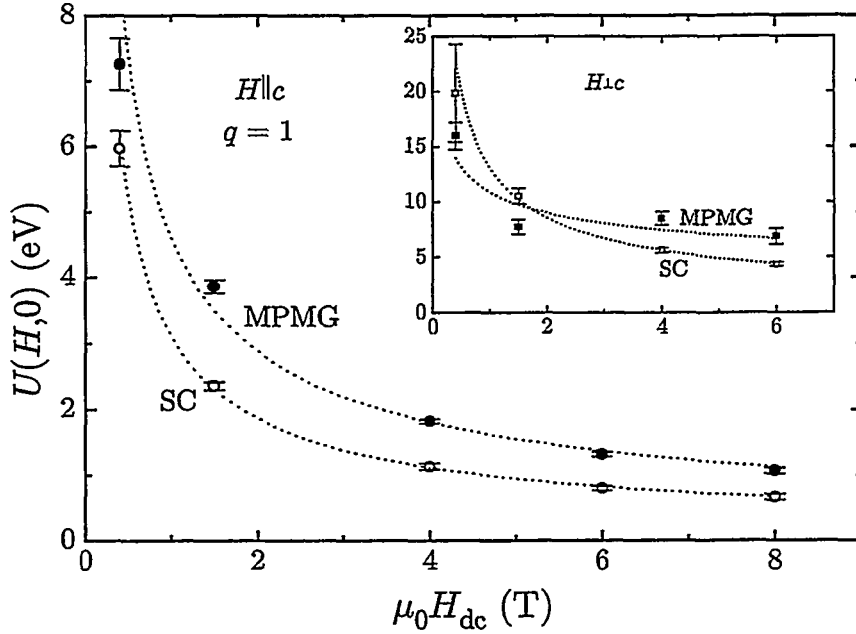


Figure 7.5: Pinning barriers $U(H, 0)$ vs. applied field $\mu_0 H_{dc}$ for the MPMG and SC samples for the $\vec{H} \parallel \hat{c}$ orientation. The points are obtained from fits of $\log f(T^*)$ data to (7.4) for an amplitude of 0.1 mT. The dotted lines are best fits to the power-law $U(H, 0) = U_0 H^{-\eta}$. See text. The inset show similar data for the $\vec{H} \perp \hat{c}$ orientation.

reasonable for the MPMG sample. Thus under the assumption that $q = 1$ we obtain a pinning potential

$$U(H, T) \approx U_0 \frac{1 - t}{H^{0.7}} \quad (7.6)$$

Following the same procedure, with identical power-law fitting functions for the field and temperature dependencies of the pinning potential, Fàbrega *et al.* found $\eta \approx 0.6$ for a single crystal of the electron-doped superconductor $\text{Pr}_{1.85}\text{Ce}_{0.15}\text{CuO}_{4-y}$ [2], and Seng *et al.* found $\eta \approx 0.5$ for a thin film YBCO sample [8]. A temptingly similar form for the barrier is the one derived for plastic creep: In a very viscous vortex liquid, the plastic deformation energy is estimated to be [10]

$$U_{pl} \sim \varepsilon \varepsilon_0 a_0 \propto \frac{1 - t}{\sqrt{H}} \quad (7.7)$$

where $\varepsilon = \sqrt{m/M} < 1$ is the anisotropy parameter, $\varepsilon_0 = (\Phi_0/4\pi\lambda)^2$ is an energy scale entering the self-energy of a vortex and the interaction between vortices [10], and $a_0 = \sqrt{\Phi_0/B}$ is the vortex separation. See also References [11, 12] for the original estimates. However, while Fàbrega *et al.* found good agreement between their IL (a LPL) and the IL that can be deduced from $U_{\text{pl}}(H, T)$, $H_{\text{irr}} \propto (1-t)^2$, [2], our fits summarized in Table 7.1 give exponents $\sim 1.4-1.5$, not 2. Since plastic creep is known to be relevant in highly anisotropic systems [2], through ε in (7.7) above, the relatively low anisotropy of YBCO could explain the disagreement between our LPL, or “IL”, exponents and that for plastic creep. Indeed, Seng *et al.* found that data for a thin film of the very anisotropic BSCCO material did fit a plastic creep picture (with an IL power-law exponent $n = 2.1$ and a $U(H, 0)$ exponent $\eta = 0.5$), whereas the same type of data for a thin film of YBCO did not (exponents: $n = 1.7$ and $\eta = 0.6$) [8].

Returning to the matter of the magnitude of the attempt frequencies, we can now use (7.4) to find a single value for each sample by a method used by Fàbrega *et al.* [2]: If we plot $\log f'_0(H) \equiv \log f_0 + \log e U(H, 0)/k_B T_c$ vs. $U(H, 0)$, we obtain straight lines extrapolating to $\log f_0$ at $U(H, 0) = 0$. See Figure 7.6. We now find the less unreasonable values $f_0 \sim 10^{16}$ Hz for the MPMG sample, and $f_0 \sim 10^{13}$ Hz for the SC sample. Alternatively, making individual fits to the Arrhenius plots for each field with the temperature dependence included in the fitting function, we find the average values $f_0 \sim 10^{14}$ Hz for the MPMG sample, and $f_0 \sim 10^{13}$ Hz for the SC sample. The spread in $\log f_0$ is ~ 4 for the MPMG sample and only just above 1 for the SC sample. These values agree with the upper bound found above from extrapolation to T_c .

Power-law with $q = 3/2$

In Figure 7.7 we plot $U(H, 0)$ obtained from fits to (7.3) with $q = \frac{3}{2}$ for both samples. The dotted lines are fits to the power-law (7.5), and the exponents obtained are $\eta \approx 1$ for both the MPMG and the SC samples:

$$U(H, T) \approx U_0 \frac{(1-t)^{3/2}}{H} . \quad (7.8)$$

As for $q = 1$ the quality of the fit is very good for the SC sample and quite fair for the MPMG sample.

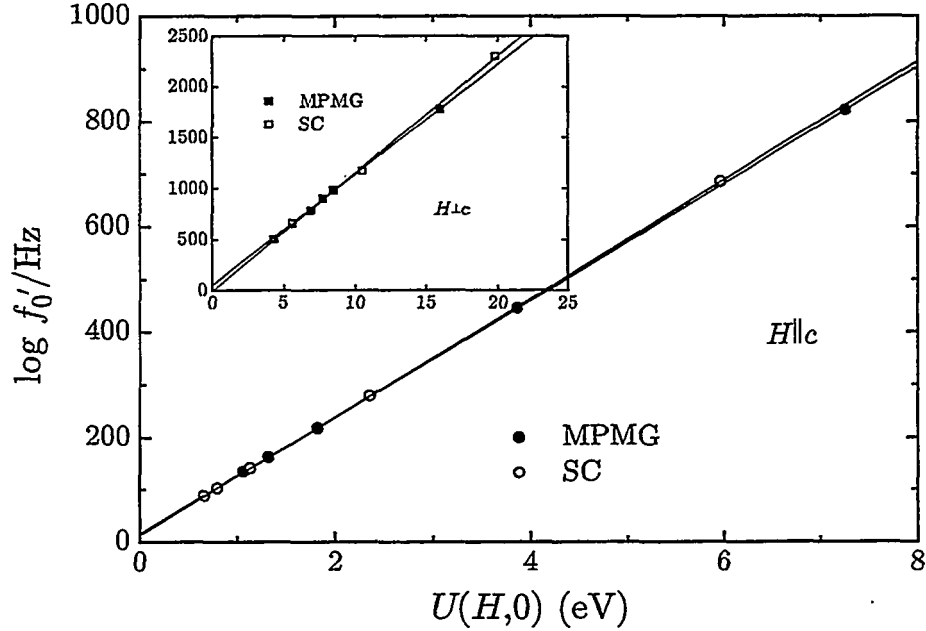


Figure 7.6: $\log f'_0(H) \equiv \log f_0 + \log e U(H, 0)/k_B T_c$ vs. $U(H, 0)$ for the MPMG and SC samples for the $\vec{H} \parallel \hat{c}$ orientation. The linear fits extrapolate to $\log f_0$ at $U(H, 0) = 0$. The inset show the corresponding results for the $\vec{H} \perp \hat{c}$ orientation.

The experimental data of Kim *et al.* for Tl-based superconductors gave a barrier $U(H, T) \propto (1 - t)^{1.5}/H^{0.71}$ [13]. For YBCO, Zeldov *et al.* reported $U(H, T) \propto (1 - t)^{3/2}/H^{0.95}$ [14], and Chien *et al.* reported $U(H, T) \simeq (1 - t)^{3/2}/H$ [15]. This latter form was observed by Yeshurun and Malozemoff to account for observed ILs [7], but also derived by Tinkham and related to the IL [16]. Our results agree very well with this form, and we also note that our LPLs lying close to the IL have the related [7, 16] power-law form $\sim (1 - t)^{3/2}$.

With the higher value for q , the prefactor f_0 is lower: We find $f_0 \sim 10^{11}$ for the MPMG sample and $f_0 \sim 10^{10}$ for the SC sample. The spreads in $\log f_0$ are ~ 3 (MPMG) and ~ 1 (SC).

In Table 7.2 we summarize our results for the thermal activation fits.

We have also let the exponent q be a *fitting* parameter, and we get very poor results for the pinning barrier vs. field (non-monotonic) and for q itself (varying

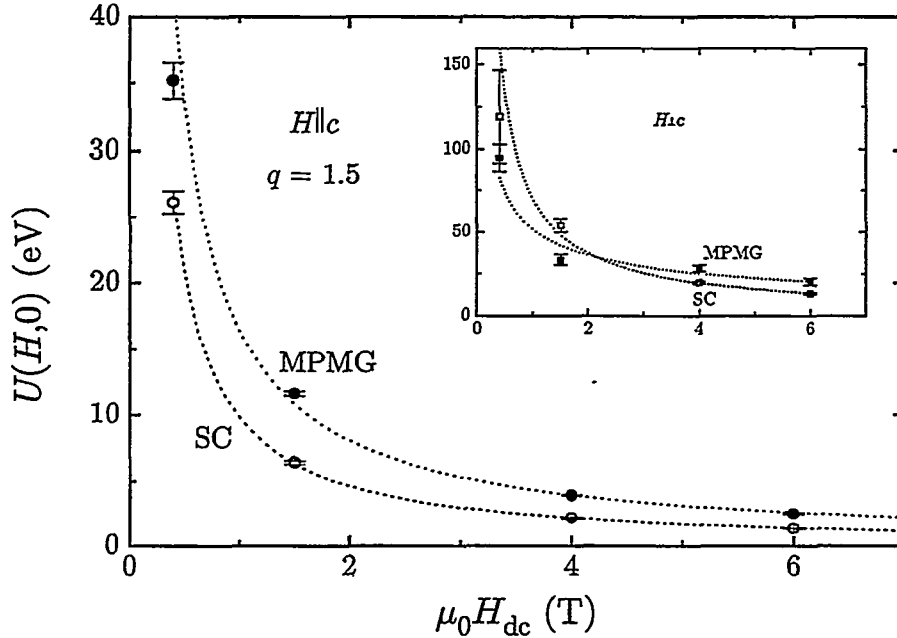


Figure 7.7: Pinning barriers $U(H,0)$ vs. applied field $\mu_0 H_{dc}$ for the MPMG and SC samples for the $\vec{H} \parallel \hat{c}$ orientation. The points are obtained from fits of $\log f(T^*)$ data to the activated form with $q = \frac{3}{2}$ for an amplitude of 0.1 mT. The dotted lines are best fits to the power-law $U(H,0) = U_0 H^{-n}$. See text. The inset show similar data for the $\vec{H} \perp \hat{c}$ orientation.

non-systematically with field, within a factor 2).

The SC data can in general be slightly better fitted than the MPMG data. We must also remember that the temperature windows are quite narrow and different fitting functions can all give fairly good quality fits. Any experimental errors in the determination of the T^* 's, say, will greatly affect the fits since the temperature change is so small from endpoint to endpoint of our experimental curves in Figures 7.3 and 7.4. The prefactor U_0 is larger for $q = \frac{3}{2}$ than for $q = 1$ since the temperature dependent factor is smaller: $(1-t)^{3/2} < (1-t)$ since $t < 1$.

For the $\vec{H} \perp \hat{c}$ orientation good Arrhenius fits are difficult to obtain as the $\log f(1/T^*)$ data show positive curvature while the Arrhenius fits, taking the temperature dependence of the pinning barrier into account, have negative

Table 7.2: Fitting parameters for the thermal activation fits to $f = f_0 e^{-U(H,T)/k_B T}$ using the pinning energy functional $U(H, T) = U_0(1-t)^q/H^\eta$ (H in A/m). Parentheses enclose unreliable fitting parameter values.

Sample	Orient.	$q = 1$			$q = \frac{3}{2}$		
		η	U_0 (eV)	f_0 (Hz)	η	U_0 (eV)	f_0 (Hz)
MPMG	$\vec{H} \parallel \hat{c}$	0.68	4.6	$\sim 10^{14}$	1.0	16	$\sim 10^{11}$
SC	$\vec{H} \parallel \hat{c}$	0.74	3.1	$\sim 10^{13}$	1.1	10	$\sim 10^{10}$
MPMG	$\vec{H} \perp \hat{c}$	(0.27)	(11)	$(\sim 10^{19})$	(0.52)	(52)	$(\sim 10^{12})$
SC	$\vec{H} \perp \hat{c}$	0.61	13	$\sim 10^{16}$	0.92	70	$\sim 10^{12}$

curvature. If we insist on doing the fitting for $q = 1$, say, we do obtain reasonable values for f_0 and $U(H, 0)$ compared to the results for $\vec{H} \parallel \hat{c}$, and for the SC sample $\eta \approx 0.6$ while for the MPMG sample the $U(H, 0)$ fit is very poor and yields $\eta \approx 0.3$. For $q = \frac{3}{2}$ the same is observed with $\eta \approx 0.9$ for the SC sample and $\eta \approx 0.5$ for the MPMG sample. See Figures 7.5 and 7.7 and Table 7.2. Extrapolating $\log f'_0$ vs. $U(H, 0)$ to $U(H, 0) = 0$ in the same way as above for $q = 1$ for $\vec{H} \parallel \hat{c}$ we find $f_0 \sim 10^{15}$ Hz for the SC sample, but $f_0 \sim 10^{27}$ Hz for the MPMG sample. Here, where f'_0 reaches magnitudes greater than 10^{1000} Hz, extrapolating to get something on the order of 10^{10} – 10^{20} Hz from only 4 data points is rather bold. See Figure 7.6.

7.3 Vortex glass

For disordered systems a vortex solid phase with no long-range translational order, the vortex glass (VG), has been proposed [17, 18], and experimental work has lent support [19–23]. In the VG the linear resistivity ρ_{lin} scales as [19]

$$\rho_{\text{lin}} \equiv \frac{E}{j} \sim (T - T_g)^\nu(z+2-D) \quad (7.9)$$

in the scaling regime around the VG transition temperature T_g . Here ν is the exponent with which the coherence length diverges at T_g , z is the dynamical exponent and D is the dimensionality of the system. YBCO is usually considered three dimensional: $D = 3$, which is consistent with the findings of Koch *et al.* [19]. In ac magnetic measurements the loss peak maximum appears for temperatures T^* where the resistivity $\rho(T^*) = \rho^* \propto f$. Now, if we approach

T_g from above, the scaling relation (7.9) tells us that T^* will approach T_g in the limit $f \rightarrow 0$, or

$$f = f_{VG}(T^*/T_g - 1)^{\nu(z-1)} \quad (7.10)$$

where f_{VG} is a proportionality factor and we have set $D = 3$. See also References [8, 18, 20, 24]. If we try to fit (7.10) to our $f(T^*)$ data with both T_g and $\nu(z-1)$ as free parameters (in addition to f_{VG} of course), the results are poor. We can however estimate T_g , or $H(T_g)$, by fitting to (7.10) if we take advantage of published results for the exponents. Koch *et al.* found $\nu(z-1) = 6.5$ for an YBCO thin film with $\vec{H} \parallel \hat{c}$ [19], Seng *et al.* got the same result on another YBCO film and Kötzler *et al.* recently reported 6.4 for a twinned YBCO crystal [25].⁴ If we adopt the value $\nu(z-1) = 6.5$ and perform the fitting to obtain the vortex glass temperature, we get the curves shown in Figure 7.8. The analysis indicate that our LPLs are in the melted phase above the vortex glass phase boundaries, consistent with qualitative arguments in Chapters 8 and 9. If we extrapolate our $f(T^*)$ data down to T_g , we find that we would need to lower the frequency to ~ 0.7 Hz for the MPMG sample and to ~ 2.5 Hz for the SC sample to make the LPLs overlap the estimated $H(T_g)$ lines.⁵ Deak *et al.* extrapolated their observed frequency dependence of the loss peak temperature T^* for an YBCO film and found that the intercept with T_g (determined from transport measurements) occurred for $f \sim 1$ Hz [26], in agreement with our results.

The corresponding fits to the $\vec{H} \perp \hat{c}$ data appear unreliable and will not be discussed. The extrapolation of $T^*(\log f)$ down to the obtained T_g do not at all converge to the same frequency for the MPMG sample; for the SC sample we do in fact find a frequency ~ 1.5 Hz, though it is unreliable.

Fitting the glass lines in Figure 7.8 to a power-law of the form (6.3) for the IL, i.e. $\mu_0 H(T_g) = \mu_0 H_0(1 - T_g/T_c)^n$, we find the prefactors and exponents listed in Table 7.3: the exponents are 1.50 and 1.53 for the MPMG and SC samples, respectively, very similar to the exponents of the LPLs.

Kötzler *et al.* performed scaling of their ac susceptibility data on cylindrical samples carefully converted into linear dynamic conductivity⁶ which they con-

⁴While for films the value $\nu(z-1) \approx 7 \pm 1$ is fairly well established, for crystals the spread is very much larger: $\nu(z-1) \approx 2.1\text{--}8.5$ [25, and references therein].

⁵The estimated frequencies are averages over the values obtained for the different dc fields after linearly extrapolating $T^*(\log f)$ down to the estimated T_g .

⁶From their measured $\chi = \mu - 1$ with μ for an infinite cylinder in the ohmic regime, given by (3.19), they extracted the complex ac penetration depth λ_{ac} and calculated the linear dynamic conductivity $\sigma(\omega) = 1/i\mu_0\omega\lambda_{ac}^2$.

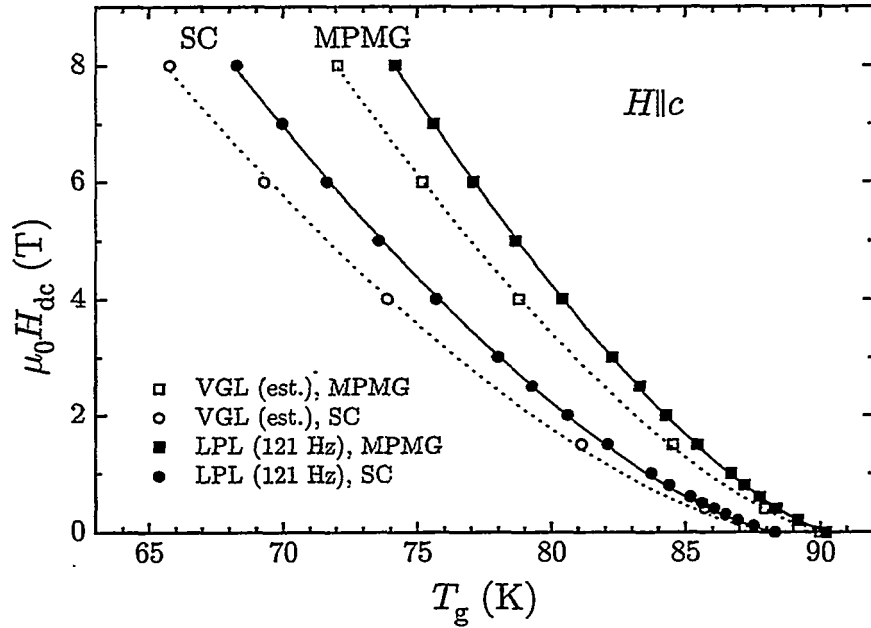


Figure 7.8: Loss peak lines for the MPMG and SC samples at 121 Hz and 0.1 mT for $\vec{H} \parallel \hat{c}$. The dotted lines are the estimated vortex glass phase boundaries obtained from fitting our results for $f(T^*)$ to (7.10) with $\nu(z-1) = 6.5$. The analysis indicates that the LPLs are due to the flux line system being in the melted phase, consistent with qualitative arguments in Chapters 8 and 9.

sequently scaled within a vortex glass picture [25]. In our data the transition (the widths of μ'' are much narrower, about 2 K at high fields) is much narrower than those of the data of Kötzler *et al.* (FWHM \sim 5–20 K at 12 T), and consequently we do not scan temperature ranges wide enough to move from a VG phase at low temperatures to linear (ohmic) response at high temperatures). Also, they use a wider frequency range (6 orders of magnitude: 3 Hz to 3 MHz) than we do (4 orders of magnitude). The fact that our samples have a quite complex cubic geometry compared to their more ideal cylinder shape would also introduce errors when converting our measured $\mu = 1 + \chi$ into σ .

Table 7.3: Fitting parameters from fitting the vortex glass lines in Figure 7.8 to a power-law of the form (6.3): $\mu_0 H(T_g) = \mu_0 H_0(1 - T_g/T_c)^n$. Parentheses enclose unreliable values.

Sample	Orient.	f_{VG} (Hz) ^a	$\mu_0 H_0$ (T)	n
MPMG	$\vec{H} \parallel \hat{c}$	0.67	87	1.50
	$\vec{H} \perp \hat{c}$	— ^b	(1202)	(1.89)
SC	$\vec{H} \parallel \hat{c}$	2.5	63	1.53
	$\vec{H} \perp \hat{c}$	(1.5)	(436)	(1.53)

^aEstimates from extrapolating $T^*(\log f)$ data down to the estimated T_g values.

^bSeveral orders of magnitude difference between estimates for different fields.

7.4 Linear and non-linear behaviour

As shown in Chapter 3, measurements of $\mu(T)$ can provide information about the state of the vortex system. Specifically, in an purely ohmic, or linear, regime the penetration of the perturbing ac signal is governed by the skin effect and for any particular sample $\mu(T)$ depends on the ratio of the resistivity to the frequency only:

$$\mu = \mu(H, \rho(T)/f) . \quad (7.11)$$

Inspired by the experimental work of Civale *et al.* on the amplitude dependence of the ac susceptibility in a Bean critical state where $\mu = \mu(H, h_{ac}/j_c(T))$ [27], we can similarly check whether (7.11) holds.⁷ The procedure is to lay out a grid of horizontal and vertical lines on top of plots of experimental $\mu'(T)$ curves for a set of geometrically spaced frequencies f_1, kf_1, k^2f_1, \dots in such a way that the corners of the resulting rectangles lie on the experimental curves. We illustrate this in Figure 7.9 where we have plotted six simulated curves for an ohmic infinite cylinder using the expression for μ' in (3.19) for six different frequencies assuming that $\log \rho$ drops linearly with decreasing T . Along the horizontal lines

$$\mu'(T) = \text{constant} \Rightarrow \rho(T)/f = \text{constant} ,$$

and along the vertical lines

$$T = \text{constant} \Rightarrow \rho(T) = \text{constant} .$$

⁷Strictly speaking, we can check whether $\mu = \mu(g(T)/f)$ holds, where $g(T)$ is some possibly relevant parameter entering the description of the magnetic state of the superconductor.

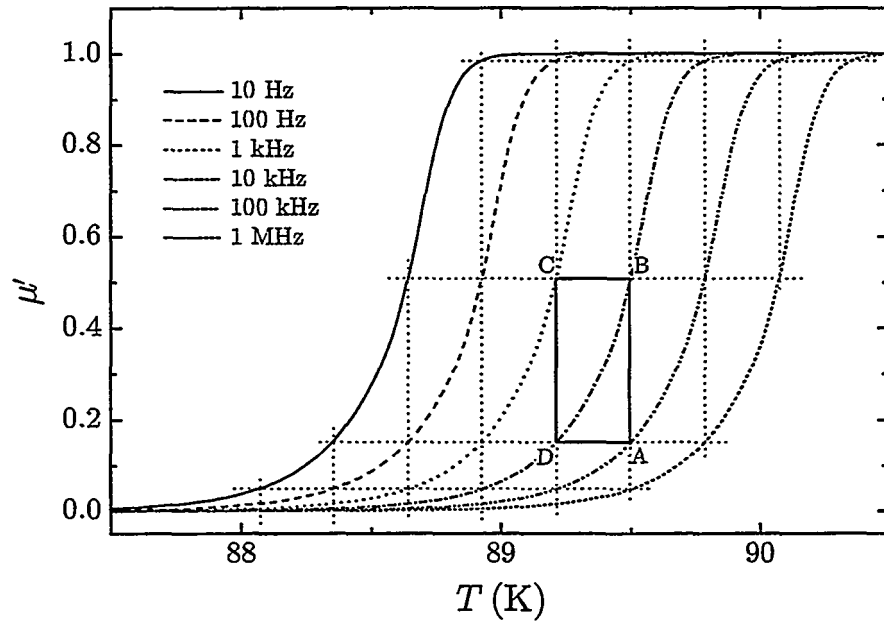


Figure 7.9: Simulated $\mu'(T)$ curves for an ohmic infinite cylinder for six geometrically spaced frequencies based on the exact expression in (3.19) with $\log \rho$ dropping linearly with decreasing T . The cylinder radius is 1 mm. The horizontal and vertical lines make up a grid that has all its grid points fall on top of the $\mu'(T)$ curves, reflecting that μ' depends on the ratio ρ/f . See text for details.

We use $\mu'(T)$ and not $\mu''(T)$ since the former function is monotonic. If all the grid points do fall on the experimental curves, (7.11) holds. Along the horizontal lines AD and BC in Figure 7.9 the ratio ρ/f is constant since μ' is. Along the vertical lines AB and CD ρ is constant since T is. Then $\rho_A = \rho_B$ while $f_A = 10f_B$, and $f_B = 10f_C$ meaning that $\rho_B = 10\rho_C$. At the same time $f_A = 10f_D$ meaning that $\rho_A = 10\rho_D$, and we can combine the relations for the resistivity to find that C and D should lie on the same vertical line, *i.e.* on the same temperature with the same resistivity, which of course they do in the simulation in Figure 7.9. So if on the plots of experimental data we can inscribe rectangles in the above manner, it is a consequence of the fact that μ is determined solely by the ratio ρ/f , which is the case in an ohmic regime, but not necessarily only there.

In Figure 7.10 we plot the measured $\mu'(T)$ at a field of 0.4 T oriented along

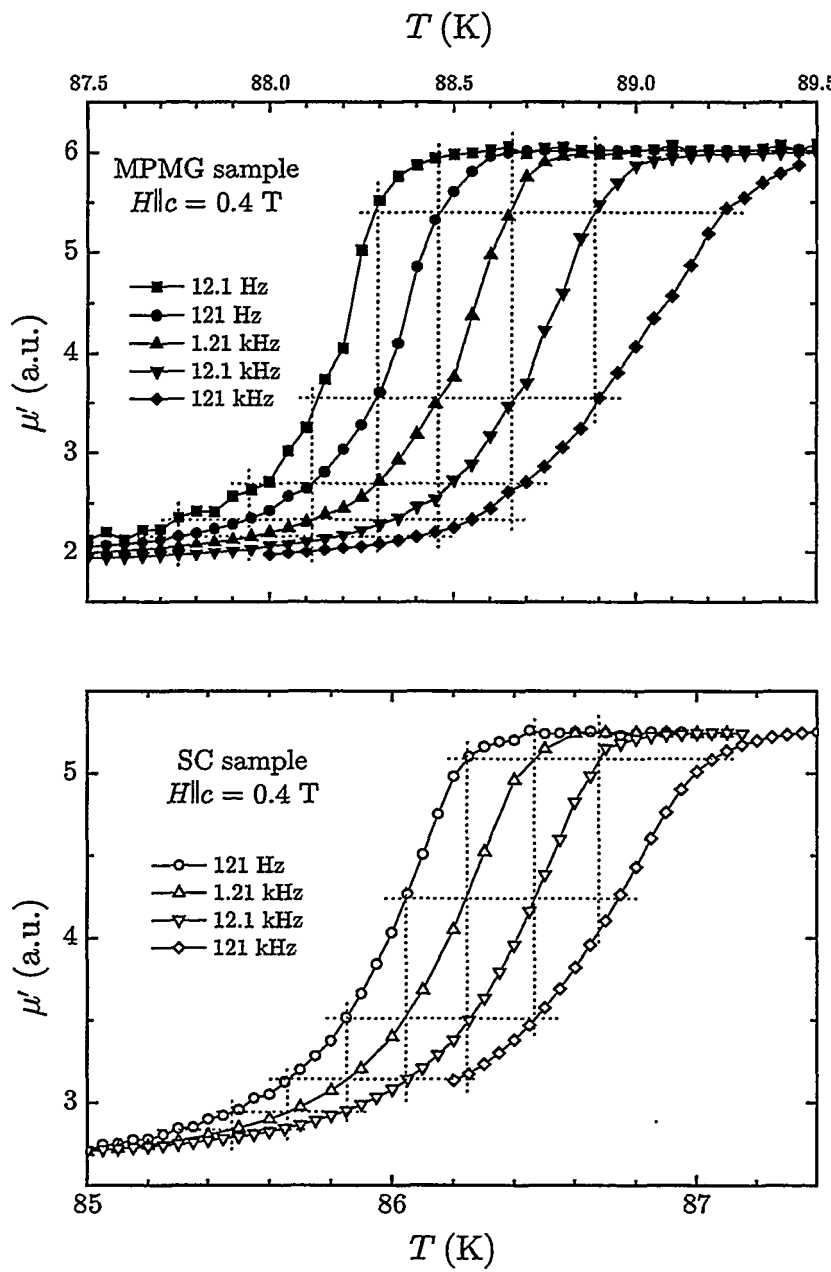


Figure 7.10: $\mu'(T)$ for the MPMG (top) and the SC (bottom) samples in 0.4 T fields oriented along the crystalline c -axes for a number of geometrically spaced frequencies. $\mu_0 h_{ac} = 0.1$ mT. The dotted grids are drawn to see whether the data correspond to ohmic response.

the crystalline c -axis for a number of logarithmically spaced frequencies for the MPMG and SC samples. Grids have been drawn, and we see that the grid points fall nicely on top of the experimental curves, within the experimental resolution. Data taken at 1.5 and 4 T for the MPMG sample (not shown here) also let us inscribe rectangles fairly successfully, though unfortunately the quality at the highest field is not very good and the uncertainty is not negligible. For the SC sample we also find that at the higher field 1.5 T the uncertainty increases and here it is somewhat harder to fit rectangles on the experimental curves. For both samples with $\vec{H} \perp \hat{c}$ all attempts to lay a grid on top of the data fail miserably. For the $\vec{H} \parallel \hat{c}$ orientation the experimental results show that the ac permeability, and hence the ac penetration depth, depends on the ratio ρ/f whereas for the $\vec{H} \perp \hat{c}$ orientation they do not. Although this is consistent with ohmic response for $\vec{H} \parallel \hat{c}$ and a penetration depth given by the skin depth, we stress that this does not rule out non-linear response; see (3.27). See also the analogous analysis at the end of the next Chapter where we discuss the amplitude dependence.

7.5 Summary and conclusions

For both our samples we find strong frequency dependence of the ac magnetic response when $\vec{H} \parallel \hat{c}$. For $\vec{H} \perp \hat{c}$ the dependence is much weaker.

The loss peak temperature is very close to linear in the the logarithm of the applied frequency, indicating thermally activated motion of vortices. Activation barriers of the simple double power-law form

$$U(H, T) \approx U_0 \frac{(1 - T/T_c)^{3/2}}{H}$$

describe our system well for $\vec{H} \parallel \hat{c}$; for $\vec{H} \perp \hat{c}$ the fits are of poorer quality. This form for U has support in the literature. The best fits are obtained for SC sample, where a temperature exponent $q = \frac{3}{2}$ and a field exponent $\eta \approx 1$ is also obtained for $\vec{H} \perp \hat{c}$. This form also agrees with our LPLs lying close to the IL power-law $\propto (1 - t)^{3/2}$, as also seen in the literature. Fitting our $\vec{H} \parallel \hat{c}$ data with $q = 1$ yields $\eta \approx 0.7$ for both samples. These are roughly the exponents for plastic pinning ($\eta = \frac{1}{2}$), which is, however, expected for very anisotropic materials.

Adopting $\nu(z - 1) = 6.5$ we can extrapolate our frequency dependent LPLs down to vortex glass transition lines. For $\vec{H} \parallel \hat{c}$ these would overlap LPLs

measured with excitation field frequencies $f \sim 1$ Hz (an order of magnitude lower than our lowest available frequency). Power-law fits to the estimated VG lines give exponents $n \approx 1.5$ for both samples when $\vec{H} \parallel \hat{c}$. The same procedure gives unreliable results for $\vec{H} \perp \hat{c}$.

Using a grid method on $\mu'(T)$ curves for geometrically spaced frequencies we find that for $\vec{H} \parallel \hat{c}$ for both samples the response has qualities consistent with ohmic (linear) behaviour. This is not true for $\vec{H} \perp \hat{c}$. The response may still be non-linear, however, see the next Chapter.

References

- [1] See for example Y. Iye, Int. J. Mod. Phys. B **3** (1989) 367; Y. Iye, T. Tamegai, T. Sakakibara, T. Goto, N. Miura, H. Takeya and H. Takei, Physica C **153–155** (1988) 26.
- [2] L. Fàbrega, J. Fontcuberta, S. Piñol, C. J. van der Beek and P. H. Kes, Phys. Rev. B **47** (1993) 15250.
- [3] C. J. van der Beek and P. H. Kes, Phys. Rev. B **43** (1991) 13032.
- [4] P. H. Kes, J. Aarts, J. van den Berg, C. J. van der Beek and J. A. Mydosh, Supercond. Sci. Technol. **1** (1989) 242.
- [5] T. T. M. Palstra, B. Batlogg, R. B. van Dover, L. F. Schneemeyer and J. V. Waszczak, Phys. Rev. B **41** (1991) 6621.
- [6] M. Tinkham, *Introduction to Superconductivity*, McGraw-Hill, New York (1975).
- [7] Y. Yeshurun and M. Malozemoff, Phys. Rev. Lett. **60** (1988) 2202.
- [8] Ph. Seng, R. Gross, U. Baier, M. Rupp, D. Koelle, R. P. Huebner, P. Schmitt, G. Saemann-Ischenko and L. Schultz, Physica C **192** (1992) 403.
- [9] L. Krusin-Elbaum, L. Civale, F. Holtzberg and C. Feild, Physica A **200** (1993) 314.
- [10] G. Blatter, M. V. Feigel'man, V. B. Geshkenbein, A. I. Larkin and V. M. Vinokur in *Vortices in high temperature superconductors*, preprint, ETH, Zürich (1993) 538 pages. Rev. Mod. Phys. **66** (1994) 1125.
- [11] V. B. Geshkenbein, M. V. Feigel'man, A. I. Larkin and V. M. Vinokur, Physica C **162–164** (1989) 239.

- [12] V. M. Vinokur, M. V. Feigel'man, V. B. Geshkenbein and A. I. Larkin, Phys. Rev. Lett. **65** (1990) 259.
- [13] D. H. Kim, K. E. Gray, R. T. Kampwirth and D. M. McKay, Phys. Rev. B **42** (1990) 6249.
- [14] E. Zeldov, N. M. Amer, G. Koren, A. Gupta, R. J. Gambino and M. W. McElfresh, Phys. Rev. Lett. **62** (1989) 3093.
- [15] T. R. Chien, T. W. Jing, N. P. Ong and Z. Z. Wang, Phys. Rev. Lett. **66** (1991) 3075.
- [16] M. Tinkham, Phys. Rev. Lett. **61** (1988) 1658.
- [17] M. P. A. Fisher, Phys. Rev. Lett. **62** (1989) 1415.
- [18] D. S. Fisher, M. P. A. Fisher and D. A. Huse, Phys. Rev. B **43** (1991) 130.
- [19] R. H. Koch, V. Foglietti, W. J. Gallagher, G. Koren, A. Gupta and M. P. A. Fisher, Phys. Rev. Lett. **63** (1989) 1511.
- [20] T. K. Worthington, F. H. Holtzberg and C. A. Feild, Cryogenics **30** (1990) 417.
- [21] P. L. Gammel, L. F. Schneemeyer and D. J. Bishop, Phys. Rev. Lett. **66** (1991) 953.
- [22] E. Sandvold and C. Rossel, Physica C **190** (1992) 309.
- [23] H. Safar, P. L. Gammel, D. J. Bishop, D. B. Mitzi and A. Kapitulnik, Phys. Rev. Lett. **68** (1992) 2672.
- [24] P. L. Gammel, J. Appl. Phys. **67** (1990) 4676.
- [25] J. Kötzler, M. Kaufmann, G. Nakielski, R. Behr and W. Assmus, Phys. Rev. Lett. **72** (1994) 2081.
- [26] J. Deak, M. McElfresh, J. R. Clem, Z. Hao, M. Konczykowski, R. Muenchhausen, S. Foltyn and R. Dye, Phys. Rev. B **47** (1993) 8377.
- [27] L. Civale, T. K. Worthington, L. Krusin-Elbaum and F. Holtzberg in *Magnetic Susceptibility of Superconductors and Other Spin Systems*, ed.s R. A. Hein, T. L. Francavilla and D. H. Liebenberg, Plenum Press, New York (1991) page 313.

Amplitude dependence

We will now consider the ac magnetic response when the frequency is kept constant (at 121 Hz). The amplitude effectively controls the current density in the sample, and by varying the amplitude we move about on the *I-V* diagram. Key elements will be the very pronounced anisotropic response, the temperature dependence of the (critical) current density and linear contra non-linear behaviour.

8.1 Loss peak lines

Figure 8.1 shows LPLs for the MPMG and SC samples for different excitation field amplitudes ranging from 0.1 to 3 mT for both field orientations. We immediately see that, contrary to the frequency dependencies of Figure 7.1, the strong amplitude dependence occurs when $\vec{h}_{ac} \perp \hat{c}$ and the weak dependence occurs for $\vec{h}_{ac} \parallel \hat{c}$. The temperature variation at fixed dc field of the LPL is extremely weak, less than 1 K, for variations of 3 mT all the way up to the highest field, 8 T. On the other hand, for $\vec{H} \perp \hat{c}$ the suppression of the loss peak maximum to lower temperatures is very pronounced. At low dc fields and for amplitudes above about 1 mT the LPLs for this orientation exist at lower temperatures than the LPLs for $\vec{H} \parallel \hat{c}$ before they turn up steeply and approach a slope that is basically amplitude independent above 3 T. This latter fact is in contrast to the frequency dependence for $\vec{H} \parallel \hat{c}$ observed in Figures 7.1 and 7.2 where the frequency dependence becomes stronger as the applied dc field increases. We will return to this crossing of the $\vec{H} \perp \hat{c}$ and $\vec{H} \parallel \hat{c}$ LPLs in Section

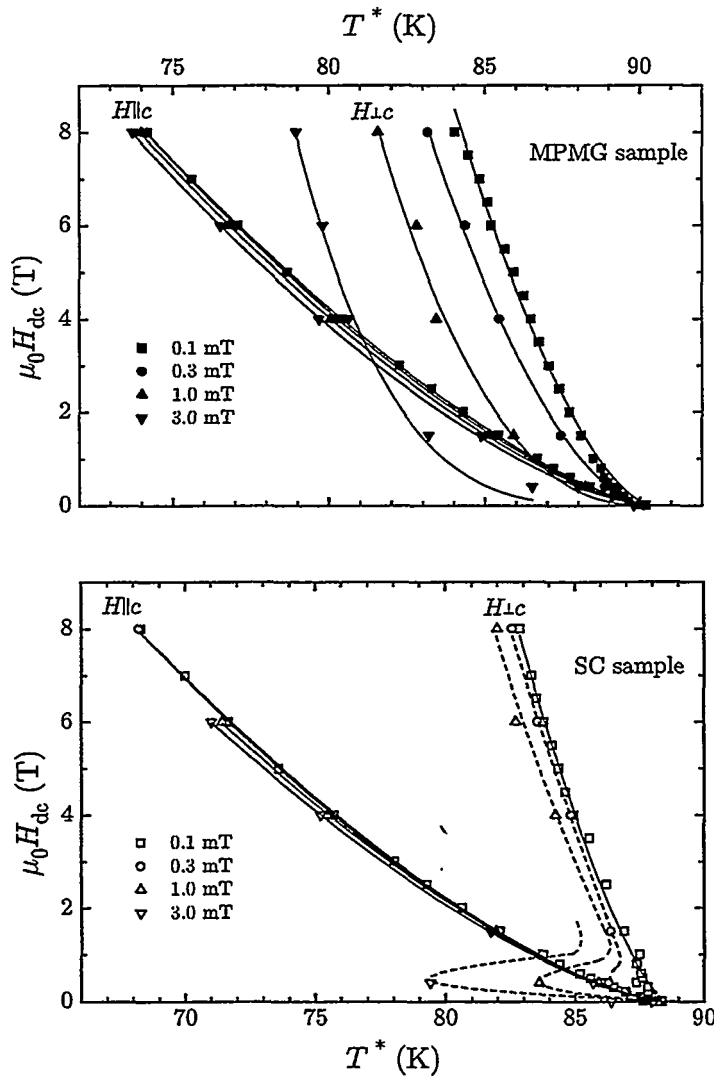


Figure 8.1: Loss peak lines LPLs of the MPMG (top) and the SC (bottom) samples plotted for different excitation field amplitudes for $\vec{H} \parallel \hat{c}$ and $\vec{H} \perp \hat{c}$. The excitation field frequency is 121 Hz. The LPLs move to lower fields and temperatures as the amplitude is increased. This effect is much stronger when $\vec{H} \perp \hat{c}$ than when $\vec{H} \parallel \hat{c}$. The solid lines for $\vec{H} \parallel \hat{c}$ are best fits to the power-law form (6.3), and the details of the fits are listed in Table 8.1 for both samples and both orientations. The solid lines for $\vec{H} \perp \hat{c}$ are to help guide the eye. The low field $\vec{H} \perp \hat{c}$ data points that are seen below the $\vec{H} \parallel \hat{c}$ data for the SC sample and are connected with dashed guiding lines are not spurious. They are the results of an anomalous response observed in the SC sample in this orientation; see Chapter 11.

Table 8.1: Fitting parameters from fitting the loss peak lines in Figure 8.1 to a power-law of the form (6.3): $\mu_0 H(T^*) = \mu_0 H_0(1 - T^*/T_c)^n$. $f = 121\text{ Hz}$.

Sample	$\mu_0 h_{ac}$ (mT)	$\vec{H} \parallel \hat{c}$		$\vec{H} \perp \hat{c}$	
		$\mu_0 H_0$ (T)	n	$\mu_0 H_0$ (T)	n
MPMG	0.1	91	1.42	648	1.63
	0.3	97	1.42	824	1.83
	1.0	101	1.40	2719	2.50
	3.0	108	1.41	23873	3.87
	Average: ^a	94	1.41	706	1.75
SC	0.1	70	1.47	401	1.43
	0.3	72	1.50	—	—
	1.0	67	1.47	—	—
	3.0	66	1.48	—	—
	Average: ^a	69	1.48	401	1.43
Y12	0.1	121	1.50	—	—

^aWeighted with respect to the least square errors for the individual fits.

8.3. In Table 8.1 we list fitting parameters for the LPLs.

Figures 7.1 and 8.1 illustrate the basic differences in the frequency and amplitude responses for the $\vec{H} \parallel \hat{c}$ and $\vec{H} \perp \hat{c}$ orientations, respectively. The amplitude dependence is much stronger, whereas the frequency dependence is much weaker, for $\vec{H} \perp \hat{c}$ than for $\vec{H} \parallel \hat{c}$. Recalling the discussion in Chapter 3 on the extremes, linear (ohmic) and non-linear responses, we could then say from the two Figures that the loss peaks occur in an ohmic-like regime for the $\vec{H} \parallel \hat{c}$ orientation, and closer to a non-linear regime (a vortex glass state, for example) for the $\vec{H} \perp \hat{c}$ orientation. The extreme variation of the fitting parameters with amplitude for the MPMG sample in the $\vec{H} \perp \hat{c}$ orientation implies that a description in terms of an IL does not apply for the higher amplitudes (*i.e.* current densities). We discuss this further in Subsection 10.4.3.

8.2 Anisotropic ac response

To see why we observe such contrasting frequency/amplitude dependencies for the two orthogonal field orientations we must first consider the ac response of

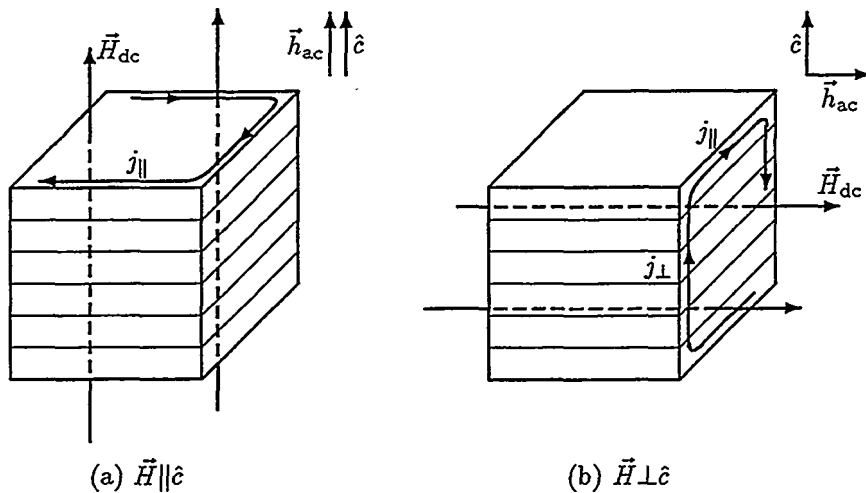
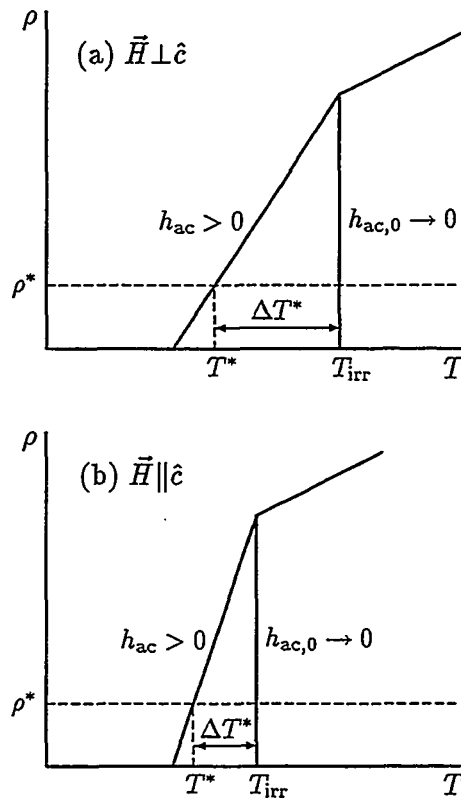


Figure 8.2: Schematic diagrams of the flux lines and the screening currents when the applied field is (a) parallel and (b) perpendicular to the crystalline c -axis. The CuO_2 planes are drawn with thin lines. In (a) the screening currents j_{\parallel} flow primarily in the CuO_2 planes. In (b) the screening currents have two components: j_{\parallel} flow *in* the CuO_2 planes and j_{\perp} flow *across* the CuO_2 planes.

the sample. We will use Figure 8.2 as a guide. For $\vec{H} \parallel \hat{c}$, see Figure 8.2 (a), the flux lines respond via the Lorentz force to the induced screening currents j_{\parallel} which circulate in the ab -planes. Thus the flux lines will tend to move toward the center of the sample when the ac currents are flowing clockwise looking down on the c direction and out towards the edges when the ac currents change direction. The effect of the dc screening currents is to direct the flux lines toward the interior of the sample. For $\vec{H} \perp \hat{c}$, as illustrated in Figure 8.2 (b), the screening currents have two components, one *parallel* to the ab -planes, j_{\parallel} , and one flowing *across* the ab -planes in the c direction, j_{\perp} . However, since this is the situation of strong intrinsic pinning proposed by Tachiki and Takahashi [1] and observed by Kwok *et al.* [2], the component j_{\parallel} produces rather weak flux line motion. On the other hand, the component j_{\perp} acts to slide the vortices parallel to the CuO_2 planes, in regions where the superconducting order parameter is reduced, meeting little resistance from pinning centers. This clearly is the weakest pinning situation of the three; vortex motion across the CuO_2 planes is strongly inhibited by the intrinsic pinning, sideways motion in the ab -planes is subject to intermediate (in this context) pinning, and the latter sliding between CuO_2 planes is the easiest motion. The field penetration is controlled by the less pinned vortices. Consequently, for a given amplitude h_{ac} , for $\vec{H} \perp \hat{c}$ the dissipation, measured by the shift in the resistivity $\Delta\rho = \rho(h_{\text{ac}}, T) - \rho(h_{\text{ac}} \rightarrow$

Figure 8.3: Schematics of the resistivity *vs.* temperature, $\rho(T)$, around T_{irr} for (a) $\vec{H} \perp \hat{c}$ and (b) $\vec{H} \parallel \hat{c}$ based on the idealization of Figure 3.5. Since the ac dissipation is largest in the former orientation (due to vortices sliding easily in and out in the regions of reduced superconducting order parameter between the CuO₂ layers; see text), we have that $\Delta\rho = \rho(h_{\text{ac}}, T) - \rho(h_{\text{ac}} \rightarrow 0, T)$ is larger, i.e. $\rho(T)$ drops slower below T_{irr} for $\vec{H} \perp \hat{c}$ than for $\vec{H} \parallel \hat{c}$. This means that for the same value of the resistivity at the loss peak maximum, $\rho(T^*) = \rho^* = \frac{1}{2}\pi\mu_0 f a^2$, i.e. for fixed frequency f and sample size a , T^* exists further below T_{irr} for $\vec{H} \perp \hat{c}$ than for $\vec{H} \parallel \hat{c}$. For our cubic samples we will consequently always be deeper into the non-linear regime for $\vec{H} \perp \hat{c}$ than for $\vec{H} \parallel \hat{c}$.



$0, T$), will be greater than the corresponding dissipation or resistivity shift for $\vec{H} \parallel \hat{c}$, or in other words, the resistivity below T_{irr} drops slower for $\vec{H} \perp \hat{c}$ than for $\vec{H} \parallel \hat{c}$. We illustrate this with the schematic $\rho(T)$ curves in Figure 8.3. For given frequency, amplitude and sample size, we see that we will then always be further into the non-linear regime — in the sense that T^* will occur at a much lower temperature below T_{irr} — for $\vec{H} \perp \hat{c}$ than for $\vec{H} \parallel \hat{c}$ (compare ΔT^* for the two orientations in Figure 8.3). This is because the value of the resistivity ρ^* that determines the peak position in μ'' is essentially fixed: the sample is cubic with the relevant size for penetration, a , nearly the same for both orientations, and $\rho^* = \frac{1}{2}\pi\mu_0 f a^2$. This in turn implies that we can expect more non-linear behaviour for the $\vec{H} \perp \hat{c}$ orientation since the further below T_{irr} the system is, the more non-linear is its behaviour [3–7].

To see more clearly the non-linearity observed in Figure 8.1, we plot the amplitude, h_{ac} , *vs.* the temperature position of the loss peak maximum, T^* , for different applied dc fields for both orientations and samples in Figure 8.4. The

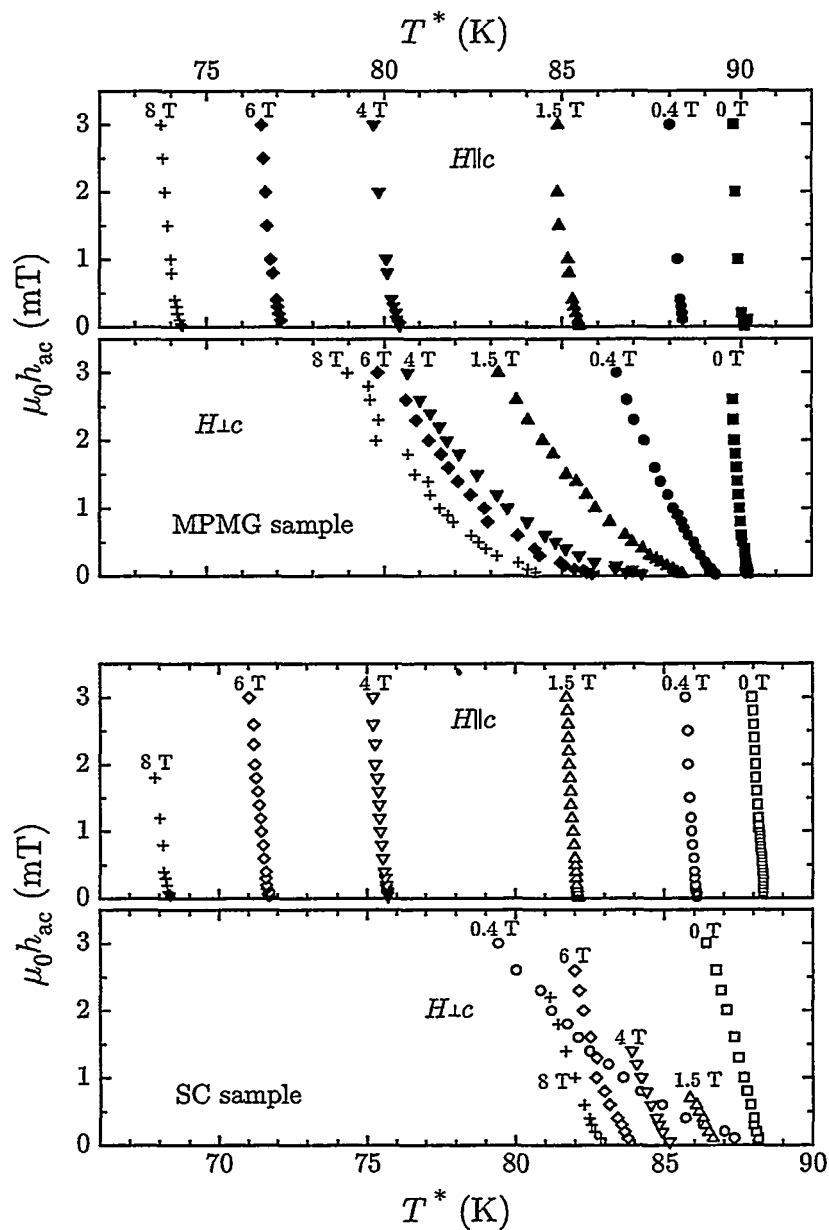
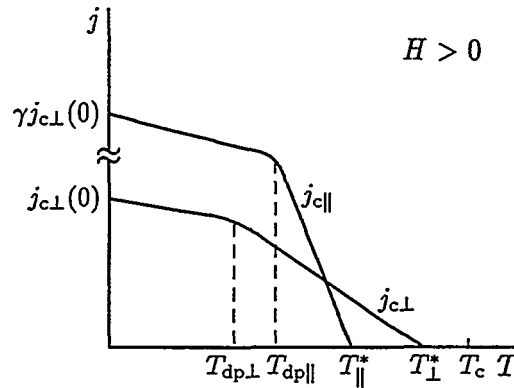


Figure 8.4: Amplitude *vs.* loss peak temperature for the MPMG (top) and SC (bottom) samples for a number of dc fields $\vec{H} \perp \hat{c}$ and $\vec{H} \parallel \hat{c}$. Note the strong non-linearity for $\vec{H} \perp \hat{c}$ whereas for $\vec{H} \parallel \hat{c}$ the loss peak temperature is practically insensitive to the magnitude of the amplitude. The frequency is 121 Hz. Note the anomalous behaviour of the $\vec{H} \perp \hat{c}$ 0.4 T curve for the SC sample; see Chapter 11.

Figure 8.5: Idealization of the temperature dependence of the anisotropic critical currents, $j_{c\parallel}(T)$ flowing in the CuO_2 planes and $j_{c\perp}(T)$ flowing across the CuO_2 planes along the c -axis. From our work we know that $j_{c\perp} > j_{c\parallel}$ at the high temperatures closer to T_c , and simple physical arguments (see text) tell us that at low temperatures $j_{c\parallel} = \gamma j_{c\perp}$.



two different regimes of amplitude dependence are apparent: (i) with $\vec{H} \perp \hat{c}$ there is a very strong amplitude dependence; T^* is extremely sensitive to the value of the amplitude; (ii) with $\vec{H} \parallel \hat{c}$ on the other hand, the situation is quite different in that T^* is practically insensitive to changes in the amplitude. These dependencies look very much as expected if for $\vec{H} \perp \hat{c}$ the peak, i.e. the penetration, occurs below T_{irr} , and for $\vec{H} \parallel \hat{c}$ it occurs near to, but above T_{irr} . The two cases are so different that two quite different regimes seem to be present in our data. The behaviour is consistent with a solid-liquid vortex picture.

8.3 Anisotropic depinned region and intersecting loss peak lines

We would now like to present a possible explanation of the intersection of the $\vec{H} \parallel \hat{c}$ and $\vec{H} \perp \hat{c}$ LPLs in Figure 8.1. As we can see, for relatively small dc fields below about 2–3 T, the LPLs for $\vec{H} \perp \hat{c}$ produced by excitation field amplitudes greater than 1 mT are found below those for $\vec{H} \parallel \hat{c}$. At higher dc fields the LPLs turn up and cross the $\vec{H} \parallel \hat{c}$. We explain this with the aid of the schematic $j_c(T)$ diagram for a finite dc field in Figure 8.5. Note that in the notation used here, \parallel and \perp refer to the direction of the field relative to the c -axis in temperature subscripts, but to the direction of the (related) currents relative to the CuO_2 planes in subscripts to current densities, penetration depths and coherence lengths. The loss peak maximum occurs at a temperature T^* in the range $T_{\text{dp}} < T^* < T_{\text{irr}}$ where the depinning temperature T_{dp} marks the

onset of the sharp drop of the critical current with temperature. Calculation¹ shows that $T_{dp\perp} < T_{dp\parallel}$. From this work, for small excitation field amplitudes, we know that $T_{\parallel}^* < T_{\perp}^*$ or $T_{irr\parallel} < T_{irr\perp}$. Thus the depinned region is much more extended in temperature for $\vec{H} \perp \hat{c}$ than for $\vec{H} \parallel \hat{c}$. For $T < T_{dp}$ it can be shown² that $j_{c\parallel} = \gamma j_{c\perp}$, where the anisotropy ratio $\gamma = 1/\varepsilon > 1$ measures the anisotropy. Consequently, the curves $j_{c\parallel}(T)$ and $j_{c\perp}(T)$ must intersect. Since in the non-linear regime T^* is determined by the relation $j(T) \approx h_{ac}/a$, the intersection will occur for some value of the amplitude h_{ac} . This does not happen at much higher fields because the LPL, and the IL, drops much faster in field for $\vec{H} \parallel \hat{c}$ than for $\vec{H} \perp \hat{c}$.

8.4 Temperature dependence of the current density

In a non-linear regime, the ac penetration follows a Bean critical state model with a penetration depth $L_B = h_{ac}/j(H, T, f)$. Here, the frequency dependent current density $j(f)$ plays the role of j_c . At high enough frequencies,³ activated jumps of vortices between pinning potential wells can be neglected and $j(H, T, f) \rightarrow j_c$, while the ac penetration depth λ_{ac} equals the Campbell penetration depth $\lambda_C = (B^2 \langle \alpha_L^{-1} \rangle / \mu_0)^{-1/2}$, which is real [10]. We however operate at more moderate frequencies and expect the induced currents $j(H, T, f)$ not to reach j_c . Others have defined j as a frequency dependent critical current

¹Thermal depinning sets in when the rms thermal displacement reaches values comparable to the coherence length: $\langle u^2(T_{dp}) \rangle_{\text{thermal}} \simeq \xi^2$, where $\langle u^2(T) \rangle_{\text{thermal}} \propto T$ [8, Table XIII]. Since $\xi_{\perp} = \gamma \xi_{\parallel}$, we then have that $T_{dp\perp} < T_{dp\parallel}$.

²One way to see this is by noting that the depairing critical current density is related to the penetration depth λ by $j_c \approx H_c/\lambda$ where H_c is the thermodynamic critical field [8]. Estimates for YBCO give depairing critical current densities of about $2 \times 10^{12} \text{ A/m}^2$ [9, Subsection 9.2.3]. Since H_c is orientationally independent then for an anisotropic superconductor the current which flows across the CuO₂ planes is given by $j_{\perp} \propto H_c/\lambda_{\perp}$ where λ_{\perp} is the penetration depth due to the shielding currents perpendicular to the CuO₂ planes. For currents parallel to the planes, the relation is similarly $j_{\parallel} \propto H_c/\lambda_{\parallel}$ where in this case λ_{\parallel} is the penetration depth perpendicular to the *c*-axis but for an applied field parallel to the *c*-axis. Since the anisotropy parameter $\gamma = \lambda_{\perp}/\lambda_{\parallel}$, then $j_{c\parallel} = \gamma j_{c\perp}$. In a private communication, V. M. Vinokur obtaines an identical result for the critical current densities in the framework of a single vortex collective pinning model. See also Reference [8, Subsection II.C.2] for a derivation for collective pinning.

³I.e. in the Campbell regime: $f \lesssim f_0$, where the “pinning frequency” $f_0 = \omega_0/2\pi$, above which pinning is irrelevant. Here $\omega_0 = \langle \alpha_L \rangle / \eta$ depends on the Labusch parameter α_L and the viscous drag coefficient η [10].

density [11, 12], but we prefer to think of it simply as a shielding current that can attain a maximum value equal to j_c (if thermally activated motion of vortices is negligible), in line with the terminology used by van der Beek *et al.* in their work on linear and non-linear ac magnetic response [10]. However, the functional form of j should be quite similar to that of j_c , different by only an approximately constant, though still frequency dependent of course, factor when the relevant pinning or activation barriers do not vary too dramatically with temperature, see Reference [10]. This would be especially true in the limited temperature range in which we operate.

8.4.1 Extracting current density from ac permeability

Since the ac permeability μ is given solely by the ratio $u = L_B/a$, see (3.25), where a is the relevant sample size, we can extract $j(H, T, f)$ from our measured $\mu(H, T, f)$ data. Fixing L_B for a given sample size, *i.e.* fixing the ratio $h_{ac}/j(H, T, f)$, we are at a fixed level $\mu' = m$. Then reading off the temperatures where $\mu' = m$ for a number of amplitudes h_{ac} we get the temperature dependence of $j(H, T, f)$. The absolute value of $j(H, T, f)$ will depend on the functional form of $\mu'(u)$, but a first estimate can be obtained by assuming *e.g.* that $u = 1$ for $\mu' = 1/2$ (half screening), as done in Reference [13], roughly equivalent of assuming that the maximum in μ'' occurs when the flux front reaches the center of the sample, leading to $j(H, T, f) = h_{ac}/a$. This latter identity is exactly the result when the sample is an infinite slab, cf. (3.9a); for an infinite cylinder the identity should read $j(H, T, f) = h_{ac}/au_{1/2}$, where $u_{1/2} = \frac{8}{5} - \frac{2}{5}\sqrt{6} \approx 0.62$, cf. (3.10a). A wider temperature range for the current density can be obtained by making use of more m values spanning the widest possible range, as suggested by Fàbrega *et al.* [14].

The very pronounced amplitude dependence of our LPLs in Figure 8.1 for the $\vec{H} \perp \hat{c}$ orientation is a signature of non-linear behaviour. In Figure 8.6 we plot the amplitudes $\mu_0 h_{ac,m}$ of the experimental $\mu'(T)$ curves *vs.* the temperatures where $\mu'(T) = m$ for a set of m values for the MPMG sample in a field of 0.4 T applied perpendicular to the c -axis. For the intermediate and higher m values a power-law

$$h_{ac,m}(T) = h_{0,m}(1 - T/T_{0,m})^{n_j} \quad (8.1)$$

with exponent $n_j = \frac{3}{2}$ fits the curves well. This power-law form for the temperature dependence of the current density agrees with the result for j_c from standard mean-field interrelations, $j_c \propto H_c/\lambda \propto H_c^2 \xi \propto (1 - t)^{3/2}$. This again

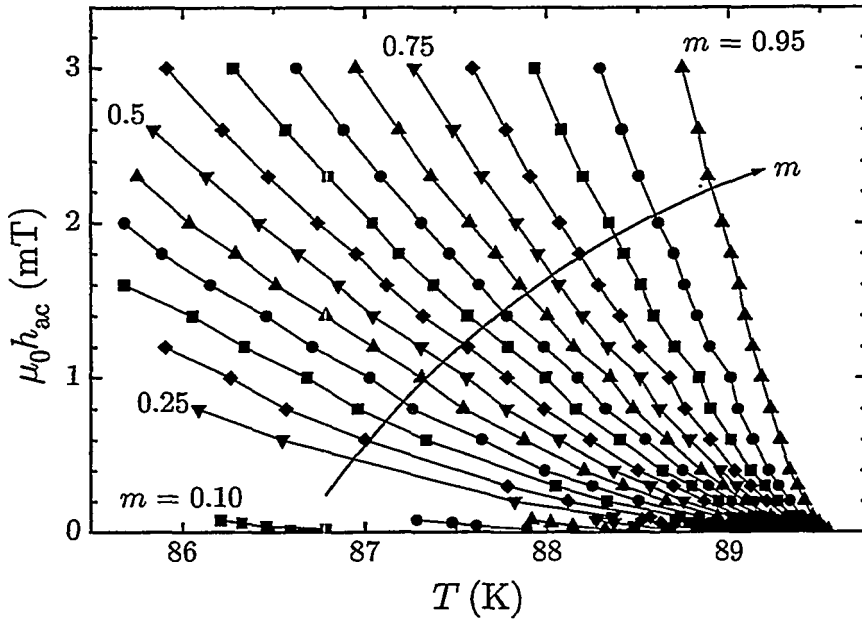


Figure 8.6: The ac field amplitude *vs.* the temperature where $\mu'(T) = m$ for a number of m values for the MPMG sample in a dc field of 0.4 T applied perpendicular to the *c*-axis.

is related to the thermal activation energy $U \propto (1 - t)^{3/2}/H$ to account for the IL in the early work of Yeshurun and Malozemoff [15]. See also Section 7.2.

Forcing the power-law with the exponent $\frac{3}{2}$ for all m and leaving $T_{0,m}$ as a fitting parameter, we get a nice data collapse when scaling $h_{ac,m}(T)$ against $h_{0,m}$. If we fix $T_{0,m}$ to some constant value, which is sensible since we aim to find a unique $j(H, T, f)$ curve, the scaling degrades, especially for the $m < 0.35$ data. See Figure 8.7 where we plot the estimated current density

$$j(H, T, f) \approx \frac{h_{0,m=1/2}}{au_{1/2}} \frac{h_{ac,m}(T)}{h_{0,m}} = \frac{h_{0,m=1/2}}{au_{1/2}} (1 - T/T_{0,m})^{n_j} \quad (8.2)$$

where $u_{1/2}$ is given by $\mu'(u_{1/2}) = \frac{1}{2}$ and $T_{0,m}$ should not depend on m . We find a current density $j(T) = j_0(1 - T/T_{0,m})^{n_j}$ with $j_0 = 0.52 \times 10^9 \text{ A/m}^2$ for the fixed parameter values $T_{0,m} = 89.55 \text{ K}$ and $n_j = \frac{3}{2}$ at 0.4 T and 121 Hz.

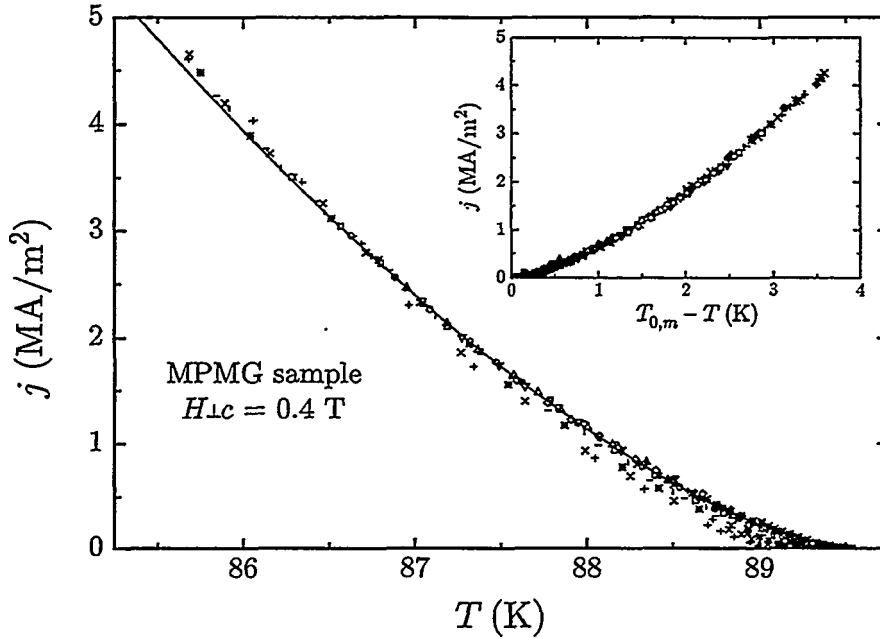


Figure 8.7: Estimated current density $j(H, T, f)$ from (8.2) based on fits to (8.1) using $T_{0,m} = 89.55$ K, corresponding to the onset of shielding, and $n_j = \frac{3}{2}$, for the MPMG sample in a 0.4 T field oriented perpendicular to the c -axis. We approximate our cubic sample as a cylinder ($u_{1/2} = 0.62$). m ranges from 0.35 to 0.95 in steps of 0.05. The experimental frequency is 121 Hz. The solid line is the extracted power-law current density $j(T) = j_0(1 - T/T_{0,m})^{n_j}$ with $j_0 = 0.52 \times 10^9$ A/m² and $T_{0,m}$ and n_j given above. The same scaling is shown in the inset but with $T_{0,m}$ as a fitting parameter, and also including data for m from 0.10 to 0.30. See text for details.

8.4.2 Discussion

If we extrapolate to lower temperatures using this result, we can make comparisons to the j_c values reported by Wacenovsky *et al.* for a very similar MPMG sample [16]. We find our extrapolated $j(T)$ to be a factor 2–3 lower than their j_c values. However, they obtained j_c by an ac inductive method at low frequencies (9 Hz), so that they could be reporting shielding current densities $j < j_c$ (see above), which would support our assumption that the induced shielding currents never reach the critical current at the relatively low frequencies we work at.

Transport measurements of j_c^{ab} (in the ab -plane) on MPMG samples for $\vec{H} \perp \hat{c}$ give the value $j_c \approx 2 \times 10^8 \text{ A/m}^2$ at 77 K and 1 T [9, Subsection 9.3.2], a factor ~ 10 larger than estimated by our extrapolation (after correcting for the field difference using the data in Reference [16]), but here we expect a rather large difference since our ac magnetic measurements probe the current density along the c -axis, j_c^c , and $j_c^c \simeq \gamma j_c^{ab}$ [8, Subsection II.C.2] where γ is the anisotropy ratio (see Table 2.1). Thus the difference is more a factor ~ 2 , not ~ 10 .

The results for the current density at 121 Hz in Figure 8.7 agree nicely with the results of Gömöry and Takács [11]. They presented $j_c(T)$ obtained from ac susceptibility measurements on a melt-grown YBCO sample with a cross section, perpendicular to the applied field of 0.5 T, of $1.1 \times 2 \text{ mm}^2$, *i.e.* slightly larger than for our MPMG sample. Superimposing our extracted $j(T)$ onto their data, we find our data, for 121 Hz, to lie inbetween their data for 40 and 123 Hz, which is reasonable due to the difference in sample size. Since we are at a lower field (0.4 T), our $j(T)$ values, and hence frequencies, are however shifted slightly up compared to what they would have been at their field (0.5 T). They find power-law exponents n_j ranging from 1.25 to 2 for frequencies from 2 to 1230 Hz, respectively.

By forcing [17] their curves for different m values onto a unique curve, Fàbrega *et al.* got a nice data collapse for $j_c(T)$ using the above procedure [14]. When extracting $m(L_B/a)$ for their rectangular ($1.90 \times 0.95 \text{ mm}^2$) $\text{Pr}_{1.85}\text{Ce}_{0.15}\text{CuO}_{4-y}$ single crystal sample and comparing to the analytical expression $\mu'(u)$ for an infinite cylinder, they also observed deviations near complete screening, *i.e.* for $m \lesssim 0.3$, and attributed it to finite size or shape effects. The reason they did not see this deviation in their scaled $j_c(f, T, H)$ curve could be that they did not use low- m cuts; they plotted much fewer points than we have in our Figure 8.7 for 18 values of m ranging from 0.10 to 0.95. In Figure 8.8 we compare the experimental $m(u)$ from our data on the MPMG sample to the analytical $\mu'(u)$ for an infinite cylinder. The data are in fair agreement with the theoretical curves. The same comparison, but for an infinite slab, is shown in the inset, with slightly poorer agreement.⁴

⁴Measured by the average difference between the data and the calculated curve, which is 0.006 ± 0.06 for the infinite cylinder case and -0.02 ± 0.08 for the infinite slab case, the latter represents the slightly poorer agreement between data and calculation.

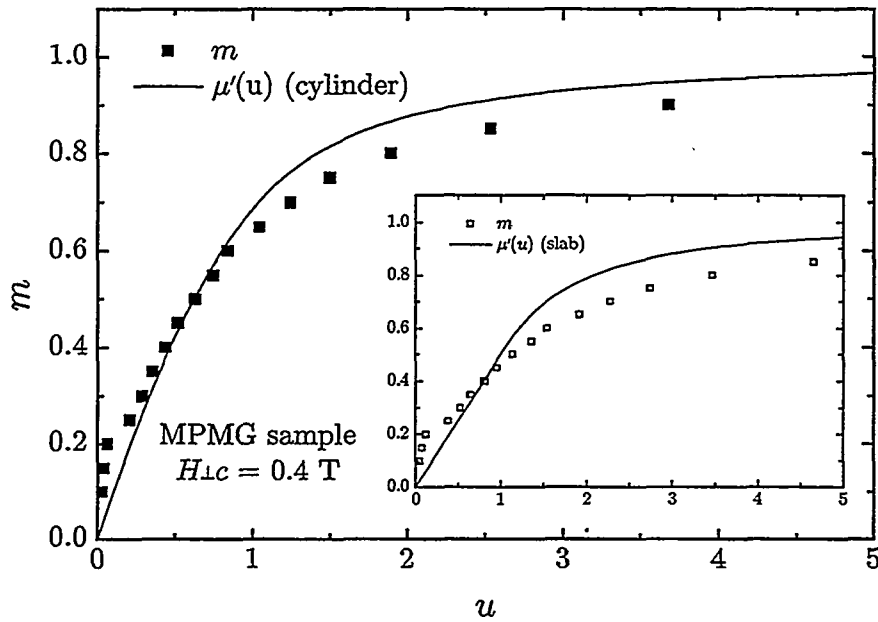


Figure 8.8: m vs. the relative penetration depth $u = L_B/a$ for the MPMG sample in a 0.4 T field $\vec{H} \perp \hat{c}$. Here $a \approx 0.75$ mm is the radius of a cylinder with the same cross section as our cubic MPMG sample. The solid line is the calculated $\mu'(u)$ for an infinite cylinder in a Bean critical state, see (3.10a) and (3.10b). The inset shows the same, but for an infinite slab with thickness $2a = 1.32$ mm, see (3.10a) and (3.10b).

8.5 Linear and non-linear behaviour

At a fixed dc field in a strongly non-linear regime, the ac permeability depends on the ratio of the excitation field amplitude h_{ac} to the shielding current $j(T)$ or $j_c(T)$ only:

$$\mu = \mu(H, h_{ac}/j(T)) \quad . \quad (8.3)$$

We can perform an analysis similar to the one described for the ohmic case in Section 7.4 above, first implemented by Civale *et al.* [13]. Now, the amplitude is the key parameter, not the frequency as in the ohmic case. Plotting $\mu'(T)$ for a set of geometrically spaced amplitudes $h_{ac,1}, kh_{ac,1}, k^2h_{ac,1}, \dots$ we lay out a grid that should have its grid points fall on top of the $\mu'(T)$ curves if (8.3) is valid. In Figure 8.9 we plot five calculated curves for a non-linear infinite cylinder using the expressions in (3.10a) and (3.10b) for five geometrically

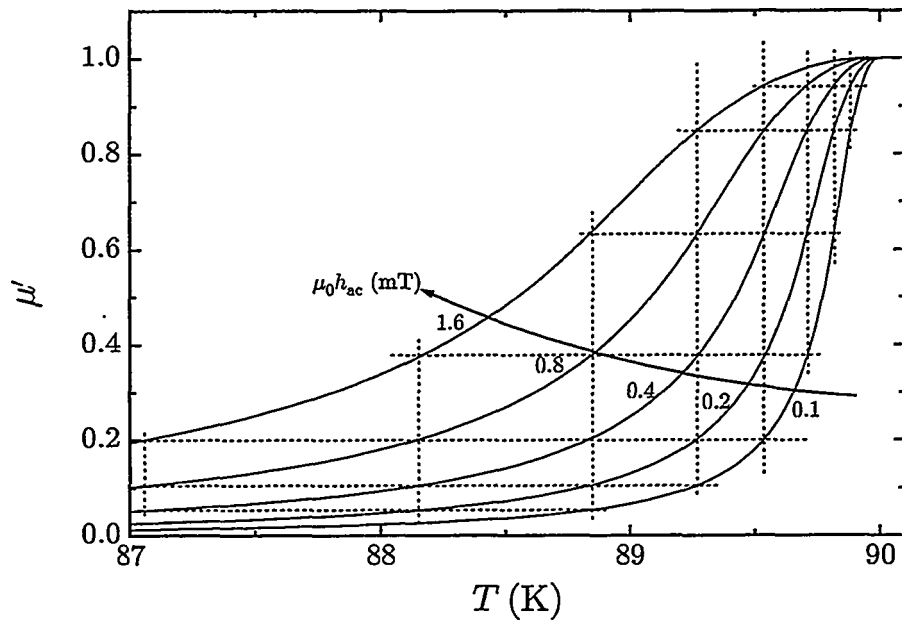


Figure 8.9: Calculated $\mu'(T)$ curves for an infinite cylinder in a non-linear (Bean critical state like) regime for five geometrically spaced amplitudes based on the exact expressions in (3.10a) and (3.10b). Here, $j(T) = j_0(1-T/T_c)^{n_j}$ with parameter values $j_0 = 10^9 \text{ A/m}^2$, $T_c = 90 \text{ K}$ and $n_j = \frac{3}{2}$. The cylinder radius $a = 1 \text{ mm}$. The horizontal and vertical dotted lines make up a grid that has all its grid points fall on top of the $\mu'(T)$ curves, reflecting that μ' depends only on the ratio h_{ac}/j .

spaced amplitudes assuming a current density similar to the power-law we found above. Along the horizontal lines

$$\mu'(T) = \text{constant} \Rightarrow h_{ac}/j(T) = \text{constant} ,$$

and along the vertical lines

$$T = \text{constant} \Rightarrow j(T) = \text{constant} .$$

We can use a discussion similar to the one for the rectangle ABCD in Figure 7.9, replacing f with h_{ac} , ρ with j and 10 with 1/2. For (8.3) to hold, we should be able to inscribe rectangles with corners falling on top of the experimental $\mu'(T)$ curves.

8.5.1 Field parallel to the *ab*-plane

In Figure 8.10 we plot measured $\mu'(T)$ curves for five different amplitudes spaced by integer factors of 2 for the MPMG sample in fields 0.4 and 4 T applied perpendicular to the crystalline *c*-axis. The corresponding data at 0.4 T for the SC sample are “contaminated” by the anomaly (see the discussion of the raw data in Chapter 5, and Chapter 11) and will not be discussed. For the lower field of 0.4 T the grid points fall nicely on top of the data, within the experimental noise, except for deviations towards the low temperature end for the largest amplitude (1.6 mT). This deviation could possibly be a result of being close to crossing over into a linear flux flow regime for the highest driving amplitude/shielding current, see Reference [10]. Such a crossover is dynamic and smooth [10]. However, according to the work of van der Beek *et al.*, the crossover from linear, at low amplitudes, to non-linear response in the vortex glass state typically occurs for amplitudes on the order of 0.1–1 mT, and the crossover from non-linear to flux flow linear response, at high amplitudes, occurs at amplitudes 2–3 orders of magnitude above those again [10]. From this it would appear unlikely that we are close to the flux flow regime with shielding currents on the order of or above the critical current. For our orientation of the field, with the flux lines sliding relatively easily between the CuO₂ planes, a flux flow scenario is in general not very unreasonable.

8.5.2 Field along the *c*-axis

A similar analysis for the MPMG sample for $\vec{H} \parallel \hat{c}$ is difficult to perform since unfortunately we have few suitable data sets. Nevertheless, the three curves we do have allow inscription of rectangles if we do reasonable corrections for noise. For the SC sample we can also have the grid points fall nicely on top of the experimental curves, but again apart from for the highest amplitude, see Figure 8.11. We have previously found that for both samples and for this $\vec{H} \parallel \hat{c}$ orientation the experiments are consistent with ohmic behaviour, see the end of the previous Chapter. We must therefore be in a regime with a response intermediate between linear and non-linear. See also the following Chapter.

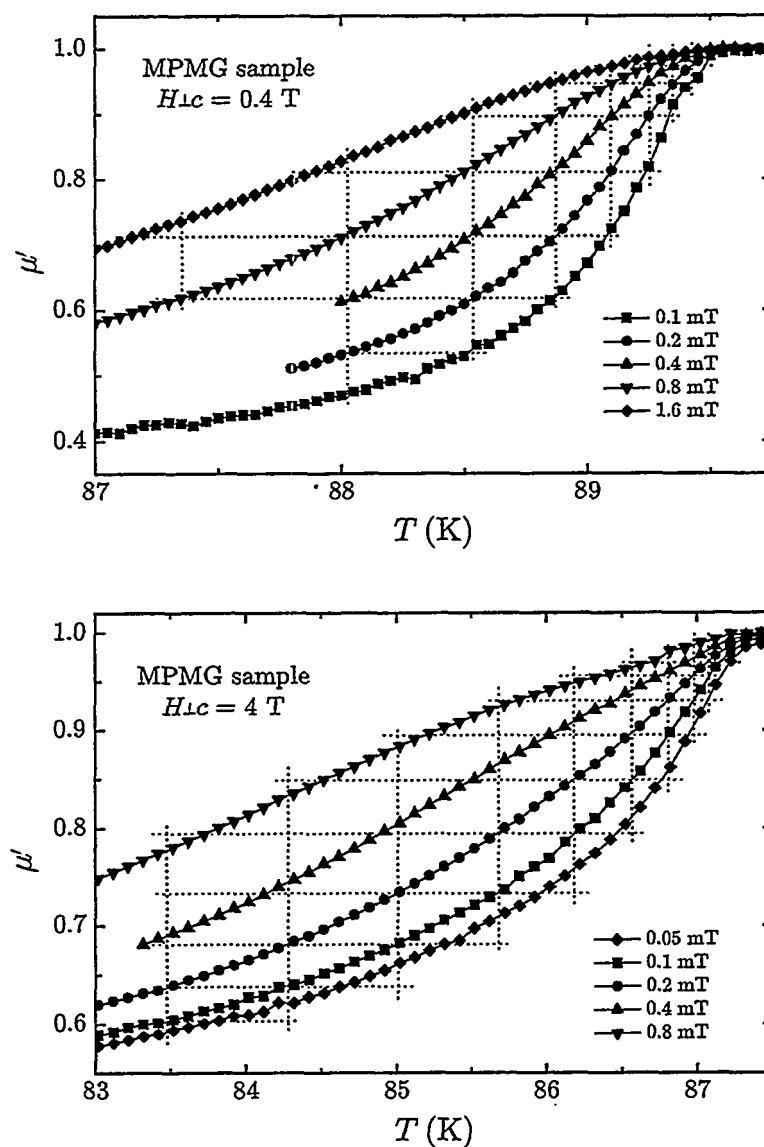


Figure 8.10: $\mu'(T)$ for the MPMG sample in fields 0.4 (top) and 4 T (bottom) applied perpendicular to the c -axis for five geometrically spaced excitation field amplitudes. The frequency is 121 Hz . The dotted grids are drawn to see whether the data are consistent with non-linear response.

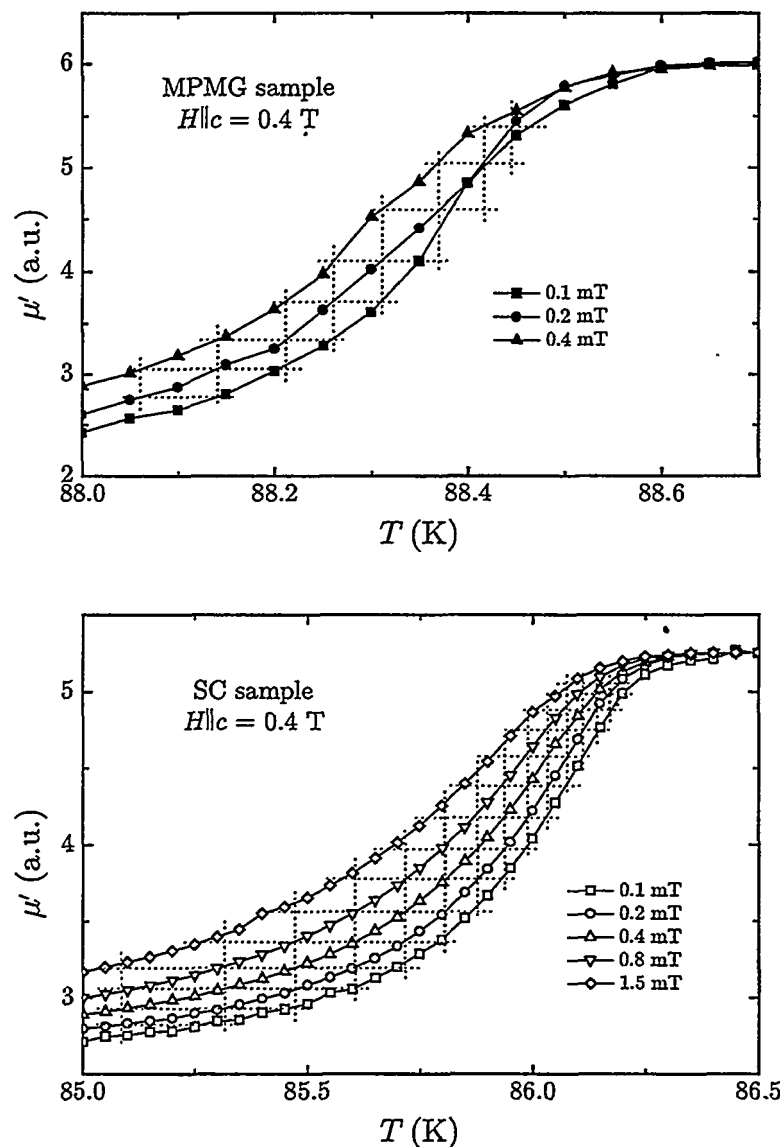


Figure 8.11: $\mu'(T)$ for the MPMG (top) and SC (bottom) samples in a field 0.4 T applied parallel to the c -axis for a number of excitation field amplitudes spaced by a factor 2 (except for the highest amplitude for the SC sample where the factor is 1.88). The frequency is 121 Hz. The dotted grids are drawn to see whether the data are consistent with non-linear response.

8.5.3 Field dependent response

For $\vec{H} \perp \hat{c}$ for both samples we meet with difficulties trying to lay grid points on the $\mu'(T)$ curves when we increase the field to 4 T in Figure 8.10. Again, this could in theory be due to crossing over into a flux flow regime, but now happening at lower amplitudes since the flux flow ac penetration depth, which is proportional to the flux density (or dc field) [10], will start to dominate over the ac penetration depth from creep in the non-linear regime, for lower amplitudes. The difference between the 0.4 and the 4 T data could be related to the difference between the low and high field portions of the LPLs in Figure 8.1: At low fields ($\lesssim 3$ T) the slopes of the LPLs decrease with increasing amplitude whereas at high fields ($\gtrsim 3$ T) the slopes are practically identical for all the amplitudes used. But the reason why this is so, is not clear.

8.6 Summary and conclusions

With $\vec{H} \parallel \hat{c}$ the response depends very weakly on the applied amplitude for both samples. With $\vec{H} \perp \hat{c}$ on the other hand there is pronounced amplitude dependence; truly dramatic for the MPMG sample. The latter orientation constitutes the weakest pinning situation in that vortices may slide easily between the CuO₂ planes where the superconducting order parameter is reduced. Consequently, penetration will occur at lower reduced temperatures for this orientation than for the $\vec{H} \parallel \hat{c}$ orientation (for our samples with equal characteristic sample dimensions in both cases), and are always closer to (if above) or deeper into the non-linear regime where the ac magnetic response is amplitude dependent.

It is reasonable to assume a Bean critical state description for the $\vec{H} \perp \hat{c}$ case. Then the penetration depth, and hence the ac permeability μ , is given by the ratio j/h_{ac} . Then for constant $\mu' \equiv m$ the temperature dependence of j has the same functional form as $h_{ac}(T)$ for fixed m . Scaling such curves taken at 0.4 T for a set of m values we obtain a power-law

$$j(T) = j_0(1 - T/T_0)^{1.5}$$

with $j_0 \approx 0.5 \times 10^9$ A/cm², in agreement with the mean field result $j_c \propto H_c/\lambda \propto H_c^2 \xi \propto (1 - T/T_c)^{3/2}$ which can be related to the activation energy $U \propto (1 - T/T_c)^{3/2}/H$ discussed in the previous Chapter.

Extracting the dependence of m above on the penetration depth, we find fair agreement with the corresponding dependence of μ' for an infinite cylinder and an infinite slab in a Bean critical state.

Using the grid method on $\mu'(T)$ curves for geometrically spaced amplitudes we find that for $\vec{H} \perp \hat{c}$ for both samples the response is consistent with non-linear behaviour (at least at the lower fields). This is also true for $\vec{H} \parallel \hat{c}$, but for this orientation we have previously also found that the response depends on the frequency in the same way as for ohmic response, and we are therefore in a regime intermediate between linear and extremely non-linear.

References

- [1] M. Tachiki and S. Takahashi, Solid State Commun. **70** (1989) 291.
- [2] W. K. Kwok, U. Welp, V. M. Vinokur, S. Fleshler, J. Downey and G. W. Crabtree, Phys. Rev. Lett. **67** (1991) 390.
- [3] R. H. Koch, V. Foglietti, W. J. Gallagher, G. Koren, A. Gupta and M. P. A. Fisher, Phys. Rev. Lett. **63** (1989) 1511.
- [4] T. K. Worthington, F. H. Holtzberg and C. A. Feild, Cryogenics **30** (1990) 417.
- [5] P. L. Gammel, L. F. Schneemeyer and D. J. Bishop, Phys. Rev. Lett. **66** (1991) 953.
- [6] E. Sandvold and C. Rossel, Physica C **190** (1992) 309.
- [7] H. Safar, P. L. Gammel, D. J. Bishop, D. B. Mitzi and A. Kapitulnik, Phys. Rev. Lett. **68** (1992) 2672.
- [8] G. Blatter, M. V. Feigel'man, V. B. Geshkenbein, A. I. Larkin and V. M. Vinokur in *Vortices in high temperature superconductors*, preprint, ETH, Zürich (1993) 538 pages. Rev. Mod. Phys. **66** (1994) 1125.
- [9] *Melt Processed High Temperature Superconductors*, ed. M. Murakami, World Scientific, Singapore (1992).
- [10] C. J. van der Beek, V. B. Geshkenbein and V. M. Vinokur, Phys. Rev. B **48** (1993) 3393.
- [11] F. Gömöry and S. Takács, Physica C **217** (1993) 297.
- [12] L. Fábregas, J. Fontcuberta, L. Civale and S. Piñol, Phys. Rev. B **50** (1994) 1199.

- [13] L. Civale, T. K. Worthington, L. Krusin-Elbaum and F. Holtzberg in *Magnetic Susceptibility of Superconductors and Other Spin Systems*, ed.s R. A. Hein, T. L. Francavilla and D. H. Liebenberg, Plenum Press, New York (1991) page 313.
- [14] L. Fàbrega, J. Fontcuberta, S. Piñol, C. J. van der Beek and P. H. Kes, Phys. Rev. B 47 (1993) 15250.
- [15] Y. Yeshurun and M. Malozemoff, Phys. Rev. Lett. 60 (1988) 2202.
- [16] M. Wacenovsky, R. Miletich, H. W. Weber and M. Murakami, Cryogenics 33 (1993) 70.
- [17] L. Fàbrega, private communication.

More on linear and non-linear response

The work of Gilchrist and Dombre showed how the ac susceptibility behaves, both in the extremes of linear (ohmic) and strongly non-linear response and for intermediate degrees of non-linearity [1]. Displaying our experimental results for the ac permeability in Cole-Cole plots (Argand diagrams), we should be able to tell what regimes we are in.

In Figure 9.1 we show the measured ac permeability for both samples for the $\vec{H} \parallel \hat{c}$ orientation. For both samples the data lie midway between the calculated curves for linear and non-linear response for the infinite cylinder geometry. The MPMG data have a notable spread with dc field, which reflects the fact that the maximum value of μ'' varies with field; see also Figure 5.1. We do not know why this is so. The SC data for the different fields, however, collapse very nicely into a narrow band. Comparing to the calculations of Gilchrist and Dombre [1], we estimate that the non-linearity parameter (see (3.26) and (3.28)) $\sigma \approx 3$ in a cylinder geometry or $\sigma \approx 7$ in a slab geometry. This result agrees with the observations we have made earlier by the gridding method in Sections 7.4 and 8.5: For $\vec{H} \parallel \hat{c}$ the ac magnetic response of both samples lies somewhere in between linear and extremely non-linear with an ac penetration depth — and hence an ac permeability — that depends on both the ratios ρ/f and h_{ac}/j , e.g. as in (3.27). Wacenovsky *et al.* have published very similar results for a MPMG sample with the same nominal composition as ours but with Y211 inclusions making up 10% of the sample volume [2].¹

¹The data in Reference [2] were taken after fast neutron irradiation (with a fluence of

In Figure 9.2 we show the results for the $\vec{H} \perp \hat{c}$ orientation. Again, the MPMG data spread out, but now quite far below the calculated lines at the bottom non-linear end.² And again, the SC data collapse into a narrow band (except for the 1 T data, but they are in the field range where the anomaly, see Chapter 11, is seen). This narrow band falls on top of the calculated line for the infinite cylinder geometry in the non-linear limit. These results indicate that both our samples are in a regime of strong non-linear behaviour when $\vec{H} \perp \hat{c}$, which agrees with the results of the grid method above.

At the time when the measurements were performed we did not focus on the linearity of the response. Consequently we did not sweep the amplitude for a set of fixed frequencies at constant temperatures, which would allow us to try to extract the non-linearity exponent σ in (3.28) nor the collective creep/VG exponent μ in (3.32). Such a set of experiments is a task for the future. The working temperatures and dc fields should be chosen so as to give large enough ranges of amplitudes and frequencies to perform meaningful fits to the relevant equations, (3.28) and (3.32). Looking at the frequency and amplitude dependent LPLs in Figures 7.1 and 8.1 the $\vec{H} \perp \hat{c}$ orientation would be the most useful in this respect, whereas the $\vec{H} \parallel \hat{c}$ orientation would be of lesser value due to its very weak amplitude dependence.

$4 \times 10^{21} \text{ m}^2$), but the LPLs were not influenced much by irradiation, and the data should be representative and good for comparison to our data.

²The very low values of μ'' are not readily understood. See also Subsection 10.4.3.

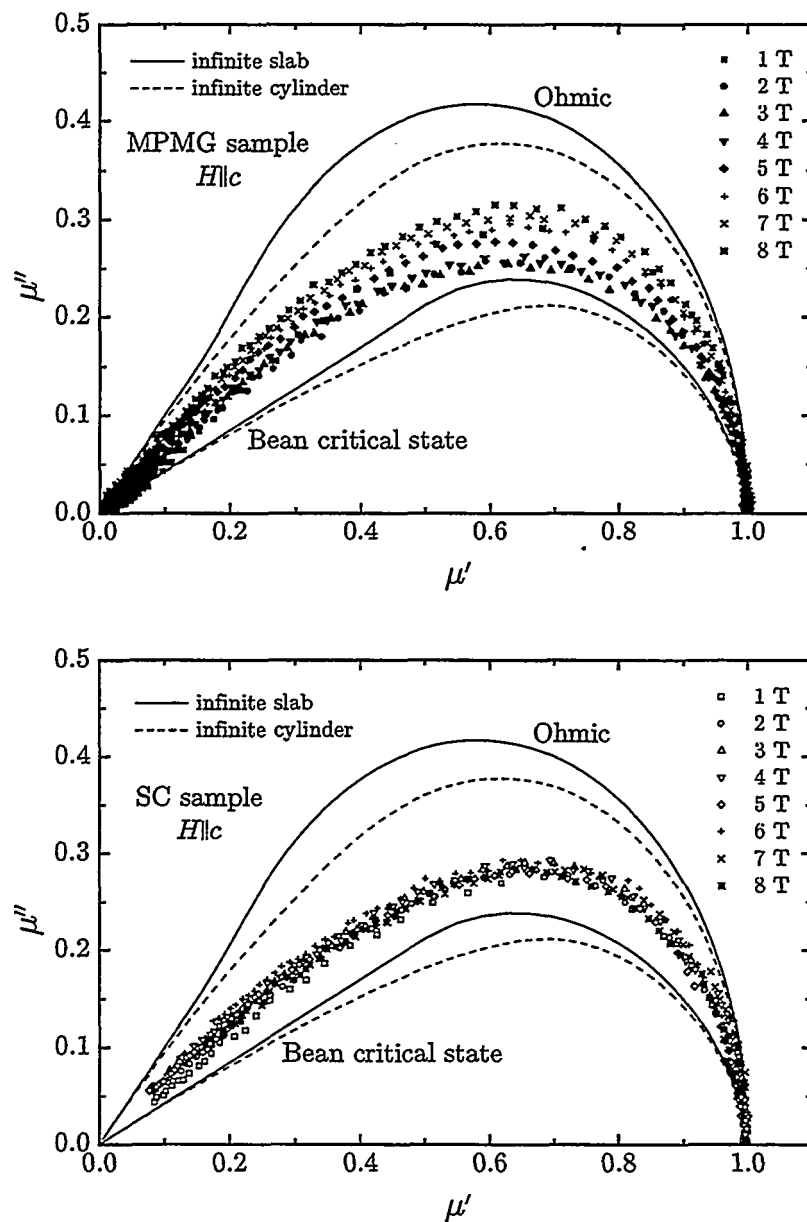


Figure 9.1: Cole-Cole plots of the ac permeability for the MPMG (top) and SC (bottom) samples for eight dc fields applied parallel to the c -axis. The excitation field amplitude and frequency are 0.1 mT and 121 Hz, respectively. The lines are the exact calculations of Figure 3.3 for linear (ohmic) and non-linear response for the infinite cylinder and slab geometries.

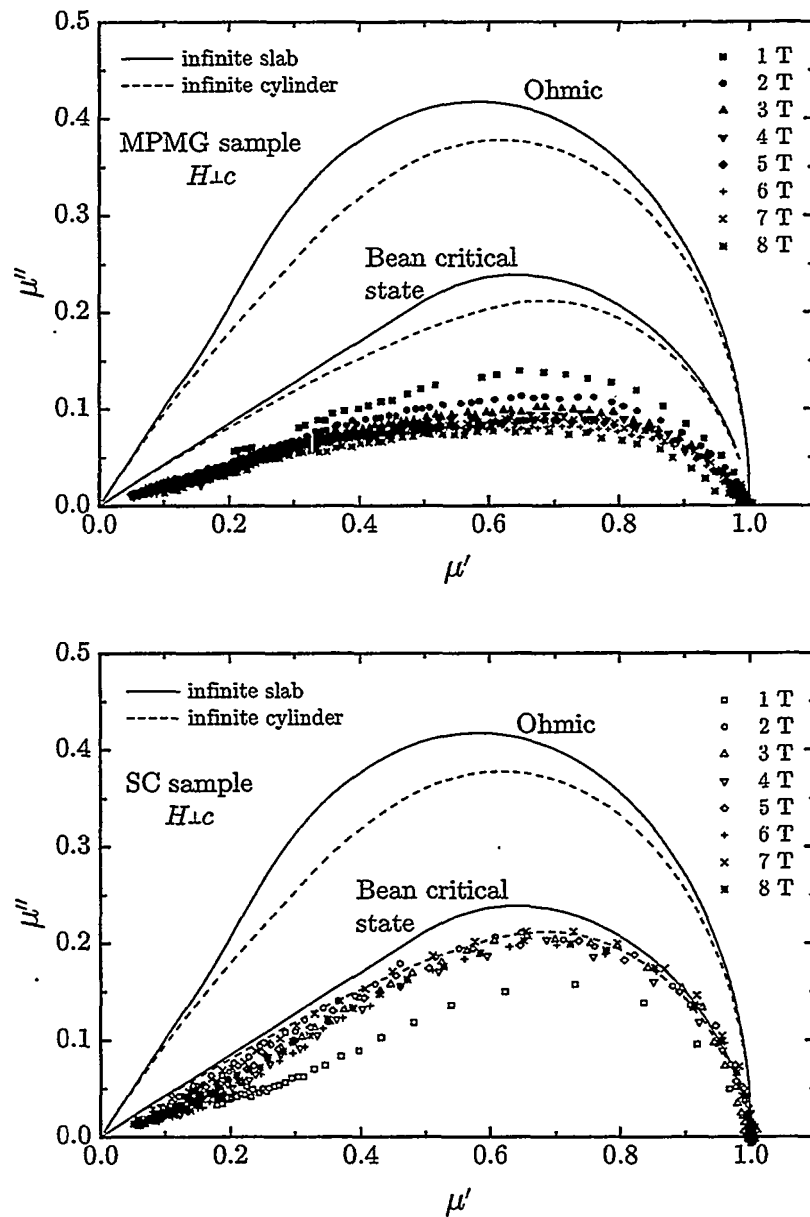


Figure 9.2: Cole-Cole plots of the ac permeability for the MPMG (top) and SC (bottom) samples for eight dc fields applied perpendicular to the c -axis. The excitation field amplitude and frequency are 0.1 mT and 121 Hz, respectively. The lines are the exact calculations of Figure 3.3 for linear (ohmic) and non-linear response for the infinite cylinder and slab geometries.

References

- [1] J. Gilchrist and T. Dombre, Phys. Rev. B **49** (1994) 1466.
- [2] M. Wacenovsky, R. Miletich, H. W. Weber and M. Murakami, Cryogenics **33** (1993) 70.

Anisotropic strong pinning by Y_2BaCuO_5 inclusions

The anisotropy in the loss peak lines is clearly seen in both the MPMG and the SC sample, but another major point of Figure 6.1 is the comparison of the MPMG sample with its Y211 inclusions and the plain SC sample.

For $\vec{H} \parallel \hat{c}$ the difference between the two samples is striking: The loss peak field $H(T^*)$ for the MPMG sample is about 1.5 times larger than that for the SC at the same reduced temperatures.¹ Making the same comparisons for the $\vec{H} \perp \hat{c}$ orientation, where there is hardly any visible difference between the two samples in Figure 6.1, we find a ratio very close to unity.

As a rough measure of the anisotropies of the samples we can compute the ratios of the $\vec{H} \perp \hat{c}$ LPL fits to those for $\vec{H} \parallel \hat{c}$. We find for the MPMG and the SC sample, by the same method as in the above paragraph, ratios ~ 4.8 and 6.3 , respectively. Reported coherence length or penetration depth anisotropy ratios are typically 5–7, see Table 2.1.

10.1 Irreversibility lines for fields along the *c*-axis

The shift of the $\vec{H} \parallel \hat{c}$ LPL, or IL, to higher temperatures and fields clearly show that the non-superconducting Y211 inclusions have the effect of stabilizing the

¹The number is the average ratio over $0.75 < T/T_c < 1$ calculated from the best fit curves.

vortex structure against thermal agitation, increasing the melting temperature. This raises the intriguing question of the effect of pinning, both weak and strong, on the IL. In a series of experiments an IBM group has probed this question using ac susceptibility on a number of different YBCO samples with the field applied along the crystalline *c*-axis. Random local defects in YBCO crystals were produced by proton irradiation. Although an order of magnitude increase of j_c was observed, the IL, defined as the LPL, did not move [1, 2]. The same behaviour was seen later upon moving from single crystals to films thicker than 1000 Å: The ILs are similar although the critical current density increases by orders of magnitude [3]. These results imply a largely pinning independent nature of the IL when the additional pinning sites are weak. The increase in j_c is presumably due to the increase in the total number of weak pins. Still later, the IL was found to move to higher temperatures and fields as j_c was increased in YBCO crystals with long ($\sim 10 \mu\text{m}$) and narrow ($\sim 50 \text{\AA}$ in diameter) strong pinning columnar defects produced by heavy ion irradiation [4]. On the other hand, Worthington *et al.* have reported melting lines on single crystal YBCO samples with enhanced disorder (naturally occurring or introduced by proton or heavy ion irradiation) that did *not* shift after heavy ion-irradiation [5]. According to Blatter *et al.*, the reported shifts of the IL could be due to the measuring technique where the IL depends on the frequency or amplitude used, and the irradiation changes the non-linear behaviour of the system (and hence the frequency or amplitude dependencies) while the actual IL, the thermodynamic phase transition line, does not shift [6, Chapter 10]. This explanation seems unlikely, since the shift that we observe would call for changes in the frequency of almost 4 orders of magnitude from 121 Hz to about 0.6 MHz (estimated from the LPLs in Figure 7.1), or for changes in the amplitude with a factor $\sim 1/200$ from 0.1 mT to about $\sim 0.5 \mu\text{T}$ (estimated from the LPLs in Figure 8.1). The question of possible shifts of the (true) IL is however still not settled, the same authors said. Anyway, we find it fruitful to assume here that the IL can move.

The pinning effect of neutron irradiation has also been studied. Fischer *et al.* report considerably enhanced j_c and a shift of the IL² to higher temperatures [7], but unfortunately fail to give explicit numbers or provide direct comparisons to the unirradiated data. A more systematic study of the influence of fast ($E > 0.1 \text{ MeV}$) neutron irradiation on j_c and the IL in MPMG samples was performed by Wacenovsky *et al.* [8]. Critical current densities

²The "IL" was determined from resistivity measurements: With fixed current and temperature, the magnetic field corresponding to a voltage of $0.1 \mu\text{V}$ was defined as the irreversibility field H_{irr} .

were increased by up to a factor 5 at low fields for $\vec{H} \parallel \hat{c}$, dropping to unity at high fields. For $\vec{H} \perp \hat{c}$ the enhancement factors were 1.5–2.5. The $\vec{H} \parallel \hat{c}$ LPLs shift up about 1 K at 8 T, but the $\vec{H} \perp \hat{c}$ LPLs shift *down* about 1 K at the same field. In comparison, our LPLs shift up by almost 5 K at 8 T upon going from the SC to the MPMG sample, whereas there is no change for $\vec{H} \perp \hat{c}$; see Figure 6.1. Experiments on an YBCO single crystal showed ILs moving first to lower (reduced) temperatures³ before increasing to higher temperatures than the unirradiated IL as the neutron fluence was increased⁴ for the $\vec{H} \parallel \hat{c}$ orientation [9, 10]. For $\vec{H} \perp \hat{c}$ the IL moved up considerably before it started to drop back to the unirradiated IL at the highest fluency level. The effect was attributed to the competition between weak collective pinning, strong pinning by the radiation induced defects⁵ and intrinsic pinning by the CuO_2 planes.

10.2 Pinning by Y_2BaCuO_5 inclusions and related defects

Our results in Figure 6.1 demonstrate that the presence of sub-micrometer non-superconducting Y211 inclusions in YBCO also has the effect, in addition to increasing j_c [11, page 222], of raising the IL to higher temperatures and fields than that of single crystal YBCO in fields parallel to the *c*-axis. The detailed nature of pinning by Y211 inclusions is not known, but the implication here is that the inclusions and/or related structural defects act as strong pinning centers providing additional stability to the vortex structure resulting in a higher vortex melting temperature when $\vec{H} \parallel \hat{c}$, similar to the proposal of Murakami *et al.* for increased critical current density for this orientation of the field [12]. These strong pins are of course superimposed upon the already existing random distribution of weak pins which act to provide the collective pinning of the flux lines. Since the Y211 inclusions drain the Y123 matrix of oxygen [13], they provide additional weak point pins that should not raise the IL. The effect of the extra oxygen vacancies would rather be to stiffen the sections of the vortices existing between the Y211 inclusions, thus rendering the pinning due to the Y211 inclusions more effective. The extra data on

³Pinning by pre-irradiation defects was weakened by the irradiation [9].

⁴At higher fluences, strong pinning centers were created [9].

⁵The high energy recoils produced strong pinning defect cascades of sizes 20–60 Å. Intermediate energy recoils produced clusters (point defects and small cascades) with diameters ~ 20 Å, and these contributed significantly to the pinning strength. Low energy recoils produced point defects as small as ~ 4 Å.

the MPMG Y1.2 (Y12) sample, which has a lower yttrium content than the MPMG (Y1.8) sample, in Figure 6.1 support this picture. Cation nonstoichiometry due to substitution of Ba by Y near the Y123/Y211 interfaces has been reported for melt-textured samples, and this chemical disorder also introduces additional point defects [14, 15]. We note that the LPL of the Y12 sample is slightly above that for the MPMG sample even though its Y211 volume content is lower than that of the MPMG sample. The difference is not very dramatic, and the critical current densities at 77 K and 1 T are equal (Subsection 4.2.1 and Reference [16]). Other ac magnetic experiments on very similar MPMG samples agree well with our results [8, 17].

There are a number of candidates for the enhanced pinning in the MPMG material: Wang *et al.* reported a high local density of *stacking faults* in the Y123 matrix near the interfaces in melt-textured YBCO and expected them to act as effective pinning centers for both $\vec{H} \perp \hat{c}$ and $\vec{H} \parallel \hat{c}$ [14]. Stacking faults and *twins* are present, but not in excess of what is seen in Y211 free YBCO [11, Chapter 5]. *Cracks* parallel to the *ab*-plane are also formed during the processing, but in fact their numbers are reduced in samples containing Y211 inclusions, and the density of *screw dislocations* is very low [11, Chapter 10]. This leaves the *Y211 inclusions* themselves, or rather the *interface* between the Y123 and Y211 matrices since the inclusions are large and insulating. The size, much larger than the vortex core (*i.e.* larger than the coherence length ξ), has been believed to render the inclusions ineffective as pinning sites. But the pinning force is given by the gradient of the potential step — *i.e.* the difference in the superconducting order parameter or the condensation energy — seen when crossing the Y123/Y211 interface. Since the interface is very clean and abrupt, as HRTEM studies have shown for the MPMG material [18] and other melt-processed YBCO materials [15, 19], since the change in the order parameter is large (dropping to zero inside the insulating Y211 inclusions) and since the inclusions are large, pinning long sections of the flux lines, the pinning force is large. That the Y211 inclusions attract flux has been clearly shown by magneto-optical visualization of the flux distribution, and the ferromagnetic Ni particles used in Bitter patterning fell onto Y211 inclusions and, most notably, on the Y123/Y211 interfaces [20]. The increased density of oxygen vacancies in the vicinity of the Y211 material render the inclusions more effective as pinning sites in that they help “stiffen” the segments of the vortices between different Y123/Y211 interfaces.

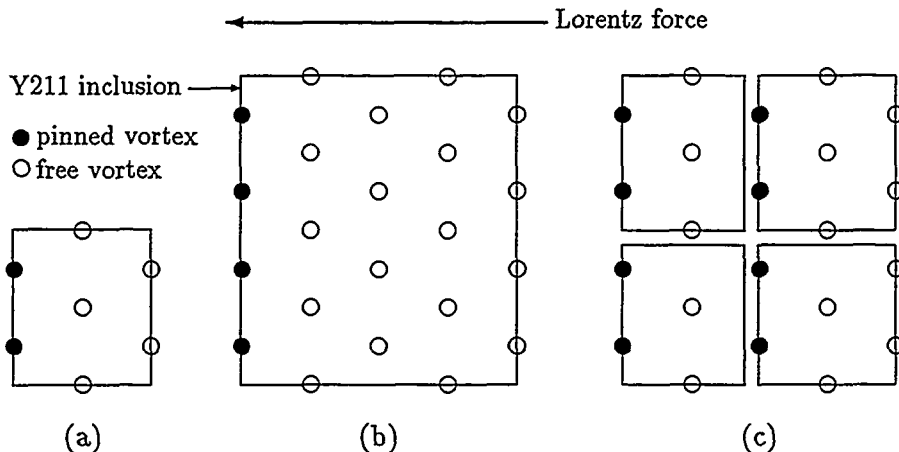


Figure 10.1: Schematic illustration of pinning by Y211 inclusions. The field direction is normal to the paper plane, and a Lorentz force tries to move the vortices to the left. The • symbols mark vortices that are pinned at the left abrupt Y123/Y211 interfaces and the o symbols mark unpinned vortices: of course it is not meaningful to have vortices inside the insulating Y211 inclusions, but we draw them here just to show that the flux density is the same. In (a) few vortices are pinned since there are few Y211 inclusions, and they are small. In (b) there are still few inclusions, but they are larger, and more vortices are pinned. In (c) there are many small inclusions and more vortices are pinned than in (b), even though the volume fraction of Y211 material is the same. The flux density B is the same in all three cases.

10.3 Strong pinning at the $\text{YBa}_2\text{Cu}_3\text{O}_7/\text{Y}_2\text{BaCuO}_5$ interface

The vortices will be pinned tangentially to the surfaces of the inclusions, i.e. on the “leeward” interface where the potential changes abruptly. The mechanism is in principle the same as the one in the work on the intrinsic pinning of the CuO_2 planes by Tachiki and Takahashi [21]. We can estimate the effect of this: The pinning depends on the size and number density of the inclusions: More vortices can be strongly pinned along the interfaces if the inclusions are large or if there are a lot of inclusions per unit volume. We illustrate this in Figure 10.1. For simplicity, we assume now that the size of a Y211 inclusion is characterized by a single length, a radius r . The length of the pinning interface then scales as r and the density scales as $1/r^3$, so for a given Y211 volume fraction a large number of small inclusions would provide the best pinning, as has also been established experimentally [18, 22]. See also

Figure 10.1. The vortex cores should not overlap, so the separation between the pinned vortices along the pinning interface should be larger than about two coherence lengths. If the vortices should pass by some of the inclusions on their way through the sample without getting pinned, extra vortices could be pinned by the skipped inclusions. Also, if many vortices are rigidly pinned, they may help to stabilize the whole vortex system at high enough fields through vortex-vortex interactions. Since the inclusions are separated by micrometer distances that are larger than the collective pinning length L_c , the vortices are subject to ordinary weak collective pinning in the bulk Y123 material.

Example

We can illustrate this with a simplified example: In our MPMG sample the Y211 volume fraction is 20%. From the TEM micrograph in Figure 4.2 showing one circular/spherical inclusion we obtain the value $r = 0.15 \mu\text{m}$. In reality, we expect a rather wide distribution of sizes [18], but we neglect that and use a single value in this example. The average distance between inclusion centers is then about $0.4 \mu\text{m}$, so this would correspond to rather dense packing. (Since for melt-textured samples the dislocation density has been reported to increase near the interface if the interparticle spacing is small or the surface curvature of the interface is high [15], there is of course a possibility that a local high density of dislocations is responsible for the increased pinning, but this has not been reported for the differently processed MPMG material, and in the TEM micrograph in Figure 4.2 we do not see the dislocation lines and nets near the interface that are seen near a very similar Y211 particle in Reference [15].) Next we assume a coherence length of $\xi = 25 \text{ \AA}$ (the GL coherence length at $T \approx 0.8T_c$ assuming $\xi(0) \approx 10 \text{ \AA}$). Then each inclusion can pin about 200 vortices separated from each other by a distance 2ξ . At our maximum field of 8 T about one in three-four vortices can then be strongly pinned if they do not bypass any inclusions. At low enough fields, up to around 2 T, all the vortices can then be accommodated by the inclusions. However, with about 75% of the vortices unpinned we would expect the MPMG LPL (and IL) at 8 T to lie closer to the SC LPL (and IL) than what we observe in Figure 6.1. This raises the question of how realistic this simple model is, or if there are flux bundle effects to take into account.

10.4 Field parallel to the ab -plane

10.4.1 No shift of the irreversibility line

Next, we will look at the opposite orientation: When $\vec{H} \perp \hat{c}$ the presence of Y211 inclusions does not move the LPL in the limit of low excitation field amplitude, *i.e.* where the LPL lies close to the IL. In this orientation the vortices would want to sit between the superconducting CuO₂ layers to minimize their energy. The superconducting order parameter only changes from being much reduced in the quasi-normal regions of the Y123 material to zero in the normal Y211 material upon crossing the interface. Pinning by the inclusions for $\vec{H} \perp \hat{c}$ should therefore be much weaker than for the $\vec{H} \parallel \hat{c}$ orientation due to this reduced barrier. One could also imagine that due to the strong intrinsic pinning by the CuO₂ layers, the vortex structure for $\vec{H} \perp \hat{c}$ is maximally stable, and that any additional pins would not affect the position of the IL. However, neutron irradiation on YBCO crystals has been proven to do exactly that, lifting the IL up [8,11]. If there is a potential for lifting the IL for $\vec{H} \perp \hat{c}$, any local high density of stacking faults due to the presence of the Y211 particles would probably not be the dominant source of strong pinning as suggested by Wang *et al.* [14] in the MPMG material since our results in Figure 6.1 do not indicate a shift of the $\vec{H} \perp \hat{c}$ IL to higher fields and temperatures with the introduction of Y211 particles.

10.4.2 Anisotropic pinning energies and forces

Another way to look at the anisotropic strong pinning is to estimate pinning energies and forces. Let the characteristic pinning length along the Y123/Y211 interface be $d \sim r$. With a roughly spherical shape of the inclusions, d will have the same value for all field orientations. The pinning energies are then proportional to the pinning volumes $\pi \xi_{ab}^2 d$ for $\vec{H} \parallel \hat{c}$ and $\pi \xi_{ab} \xi_c d$ for $\vec{H} \perp \hat{c}$, and they differ by a factor equal to the anisotropy ratio $\gamma = \xi_{ab}/\xi_c$. The pinning force is the gradient of this, and the relevant length scale for changes in the energy is ξ_{ab} in both cases,⁶ and again the difference is a factor ξ_{ab}/ξ_c . The pinning should therefore be strongest with the field along the c -axis, in accord with what we observe and the proposal of Murakami *et al.* [12].

⁶This is trivial when $\vec{H} \parallel \hat{c}$. When $\vec{H} \perp \hat{c}$, the layering strongly inhibits vortex motion across the CuO₂ planes and leaves ξ_{ab} as the relevant coherence length.

10.4.3 Substantial ac losses

The Y211 inclusions do however affect the ac response: As seen from Figure 5.7 where we plot the full width at half maximum (FWHM) of the loss peaks, when $\vec{H} \perp \hat{c}$ substantial losses are observed over much wider temperature ranges in the MPMG sample than in the SC sample. From a practical point of view this could have implications because the increased losses might inhibit further technological exploitations of this material, or confine it solely to dc applications. Of course, even with moderately strong ac excitations there are large losses in the SC sample when $\vec{H} \perp \hat{c}$. The large insulating Y211 inclusions wipe out the pinning effects of the voids and defects between the layers that would have been there if the Y211 material had not replaced Y123 material, leading to increased dissipation. Also, over large regions in the MPMG material flux is free to move also in the directions where it would otherwise meet the large barriers set up by the CuO_2 layers: The CuO_2 planes terminate on the inclusions, and the flux that is pinned on the Y123/Y211 interface has less of a barrier to overcome in moving parallel to the c -axis. In addition, because the Y211 inclusions deplete the Y123 matrix of oxygen [13], it is reasonable to suppose that the CuO_2 planes closer to the interface are more oxygen deficient than the bulk material and hence have a lower superconducting order parameter lowering the barrier to flux motion even more. Microcracks can be present in melt-processed materials [23] allowing easier flux penetration when $\vec{H} \perp \hat{c}$. But Y211 inclusions can on the other hand help relieve the stresses causing the cracks [11, 23]. The expanded lossy regions are also reflected in Figure 8.4 where we plot the loss peak temperature *vs.* excitation field amplitude for several dc fields. While the effect of increasing the dc field on the SC curves is only a downward parallel shift in temperature, for the MPMG curves the slope also decreases with increasing dc field. That is, for the same dc field the lossy behavior starts at lower temperatures, or alternatively, at lower amplitudes, reflecting weaker overall pinning for the MPMG sample. This is alternatively seen from loss peak lines upon increasing the amplitude. For $\vec{H} \parallel \hat{c}$ the amplitude dependence is almost negligible, see Figure 8.1 or alternatively Figure 9.2. However, close to the loss peak maximum, *i.e.* around T^* , the loss per cycle as measured by $\mu''(T)$ is smaller for the MPMG sample than for the SC sample; see Figure 5.2. We fail to see any immediate reason for this puzzling — in the light of the above considerations — behaviour, and just acknowledge that the complexity of the problem for this orientation (in which cracks and stacking faults give their largest contribution to the total pinning) is considerable with two different components of the screening currents and a plentitude of different

origins of pinning. The complex mixture of pinning sites and the insulating inclusions probably invalidates conventional discussion of models (such as FLL melting or vortex glass) based on more homogeneous pinning situations, and is then probably also responsible for the puzzling development of $\mu''(T)$ with dc field in Figure 5.2 and the dramatic shift of the LPLs with amplitude in Figure 8.1.

10.5 Summary and conclusions

We find by comparing to the SC (single crystal) sample that the Y211 inclusions and/or any related defects in the MPMG material have the effect of moving the LPL, and the IL, to higher fields and temperatures when $\vec{H} \parallel \hat{c}$. This indicates strong pinning, and after considering various pinning mechanism we believe that the strong pinning occurs at the abrupt Y123/Y211 interfaces.

A similar shift of the LPL (and IL) is not observed when $\vec{H} \perp \hat{c}$. Simple pinning force estimates suggest that the pinning force is stronger when $\vec{H} \parallel \hat{c}$ by a factor γ , the anisotropy ratio.

Substantial ac losses are however observed for the $\vec{H} \perp \hat{c}$ orientation. Possible explanations for this effect is that the Y211 inclusions wipe out whatever pins would have been there in an uninterrupted Y123 matrix, and also that the inclusions reduce the effect of the intrinsic pinning since the superconducting CuO₂ layers are interrupted over large areas.

References

- [1] L. Civale, A. D. Marwick, M. W. McElfresh, T. K. Worthington, A. P. Malozemoff, F. H. Holtzberg, J. R. Thompson and M. A. Kirk, Phys. Rev. Lett. **65** (1990) 1164.
- [2] L. Civale, M. W. McElfresh, A. D. Marwick, F. Holtzberg, C. Feild, J. R. Thompson and D. K. Christen, Phys. Rev. B **43** (1991) 13732.
- [3] L. Civale, T. K. Worthington and A. Gupta, Phys. Rev. B **43** (1991) 5425.
- [4] L. Civale, A. D. Marwick, T. K. Worthington, M. A. Kirk, J. R. Thompson, L. Krusin-Elbaum, Y. Sun, J. R. Clem and F. Holtzberg, Phys. Rev. Lett. **67** (1991) 648.
- [5] T. K. Worthington, M. P. A. Fisher, D. A. Huse, J. Toner, A. D. Marwick, T. Zabel, C. A. Feild and F. Holtzberg, Phys. Rev. B **46** (1992) 11854.
- [6] G. Blatter, M. V. Feigel'man, V. B. Geshkenbein, A. I. Larkin and V. M. Vinokur in *Vortices in high temperature superconductors*, preprint, ETH, Zürich (1993) 538 pages. Rev. Mod. Phys. **66** (1994) 1125.
- [7] K. Fischer, G. Leitner, G. Fuchs, M. Schubert, B. Schlobach, A. Gladun and C. Rodig, Cryogenics **33** (1993) 97.
- [8] M. Wacenovsky, R. Miletich, H. W. Weber and M. Murakami, Cryogenics **33** (1993) 70.
- [9] F. M. Sauerzopf, H. P. Wiesinger, H. W. Weber, G. W. Crabtree, M. C. Frischherz and M. A. Kirk, Supercond. Sci. Technol. **5** (1992) S105.
- [10] F. M. Sauerzopf, H. P. Wiesinger, W. Kritscha, H. W. Weber, M. C. Frischherz and H. Gerstenberg, Cryogenics **33** (1993) 8.

- [11] *Melt Processed High Temperature Superconductors*, ed. M. Murakami, World Scientific, Singapore (1992).
- [12] M. Murakami, S. Gotoh, H. Fujimoto, K. Yamaguchi, N. Koshizuka and S. Tanaka, *Supercond. Sci. Technol.* 4 (1991) S49.
- [13] R. Miletich, M. Murakami, A. Preisinger and H. W. Weber, *Physica C* 209 (1993) 415.
- [14] Z. L. Wang, A. Goyal and D. M. Kroeger, *Phys. Rev. B* 47 (1993) 5373.
- [15] D. F. Lee, M. Mironova, V. Selvamanickam and K. Salama, *Interface Science* 1 (1993) 385.
- [16] N. Nakamura, private communication.
- [17] M. Wacenovsky, R. Miletich and H. W. Weber, *Supercond. Sci. Technol.* 5 (1992) S184.
- [18] M. Murakami, K. Yamaguchi, H. Fujimoto, N. Nakamura, T. Taguchi, N. Koshizuka and S. Tanaka, *Cryogenics* 32 (1992) 930.
- [19] Z. L. Wang, R. Kontra, D. M. Kroeger, A. Goyal and R. K. Williams, *Interface Science* 1 (1993) 321.
- [20] M. Murakami in *Phenomenology and Applications of High-Temperature Superconductors*, ed.s K. S. Bedell, M. Inui, D. Meltzer, J. R. Schrieffer and S. Doniach, Addison Wesley, Reading, Massachusetts, USA (1992) page 103.
- [21] M. Tachiki and S. Takahashi, *Solid State Commun.* 70 (1989) 291.
- [22] B. Ni, M. Kobayashi, K. Funaki, K. Yamafuji and T. Matsushita, *Jap. J. of App. Phys.* 30 (1991) L 1861.
- [23] P. J. Kung, M. P. Maley, M. E. McHenry, J. O. Willis, M. Murakami and S. Tanaka, *Phys. Rev. B* 48 (1993) 13922, and references therein.

The anomalous response in the SC sample

In this Chapter we will focus on the anomalous ac magnetic response observed in the SC sample at intermediate fields oriented perpendicular to the crystalline *c*-axis. The anomaly manifests itself as a dramatic broadening of the loss peak and a change of the general shape of the real and imaginary components of μ , see for example the 1 T data of Figure 5.2 and the 0.4 T data of Figures 5.4 and 5.6. The most striking appearance is as the peak between 0 and 1 T in the FWHM curve in Figure 5.7. The anomaly is *not* seen in zero field or in fields above 2 T (see Figure 5.7). No anomaly is observed for $\vec{H} \parallel \hat{c}$, nor is it present in the more disordered MPMG sample; see Figure 11.1.

Figure 11.2 shows two anomalous loss peaks and their derivatives at 0.5 and 1.0 T. Below we will use L (left) and R (right) when referring to the two features (the “maximum” and the “bump”, or *vice versa*, depending on the applied dc field, amplitude and frequency, as seen in Figures 11.2 and 11.3) of each loss peak marked by the arrows in Figure 11.2. We note that increasing the dc field reduces the magnitude of L while R stays essentially the same.

Tilting the field 20° results in quite similar anomalous loss peaks observed within the same dc field range, but L grows slightly and R shrinks slightly compared to the original $\vec{H} \perp \hat{c}$ orientation.

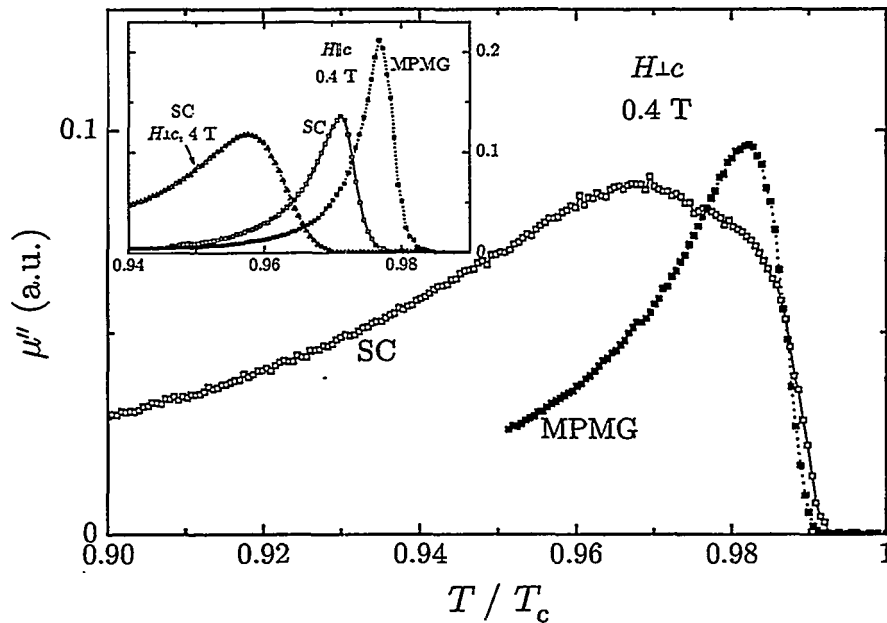


Figure 11.1: Loss peaks for the SC and MPMG samples in a 0.4 T field applied perpendicular to the c -axis. The difference between the two is striking with an anomalous broadening and change of shape for the SC sample data. The inset shows the corresponding data for $H \parallel \hat{c}$, but also the loss peak at 4 T for the SC sample with $H \perp \hat{c}$. The excitation field amplitude and frequency are 0.4 mT and 121 Hz, respectively.

11.1 Excitation field dependence

If we examine the temperature position T^* of the absolute maximum of μ'' in the H - T plane as a function of the excitation field amplitude h_{ac} , see Figure 8.1, we find that T^* drops dramatically to lower temperatures when h_{ac} is increased: Going from 0.1 mT to 3.0 mT at 0.4 T, T^* drops 8 K, compared to only 2.6 K for the MPMG sample. Also when h_{ac} increases, L grows and moves rapidly to lower temperatures while R shrinks and does *not* move. We see this clearly in Figure 11.3 where we plot the derivatives $d\mu''/dT$ of the loss peaks for a number of different amplitudes. The zero-crossings correspond to the loss peak maxima at T^* and move quickly to lower temperatures. The flattening out of the derivatives on the other hand occur at the same temperature, just below 87 K, for all amplitudes. Thus these curves indicate that the system goes from

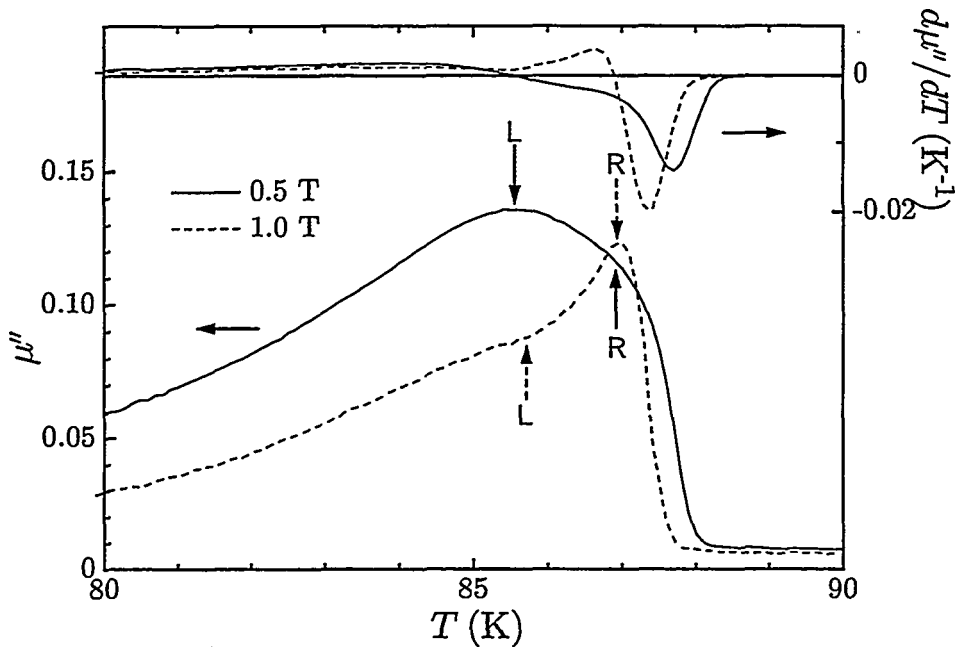


Figure 11.2: Loss peaks and their derivatives at 0.5 and 1.0 T for the SC sample. The excitation field amplitude and frequency are 0.4 mT and 13 kHz, respectively. See text on the arrows marked L and R.

linear to strongly non-linear behaviour as the temperature is decreased below 87 K. In this case, at 0.4 T, L is the “maximum” and R the “bump”. In Figure 11.2 the opposite is true at 1 T.

When the frequency f increases, L moves to higher temperatures, but R does not seem to move — the frequency range used is rather narrow, and the frequency dependence of the anomalous loss peaks is quite weak.

The anomaly is also strikingly displayed in Figure 11.4 where we plot the FWHM of μ'' vs. H_{dc} . Upon increasing either the amplitude h_{ac} or the frequency f , the half-width blows up dramatically within the field range from 0 upto about 2 T, the maximum being roughly proportional to h_{ac} and $\log f$.

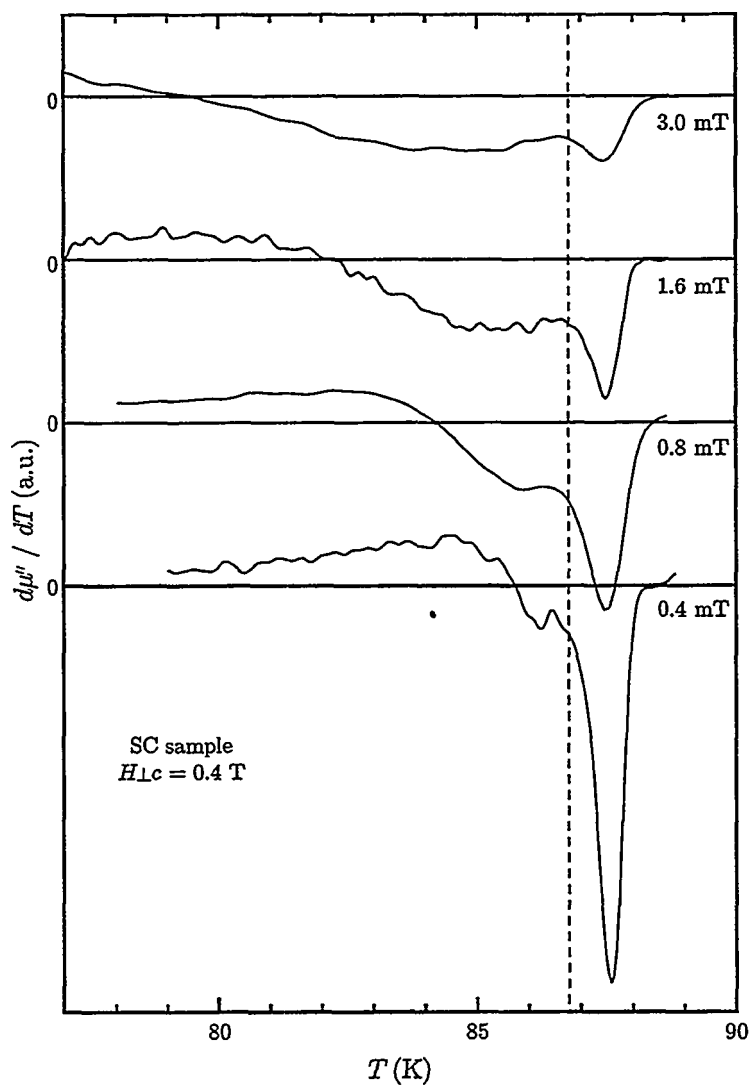


Figure 11.3: $d\mu''/dT$ vs. T for the SC sample for different amplitudes in a dc field of 0.4 T applied perpendicular to the c -axis. The curves are numerical derivatives taken after smoothing the original $\mu''(T)$ data, and are displaced vertically for clarity. The horizontal lines represent the zero-level for each curve. The zero-crossings correspond to the loss peak maxima at T^* , and the dashed vertical line identify the anomaly associated here with the flattening out of the curves just below 87 K — independent of amplitude.

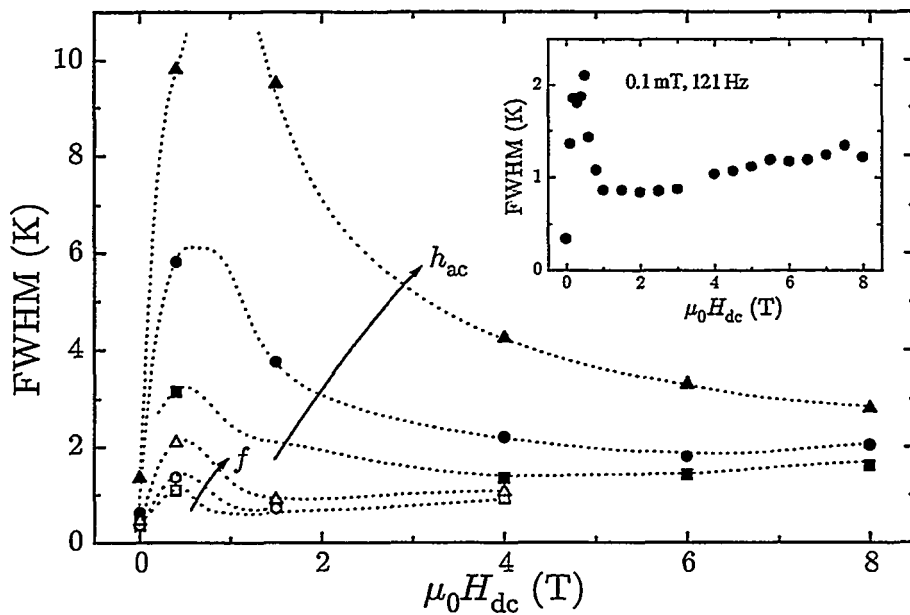


Figure 11.4: Full width at half maximum (FWHM) of the loss peaks *vs.* applied field. Closed symbols: 0.2, 0.4 and 1.0 mT at 121 Hz. Open symbols: 1.21, 12.1 and 121 kHz at 0.1 mT. Inset: 0.1 mT and 121 Hz. Dashed lines are drawn to guide the eye.

11.2 Origin of the anomaly

11.2.1 Granularity?

In granular samples two maxima are often observed in $\mu''(T)$: one at high temperature due to the penetration into the individual grains (small size) and the second, broader and at lower temperature, due to the penetration into the sample against the bulk intergranular shielding currents (large size). This type of behaviour occurs at all fields, in particular also in zero field, and is of course independent of orientation since the grains are randomly oriented. Consequently, since we do not observe the anomaly in zero field and above 2 T, and since we see it with the field oriented along the *c*-axis, the anomaly is inconsistent with granularity.

11.2.2 "Oriented granularity" due to cracks?

Matsushita *et al.* have presented loss peaks very similar to ours for a large QMG (quench and melt growth) sample with a relatively small fraction of Y211 to increase the number of cracks (mean separation $20\ \mu\text{m}$) [1]. In a dc field of 1 T applied perpendicular to the c -axis they observed loss peaks very similar to the 1 T curve in Figure 11.2. For a similar sample without cracks, the anomaly was not seen. Unfortunately, this was not commented on at all by the authors, but from the very limited information presented, it seems one could attribute the anomaly to cracks in the sample. This would explain why the anomaly is only seen when close to the $\vec{H} \perp \hat{c}$ orientation. Perhaps then we can speak of an "oriented granularity" in the sense that the cracks effectively divide the sample into a number of thin platelets with the large faces perpendicular to the c -axis. Then one could imagine flux penetrating first into the individual platelets from the cracks, at high temperatures, before bulk shielding currents flow at low temperatures. In analogy with the granular materials two maxima, or one maximum and a "bump", would then be seen in $\mu''(T)$. But it is not at all clear why the two maxima would behave so qualitatively differently when e.g. the amplitude changes.

11.2.3 Misorientation?

Double peaks in μ'' have been reported for intermediate fields oriented off the crystalline axes [2] beyond the lock-in angle $[\cdot]$. They correspond to the penetration of different components of the field at right angles to each other under anisotropic conditions mimicing geometry related effects as described by Brandt [3]. We could imagine a slight misorientation of the field with respect to the ab -plane. Since $\mu'' \propto h_{ac}$, see (4.1), the relevant direction of h_{ac} is perpendicular to the c -axis since the signal due to a very small h_{ac} component along the c -axis would be negligible compared to that of the main component. There are then two penetrating systems: (a) the nominal $\vec{h}_{ac} \parallel \vec{H}_{dc}^\perp \perp \hat{c}$ and (b) $\vec{h}_{ac} \perp \vec{H}_{dc}^{\parallel} \parallel \hat{c}$. The latter, (b), would be responsible for the extra feature in the loss peaks in Figure 11.2. For small misorientations $H_{dc}^{\parallel} \ll H_{dc}^\perp \simeq H_{dc}$. We could identify L with (a) and R with (b) since the penetration for $\vec{H}_{dc}^\perp \perp \hat{c}$ happens at lower temperatures than the penetration for the much smaller components $\vec{H}_{dc}^{\parallel} \parallel \hat{c}$, cf. Figures 6.1 and 8.1. Also, the amplitude dependence of the peak position is very pronounced in the first orientation, but small in the second. The limited dc field range would be a consequence of the field

dependence of the lock-in angle [] and the stiffening of the vortices due to their mutual interaction at high fields; see also Reference [2]. Additional data taken 20° off the $\vec{H} \perp \hat{c}$ orientation also fit into this picture.

There are however complications: First, in the limited dc field range L moves very rapidly down in temperature upon increasing the amplitude, see Figure 8.1. This is not consistent with a misorientation picture and the corresponding situation for the MPMG sample in Figure 8.1. Second, data for increasing frequencies indicate that L moves up in temperature and R does not seem to move, in contrast to the behaviour of the loss peak lines in Figure 7.1. Third, tilting the sample 20° is expected to decrease the component of \vec{h}_{ac} perpendicular to the c-axis, but the magnitude of L is observed to increase. In this orientation, however, the situation might be more complicated in that also the signal from the situation with $\vec{h}_{ac} \parallel \vec{H}_{dc} \parallel \hat{c}$ contributes. But (b), i.e. $\vec{h}_{ac} \perp \vec{H}_{dc} \parallel \hat{c}$, is not equivalent to $\vec{h}_{ac} \parallel \vec{H}_{dc} \parallel \hat{c}$, and full correspondence is not necessarily implied.

11.2.4 Phase transition?

We cannot rule out a phase transition of some type occurring, primarily due to the amplitude of R which we have unambiguously observed in the derivatives $d\mu''/dT$, and perhaps also due to frequency independence. Our observation could be the ac response counterpart to the I-V measurements made on single crystal YBCO samples with enhanced disorder by Worthington *et al.* [4]. They claimed to observe separate glass and melting transitions at relatively low dc fields, and speculated that the high temperature transition is a remnant of the first order melting transition and exists, in a clean system, at the same temperature with the vortex glass transition. With disorder the melting transition becomes rounded, and as the disorder gets sufficiently strong it becomes unobservable. There are several similarities between our observed anomaly and the results of Worthington *et al.*: the anomaly is not present in zero field and it goes away at high fields; it goes away with increasing disorder, i.e. it is not seen in the more disordered MPMG sample. This is of course all suggestive. With the ac permeability as a measure of flux penetration, it is not immediately clear how the extra structure in $\mu''(T)$ would result. Possibly, passing through the melting and the vortex glass transitions the shielding capabilities change relatively abruptly across at least one of the transitions and the loss peak attains an extra feature; see the next Subsection. The reason why the melting transition identified with R would be amplitude independent

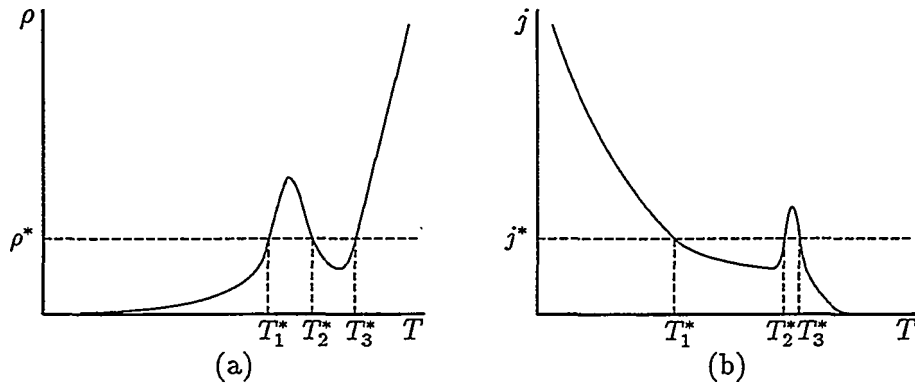


Figure 11.5: Schematic illustrations of non-monotonic (a) resistivity and (b) (critical) current density. The loss peak $\mu''(T)$ attains its maximum value(s) for temperatures where (a) $\rho = \rho^* \approx \mu_0 \omega^* / 2a^2$, see (3.23), or (b) $j = j^* \approx h_{ac}^* / a$, see (3.22), depending on what response regime we are in. We see that depending on the value of ρ^* or h_{ac}^* the loss peak will display 1, 2 or 3 maxima corresponding to the number of intersections of ρ^* or h_{ac}^* with $\rho(T)$ or $j(T)$, respectively.

in ac magnetic experiments could be that FLL melting is seen for no or very little pinning, and it is the pinning that produces the non-linearity and the amplitude dependence.

11.2.5 Peak effect: non-monotonic (critical) current density?

Finally, multiple peaks have also been observed and explained [5–7] in terms of the peak effect [8]: if the (critical) current density (or the resistivity) shows non-monotonic temperature dependence the matching of the ac penetration depth λ_{ac} with the characteristic sample size a can happen more than once upon decreasing the temperature; see the illustrations in Figure 11.5.

Giapintzakis *et al.* observed a very narrow peak at high temperature which they correlated with the melting transition in their clean YBCO samples [7]. The temperature position of this peak did not shift with changing amplitudes, in the same way as our R feature does not move. At lower temperatures $\xi'' = \mu''$ developed into a much broader peak, with some structure, that shifted rapidly down in temperature as the amplitude was increased, as our L feature does. Also, the magnitude (maximum) of the low temperature peak increased with increasing amplitude, again similar to what we observe. So, our loss peaks behave suggestively similar to those of Giapintzakis *et al.*, except that the effect

is notably more subtle in our case where we would have to assign the sharp dissipative onset and R at high temperature the role of their sharp melting peak. In the peak effect picture this would correspond to a much less dramatic break of monotony, perhaps even only a small deviation from smoothness, of the (critical) current density with temperature.

The cause of the peak effect was suggested by Giapintzakis *et al.* to be an enhancement of j_c at high temperatures due to adjustment of the flux lines to the (relatively few) pinning centers, a process assisted by softening of the FLL prior to its melting. This explanation was also given by Ling and Budnick for similar results for YBCO with $\vec{H}_{dc} \perp \hat{c} \parallel \vec{h}_{ac}$ [5]. We could hence propose that our anomaly is a weak remnant of the melting of the FLL smeared by disorder, *i.e.* a larger density of pins, in our sample. The fact that Giapintzakis *et al.* observed their multiple peaks with $\vec{H} \parallel \hat{c}$ does not conflict with our results obtained with $\vec{H} \perp \hat{c}$: the important point is that in both cases the ac response is non-linear with penetration governed by the same parameter: the (critical) current density. We do, however, not observe a high temperature peak in the current density in Figure 8.7, but this could well be due to the subtlety of the effect in our case. A possible reason for the amplitude independence of the temperature position of the melting peak/feature is given at the end of the previous Subsection. The limited field range could be due to, at the high field end, the increased disorder that high fields can bring with them [9], totally smearing the melting transition; Safar *et al.* have reported a melting line crossing over into a vortex glass line above about 10 T [10].

11.3 Summary and conclusions

We observe anomalous loss peaks $\mu''(T)$ for the SC sample for intermediate fields $\vec{H} \perp \hat{c}$: an extra “feature” (or “peak”) appears, and the FWHM blows up dramatically.

The high temperature feature does not move in temperature when the excitation field amplitude changes while the low temperature feature moves very rapidly down in temperature and behaves roughly like the corresponding single smooth loss peaks of the MPMG sample.

Granularity cannot explain the extra feature, nor can cracks producing an “anisotropic granularity”. Misorientation, with two different penetrating systems, does not provide a consistent explanation for the anomalous loss peaks.

The two features might represent two separate phase transitions, a high temperature melting transition and a low temperature vortex glass transition observable in a limited field range. It seems plausible that the high temperature feature is a weak remnant of the melting transition, and that softening of the FLL prior to melting results in better adjustment to pinning sites causing a momentary increase, or flattening out, of the temperature dependent critical current density and hence non-smooth loss peaks.

References

- [1] T. Matsushita, E. S. Otake, B. Ni, K. Kimura, M. Hashimoto and H. Küpfer, Physica C **196** (1992) 98.
- [2] L. Krusin-Elbaum, L. Civale, T. K. Worthington and F. Holtzberg, Physica C **185-189** (1991) 2337.
- [3] E. H. Brandt, Phys. Rev. Lett. **68** (1992) 3769.
- [4] T. K. Worthington, M. P. A. Fisher, D. A. Huse, J. Toner, A. D. Marwick, T. Zabel, C. A. Feild and F. Holtzberg, Phys. Rev. B **46** (1992) 11854.
- [5] X. Ling and J. I. Budnick in *Magnetic Susceptibility of Superconductors and Other Spin Systems*, ed. R. A. Hein, T. L. Francavilla and D. H. Liebenberg, Plenum Press, New York (1991).
- [6] G. D'Anna, M.-O. Andre and W. Benoit, Europhys. Lett. **25** (1994) 225.
- [7] J. Giapintzakis, R. L. Neiman, D. M. Ginsberg and M. A. Kirk, preprint (1994).
- [8] A. M. Campbell and J. E. Evetts, Adv. Phys. **21** (1972) 199.
- [9] G. Blatter, M. V. Feigel'man, V. B. Geshkenbein, A. I. Larkin and V. M. Vinokur in *Vortices in high temperature superconductors*, preprint, ETH, Zürich (1993) 538 pages. Rev. Mod. Phys. **66** (1994) 1125.
- [10] H. Safar, P. L. Gammel, D. A. Huse, D. J. Bishop, W. C. Lee, J. Giapintzakis and D. M. Ginsberg, Phys. Rev. Lett. **70** (1993) 3800.

Magnetostriction in single crystal $\text{Bi}_2\text{Sr}_2\text{CaCu}_2\text{O}_8$

Applying a magnetic field to a conductor or superconductor will result in sample size changes: magnetostriction. Below we present measured magnetostriction hysteresis loops and relaxation curves for a platelet $\text{Bi}_2\text{Sr}_2\text{CaCu}_2\text{O}_8$ (BSCCO) single crystal. The results are viewed in terms of a pinning-induced magnetostriction model. Some related magnetization results are also included.

12.1 Introduction

Recently, Ikuta *et al.* laid out the basics for pinning-induced magnetostriction in superconductors [1]. Their simple and elegant approach was demonstrated to have very sound relevance to the measured magnetic field induced sample size changes of a single crystal BSCCO. Their pinning approach was different from the previously applied thermodynamic considerations [2–4] and also went beyond the mentioning of pinning by Isino *et al.* [5] and by Brändli and Griessen [3].

Once a field profile has been established in a sample by a field ramp or sweep, creep processes will work towards flattening the profile: the magnetization relaxes. Similarly, with relaxing field gradients, or currents, the magnetostrictive forces exerted on the sample will decrease and its zero-field size will be restored in time. Measurements of sample expansion or contraction relaxation

will therefore parallel and complement the standard $M(t)$ measurements. In fact, within the pinning-induced magnetostriction model of Ikuta *et al.* [1], the size change can be viewed as a “second order magnetization” in that it is proportional to the sample average of the difference of the *squares* of the local flux density and the external applied field, whereas the magnetization involves the average *linear* difference.

There are several ways to measure size changes with high resolution, including interferometry, tunneling and small-angle magnetization rotation [6, and References therein]. Capacitance dilatometry is a very simple but also very powerful non-destructive technique. With the attofarad resolution of a good capacitance bridge, sample size changes down to ångstrøms, or even smaller, can be resolved.

As pointed out by Ikuta *et al.* [1], a possible advantage of magnetostriction measurements over the standard magnetization measurements is that the anisotropy of the sample can be much better mapped since the size changes in different directions can be measured simultaneously and completely independently of each other and of the orientation of the applied field.

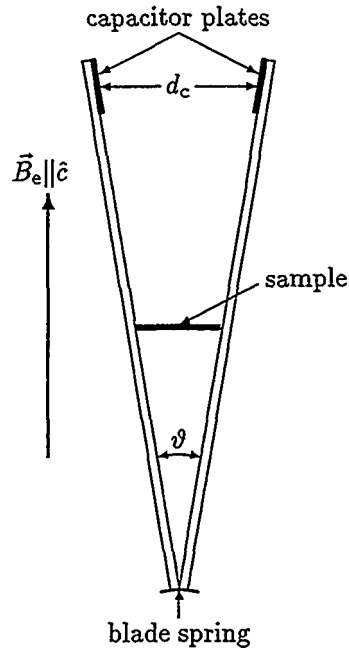
Below we report on low temperature magnetostriction measurements on a BSCCO sample, presenting hysteresis loops and relaxation curves. We make brief comparisons to complementary magnetization experiments. Section 12.2 gives the experimental details on sample, setups and methods. In Section 12.3 we lay out the phenomenology and models before we present and discuss our results in Section 12.4 and end with a summary and conclusions in Section 12.5.

12.2 Experimental

The sample used for the experiments is a BSCCO single crystal produced by the travelling solvent floating zone (TSFZ) method [7] from a starting composition of $\text{Bi}:\text{Sr}:\text{Ca}:\text{Cu} = 2:1.8:1:2$. $T_c = 87.5\text{ K}$ was determined for a sample from the same batch by SQUID measurements. The sample dimensions are $2.50 \times 2.45 \times 0.16\text{ mm}^3$, with the *c*-axis along the shortest dimension.

The external magnetic field (up to 6 T) is applied along the *c*-axis. This geometry of course complicates quantitative analysis since there will be substantial demagnetization effects. A sweep rate of 10 mT/s is used.

Figure 12.1: Schematic of the magnetostriction cell. The sample is placed halfway up between the two scissor arms. At the bottom end the arms are connected by a blade spring strong enough to bring the arms together with no sample mounted, but weak enough to not influence the measurements. At the upper ends we find the capacitor plates (gold film on quartz) with areas $A = 1.271 \text{ cm}^2$. The angle ϑ is strongly exaggerated; in the actual cell the capacitor plates are very close to being parallel ($\vartheta \sim 10^{-3}$). The plate separation $d_c \approx 50 \mu\text{m}$ during measurements. The sample dilatation is then $\Delta L = \frac{1}{2}d_c = \frac{1}{2}\epsilon_0 A(1/C - 1/C_0)$ where ϵ_0 is the vacuum permittivity and C and C_0 are the measured capacitances in field and in zero field, respectively; typical values are on the order of 10 pF.



The length changes are measured in the ab -plane, along the longest dimension of the sample, with a capacitance dilatometer made after a design by Brändli and Griessen [8]. See Figure 12.1 for a schematic drawing. The resolution in our measurements is better than 1 Å, perhaps as good as 0.1 Å.

Magnetization is measured with a vibrating sample magnetometer (VSM) with a sweep rate of 8 mT/s.

12.3 Pinning-induced magnetostriiction

Subjecting a superconducting sample to an external magnetic field will result in forces that compress or expand the sample. This is a trivial consequence of the magnetic properties of superconductors: their ability to completely or partially shield out magnetic fields will lead to inhomogeneities in the field distribution. The result can be seen as magnetic pressure exerted on the sample in thermodynamical terms and/or, in the case of type-II superconductors, through the sum of the forces felt by the sample from individual vortices acting on pinning sites under the influence of the superconducting shielding currents.

Whatever the detailed mechanism, it has been established that the magnetic pressure can damage the material: Ren *et al.* recently reported experiments on quasi-permanent magnets of high-pinning melt-textured YBCO activated at 49 K with a 14 T field. The outward magnetic pressure from the trapped field B_t was proportional to B_t^2 (in agreement with our results in (12.3) below) and was strong enough to crack the samples [9]. In fact, the work of the University of Tokyo group of Ikuta *et al.* [1] was initiated after a student kept breaking samples in high fields!

In the thermodynamic picture of Brändli [4], the starting point is a magnetic stress tensor, similar to the Maxwell tensor [10, pages 239ff] but including effects of internal field induced volume changes or deformations. Hydrostatic and shape-dependent (demagnetization) terms can be identified. Surface currents also contribute. Very good agreement between theory and experiment has been achieved [4]. Typical values for the magnetostriction, the relative size change, are on the order of 10^{-8} at fields up to 0.1 T for low-temperature type II superconducting materials [2–4]. Unfortunately, the transition to samples of high temperature superconductors is not trivial due to their more complex geometries and sizes.

A different approach focusses on pinning-induced magnetostriction [1]. The stress is here the collective result of individual vortices tending to “fall down” the field gradients inside the sample while pulling on the pinning sites they sit in (or pass through). The pinning force balances the Lorentz force, and is, per vortex and unit length and in one dimension (*i.e.* for an infinite slab geometry),

$$f_p = \frac{\Phi_0}{\mu_0} \frac{\partial B(x)}{\partial x} \quad (12.1)$$

where the flux quantum Φ_0 represents the vortex and the remaining factors make up the current density. In terms of a pinning force density F_p , the local flux density $B(x)$ is substituted for Φ_0 and we have

$$\frac{\partial \sigma(x)}{\partial x} = F_p = \frac{1}{\mu_0} B(x) \frac{\partial B(x)}{\partial x} \quad (12.2)$$

where $\sigma(x)$ is the (internal, local) stress. Solving, we have

$$\sigma(x) = -\frac{1}{2\mu_0} [B_e^2 - B(x)^2] \quad (12.3)$$

with B_e as the flux density at the sample surface. The relative total length change of the sample is the sum of all the local displacements $du = dx\sigma(x)/c_{11}$,

that is

$$\frac{\Delta L}{L} = -\frac{1}{2c_{11}\mu_0 a} \int_0^a dx [B_e^2 - B(x)^2] , \quad (12.4)$$

as derived by Ikuta *et al.* [1]. Here $L = 2a$ is the sample length and the relevant elastic constant (in the ab -plane) is $c_{11} = 125.2$ GPa [11]. The sample is symmetrically centered about $x = 0$. On this form the magnetostriiction $\Delta L/L$ resembles a “second order magnetization” since the magnetization is

$$\mu_0 M = -\frac{1}{d} \int_0^d dx [B_e - B(x)] . \quad (12.5)$$

Simulated critical state magnetostriiction and magnetization hysteresis loops require knowledge of the actual shape of the flux profiles $B(x)$ or the field dependence of the critical current density $j_c(B)$ since $\mu_0 j_c = -\partial B(x)/\partial x$. Of course, it is in principle possible to extract the $j_c(B)$ functional from experimental magnetostriiction and magnetization data, see Appendix B.

Rearranging (12.4) into

$$c_{11}\Delta L = -\frac{1}{\mu_0} \int_0^d dx [B_e^2 - B(x)^2] \quad (12.6)$$

the result apparently completes the circle and ties the connection to the thermodynamical approach and the magnetic stress tensor: the left hand side is just the elastic reaction force to the right hand side’s change in what is almost¹ the magnetic field energy due to the presence of the sample and its diamagnetic response. That is, the change in magnetic field energy goes into elastic deformation. But the actual flux profiles still have to be found, *e.g.* from considering the nature of the pinning and its effects.

A full three dimensional treatment requires solving $\nabla \bar{\sigma}(\vec{r}) = -\mu_0^{-1} \nabla \times \vec{B}(\vec{r}) \times \vec{B}(\vec{r})$ where $\bar{\sigma}(\vec{r})$ is the stress tensor. This is not trivial, especially when demagnetization plays an important role and the boundary conditions are more complicated. The simplified one dimensional approximation is nevertheless very much capable of illustrating the prominent features.

There will also be a contribution from surface “Meissner” currents to the magnetostriiction [4]. Below H_{c1} no flux will penetrate and the sample will feel a hydrostatic-like magnetic pressure from the expelled flux. But since the

¹The magnetic field energy density is $\frac{1}{2}\mu_0 H B$ whereas in (12.6) the vacuum permeability μ_0 is replaced by the actual permeability μ which varies with the applied field $H \equiv B_e/\mu_0$.

Ginzburg-Landau parameter κ is so large for high temperature superconductors, or alternatively $\mu_0 H_{c1}$ so small ($\sim 10^{-2} \text{ T}$), we can neglect this contribution since the flux densities outside and inside the surface layer are for all practical purposes equal at the fields we operate at (teslas).

Pinning does not always dictate how vortices penetrate into the sample. For thin flat samples of BSCCO single crystals, *i.e.* similar to our sample, Zeldov *et al.* have reported an irreversibility line (IL) due to geometrical barriers at high temperatures, flux penetration governed by surface barriers (surface pinning) at intermediate temperatures, but bulk pinning determines the IL below 22 K [12] where we operate. See also References [13, 14].

Relaxation

At finite temperatures, thermal fluctuations will allow finite magnetization/shielding currents j to drive vortices so as to relieve the inhomogeneous flux distribution. That is, these creep processes will break the critical state and the balance between the pinning and the Lorentz forces. The result will be a relaxing magnetostriction. See Subsection 2.3.2 for details on relaxing current density.

Quantitative comparisons of experimental data and theory call for complete knowledge of the time-dependent current profiles $j(\vec{r}, t)$, the activation barrier's current dependence $U(j)$ and the field dependence of the current $j(B)$. With the forbidding effect of demagnetization of typical sample shapes and sizes, we are left with a very complicated matter. Therefore, we will restrict ourselves to only limited quantitative analysis and focus on qualitative discussion of our experimental results.

12.4 Results and Discussion

12.4.1 Hysteresis loops

In Figure 12.2 we show measured magnetostriction loops on the BSCCO sample and include a simulated loop based on Equation (12.4) for a simplified Bean-model [15] for comparison. We notice the four fundamental characteristica of magnetostrictive behaviour in parallel fields, all reflected in Figure 12.2:

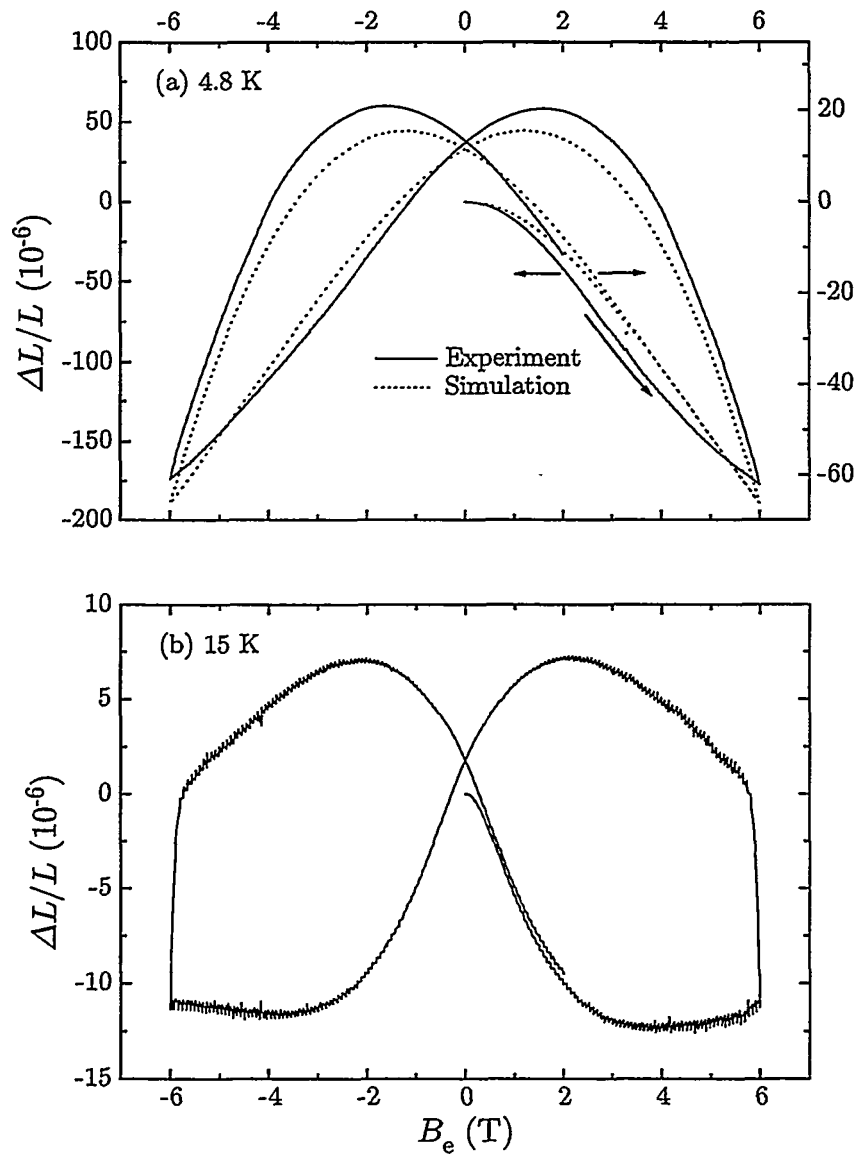


Figure 12.2: Magnetostriction hysteresis loops of the BSCCO single crystal at (a) 4.8 K and (b) 15 K. The field was applied along the crystalline c -axis and ΔL measured in the ab -plane. $d = 1.25$ mm. A Bean model simulation using the experimental parameter values and $j_c = 3 \times 10^9$ A/m 2 is included in (a). The width of the hysteresis increases and the magnitude decreases with decreasing j_c .

1. Upon increasing the applied field from zero, the sample contracts.
2. Decreasing the field from its maximum value the sample quickly expands.
3. When returning to zero applied field, the magnetostriction is still positive as $B > B_e$ everywhere in the sample.
4. The hysteresis is symmetric about $B_e = 0$, as opposed to magnetization loops.

The noise seen at 15 K is systematic; when the magnitude of the field increases during the sweep, the difference between the measured magnetostriction and a smooth approximation to it repeatedly increases slowly before suddenly falling back to approximately the initial value and starting over again. The period of these sawtooth-like oscillations is 0.08 T over the full field range, but the amplitude increases with increasing magnitude of the field and reaches about 0.5 ppm. Upon close inspection the same noise, with the same period and amplitude, is observed also at 4.8 K, but is much less visible since the signal to noise ratio is an order of magnitude larger than at 15 K. This suggests that the noise is purely an experimental artifact. The shape and the constant period of the oscillations and also the absence of any oscillations in the magnetization data in Figure 12.3 below exclude an explanation in terms of the de Haas-van Alphen effect found in metals, connected to the shape of the Fermi surface [16].

The simulated loop agrees quite well with the experimental one. The extreme demagnetization can account for the difference in magnitude of the values for the magnetostriction. We can naively approximate the sample to an ellipsoid to find the scalar $D \approx 0.9$. The effective maximum field is then $B_{\text{exp}}^{\max} = B_e^{\max} + D\mu_0 M_{\text{exp}}^{\max} \approx (6 + 0.9 \times 9) \text{ T} = 14 \text{ T}$ (M_{exp}^{\max} from Figure 12.3). Using 14 T as the maximum field, the Bean model magnetostriction simulation reaches 1.9×10^{-4} , close to the measured value.

The very large values seen at 4.8 K, on the order of 10^{-4} , indicate very large critical current densities or effective pinning. Increasing the temperature reduces j_c and hence ΔL , as seen from the data in Figures 12.2 (a) and (b). The qualitative field dependence also changes with temperature, being more prominent at the higher temperature 15 K than at the lower 4.8 K in that a local minimum is observed around 4 T when sweeping up the field. This is consistent with a stronger field dependence of j_c at higher temperatures and an almost Bean-like behaviour at the lower temperature. Using for example a field dependence of the critical current density of the form $j_c(B) = j_0 \exp(-B/B_0)$ [17] it is possible to reproduce the local minimum seen at 15 K [1].

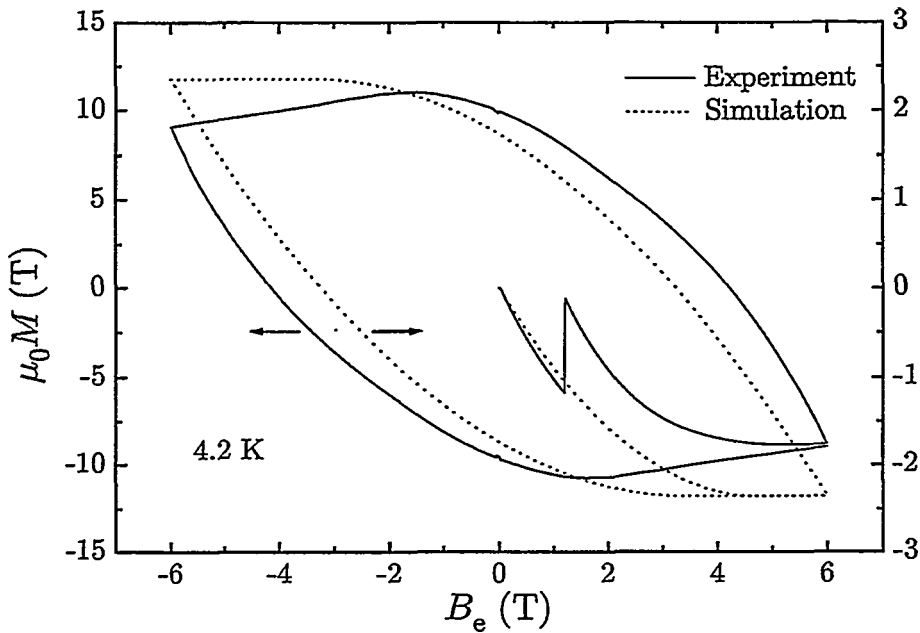


Figure 12.3: Magnetization loop of the BSCCO single crystal at 4.2 K. A Bean model simulation using the experimental parameter values and $j_c = 3 \times 10^9$ A/m² is included. The field was applied along the crystalline *c*-axis. Notice the flux jump occurring around 1 T during the initial magnetization.

In Figure 12.3 we show the magnetization loop corresponding to the magnetostriction loop in Figure 12.2 (a), only at a slightly lower temperature. A Bean-model simulated loop is included. Notice the occurrence of (what most probably is) a flux jump during the virgin magnetization process. The relatively weak field dependence after full penetration at about 2 T would justify the use of the Bean model as a first approximation at this low temperature, supporting the comparison to the Bean model in the above paragraph. A simplistic check of the correlation between the two experimental methods is to calculate j_c from the (maximum) width of the M -loop and the slope of the $\Delta L/L$ -loop within the Bean model. The results are $j_c^M \approx 14 \times 10^9$ A/m² and $j_c^{\Delta L/L} \approx 8 \times 10^9$ A/m², a difference of less than a factor 2.

12.4.2 Relaxation curves

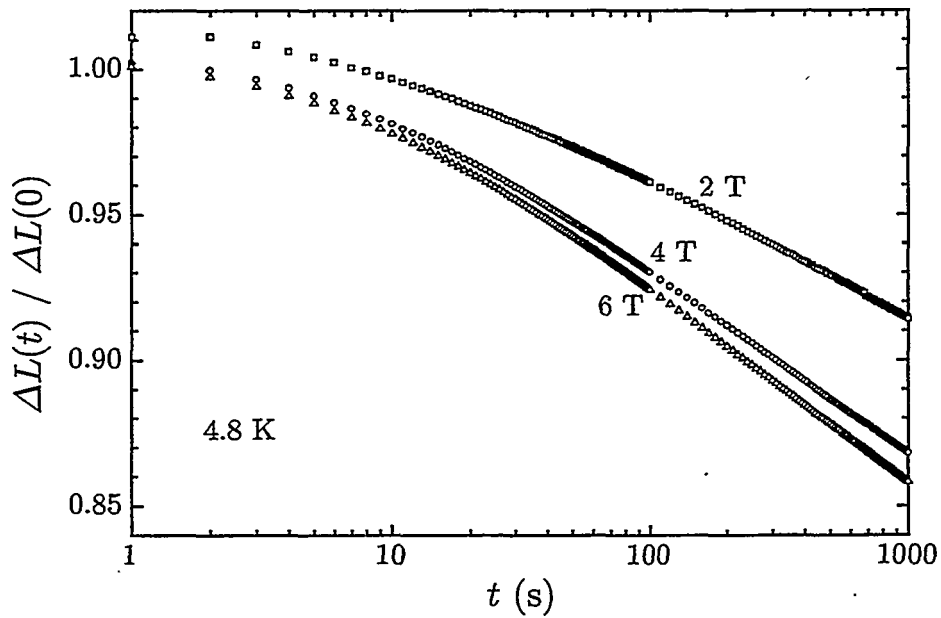


Figure 12.4: Magnetostriction relaxation at different external magnetic fields at 4.8 K. The data were recorded after increasing the field from -6 T to the indicated value.

Magnetostriction relaxation curves at different magnetic fields after increasing the field from -6 T are shown in Figure 12.4. Not surprisingly, the relaxation happens faster upon increasing the field, and is slightly faster than logarithmic at long times. The corresponding magnetization data shown in Figure 12.5 show the same change of rate with field and also the commonly observed logarithmic decay at long times. Comparing to the data in Figure 12.4, we find that even though the temperature is somewhat higher there, the magnetostriction decays slower than the magnetization. Both these characteristic agree with a Bean model approximation, as also noted by Ikuta *et al.* [18]: $M(t)$ is linear, while $\Delta L(t)$ is quadratic in $\log(t)$ (cf. Equation (12.7) below), and the normalized $M(t)$ has a larger relaxation rate than the normalized $\Delta L(t)$ since M has the opposite sign of B_e during an increasing-field sweep (cf. Figure 12.3) [19].

The very small difference between the 4 and 6 T curves in Figure 12.4 and between the 2 and 4 T curves in Figure 12.5 indicate an almost field independent j_c . The overshoot of and large gap up to the 2 T curve in Figure 12.4 may

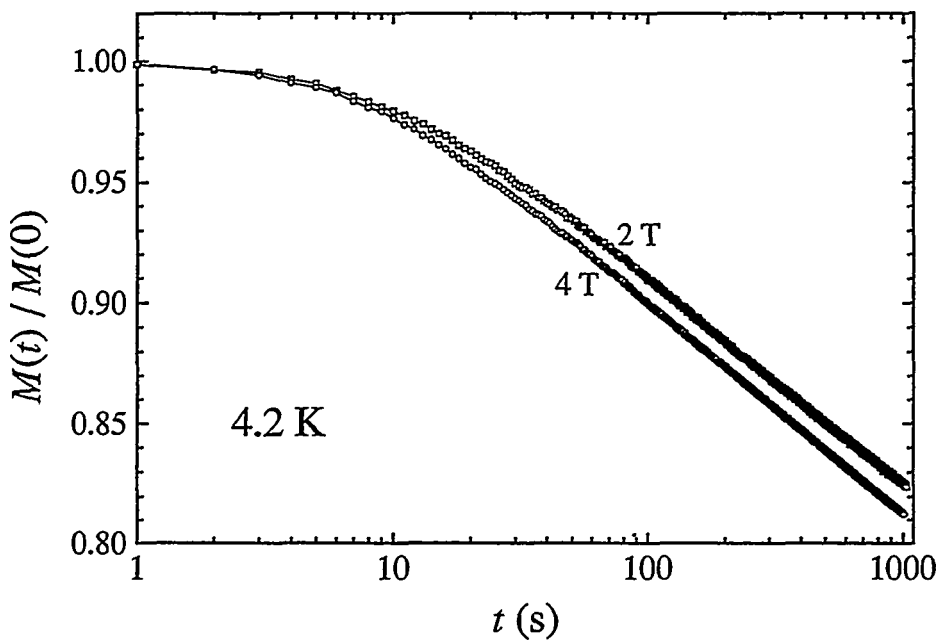


Figure 12.5: Magnetization relaxation curves at two external magnetic fields at 4.2 K.

at first appear to contradict such an interpretation of the low-temperature results. But this behaviour of lower-field curves easily fit in when we carefully take the experimental sweep history into account: With the finite values (± 6 T) for the reversal fields there will be remnants of the flux profiles from the previous sweep in the opposite direction near the sample center for low enough sweep-up fields. If the sweep up is stopped at a field smaller than, in the Bean model, the difference between the penetration field and the magnitude of the field at the sample center at -6 T, such a deviation will be observed: overshoot at short times and slower relaxation. In Figure 12.6 we plot simulated relaxing flux profiles and the corresponding magnetostriction and magnetization relaxation curves illustrating this. A reasonable choice of zero-time critical current density very nicely reproduces the observed temporal behaviour of the magnetostriction and the magnetization at different fields.

More dramatic overshoots have been observed in magnetostriction measurements on $(La_{0.93}Sr_{0.07})_2CuO_y$ [20]. These overshoots are simple consequences

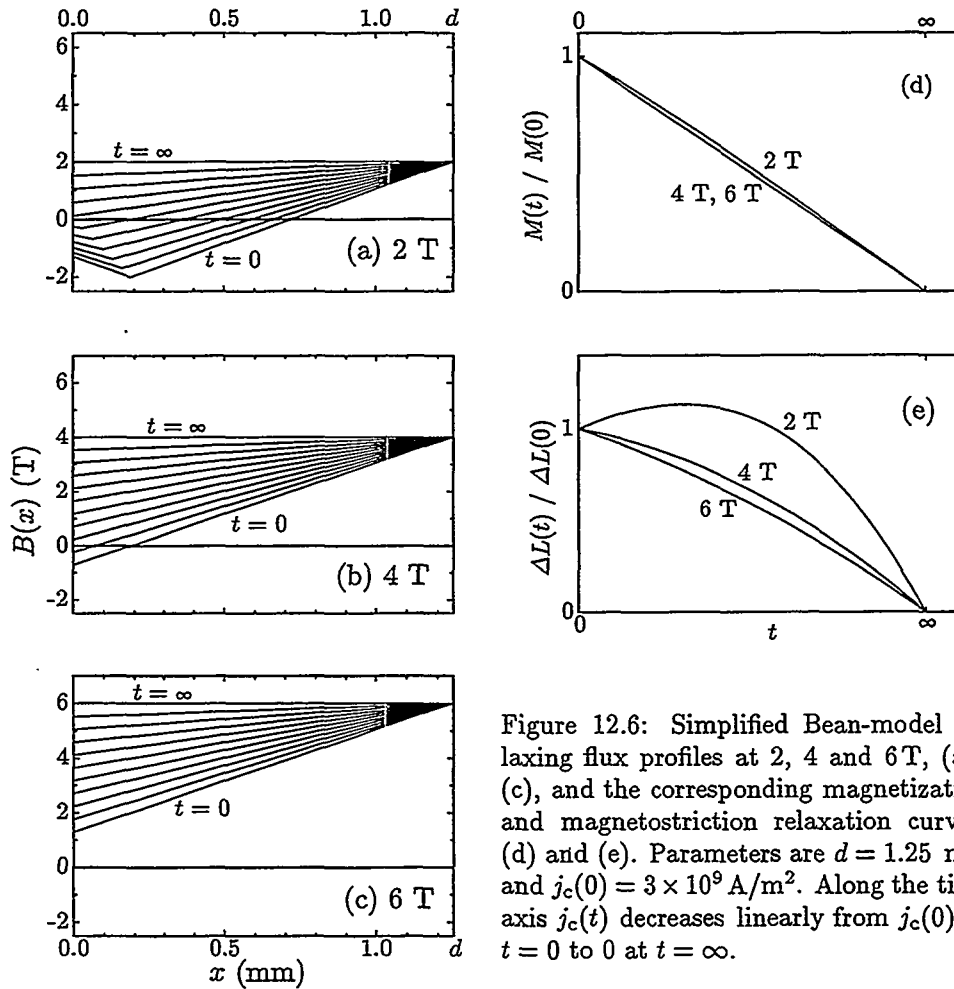


Figure 12.6: Simplified Bean-model relaxing flux profiles at 2, 4 and 6 T, (a)-(c), and the corresponding magnetization and magnetostriction relaxation curves, (d) and (e). Parameters are $d = 1.25$ mm and $j_c(0) = 3 \times 10^9 \text{ A/m}^2$. Along the time axis $j_c(t)$ decreases linearly from $j_c(0)$ at $t = 0$ to 0 at $t = \infty$.

of the time-dependent magnetostriction: within a Bean model

$$\frac{\Delta L(t)}{L} = -\frac{B_e d}{2c_{11}} j_c(t) + \frac{\mu_0 d^2}{6c_{11}} j_c(t)^2 \quad (12.7)$$

when the $t = 0$ profile is a single straight line, that is, it has general validity only for infinite reversal field values. The parabolic j_c -dependence opens up for exotic relaxation curves with overshoots and zero-crossings under the right circumstances, *i.e.* for different initial j_c values: (a) Standard, monotonic relaxation curves are observed when $j_c(0) < 3B_e/2\mu_0 d$ (a in Figure 12.7), (b) overshoots if $3B_e/2\mu_0 d < j_c(0) < 3B_e/\mu_0 d$ (b in Figure 12.7), and (c) zero-crossings if $j_c(0) > 3B_e/\mu_0 d$ (c in Figure 12.7).

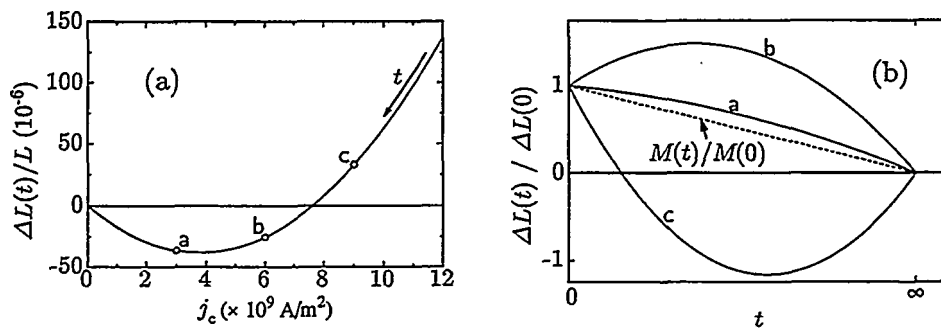


Figure 12.7: (a) Time-parametric plot of magnetostriction *vs.* current density, which decreases with time, in a Bean approximation with infinite reversal fields, cf. Equation (12.7). The parabolic shape opens up for the exotic relaxation curves in (b) whereas the linear $M(j_c(t)) = -j_c(t)d/2$ does not. The points a–c refer to different relaxation starting points resulting in the qualitatively different relaxation curves seen in (b) (see text). The straight dashed line in (b) is the magnetization relaxation curve $M(t)/M(0) = j_c(t)/j_c(0)$, the same for all fields and initial values of j_c on this axis where $j_c(t)$ decreases linearly from $j_c(0)$ at $t = 0$ to 0 at $t = \infty$. Here $d = 1.25$ mm and $B_e = 4$ T.

The overshoot and gap could also be experimental artifacts, results of a time lag in the logging of the capacitance: The capacitance was in some cases observed to be fed from the capacitance bridge to the computer after a delay of 2–3 seconds. If this is the case for the 2 T curve in Figure 12.4, the time origin for this curve should be shifted to $t = 2\text{--}3$ s and ΔL normalized against $\Delta L(2\text{--}3\text{s})$. But this can not explain the large gap at long times, and dividing by a factor ≈ 1.01 does not eliminate the gap either, only marginally reduces it.

Increasing the temperature will lead to an increased relaxation rate. In Figure 12.4, at 4.8 K, the magnetostriction is reduced by less than 6% after 1000 s. In Figure 12.8, at 15 K, however, it is flattening out around the 30% level after the same time lapse — a truly dramatic change. We also see in Figure 12.8 that the 2 T curve is about to cross and go below the 4 T curve after 1000 s, a puzzling behaviour that we fail to explain.

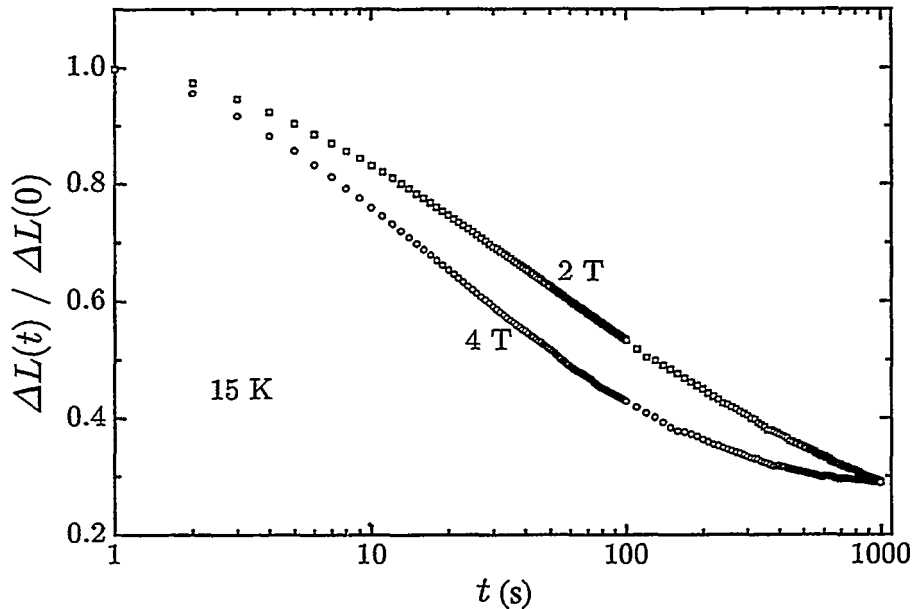


Figure 12.8: Magnetostriiction relaxation at two external magnetic fields at 15 K.

12.5 Summary and Conclusions

We have observed dramatic size changes in a single crystal BSCCO sample in magnetic fields up to 6 T. The behaviour is in accord with the pinning-induced magnetostriiction model. Left to relax, the sample size was restored slower than the magnetization vanished. An overshoot in a magnetostriiction relaxation curve taken at 2 T is explained in terms of the time evolution of a flux profile taking the field sweep history carefully into account.

While our work has not concentrated on making careful quantitative comparisons since the large demagnetization effects prohibit this, such analysis can be made if the field is applied along the *ab*-plane of the sample to minimize demagnetization effects [21].

Our results showing giant magnetostriiction demonstrate how when using high-temperature superconductors care should be taken to ensure that the materials do not break under applied magnetic pressure.

References

- [1] H. Ikuta, N. Hirota, Y. Nakayama, K. Kishio, and K. Kitazawa, Phys. Rev. Lett. **70** (1993) 2166.
- [2] G. Brändli and F. D. Enck, Phys. Lett. **26 A** (1968) 360 and Errata **27A** No. 1 (1968).
- [3] G. Brändli and R. Griessen, Phys. Rev. Lett. **22** (1969) 534.
- [4] G. Brändli, Phys. Kondens. Mater. **11** (1970) 93; *ibid.* **111**.
- [5] M. Isino, T. Kobayashi, N. Toyota, T. Fukase, and Y. Muto, Phys. Rev. B **38** (1988) 4457.
- [6] R. A. Brizzolara and R. J. Colton, Journal of Magnetism and Magnetic Materials **88** (1990) 343.
- [7] N. Motohira *et al.*, J. Ceram. Soc. Jpn. **97** (1989) 994.
- [8] G. Brändli and R. Griessen, Cryogenics **13** (1973) 299.
- [9] Y. Ren, R. Weinstein, J. Liu, R. P. Sawh and C. Foster, submitted to Physica C (April 1995).
- [10] J. D. Jackson, *Classical Electrodynamics*, 2nd ed., John Wiley & Sons, New York (1975).
- [11] M. Boekholt, J. V. Harzer, B. Hillebrands, and G. Güntherodt, Physica C **179** (1991) 101. J. Wu, Y. Wang, H. Shen, J. Zhu, Y. Yan, and Z. Zhao, Phys. Lett. A **148** (1990) 127 report a value $c_{11} = 1.3 \times 10^{11}$ Pa.
- [12] E. Zeldov, D. Majer, M. Konczykowski, A. I. Larkin, V. M. Vinokur, V. B. Geshkenbein, N. Chikumoto and H. Shtrikman, preprint, submitted to Phys. Rev. Lett.

- [13] E. Zeldov, A. I. Larkin, V. B. Geshkenbein, M. Konczykowski, D. Majer, B. Khaykovich, V. M. Vinokur and H. Shtrikman, preprint, submitted to Phys. Rev. Lett.
- [14] E. Zeldov, A. I. Larkin, M. Konczykowski, B. Khaykovich, D. Majer, V. B. Geshkenbein and V. M. Vinokur, Physica C **235–240** (1994) ???.
- [15] C. P. Bean, Rev. Mod. Phys. **36** (1964) 31.
- [16] See for example N. W. Ashcroft and N. D. Mermin, *Solid State Physics*, Saunders College, USA (1976) Chapter 14.
- [17] P. Chaddah, K. V. Bhagwat, and G. Ravikumar, Physica C **159** (1989) 570.
- [18] H. Ikuta, N. Hirota, L. K. Heill, K. Kishio, and K. Kitazawa, Physica B **194–196** (1994) 1847.
- [19] L. K. Heill, H. Ikuta, N. Hirota, Y. Nakayama, K. Kishio, and K. Kitazawa, Physica C **235–240** (1994) 2925.
- [20] H. Ikuta, K. Kishio and K. Kitazawa, J. Appl. Phys. **76** (1994) 4776.
- [21] A. Schmidt, F. Stellmach and S. Ewert, Physica B **194–196** (1994) 1787.

ac permeability of an infinite slab in the Bean critical state

[This Appendix is a typeset *Maple V3* worksheet. It is perhaps not very pedagogical, but at least the author understands what goes on.]

We introduce the reduced profiles

$$\beta(u, \tau, \xi) = \frac{b_{\text{ac}}(u, \tau, \xi)}{\mu_0 h_{\text{ac}}} \quad (\text{A.1})$$

where $u = h_{\text{ac}}/j_c a$ is the reduced penetration depth, $\tau = \omega t$ and $\xi = x/a$ is the reduced position:

$$\beta_0(u, \xi) = 1 - \frac{1 - \xi}{u} \quad (\text{A.2})$$

$$\beta_1(u, \tau, \xi) = \cos \tau + \frac{1 - \xi}{u} \quad (\text{A.3})$$

$$\beta_2(u, \tau, \xi) = \cos \tau - \frac{1 - \xi}{u} \quad (\text{A.4})$$

β_0 is the initial profile, β_1 the decreasing part of the profile as the applied field decreases during the first half period, and β_2 is the increasing part of the profile during the second half period. For $u < 1$, we integrate $\beta(u, \tau, \xi)$ from $\xi_m = \max(0, 1 - u)$ to $\xi = 1$ via the peak at $\xi_p = \max(0, 1 - u(1 - \cos \tau)/2)$ to obtain the average induction $\bar{b}(u, \tau)$ (ξ_m is the innermost point the flux can reach in to, and ξ_p is the point where the positive and negative slope parts of

the profile meet):

$$\xi_{m,u<1}(u) = 1 - u \quad , \quad \xi_{m,u>1} = 0 \quad , \quad \xi_p(u, \tau) = 1 - u \frac{1 - \cos \tau}{2} \quad (\text{A.5})$$

τ_0 is the time at which $\xi_p(u, \tau)$ goes negative for $u > 1$, and ξ_p should be set to zero ($\xi_p(u, \tau)$ really equals $\max(0, 1 - u(1 - \cos \tau)/2)$, but we can split this in the time τ instead for $u > 1$. $\xi_p(u, \tau) > 0$ for $u < 1$):

$$\tau_0(u) = \arccos\left(1 - \frac{2}{u}\right) \quad (\text{A.6})$$

The average induction for $u < 1$ (we should later perform time integration from $\tau = 0$ to $\tau = 2\pi$, but the symmetry in the problem makes the two halves, from $\tau = 0$ to $\tau = \pi$ and from $\tau = \pi$ to $\tau = 2\pi$, equal: $\int_0^\pi d\tau \bar{b} \cos \tau = \int_\pi^{2\pi} d\tau \bar{b} \cos \tau$, since $\bar{b}(\tau > \pi) = -\bar{b}(\tau - \pi)$ and $\cos(\tau - \pi) = -\cos(\tau)$ and $\sin(\tau - \pi) = -\sin(\tau)$.) The average ac induction calculated from the all the relevant linear parts of the profile is then

$$\bar{b}_{u<1}(u, \tau) = \frac{u}{4} + \frac{u}{2} \cos(\tau) - \frac{u}{4} \cos(\tau)^2 \quad (\text{A.7})$$

The average induction for $u > 1$ before $\xi_p(u, \tau)$ goes negative (at $\tau_0(u)$) is

$$\begin{aligned} \bar{b}_{u>1,1}(u, \tau) &= \left(1 - u \frac{1 - \cos \tau}{2}\right) + \cos \tau - \left(1 - u \frac{1 - \cos \tau}{2}\right) \cos \tau \\ &\quad - \frac{3}{2u} \left(1 - u \frac{1 - \cos \tau}{2}\right) + \frac{1}{u} \left(1 - u \frac{1 - \cos \tau}{2}\right)^2 \end{aligned} \quad (\text{A.8})$$

The average induction for $u > 1$ after $\xi_p(u, \tau)$ goes negative (at $\tau_0(u)$) is

$$\bar{b}_{u>1,2}(u, \tau) = \cos \tau + \frac{1}{2u} \quad (\text{A.9})$$

The ac permeability for $u < 1$ is then

$$\mu'_{u<1}(u) = \frac{2}{\pi} \int_0^\pi d\tau \cos \tau \bar{b}_{u<1}(u, \tau) \quad (\text{A.10})$$

$$\mu''_{u<1}(u) = \frac{2}{\pi} \int_0^\pi d\tau \sin \tau \bar{b}_{u<1}(u, \tau) \quad (\text{A.11})$$

For $u > 1$ (time integral split in two around $\tau_0(u)$):

$$\mu'_{u>1}(u) = \frac{2}{\pi} \left(\int_0^{\tau_0(u)} d\tau \cos \tau \bar{b}_{u>1,1}(u, \tau) \right)$$

$$+ \int_{\tau_0(u)}^{\pi} d\tau \cos \tau \bar{b}_{u>1,2}(u, \tau) \Big) \quad (\text{A.12})$$

$$\begin{aligned} \mu''_{u>1}(u) = & \frac{2}{\pi} \left(\int_0^{\tau_0(u)} d\tau \sin \tau \bar{b}_{u>1,1}(u, \tau) \right. \\ & \left. + \int_{\tau_0(u)}^{\pi} d\tau \sin \tau \bar{b}_{u>1,2}(u, \tau) \right) \end{aligned} \quad (\text{A.13})$$

So, finally, we get the very simple result for $u < 1$:

$$\mu'_{u<1}(u) = \frac{1}{2}u, \quad \mu''_{u<1}(u) = \frac{2}{3\pi}u \quad (\text{A.14})$$

And for $u > 1$ we get, after tidying up:

$$\begin{aligned} \mu'_{u>1}(u) = & 1 + \frac{4}{3\pi} \left(1 - \frac{1}{u} \right) \sqrt{\frac{1}{u} - \frac{1}{u^2}} - \frac{u}{\pi} \sqrt{\frac{1}{u} - \frac{1}{u^2}} \\ & - \left(\frac{1}{\pi} - \frac{u}{2\pi} \right) \arccos \left(1 - \frac{2}{u} \right) \end{aligned} \quad (\text{A.15})$$

$$\mu''_{u>1}(u) = \frac{2}{\pi u} \left(1 - \frac{2}{3u} \right) \quad (\text{A.16})$$

The loss peak has its maximum value

$$\mu''_{\max} = \mu''_{u>1,max} = \frac{3}{4\pi} \quad (\text{A.17})$$

at $u = 4/3$.

Critical current density from magnetization and magnetostriiction data

It is possible to derive the functional dependence of the critical current density on magnetic field from measurements of magnetization and/or magnetostriiction.

We have for the magnetization $\mu_0 M \equiv S_M$ and the magnetostriiction $\Delta L/L \equiv S_\Delta$

$$S_M = -\frac{1}{a} \int_0^a dx [B_e - B(x)] = -\frac{1}{a} \left[B_e a - \int_{x_0}^a dx B(x) \right] \quad (\text{B.1a})$$

$$\begin{aligned} S_\Delta &= -\frac{1}{2c_{11}\mu_0 a} \int_0^a dx [B_e^2 - B(x)^2] \\ &= -\frac{1}{2c_{11}\mu_0 a} \left[B_e^2 a - \int_{x_0}^a dx B(x)^2 \right] \end{aligned} \quad (\text{B.1b})$$

where $x_0 = \max\{0, B_e/\mu_0 j_c(B_e)\}$. Assuming the critical state model applies, we have

$$\frac{dB}{dx} = -\mu_0 j_c(B) \Rightarrow dx = -\frac{dB}{\mu_0 j_c(B)} \quad (\text{B.2})$$

and may then rewrite the integrals:

$$S_M = -\frac{1}{\mu_0 a} \int_{B(x_0)}^{B_e} dB \frac{B}{j_c(B)} - B_e \quad (\text{B.3a})$$

$$S_{\Delta} = -\frac{1}{2c_{11}\mu_0^2 a} \int_{B(x_0)}^{B_e} dB \frac{B^2}{j_c(B)} - \frac{1}{2c_{11}\mu_0} B_e^2 . \quad (\text{B.3b})$$

The derivatives with respect to the applied field B_e are

$$\frac{\partial S_M}{\partial B_e} = -\frac{1}{\mu_0 a} \frac{B_e}{j_c(B_e)} - 1 \quad (\text{B.4a})$$

$$\frac{\partial S_{\Delta}}{\partial B_e} = -\frac{1}{2c_{11}\mu_0^2 a} \frac{B_e^2}{j_c(B_e)} - \frac{1}{c_{11}\mu_0} B_e , \quad (\text{B.4b})$$

giving the following expressions for the critical current density:

$$j_c(B_e) = -\frac{1}{\mu_0 a} \frac{B_e}{1 + \partial S_M / \partial B_e} \quad (\text{B.5a})$$

$$j_c(B_e) = -\frac{1}{2\mu_0 a} \frac{B_e^2}{B_e + c_{11}\mu_0 \partial S_{\Delta} / \partial B_e} . \quad (\text{B.5b})$$

These expressions can be used to extract the field dependence of the critical current from the measured quantities S_M and/or S_{Δ} .

Without demagnetization the above expressions for j_c are valid in the sense that we can plug in nominal (magnet) field values B_e and measured values for S_M and/or S_{Δ} and obtain the "true" $j_c(B)$ functional.

However, with a realistic geometry demagnetization effect must be taken into account. The effective field B_{eff} is

$$B_{\text{eff}} = B_e - D \cdot \mu_0 M(B_e) \quad (\text{B.6})$$

where the demagnetization factor D may well be non-scalar. Here we assume a scalar D for simplicity. With B_{eff} as the "real" field, we have

$$j_c(B_{\text{eff}}) = -\frac{1}{\mu_0 a} \frac{B_{\text{eff}}}{1 + \partial S_M / \partial B_e} \quad (\text{B.7a})$$

$$j_c(B_{\text{eff}}) = -\frac{1}{2\mu_0 a} \frac{B_{\text{eff}}^2}{B_{\text{eff}} + c_{11}\mu_0 \partial S_{\Delta} / \partial B_e} \quad (\text{B.7b})$$

with $\partial S_M / \partial B_e$ and $\partial S_{\Delta} / \partial B_e$ as measured quantities and B_{eff} as a derived quantity being functions of the applied nominal field B_e .